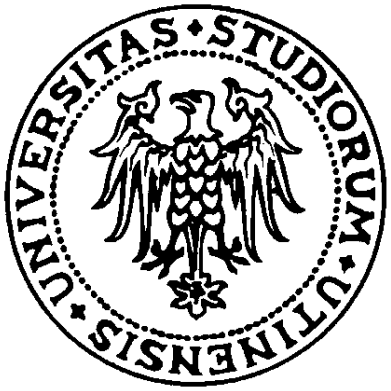

UNIVERSITÀ DEGLI STUDI DI UDINE

Facoltà di Ingegneria

Dottorato in Ingegneria Industriale e dell'Informazione

Dipartimento di Ingegneria Elettrica, Gestionale e Meccanica

Tesi di Dottorato

NUMERICAL ANALYSIS OF COUPLED THERMAL-ELECTROMAGNETIC PROBLEMS IN SUPERCONDUCTING CABLES

Supervisore:
Prof. Fabrizio Bellina

Dottorando:
Giulio Manfreda

Coordinatore:
Prof. Paolo Gardonio

Ciclo XXVII

Struck me kinda funny seemed kind of funny sir to me
How at the end of every hard earned day people find some reason to believe.
Bruce Springsteen, Reason To Believe

To my "old" and "new" families,
that are my reason to believe.

Contents

Abstract

Superconducting materials, being characterized by a negligible electrical resistance under peculiar working conditions, provide extraordinary electromagnetic performances. The research field on electromagnets has taken a lot of advantages from this technology, since the huge electrical current densities that these materials sustain enable to produce very strong magnetic fields, up to more than 10 T, with negligible losses compared to the normal-conducting coils. The development of superconductors technology during the last years has enabled projects that only some decades ago were considered not feasible, both technically and economically. Among them, the most notable are fusion reactors like *ITER*, presently under construction in Cadarache (France), and particle accelerators for high energy physics such as the *Large Hadron Collider* (LHC) operating at CERN in Geneva (Switzerland).

The present work regards the *THELMA code*, a coupled thermal-electromagnetic numerical model for the description of superconducting cables and magnets. This software was initially intended for the simulation of the electromagnetic behavior in the so-called *Cable-In-Conduit-Conductors* (CICC), largely used in fusion machines like ITER. During the PhD activity, a brand-new thermal model has been developed and added to the pre-existing code to describe problems in which the system thermal evolution cannot be assessed a priori. Moreover, the code has been extended to deal also with the *Rutherford cables*, a type of superconducting cable widely used in accelerator magnets like those of LHC. Finally, the code has been applied to several case studies, both in the field of accelerator and fusion magnets.

This thesis is structured in the following way.

The first two chapters are a general introduction to superconductivity: the first is a presentation of this phenomenon and its applications, intended for readers that are not familiar with this technology, whereas the second is a more detailed description of the superconducting wires and cables studied during this PhD activity.

In the second part of the thesis, the THELMA numerical code is widely described. In chapter 3, the geometrical, electromagnetic and thermal models are presented, with a particular focus on the brand-new parts developed during this PhD activity, such as the Rutherford cable geometrical model, the thermal model and the coupling among electromagnetic and thermal routines. The THELMA model for electrical and thermal contact resistances is instead widely explained in chapter 4, together with the numerical analysis of several experimental measurements on both

Rutherford and CICC cables.

The third part of the work is instead focused on some examples of the application of the THELMA coupled code, performed during the PhD activity. In chapter 5 the analysis of the voltage-temperature characteristic on a CICC sample is presented, as a validation and an example of the code capability of reproducing non-trivial experimental findings. In chapter 6, the problem of the longitudinal propagation of a thermal-electromagnetic instability (quench) in impregnated Rutherford coils is analyzed with experimental, analytical and numerical tools. In chapter 7, the predictive analyses in terms of current distribution and losses in the CICC magnet NAFASSY are reported. Further details regarding useful material properties and some analytical and numerical models can be found in the appendices.

Sommario

I materiali superconduttori, essendo caratterizzati in particolari condizioni da una resistenza elettrica trascurabile, offrono straordinarie prestazioni elettromagnetiche. La ricerca sugli elettromagneti ha ottenuto notevoli vantaggi da questa tecnologia, in quanto le enormi densità di corrente elettrica che questi materiali sopportano possono essere usate per generare campi magnetici estremamente intensi, anche maggiori di 10 T, con delle perdite trascurabili in confronto agli avvolgimenti normoconduttivi. Lo sviluppo della tecnologia dei superconduttori avvenuto negli ultimi anni ha permesso progetti che solo pochi decenni fa erano considerati irrealizzabili, sia dal punto di vista tecnico che economico. Tra questi, i più importanti sono senz'altro i reattori per fusione nucleare come *ITER*, attualmnente in costruzione a Cadarache (Francia), e acceleratori di particelle per la fisica delle alte energie come il *Large Hadron Collider* (LHC) del CERN a Ginevra (Svizzera).

In questa tesi viene presentato il codice *THELMA*, un modello numerico per la descrizione accoppiata del comportamento termo-elettromagnetico di cavi e magneti superconduttori. Questo codice era stato inizialmente creato per la simulazione del comportamento elettromagnetico dei cosiddetti *Cable-In-Conduit-Conductors* (CICC), ampiamente usati in macchine per la fusione nucleare come ITER. Durante l'attività di dottorato, è stato implementato un nuovo modello termico in aggiunta al codice preestitente, in grado di descrivere problemi nei quali l'evoluzione termica del sistema non può essere prevista a priori. Inoltre, il codice è stato esteso per descrivere i *cavi di tipo Rutherford*, usati comunemente nei magneti per acceleratori di particelle come quelli di LHC. Infine, il codice è stato applicato per l'analisi di diversi casi di studio, sia nell'ambito dei magneti per acceleratori di particelle che per fusione nucleare.

La tesi è strutturata nella seguente maniera.

I primi due capitoli sono un'ampia introduzione alla superconduttività: il primo è una presentazione generale di questo fenomeno e sulle sue applicazioni, pensata per chi non dovesse avere familiarità con questa tecnologia, mentre il secondo contiene una descrizione più dettagliata dei fili e cavi superconduttori presi in considerazione durante questo dottorato di ricerca.

Una descrizione dettagliata del codice numerico THELMA è invece riportata nella seconda parte della tesi. Nel capitolo 3 vengono presentati i modelli geometrici, elettromagnetici e termici, con particolare dettaglio relativamente alle parti svilup-

pate durante l'attività di dottorato, quali il modello geometrico del cavo Rutherford, il modello termico e l'accoppiamento tra il modello termico e quello elettromagnetico. Il modello di THELMA per le resistenze di contatto elettriche e termiche è invece descritto nel capitolo 4, insieme all'analisi numerica di alcuni misure sperimentali sia su cavi Rutherford che CICC.

La terza parte della tesi è invece focalizzata su alcuni esempi di applicazione del codice accoppiato THELMA, svolti durante l'attività di dottorato. Nel capitolo 5 viene analizzata la caratteristica tensione-temperatura di un campione di cavo CICC, quale esempio di validazione sperimentale nella quale il codice è in grado di riprodurre fenomeni di difficile comprensione. Il capitolo 6 presenta il problema della propagazione longitudinale di un'instabilità termo-elettromagnetica in avvolgimenti impregnati di cavi Rutherford, analizzato con strumenti sperimentali, analitici e numerici. Nel capitolo 7 sono invece descritte le analisi predittive in termini di perdite e distribuzione di corrente riguardo il magnete CICC NAFASSY. Ulteriori dettagli riguardanti le proprietà dei materiali e alcuni modelli analitici e numerici sono infine riportati nelle appendici.

Part I

Introduction

Chapter 1

Superconductivity and its Applications

Superconductivity has been discovered about one century ago. A lot of effort has been put in these years by physicists and engineers to understand the non-trivial properties of this state of matter, in order to take these materials out of the laboratories and employ them in industrial applications. In this chapter the characterizing properties of superconducting materials will be described, together with the milestones in their discovery. These materials will be then classified according to their thermal, magnetic and electric behavior. Some theoretical models will be briefly summarized, and a description of the typical parameters used for the experimental characterization of practical samples will follow. Finally, the most important areas in which applied superconductivity is employed will be presented. They cover almost all the engineering spectrum, ranging from high performance electromagnets to very high precision detectors, from magnetic levitation to electric power transfer and electronics.

1.1 The Discovery of Superconductivity

In 1908 the Dutch physicist *Heike Kammerlingh Onnes* was the first scientist able to liquefy helium [135], a discovery that granted him the Nobel Prize in 1913. The liquid phase of a substance cannot exist over the so-called *critical point*, that is only 5.1953 K at a pressure of 0.22746 MPa for helium. Thus, Onnes had to use several pre-cooling cycles to reach such low temperatures in his laboratory in Leiden, that became at the time the coldest place on Earth. This achievement is one of the most important discoveries of the previous century, since it permits to investigate physical conditions that previously were completely inaccessible.

One of the most striking surprises in this new field of investigation was found by Onnes himself in 1911, during his studies on the electrical behavior of metals at very low temperatures. In 1900, Paul Drude already postulated that the electric resistance in metals is a consequence of the free electrons scattering produced by the ions of the crystal lattice. These interactions stop at absolute zero temperature, nullifying the resistance in a pure crystal, whereas a real sample exhibits a residual resistivity related to the scattering produced by impurities. This model is valid for a large class of metals, with copper, silver, aluminum among the others. As an example, the copper resistivity ρ_E as a function of temperature is plotted in Figure 1.1, whereas a detailed description of material properties at very low temperature is reported in Appendix A.

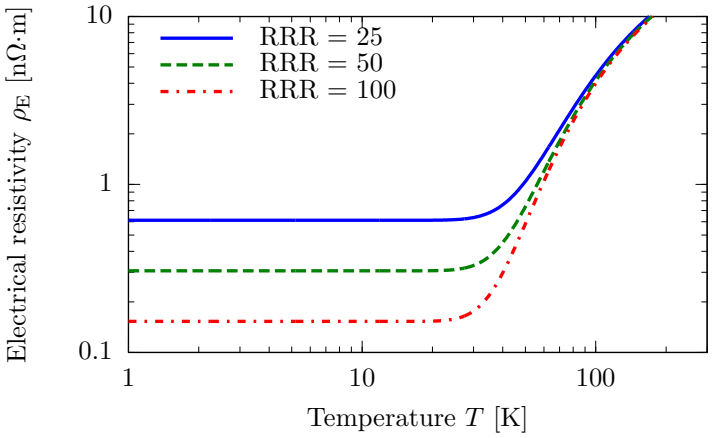

Figure 1.1: Copper electrical resistivity as a function of temperature for three different levels of residual resistivity ratio (RRR), with data from [113]. At low temperatures the constant contribution of the impurities is evident.

However, at the beginning of the 20$^{\text{th}}$ century the actual behavior of metals at very low temperatures was still an unsolved problem, since scientists like Lord Kelvin assumed a strong resistivity increase near absolute zero due to diminished electron mobility [170]. Therefore Onnes was interested to find proofs or denials to these theories. Against all expectations, he found a sudden drop in the electrical

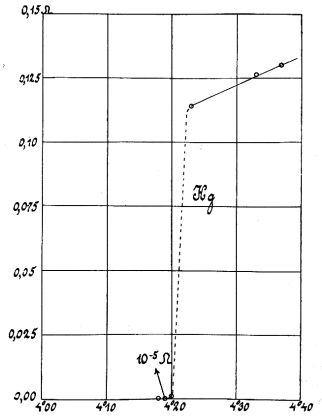

Figure 1.2: Electrical resistance of a mercury sample at low temperature as measured by Onnes in 1913 [136].

resistivity ρ_{E} of mercury at about 4.2 K. In Figure 1.2 Onnes' measurements [136] are reported. These results were in contrast with all available theoretical models, and were therefore considered the sign of a new state of matter, that was named *superconductivity*. Many elements and composites exhibit this transition at different *critical temperatures* T_{c} .

Some years after, it was also discovered that a superconductive specimen is not simply a *perfect conductor*, that is a material characterized by $\rho_{\mathrm{E}} = 0$. In Figure 1.3 the behavior in applied magnetic field of a superconductor and of a perfect conductor is compared. No difference can be found if the magnetic field is applied after the change of state from normal conductivity, as reported in Figure 1.3a. Both specimens would exclude the magnetic field from their interior because of the screening supercurrents that would be induced on the surfaces of the samples according to Faraday-Neumann-Lenz law . These screening currents are induced also on normal conductors but they are quickly dumped because of the Joule losses, whereas they persist if the resistivity is zero. On the other hand, a different behavior is observed if the change of state happens after the application of an external magnetic field, as in Figure 1.3b. A perfect conductor should indeed trap and maintain the magnetic field present inside before the change of state, whereas a superconductor exhibit the *perfect diamagnetism*, that is the complete expulsion of magnetic flux for the interior of the sample. This unexpected effect was first observed by the German physicists *Fritz Walther Meissner* and *Robert Ochsenfeld* in 1933 [121].

1.2 Theory of Superconductivity

Many theoretical physicists tried to explain the unexpected properties of the superconducting samples. In this section the most important models that have been proposed will be briefly summarized.

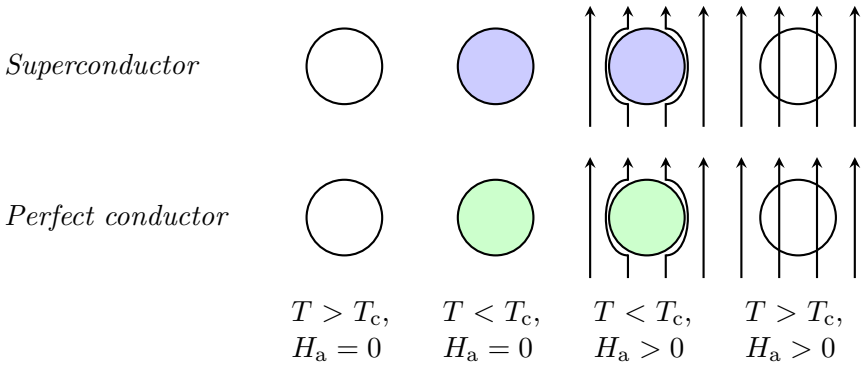

(a) Field applied after the change of state.

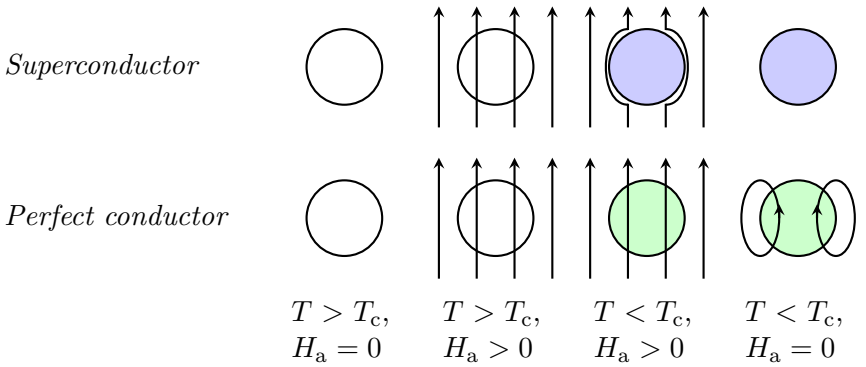

(b) Field applied before the change of state.

Figure 1.3: Behavior of a superconductor and of a perfect conductor in an applied magnetic field H_a.

1.2.1 Phenomenological Models

In 1934 *Cornelis Jacobus Gorter* and *Hendrik Brugt Gerhard Casimir* [76] proposed a phenomenological model in which the superconductor is represented as the superposition of two fluids, one composed by normal-conducting carriers and one with a concentration n_s per unit volume of *superelectrons* that are responsible of the superconductivity. This assumption was the basis for the *London Equations*, developed by the brothers *Fritz* and *Heinz London* in 1935 [102], the first model capable to explain the perfect diamagnetism in superconductors. The model can be deduced starting from the Drude equation for an electron with mass m and charge $-e$:

$$m\frac{\mathrm{d}\mathbf{v}_{el}}{\mathrm{d}t} = -e\mathbf{E} - \frac{m\mathbf{v}_{el}}{\tau_{scat}}, \tag{1.1}$$

where $\mathbf{v}_{el}$ is the particle velocity, $\mathbf{E}$ an applied electric field and τ_{scat} the scattering relaxation time. For a non-resistive material $\tau_{scat} \to \infty$, therefore the second term

of the second member of Eq. (1.1) vanishes. Defining the transport super-current density due to superelectrons as $\mathbf{J}_\mathrm{t} = -n_\mathrm{s} e \mathbf{v}_\mathrm{el}$, the *first London equation* can be obtained:

$$\frac{\mathrm{d}(\Lambda \mathbf{J}_\mathrm{t})}{\mathrm{d}t} = \mathbf{E}, \tag{1.2}$$

where

$$\Lambda = \frac{m}{n_\mathrm{s} e^2}. \tag{1.3}$$

Equation (1.2) replaces for a perfect conductor the Ohm's law, but it is not able to take into account the Meissner-Ochsenfeld effect. Indeed, applying the Maxwell equations:

$$\nabla \times \mathbf{E} = -\frac{\mathrm{d}\mathbf{B}}{\mathrm{d}t}, \tag{1.4}$$

$$\nabla \times \mathbf{H} = \mathbf{J}_\mathrm{t}, \tag{1.5}$$

together with Eq. (1.2), the following equation for the magnetic field can be obtained:

$$\nabla^2 \frac{\mathrm{d}\mathbf{H}}{\mathrm{d}t} = \frac{\mu_0}{\Lambda} \frac{\mathrm{d}\mathbf{H}}{\mathrm{d}t}. \tag{1.6}$$

A time and space independent solution $\mathbf{H}(\mathbf{r}, t) = \mathbf{H}_0$ for this equation exists, and this is incompatible with perfect diamagnetism since the magnetic field must decay inside the superconductor. Thus, the *second London equation* is considered:

$$\nabla \times (\Lambda \mathbf{J}_\mathrm{t}) = -\mathbf{B}, \tag{1.7}$$

where $\mathbf{B}$ is the magnetic induction. Applying Eq. (1.7) together with Eq. (1.5) the following result can be obtained:

$$\nabla^2 \mathbf{H} = \frac{\mu_0 \mathbf{H}}{\Lambda} = \frac{\mathbf{H}}{\lambda^2}, \tag{1.8}$$

that correctly models the perfect diamagnetism, since it predicts an exponential decrease of the magnetic field from the surface to the interior of the sample, with a *penetration depth* λ according to London:

$$\lambda = \sqrt{\frac{m}{\mu_0 n_\mathrm{s} e^2}}. \tag{1.9}$$

The order of magnitude of λ in pure classic superconductors is 50 nm.

The Gorter-Casimir and London theories were generalized in 1950 by *Vitaly Lazarevich Ginzburg* and *Lev Landau* in the so-called *GL-theory* [98], based on the *superconducting order parameter* Ψ, that is a wave function defined as $n_\mathrm{s} = |\Psi|^2$. In a superconducting-normal conducting boundary, $|\Psi|^2$ decays along the so-called *coherence length* ξ, with typical values in pure superconductors of 300 nm. The ratio:

$$\kappa = \frac{\lambda}{\xi}, \tag{1.10}$$

is called *Ginzburg-Landau parameter* and it is important to classify superconducting materials, as it will be explained in the following.

1.2.2 Microscopical Models

None of the models just summarized is intended to explain the causes of the superconductivity, but only to reproduce the main macroscopical experimental results regarding superconducting samples. The first microscopic theory able to describe in detail the behavior of several classes of superconductors is the *BCS theory*, from the names of the three American physicists *John Bardeen, Leon Cooper* and *John Robert Schrieffer* that postulated it in 1957 [13]. This theory, that was worth a Nobel Prize in 1972, describes the superconductivity as a macroscopic quantum phenomenon.

A qualitative explanation can be given considering a couple of electrons in a lattice of positive ions. The first electron, when moving inside the lattice, perturbs the ions, that displace towards this first particle. This displacement of ions locally polarizes the lattice with a positive charge, and the second electron will be attracted by this perturbation due to the Coulomb forces. In normal metals, this attraction is by far exceeded by the Coulombian repulsion between the couple of electrons, that are particles of same charge. Instead in superconductors the two electrons are coupled together and a net attraction remains. This couple of electrons is called *Cooper pair* and it is characterized by a distance between the particles lower than the coherence length ξ.

More precisely, in BCS theory Cooper pairs are quasi-particles that follow the *Bose-Einstein statistics* instead than the Fermi-Dirac one. Since the Pauli exclusion principle does not apply to bosons, Cooper pairs form a condensate in the so-called *BCS ground state*, separated by an *energy gap* $\Delta(T)$ from the normal conducting state, with a limiting value at 0 K [165]:

$$2\Delta(0) = 3.528\, k_{\mathrm{B}}\, T_{\mathrm{c}}, \tag{1.11}$$

where $k_{\mathrm{B}} = 1.38 \cdot 10^{-23}$ J/K is the Boltzmann constant. 2Δ is equal to the minimum energy required to break the Cooper pair and return to the normal conducting state. The coupling between the electrons of the pair can be expressed in terms of an exchange of *phonons*, that are quasi-particles that represents lattice vibration quanta. *Lev Petrovich Gor'kov* demonstrated in 1959 [75] that the GL theory is equivalent to the BCS theory in the limiting case in which $T \approx T_{\mathrm{c}}$ and the magnetic vector potential $\mathbf{A}$ does not change very rapidly, creating a bridge between the phenomenological and microscopic descriptions of superconductors.

BCS theory is valid in the so-called weak-coupling limit between electrons and phonons, whereas generalizations like *Eliashberg theory* [64] and its developments [97] [120] are valid also in the strong-coupling limits. However, there are still some classes of superconductors, introduced in the following section, in which no complete theory is available.

1.3 Critical Parameters

For engineering purposes, superconducting materials are described by means of some *critical parameters*. As already explained, the temperature at which the supercon-

ductive transition happens is called *critical temperature* T_c. Other important critical parameters are the *critical field* and the *critical current density*, that are the maximum magnetic field and current density that the sample can sustain without losing its superconductive properties. All these parameters are described below. The last parameter is the *critical frequency* f_c. Starting from the Gorter-Casimir two fluids model, the normal and the superelectrons can be considered analogous to the parallel between a resistance R and an inductance L [165]. Such a circuit exhibits an inductive behavior below the characteristic frequency $f_0 = R/(2\pi L)$, whereas at higher frequencies the resistive branch becomes dominant. The critical frequency of a superconductor can be estimated with such a model, obtaining an order of magnitude of 10^{11} Hz. However, since for most applications the working frequency is much lower than f_c, this parameter will be neglected in the following.

1.3.1 Critical Temperature

The critical temperature allows to share the superconductors between two main classes. In the beginning, all the superconducting elements and alloys discovered were characterized by very low critical temperatures, lower than 25 K. Such low temperatures can be obtained only using liquid helium as coolant or employing a cryocooler. In Table 1.1 the most important superconductive elements and composites of this class, called *Low Temperature Superconductors* (LTS) are reported together with their critical temperature at zero applied magnetic field. Niobium is the element with the highest known critical temperature, nevertheless composites can have critical temperatures much higher than their constituents. All LTS materials can generally be described by the microscopic theories summarized in the previous section. For engineering purposes, the most important materials are the alloy *Nb-Ti* and the composite Nb_3Sn (see Figure 1.4a).

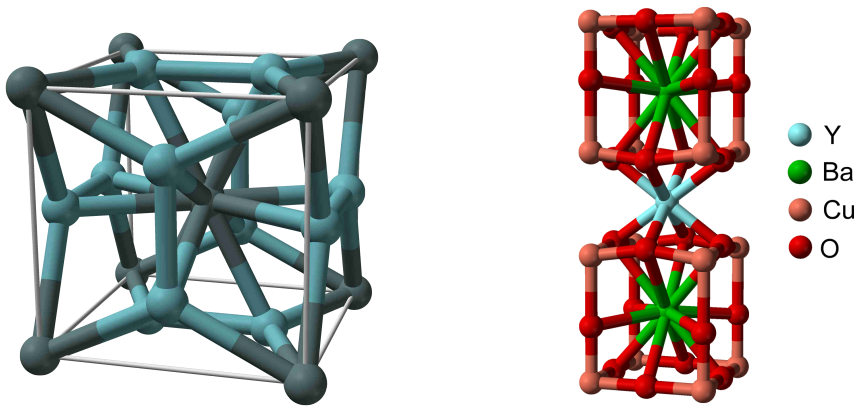

(a) Nb_3Sn. Grey balls represent tin, blue niobium. (b) YBCO.

Figure 1.4: Schematized unit cells for some superconductors.

Table 1.1: Critical temperature $T_{c,0}$ at zero magnetic field and critical field $B_{c,0}$ at 0 K of some LTS elements and composites. In the latter case $B_{c,0}$ is replaced by $B_{c2,0}$.

(a) Type I superconducting elements.

Element	$T_{c,0}$ [K]	$B_{c,0}$ [mT]	*References*
Ti	0.40	5.6	[142]
Ga	1.083	5.92	[142]
Al	1.175	10.5	[142]
Sn	3.722	30.5	[142] [117]
Hg(β)	3.949	33.9	[142]
Hg(α)	4.154	41.1	[142]
Pb	7.196	80.3	[142]

(b) Type II superconducting materials.

Material	$T_{c,0}$ [K]	$B_{c2,0}$ [T]	*References*
V	5.40	0.268	[142]
Nb	9.29	1.04	[142]
Nb-44w/o Ti	9.3	15	[188]
Nb-25w/o Ti	10.1	9.3-10	[188] [142]
V_3Ga	16.5	19.6	[117] [124]
Nb_3Sn	18.0	25	[72]
Nb_3Al	18.7	15-20	[188] [69]
$Nb_3(Al_{0.8}Ge_{0.2})$	20.7	43.5	[188]
Nb_3Ge	23.0	38	[188]

A breakthrough in superconductivity was achieved in 1986 by the German physicists *Johannes Georg Bednorz* and *Karl Alexander Müller*, that found superconductivity in a ceramic composite based on lanthanum, barium and copper oxides, with a critical temperature of 35 K [16]. This result, rewarded with Nobel Prize in 1987, was the first discovery of a new class of superconductors called *High Temperature Superconductors* (HTS). These materials are based on copper-oxides planes embedded in the lattice like in Figure 1.4b. Some HTS have a critical temperature higher than 77 K, and this permits cooling with liquid nitrogen, making this technology cheap and very promising for industrial applications. The most important materials of this class are $YBa_2Cu_3O_{7-\delta}$ (*YBCO*), with a critical temperature of 93 K [190], and $Bi_2Sr_2Ca_{n-1}Cu_nO_{2n+4+\delta}$ (*BSCCO*), with a critical temperature of 107 K if $n = 3$ [106]. BCS theory is not able to describe HTS, that still lack a complete theoretical modeling.

Recently, the discovery of superconductivity in *magnesium diboride* (MgB_2) at

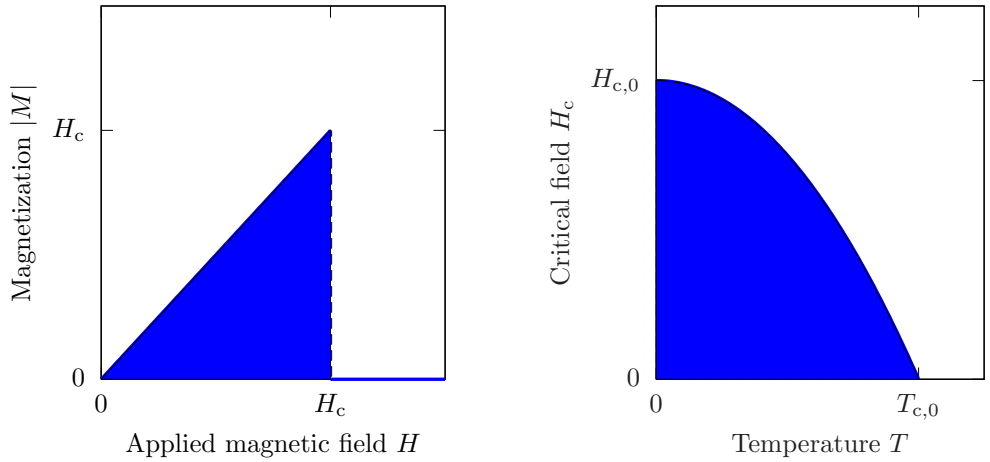

(a) Magnetization curve.

(b) Temperature dependence of H_c.

Figure 1.5: Critical field in type I superconductors. The filled areas in diagrams represent the superconductive state.

39 K [127] has aroused a lot of interest, since this material is relatively cheap compared to HTS that frequently feature rare elements in their composition. Furthermore, the material can be described by means of the BCS theory, differently from the other superconductors with similar critical temperatures.

1.3.2 Critical Field

Type I Superconductors

In 1914, when applying a magnetic induction of only 60 mT on a superconductive lead sample, Onnes discovered that an applied magnetic field can destruct the superconductive state. This was a great disappointment for scientists and engineers, since this phenomenon seemed to prevent practical applications for superconductive materials. Several elements like tin, mercury, lead are indeed superconductive up to the application of a magnetic field called *critical field* H_c. Below this value, the superconductive sample is a perfect diamagnet, therefore its magnetization is $\mathbf{M} = -\mathbf{H}$. When H_c is reached superconductivity is lost, and the material turns into a normal conductor. A typical magnetization curve for this kind of materials, called *type I superconductors*, is reported in Figure 1.5a. H_c can be easily deduced from thermodynamical considerations [165] and its temperature dependence is generally expressed with the approximated relation, plotted in Figure 1.5b:

$$H_c \approxeq H_{c,0}\left[1 - \left(\frac{T}{T_c}\right)^2\right], \tag{1.12}$$

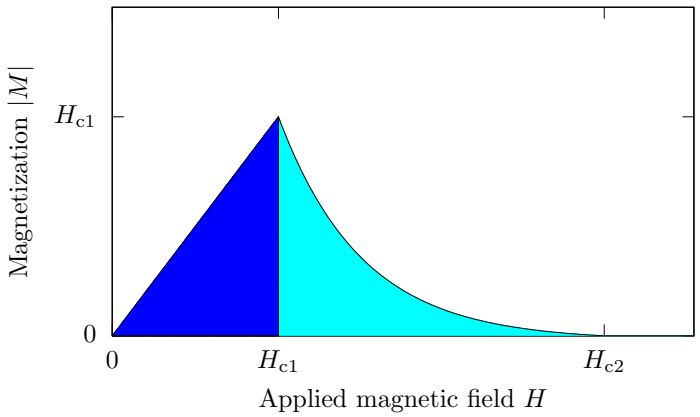

Figure 1.6: Magnetization curve in a type II superconductor. The dark filled area represents the superconductive state, the light filled area the mixed state.

where $H_{c,0}$ is the critical field at $T = 0$ K. Since the critical magnetic induction $B_c = \mu_0 H_c$ for type I superconductors is in the range $10 - 100$ mT (see Table 1.1a), they are generally not useful for engineering purposes.

Type II Superconductors

In 1937 the Russian physicist *Lev Vasilyevich Shubnikov* [155] discovered a new class of materials, called *type II superconductors*. Examples from this class are niobium, vanadium, technetium and the large part of superconducting alloys and compounds. These materials are characterized by three different states. Below the so-called *lower critical field* H_{c1}, the material behaves in the same way as a type I superconductor. Above H_{c1}, in the so-called *mixed state*, the material still exhibits zero resistance and the perfect diamagnetism is lost, thus the field can penetrate in the sample in the form of quantized flux vortices or *fluxoids*. The flux quantum is equal to:

$$\Phi_0 = \frac{h}{2e} \approxeq 2 \cdot 10^{-15} \text{ Wb}, \tag{1.13}$$

where h is the Planck constant. The fluxoids arrange themselves in a regular triangular pattern, named *Abrikosov lattice* from the name of the Russian physicist that theoretically explained their formation in 1957 [3]. His theory of the mixed state, together with Gor'kov development of Ginzburg-Landau theory, forms the so-called *GLAG-model*. The mixed state lasts up to the *upper critical field* H_{c2}, that can be orders of magnitude higher than the critical field of type I superconductors, as reported in Table 1.1b. Above H_{c2} the specimen turns into a normal conductor. In Figure 1.6 an example of a type II magnetization curve is reported.

The mixed state can be qualitatively understood remembering that the superconducting order parameter decays along the coherence length ξ, whereas the magnetic

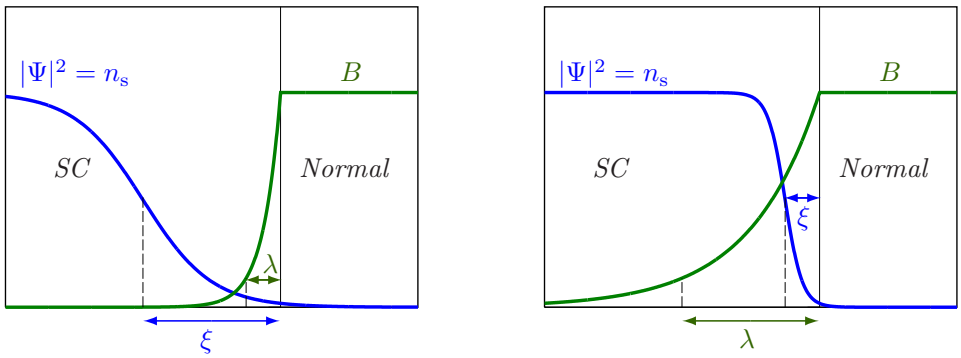

(a) Type I. (b) Type II.

Figure 1.7: Qualitative comparison between magnetic induction B penetration and superconductivity state decay at a normal-superconductor (SC) boundary.

field decreases along the penetration depth λ. If a fluxoid penetrates the material, screening currents should flow around it to maintain the diamagnetism in the remaining part of the material. If $\xi \gg \lambda$, like in Figure 1.7a, the screening currents should flow in a resistive region where the superconducting order parameter is already decayed. In this case, that is for type I superconductors, these currents would cause an ohmic loss and the mixed state is therefore not stable from an energetic point of view. Conversely, if $\xi \ll \lambda$ (see Figure 1.7b) like in type II superconductors, the screening currents can flow where the superconducting order is not yet completely decayed. The Ginzburg-Landau parameter $\kappa = \lambda/\xi$ is particularly useful in this case to establish the class to which a material belongs, since according the GLAG theory:

- for $\kappa < 1/\sqrt{2}$ the material is type I;
- for $\kappa > 1/\sqrt{2}$ the material is type II.

1.3.3 Critical Current Density and Pinning

Type II superconductors are the most important ones for technological applications since they can sustain strong applied fields. However, if we feed a superconductor of this kind with a transport current density $\mathbf{J}_t$, the Ampère law (Eq. 1.5) predicts an inhomogeneity in the density of the fluxoids. This leads to a repulsive Lorentz force between them, causing a movement from the high field regions to the low field ones. The consequence of this mechanism is an ohmic loss, that would prevent the type II superconductors to carry much current.

Nevertheless, in real superconductors the fluxoids can be pinned to certain positions in the crystal lattice by inhomogeneities like impurities, grain boundaries, dislocations where the superconducting order parameter is depressed. Therefore the

repulsive Lorentz force can be counterbalanced by a bulk *pinning force* per unit volume, due to the interaction between fluxoids and these inhomogeneities called *pinning centers*. The maximum value of this force $\mathbf{F}_{\mathrm{p,max}}$ defines theoretically the so-called *critical current density* $\mathbf{J}_{\mathrm{c}}$:

$$\mathbf{F}_{\mathrm{p,max}} = -\mathbf{J}_{\mathrm{c}} \times \mathbf{B}, \tag{1.14}$$

that is the maximum value of the transport current density that the superconductor can sustain without losses. J_{c} is a characteristic of the material and depends on temperature T and applied magnetic induction B, therefore a *critical surface* that divides the normal-conducting to the superconducting state in the parameter space is typically defined. Some materials, like Nb_3Sn, are very sensitive also to the mechanical deformation state, therefore strain ε dependence is carefully accounted. The critical surface for a Nb-Ti wire, normalized to a reference value $J_{\mathrm{c0}} = J_{\mathrm{c}}(4.2\ \mathrm{K}, 5\ \mathrm{T})$, is reported in Figure 1.8a. In Figure 1.8b the critical surface of a Nb_3Sn wire at the temperature of 4.2 K is reported, as an example of the strain dependence. In chapter 2 the most important functions used to describe the critical current in Nb-Ti and Nb_3Sn wires are summarized.

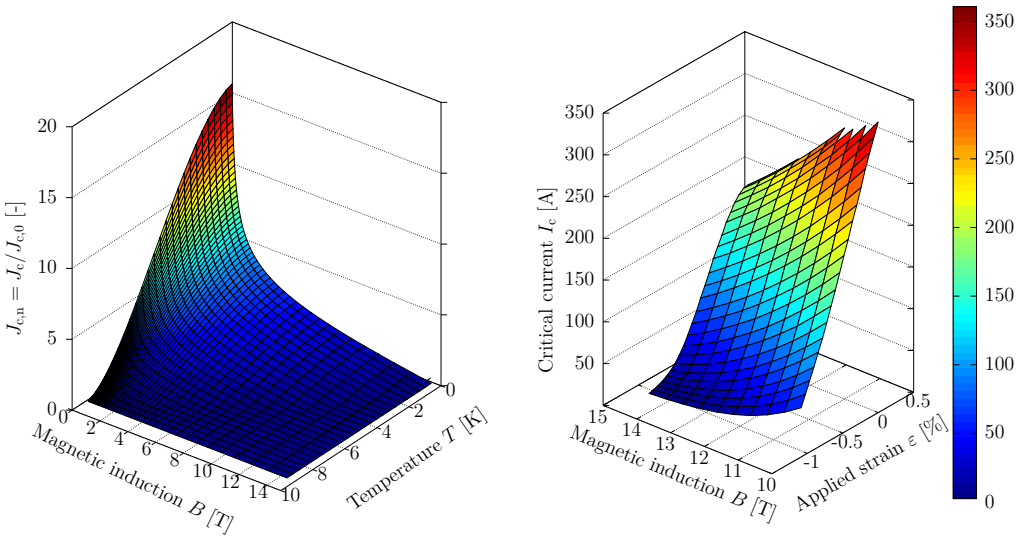

(a) The critical surface of a typical Nb-Ti LHC wire as a function of temperature and magnetic induction [26].

(b) The critical surface of a Nb_3Sn wire as a function of magnetic induction and applied strain, measured at 4.2 K [168].

Figure 1.8: Examples of critical surfaces for Nb-Ti and Nb_3Sn wires.

The maximum pinning force is not constant with magnetic induction. A first quantitative relation was found by Fietz and Webb [68]:

$$F_{\mathrm{p,max}} \propto \frac{{B_{\mathrm{c2}}}^{\nu}}{\kappa^{\gamma}} f(b), \tag{1.15}$$

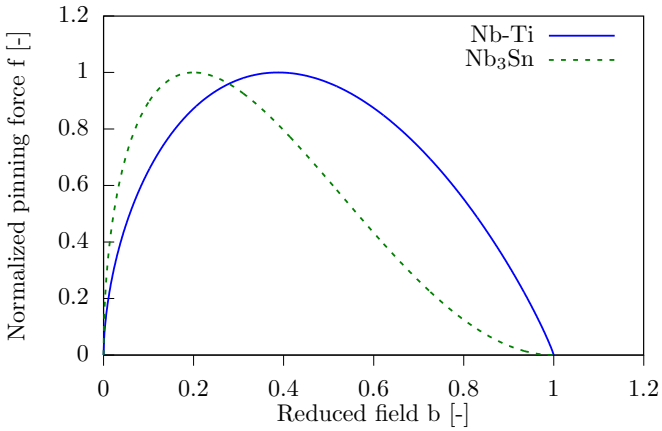

Figure 1.9: Typical pinning force behavior in Nb-Ti and Nb_3Sn.

where ν and γ are empirical constants, $b = B/B_{c2}$ is the *reduced field*, B_{c2} is the upper critical induction, κ is the Ginzburg-Landau parameter and f is a suitable function of the reduced field only. f is equal to zero for $b = 0$ and $b = 1$ and it exhibits a maximum at intermediate fields. The explanation of this behavior is due to Kramer [96] and it is related to the interactions between fluxoid lattice and pinning centers [188]. At low field indeed, the Abrikosov triangular lattice of fluxoids is very stiff, and it does not fit well on the disordered distribution of inhomogeneities in the bulk. The net pinning force is therefore low, since every pinning center is exerting forces in different directions on different fluxoids. On the other hand, approaching the upper critical field the fluxoid density is so high that the efficiency of the pinning mechanism decreases down to zero. f is generally expressed in the form:

$$f = b^p(1-b)^q \tag{1.16}$$

where p and q are the *pinning coefficients*. The pinning exponents vary a lot with different materials and samples. In Figure 1.9 typical behaviors of pinning force as a function of applied field are reported, with values normalized to the maximum pinning force available. In Nb-Ti the pinning force is almost symmetrical, whereas in Nb_3Sn the maximum is displaced toward low fields.

Equation (1.16) is also employed to estimate the upper critical induction using the *Kramer function* f_K:

$$f_K = [J_c B^{1-p}]^{\frac{1}{q}}. \tag{1.17}$$

Considering $J_c = F_{p,max}/B$ and Eq. (1.16) the result is:

$$f_K \propto 1 - b = \frac{B_{c2} - B}{B_{c2}}, \tag{1.18}$$

that is a linear function of magnetic induction B and it can be used to extrapolate the so-called *Kramer critical field* $B_{c2,K}$. In Figure 1.10 a typical Kramer plot is

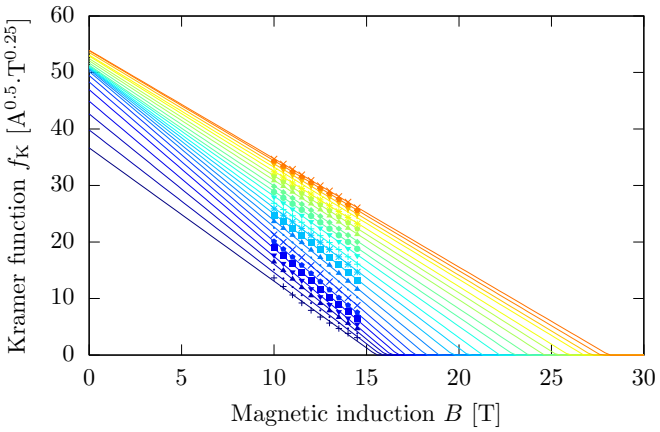

Figure 1.10: Example of a Kramer plot for a Nb_3Sn wire. Data at 4.2 K and various levels of strain from [168], pinning force exponents p and q respectively 0.5 and 2.

reported for a Nb_3Sn strand. The markers represent experimental data at different levels of applied strain. Extrapolating the linear behavior, it is possible to estimate $B_{c2,K}$ as the intercept of the straight lines on the x axis.

For $J_t \geq J_c$ the maximum pinning force is exceeded and the fluxoids start to move, generating an electric field according to Faraday-Neumann-Lenz law. This ohmic loss is modeled with the so-called *flux-flow resistivity* ρ_{ff} ($\Omega \cdot m$):

$$E(J) = \rho_{ff}(J_t - J_c), \tag{1.19}$$

where E is the electric field. The flux-flow resistivity can be approximated as [165]:

$$\rho_{ff} \approx \rho_n \frac{B}{B_{c2}}, \tag{1.20}$$

where ρ_n is the normal-state resistivity of the material.

1.4 Experimental Characterization

The critical current I_c at high magnetic inductions is generally estimated on practical samples through voltage-current measures. However, the theoretical linear behavior of Eq. (1.19) is never observed in real superconductors, whereas a non-linear transition is typically measured, see for example Figure 1.11. An experimental standard for the definition of I_c must therefore be adopted: different criteria are possible and have been proposed [38] [48], based on the resistivity onset, on the dissipated power density, on the take-off point or on the linear extrapolation of flux-flow resistivity. However, none of these methods is commonly used, since an electric voltage criterion is typically considered, according to which the voltage-current characteristic (VAC)

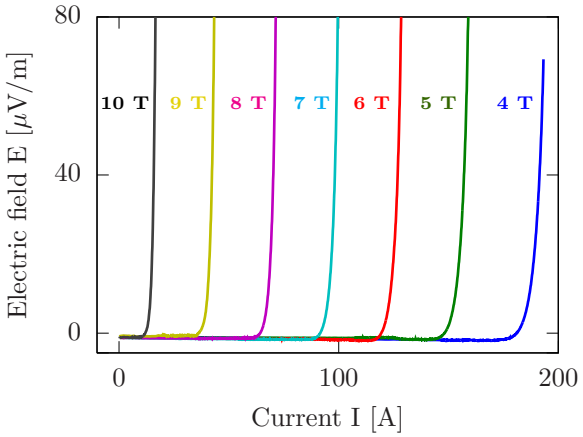

Figure 1.11: The VAC of a Nb-Ti NIST wire measured [4] at different levels of magnetic induction at the temperature of 4.2 K.

of a superconductor is expressed with the so-called *power law*:

$$E(I) = E_c \left(\frac{I}{I_c}\right)^n \tag{1.21}$$

where E_c is the so-called *critical electric field*, typically in the range of 10 μV/m. I_c is the critical current measured with this electric field criterion, that is the worldwide typical reference for the experimental characterization of superconductors. The n-index can be computed as the logarithmic slope of the VAC:

$$n = \frac{\mathrm{d}(\ln E)}{\mathrm{d}(\ln I)} = \frac{I}{E}\frac{\mathrm{d}E}{\mathrm{d}I}. \tag{1.22}$$

Typical values of n are between some units and some tens.

According to [38] the concept of n-index was first introduced by Walters [181]. In an early work [176] Voelker observed that the logarithmic slope of the VAC slowly varies with field and current for a given sample of wire, while it can be very different from sample to sample, due to damages, twisting, metallurgical treatment, copper-to-superconductor bond or some other features. Sometimes, instead of Eq. (1.21) an exponential fit is used to empirically parametrize the VAC [57] [70] [94].

Some attempts have also been made to empirically characterize the behavior of n-index of a Nb_3Sn superconductor as a function of temperature T, magnetic induction B and applied strain ε [161] [163]. The correlation between critical current I_c and n-index is very frequently expressed as:

$$n = 1 + r(T,\varepsilon) \cdot [I_c(B,T,\varepsilon)]^{s(T,\varepsilon)} \tag{1.23}$$

where r and s are two arbitrary functions of T and ε only. r is reported to vary weakly with temperature and strain (up to 20%) while s is typically in the range

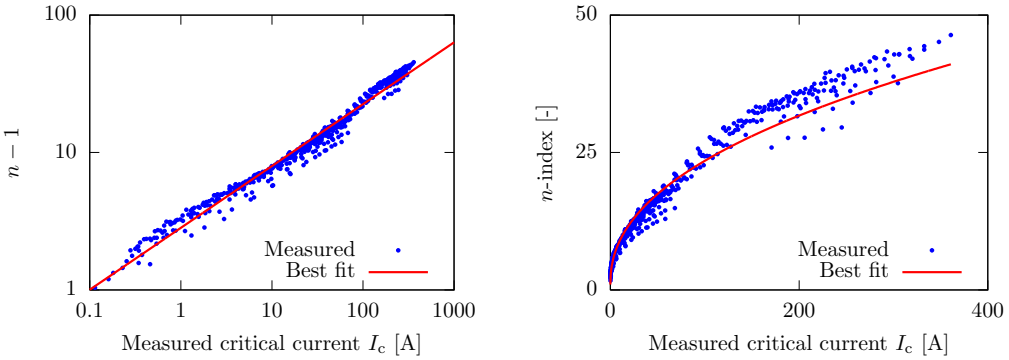

Figure 1.12: Correlation between n-index and I_c for a Nb_3Sn wire, in log (left) and linear scales (right). The solid line shows the best fit with Eq. (1.23).

$0.4 - 0.5$. In Figure 1.12 an example of this correlation is plotted, with data from a Nb_3Sn wire [168].

These parametrizations lead to similar results in the range $10 - 100\,\mu V/m$, that is the most investigated, while none of these models is expected to be completely accurate in the full range of the VAC. Indeed, according to [163], different n-indexes can be measured at different levels of electric field and at the same values of magnetic induction, temperature and applied strain, suggesting deviations from Eq. (1.21).

A lot of effort has been put to explain the VAC non-linearity and to predict the behavior on a broader electric field range. Some of these models are based on:

- *Josephson junction coupling* between grains [128];
- *sausaging* [63];
- *flux creep* [156] [164];
- I_c *statistical distribution* [60] [79] [80] [85] [112] [183].

The first two approaches are focused on the role of defects inside the bulk material. Flux creep is the jump of fluxoids from a pinning center to another activated by thermal motion. It causes an uncertainty in the theoretical definition of J_c that can explain the VAC curvature in the case of samples with low concentration of defects (like single crystals, thin films etc.). On the opposite, the last approach neglects the microscopical characteristics of the material, focusing on a general statistical description of a macroscopic sample. This approach, as reported in Appendix B, has been considered in detail in the present thesis to better understand the voltage-current characteristic in superconducting wires and to outline how much the statistical dispersion of the critical current in a sample can affect the performances.

1.5 Applications

Superconducting materials can be employed in any application in which very high current density and magnetic induction are required with a low energy consumption. In high performance electromagnets, large values for critical field and current are generally preferred than a high value for critical temperature. Indeed, iron-dominated normal-conducting magnets are limited by ferromagnetic materials saturation above $1 - 2$ T and by aluminum and copper current densities, that in steady-state cannot exceed $1 - 2$ A/mm^2 for air-cooled coils and 10 A/mm^2 for water-cooled ones, to avoid excessive heating [193]. For magnetic fields up to about 20 T, superconducting materials allow these limits to be easily exceeded, since much lower losses are generated. In Figure 1.13a typical critical current densities available at 4.2 K in different superconducting materials are reported as a function of magnetic induction. The characteristics of HTS superconductors like YBCO and BSCCO are very promising, especially at extremely high fields, compared to the much common and well-known LTS materials. However, it is important to notice that presently YBCO can be engineered only in the form of anisotropic samples like thin tapes. Notable differences can be observed if the field is applied in the normal or parallel direction with respect to the current. On the other hand, BSCCO can be drawn into a round wire, but the process is very expensive since it implies very strong pressures and a large amount of silver. As regards the magnesium diboride, its critical field is presently too low to fulfill the requirements of high field electromagnets.

The values reported in Figure 1.13a are related to the superconductor bulk, whereas in real superconducting wires and tapes a significant part of the cross-section area is occupied by other materials. This is mandatory in order to improve the mechanical behavior of the conductor and the thermal stability in the case of a local transition from superconducting to normal state. Another important parameter is therefore the *engineering critical current density* J_e, defined as the critical current normalized to the total cross-section area of the conductor. Previous data can be therefore renormalized in terms of $\mathbf{J}_e$, obtaining Figure 1.13b, in which the good performance of the LTS materials is much emphasized.

In the following paragraphs the most important areas in which the remarkable electromagnetic performances of superconductors are employed will be summarized.

1.5.1 High Energy Physics

High energy physics (HEP) is the branch of science that studies the fundamental constituents of matter and their interactions, mainly in the framework of the so-called *Standard Model*. Proof of these theories can be found only by colliding particles at higher and higher energies, necessary to reveal some phenomena. This task is done in *particle accelerators*, like the *Tevatron* at Fermilab, the *Hadron-Electron Ring Accelerator* at DESY in Germany, the *Relativistic Heavy Ion Collider* at Brookhaven National Laboratory and the *Large Hadron Collider* (LHC) at CERN in Geneva

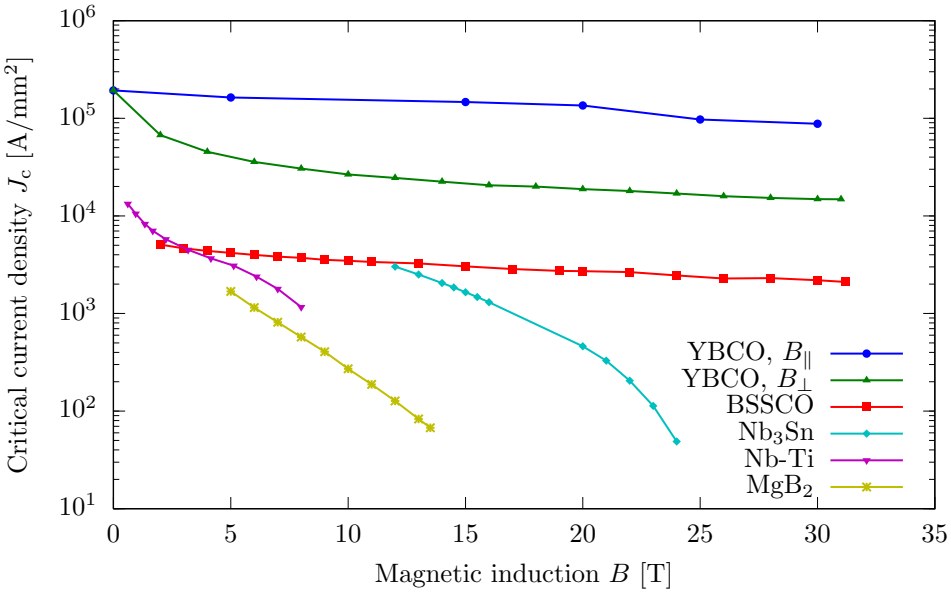

(a) Critical current density J_c.

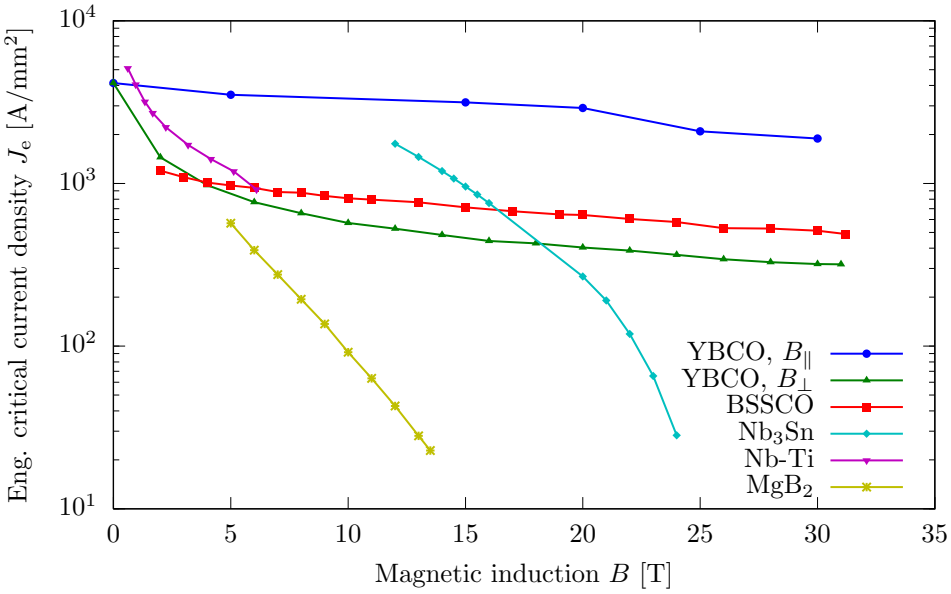

(b) Engineering critical current density J_e.

Figure 1.13: Comparison between critical current densities of different materials as a function of magnetic induction at 4.2 K. Original data compilation courtesy of Peter J. Lee, NHMFL-FSU. The complete references for each dataset can be found in [100].

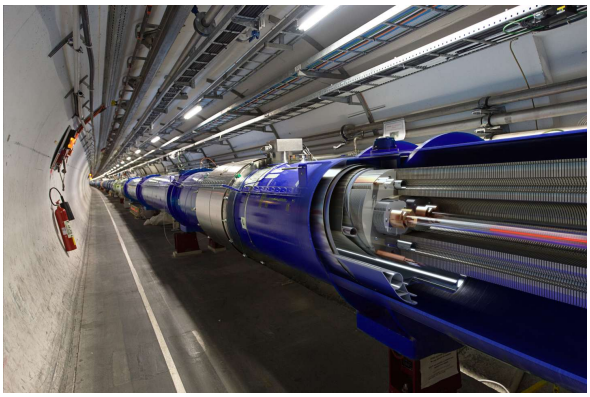

(a) 3D cut of a LHC dipole in the tunnel.

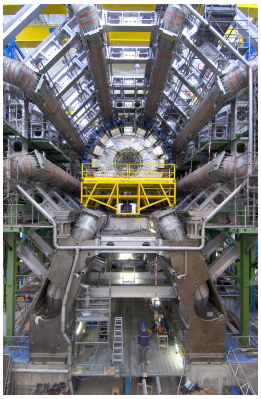

(b) ATLAS detector.

Figure 1.14: Superconductive magnets at CERN (© CERN).

(CH). LHC, in which two counter-rotating proton beams are collided to an energy up to 7 TeV/beam, is the largest existing accelerator [145]. To reach such high energies, the particles are accelerated by radio-frequency cavities on a circular track called *synchrotron*. A bending force is required to keep the beam on the circular path, and high-field superconducting magnets are needed to this purpose. Indeed, in an accelerator the proton beam energy E in TeV scales with the relation:

$$E \approxeq 0.3\, B \cdot R \tag{1.24}$$

where B is the magnet induction in T and R is the bending radius in km. To obtain the 7 TeV energy in LHC, the curvature radius of the beam is 2.804 km and the magnetic induction, larger than 8 T, is achieved with Nb-Ti superconducting magnets, cooled at 1.9 K by super-fluid helium. Along the 27 km of the accelerator tunnel 1232 superconducting dipoles are present, each 15 m long and with a mass 30 tons. An image of one of these dipoles in the tunnel is reported in Figure 1.14a. LHC needs further 500 large magnets and 7724 small-size correctors (up to dodecapole order) to precisely control the beam trajectory and focusing. To obtain the same results with iron-dominated normal-conducting magnets a ring of 100 km would be required, and the Joule power dissipated in coils would be more than 20 times larger than the cooling power exerted by the existing LHC machine [148].

In LHC four big detectors are placed in the so-called *insertion regions* to study the particle collisions, and also in this case applied superconductivity plays an important role. Indeed, the two largest detectors, ATLAS and CMS, feature very large superconducting magnets to bend charged particles produced during the collisions. In Figure 1.14b an image of the giant ATLAS barrel toroid magnet is reported.

The first beam of LHC was successfully delivered in September 2008. A remarkable result was achieved on July 2012, with the announcement of the first experimental discovery of the Higgs' boson. This particle was theorized in 1964 by Peter Higgs and other physicists, and it has a fundamental role to solve some

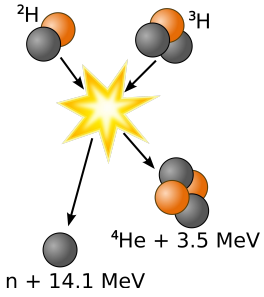

Figure 1.15: Diagram of the deuterium-tritium fusion reaction.

inconsistencies in the Standard Model. In future, the accelerator will be upgraded to enhance the experimental accuracy and to permit new discoveries. The machine *luminosity*, that is related to the number of events (collisions) per unit area and unit time, will be increased, since running the accelerator without a significant luminosity increase will lead only to marginal statistical gain. In the next version of the accelerator, called *HiLumi-LHC* (HL-LHC), some magnets will be replaced with Nb_3Sn technology, in order to improve the focusing and thus the luminosity of the beam, pushing the highest field in magnets to about 12 T [166].

Another notable accelerator complex under development is the *Facility for Antiproton and Ion Research* (FAIR) at the GSI in Darmstadt, Germany [126], that will provide high intensity beams of ions and antiprotons for experiments in nuclear, atomic and plasma physics. It will feature two synchrotrons, named SIS100 and SIS300, in the same tunnel. The accelerator ring, 1.1 km long, is much smaller compared to LHC, whereas the superconducting magnets will operate at a very high field ramp rate, up to 4 T/s compared to the 7 mT/s that is the nominal value for LHC. A lot of effort is therefore put to appropriately design the magnets for a long lifetime and safe operation.

1.5.2 Controlled Thermonuclear Fusion

Nuclear fusion is the atomic reaction that takes place continuously in active stars, in which two or more atoms join together forming heavier atoms and releasing large amounts of energy according to well-known Einstein's formula $E = mc^2$. For example, in Figure 1.15 one atom of deuterium and one of tritium can fuse together creating a helium atom and a neutron releasing a total energy of 17.6 MeV. However, to start this process it is mandatory to overcome the repulsive Coulomb forces between the atom nuclei. On Earth this can be done creating a *thermonuclear plasma*, that is a ionized gas with a temperature of more than 150 million degrees in which the electrons become separated from nuclei.

The *International Thermonuclear Experimental Reactor* (ITER) is a project, signed by China, European Union, India, Japan, Korea, Russia and United States, that aims at proving the viability of nuclear fusion as an energy source. Nuclear fusion would have indeed many advantages. Small amounts of fuel are required: only

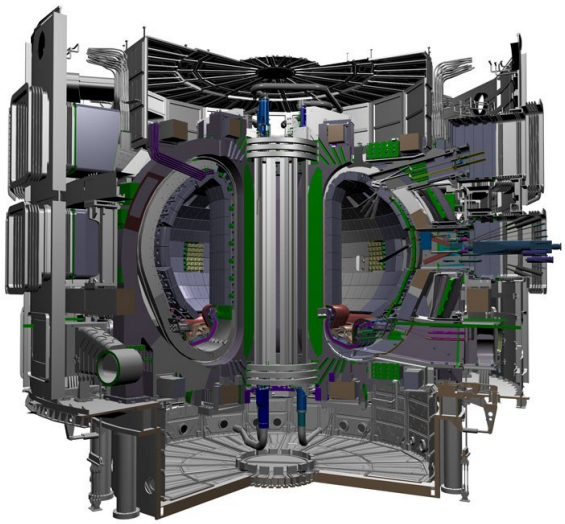

Figure 1.16: ITER tokamak design (courtesy of ITER organization).

250 kg per year for a 1 GW plant. Furthermore, deuterium can be easily obtained from seawater. Tritium instead would be continuously bred from the plasma neutrons interacting with the lithium present in the blanket surrounding the machine vacuum chamber. The only by-product of the reaction, helium, is not harmful since it is a noble and non-toxic gas. Finally, the fusion reaction is intrinsically safe, since the process would stop in the case of a loss of control, differently from nuclear fission where a runaway would take place.

The development of ITER reactor is underway in Cadarache, in the south of France. In this machine, a toroidal reactor called *tokamak* will contain the hot plasma in which the deuterium-tritium reaction will take place (see Figure 1.16). The created neutrons will carry away about 80% of the reaction energy from the plasma, and they will be absorbed by the walls of the machine, generating heat. Since ITER is a demonstration plant, this heat will be dispersed through cooling towers, whereas in future commercial reactors it will be converted into electric energy.

Due to its high temperature, the plasma cannot be enclosed by any material container. However, since the plasma is an ionized gas, it is subjected to Lorentz force. Thus, it is possible to control and confine the plasma inside the tokamak using strong magnetic fields, provided by a very complex superconducting magnet system [122], cooled with forced-flow super-critical helium at an inlet temperature of 4.5 K. In the case of ITER, the magnetic field configuration is achieved by:

- 18 D-shaped *Toroidal Field* (TF) Nb_3Sn coils that will provide a steady field of 5.30 T at the torus major radius, 6.20 m. The nominal peak field of the magnet will be 11.8 T at a current of 68 kA, with a total stored magnetic energy of about 41 GJ;

- 6 Nb_3Sn coil modules that will form the *Central Solenoid* (CS), featuring a peak field of 13 T. These modules will be independently fed with a current between 40 and 45 kA to induce a current in the plasma and to control the vertical stability;
- 6 *Poloidal Field* (PF) coils that will be fed with a current between 45 and 55 kA to keep the plasma away from the tokamak walls. The peak field of these magnets will be lower, about 6 T, permitting the use of Nb-Ti technology;
- 18 Nb-Ti *Correction Coils* (CC) will control possible instabilities in the plasma and correct eventual field errors.

The facility is expected to be completed in 2019, with the first plasma to be produced in 2020. The machine will operate with pure hydrogen fuel up to 2027 to study and check the plasma operation in different regimes. After that, the first deuterium-tritium reactions will be generated with increasing levels of power.

After ITER project, the *Demonstration Power Plant* (DEMO) will demonstrate the large-scale production of electrical power and tritium fuel self-sufficiency. The design of the $2-4$ GW machine will be completed by 2017 and the operations are planned to start in the 2030s, with the intent to have a first commercial fusion power plant ready by 2050.

1.5.3 Nuclear Magnetic Resonance

Some atom nuclei, when exposed to magnetic fields, can absorb and re-emit an electromagnetic radiation at a particular frequency that is proportional to the applied field strength. This phenomenon is called *Nuclear Magnetic Resonance* (NMR) and it is due to the spin precession of protons or magnetized nuclei in magnetic fields according to the *Larmor frequency*:

$$f = \gamma B \tag{1.25}$$

where γ is the *gyromagnetic ratio* of the particle, that is the ratio of its magnetic dipole moment to its angular momentum. Larmor frequency is typically in the range of MHz. For example, for a proton $\gamma = 42.576$ MHz/T, therefore the resonance spans from about 43 MHz at 1 T to 900 MHz at 21 T.

Several applications of this phenomenon exist. NMR is widely employed for example in spectroscopy, to determine the chemical and physical properties of atoms and molecules (see Figure 1.17a), and in petroleum industry to analyze rock porosity and structure. However, the most important industrial application is the *Magnetic Resonance Imaging* (MRI), that is a medical imaging technique widely used in radiology with more than 3000 equipments annually installed worldwide [105]. Since hydrogen is present in every tissue of human body because of water, it is possible to apply proton NMR to obtain images of internal organs useful for non-invasive diagnosis, like the one reported in Figure 1.17b. The resolution of this technique depends

(a) A 21 T/900 MHz NMR spectroscope.

(b) The MRI of an human head.

Figure 1.17: Nuclear Magnetic Resonance.

on the applied magnetic induction and on the field quality, therefore superconducting magnets are the best solution for high performance systems. In particular in the case of whole body scanners, only superconducting magnets can produce fields well above 0.5 T with the required homogeneity, that is less than 10 ppm peak-to-peak [105]. Presently, the largest whole body scanner under development is the 11.75 T/500 MHz ISEULT Nb-Ti magnet with a warm bore of 900 mm [105].

1.5.4 Other Applications

Electromagnets producing very strong and precise fields are the most important, but not the only area in which applied superconductivity is employed. Increasing interest by the electric power industry is demonstrated by several projects focused on superconducting power cables [132]. For example, the possibility to store electric energy in a loss-less way with technologies like superconducting flywheels or *Superconducting Magnetic Energy Storage* (SMES) is very interesting in particular in the field of renewable energies, where the intrinsic intermittency of these resources is a significant obstacle for their complete development. Moreover, superconductivity can also be employed to increase the power conversion efficiency by means of low-loss motors and turbines. Finally, very promising applications are available also in electronics, thanks to the Josephson junction effect, and in transportation, with the Maglev as an important example.

Power Cables

Some attempts have been done in order to employ the high current density available in superconducting materials to transfer energy without losses in the electric power grids. At the beginning of the 2000s, a 120 m BSCCO demonstration cable was installed near the Frisbie substation in Detroit (USA), connecting the low voltage

side of a transformer with a circuit rating of 100 MVA to a 24 kV bus. However, the system was not put in continuous operation because of vacuum leak issues [159]. In 2006, a 350 m BSCCO cable rated 34.5 kV / 800 A has been installed between two substations in Albany (USA) and has operated for 7000 hours without failures [116]. The same cable has been then upgraded replacing 30 m of the old conductor with a new generation YBCO cable [191]. A recent important milestone is the German AmpaCity project [158], that has successfully installed a 10 kV, 40 MVA HTS system that started operations in May 2014 in the city of Essen. The system is composed by 1 km cable, presently the longest operating HTS system, and a fault current limiter. Finally, a remarkable project is under development at CERN [11]. All the cables used for the current transfer from power converters to the LHC magnets will be replaced with HTS links before 2023. More than 1000 km of conductors carrying altogether more than 150 kA will be required. Presently, only few HTS links are already installed in LHC.

Electronics and Josephson Junctions

The use of superconductors in electronics is based on the so-called *Josephson Junction* (JJ). It is composed by two electrodes coupled by a weak link, that can be for example a tiny sheet of insulator. In normal conditions, no current should flow if a voltage is applied between the two electrodes, whereas a current can be measured if the two electrodes are superconducting. This phenomenon is related to the quantum tunneling applied to the Cooper pairs, and it was predicted by the physicist *Brian Josephson* in 1962. Many applications of this principle are possible. For example, *Superconducting QUantum Interference Devices* (SQUIDs), composed by the parallel of two JJ, are the most precise existing magnetometers, with a noise floor close to few $\mathrm{fT/Hz^{1/2}}$ [132]. On the other hand, digital electronics technologies based on JJ like *Rapid Single Flux Quantum* can be very fast and considerably less power consuming than traditional CMOS, and they have been already employed in wide bandwidth satellite communications and signal intelligence applications [132].

Levitation and Maglev

In the field of transportation, the superconductivity can be employed in the so-called *Maglev* trains [99], in which strong electromagnets are installed on board and along the track. Their magnetic field is controlled in order to levitate the vehicle just above the track, eliminating the mechanical friction with the rail. In this way, extremely high speeds can be achieved, with a record of 581 km/h obtained in 2003 by the SCMaglev in Yamanashi prefecture in Japan [132]. A remarkable project under development is the Chuo Shinkansen high-speed railway in Japan [132], that will link Tokyo-Nagoya-Osaka at a maximum speed of 505 km/h. Commercial operation between Tokyo and Nagoya is planned to start in 2027, whereas the extension to Osaka is planned for 2045.

1.6 Aim of the Thesis

Complex engineering must be employed to meet the demanding requirements of fusion and accelerator magnets, in terms of field strength, quality and reliability. Indeed, in some cases superconducting magnets can be subjected to electromagnetic-thermal instabilities (*quenches*), that can seriously damage the windings if they have not been correctly designed. A multi-physics approach is therefore mandatory in both the analysis and the design of superconducting magnets, since thermal parameters depend on the electromagnetic behavior and viceversa. In addition, mechanics plays a significant role and cryogenics and liquid helium dynamics must be considered. Furthermore, local properties difficult to control and predict, such as the electrical and thermal contact resistances, have a paramount role for the correct operation of superconducting cables, and very extensive experimental characterizations are hardly feasible, due to the large cost of full-scale prototypes and test equipments. A possible strategy is therefore to develop complex theoretical models to understand the behavior of small-scale samples, enhance their performance and infer the working condition limits for the complete systems. This task must be done mainly with numerical tools, since analytical approaches can deal only with very simplified cases. The present work is therefore focused on the numerical modeling of superconducting cables for fusion and accelerator magnets, in particular in terms of their thermal and electromagnetic behavior.

To enhance the cable performances in terms of stability, a careful design at both the strand and the cable level is developed, as widely explained in chapter 2. At the strand level, the filament size and arrangement in the cross-section, together with stabilizing materials are carefully evaluated. At the cable level, different geometrical approaches are considered in fusion and accelerator magnets. In fusion magnets, where fast transient phenomena can be present due to the plasma, and the field quality is not so stringent, cables are made of hundreds of strands twisted in subsequent stages and rely on the possibility of a current transfer among them and an efficient cooling. This technology is called *Cable-In-Conduit-Conductor* (CICC). In accelerator magnets, where the accuracy of the magnetic field is of paramount importance, the superconducting cable is made according to the *Rutherford geometry*, in which few transposed strands are tightly packed to form a rectangular or trapezoid cross-section. Two superconducting materials are considered in the present work, since they are presently the most important: Nb-Ti and Nb_3Sn. The first one combines very good mechanical properties with a well-established fabrication process, whereas the second one can give much better performances in terms of magnetic field and current density, at the cost of a poorer mechanical behavior.

Special purpose numerical models are very often used to deal with such unconventional cable designs and physical aspects. The numerical code developed and used during this PhD activity, THELMA, is described in detail in chapter 3. Although the THELMA code was originally intended for the electromagnetic and thermal simulation of CICCs cables and joints, it can now deal also with Rutherford cable

modeling, thanks to the brand-new routines developed during this PhD activity. The THELMA electromagnetic modules model superconducting cables as suitable lumped and distributed equivalent electrical networks. The code is able to predict the current distribution among the wires, the voltages and the losses resulting from eddy currents or from local transitions from superconducting to normal conducting state. The validity of the THELMA electromagnetic modules has been already checked several times by means of comparison of numerical results with experimental data measured on CICC cables and joints samples.

During this PhD activity, a further thermal module has been developed, whose focus is to describe the heat propagation along and among superconducting wires, taking into account the non-linearity of the thermal material properties. With this new module, the thermal analysis of superconducting cables can be carried out in both adiabatic cases, in which the heat propagation to the coolant can be neglected, and forced-flow cooling, provided that the thermodynamical conditions of the coolant can be considered stationary. Following the concept of a multi-physics approach, the thermal module is coupled with the electromagnetic routines, in order to increase the accuracy of the numerical results.

Since superconducting cables are not monolithic conductors, a primary physical aspect to be considered is the current and heat transfer among adjacent wires. An advanced understanding of the contact mechanism is indeed fundamental to guarantee the cable performance and to enhance its stability. This can be achieved only with a correct setting-up of the model parameters, possible only on the basis of calibration experiments, that can be reproduced by the code. The THELMA code has been already used to accurately model the experimental setups for the measurement of the electrical contact resistances among superconducting wires in CICCs for fusion magnets. During this PhD activity, as explained in chapter 4, the code has been applied also to the case of Rutherford cables. In addition, further analyses have been performed on CICC cables and joints, considering a novel statistical approach that is able to better reproduce and understand the experimental data.

After the complete description of the physics modeled in the numerical code and the related parameters, the versatile capabilities of the THELMA code are then demonstrated by means of some case studies analyzed during this PhD activity.

First of all, in chapter 5 the experimental data taken on a CICC sample for ITER production are analyzed with the THELMA code, showing its effectiveness in describing the behavior of a complex superconducting cable from both the electromagnetic and the thermal point of view.

The THELMA code is also useful in reproducing the experimental behavior of other objects, such as impregnated Rutherford cables. Thus, in chapter 6, the quench propagation in a magnet wound with a Rutherford cable is described with analytical, experimental and numerical methods. Then, in chapter 7, a predictive analysis of the losses and current distributions in a CICC magnet is presented, as an example of the THELMA code capability in modeling very complex objects in an accurate way. The main findings of all these analyses are finally summarized in chapter 8.

Chapter 2

Superconductor Technology for Fusion and Accelerator Magnets

The extraordinary electromagnetic behavior of superconducting materials is not easy to be translated into simple designs for magnet windings. Fusion and accelerator magnets indeed require very demanding performances in terms of magnetic field strength and homogeneity, and furthermore they are also characterized by very complex and noisy working conditions, in which radiations, fast magnetic field fluctuations, thermal inhomogeneities and huge mechanical stresses are present. As it is explained in this chapter, these phenomena can seriously affect the superconductor performance in terms of stability. Thus, practical superconductors feature complex designs, in order to ensure the safe and continuous magnet operation and to optimize the desired performance. Generally, a multi-scale approach is used, starting from micrometric superconducting filaments, to superconducting wires (strands) in which thousands of filaments are embedded, to large superconducting cables capable to carry tens of kA.

In this chapter, the design and the fabrication of the most common superconducting strands are summarized. In particular, the description is focused on Nb-Ti and Nb_3Sn strands, since they are the workhorse for machines like ITER and LHC. Then, the Rutherford cables and Cable-In-Conduit-Conductors (CICC) are analyzed, emphasizing their advantages and drawbacks. Rutherford cables are the main superconducting cable design for accelerator magnets, whereas CICCs will be largely employed in ITER.

2.1 Superconducting Strands

Superconducting wires or *strands* are composed by a large amount of tiny twisted superconducting filaments embedded in a normal-conducting matrix, typically made of copper, as shown in Figure 2.1. This very complex design has been developed to enhance the conductor performances in terms of *stability*. In the following, the concept of stability in superconducting wires is summarized with a particular focus on the *minimum propagating zone*, the *flux jumping* and the *inter-filamentary coupling*. Then, Nb-Ti and Nb_3Sn strands are described, as regards their manufacturing process and the most common *scaling laws*, that are semi-empirical relations that describe the critical current as a function of field, temperature and strain.

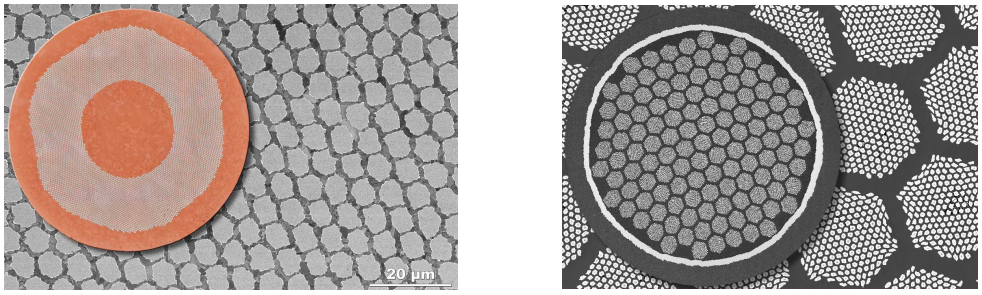

(a) CERN LHC reference Nb-Ti strand. (b) Nb_3Sn bronze-route strand.

Figure 2.1: Superconducting strand cross-sections with magnification of their filaments (courtesy of Peter J. Lee, NHMFL-FSU).

2.1.1 Design and Stability

Minimum Propagating Zone

The concept of stability in applied superconductivity is related to the material behavior when it is affected by localized depositions of energy, generally referred as *disturbances*. Many phenomena can indeed cause a disturbance in a superconducting wire: heat leaks from the cryogenic system, mechanical displacements or friction, eddy current losses, magnetic field fluctuations, etc. In any case, the critical current of the superconducting strand can be locally depressed, moving the working condition over the critical surface to the normal-conducting state. The wire starts therefore to generate heat, that may diffuse along the strand and turn all the superconductor into a normal conductor. Assuming adiabatic conditions and a point disturbance heating up the wire up to the critical temperature T_c, it can be demonstrated [188] that the propagation of the disturbance happens if its initial length is larger than the so-called *minimum propagating zone*:

$$l_{\mathrm{MPZ}} = \sqrt{\frac{2k(T_c - T_0)}{\rho_E J_c^2}}, \tag{2.1}$$

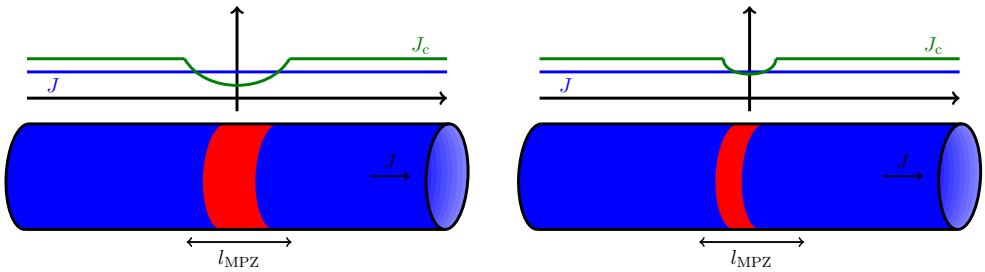

(a) Disturbance recovering.

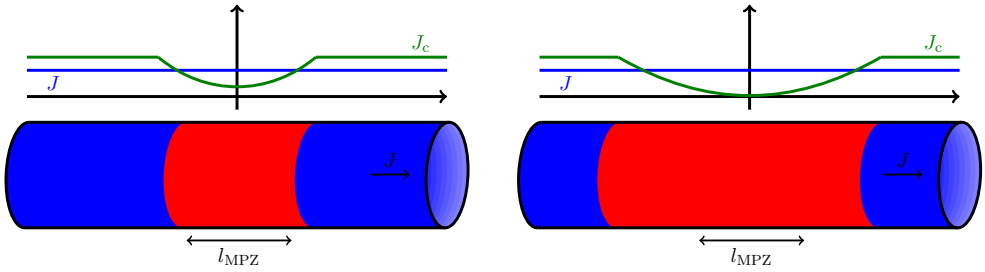

(b) Disturbance causing a quench.

Figure 2.2: Sketch of the minimum propagating zone in a superconducting strand.

where k and ρ_E are respectively the thermal conductivity and the electrical resistivity of the normal-conducting material, T_c is the critical temperature, T_0 is the coolant temperature and J_c is the critical current density. If the initial perturbation length is lower than l_{MPZ}, as shown in Figure 2.2a, the strand cooling capability exceeds the generated heat and the disturbance is recovered; conversely, the disturbance propagates and a so-called *quench* affects the material, as in Figure 2.2b. During a quench the large amount of energy stored in the magnet is dissipated as heat, that can seriously damage or even melt the winding if no protection system is foreseen.

If bulk superconducting strands were employed, i.e. without any additional resistive material embedded, the order of magnitude of l_{MPZ} would be micrometers, therefore any tiny perturbation would trigger a potentially harmful instability. This is due to the ratio k/ρ_E that is relatively small in many superconducting materials over the critical surface. To solve this issue, composite wires made of superconductor and copper are used. The normal-state electrical resistivity of copper is indeed some orders of magnitude lower than the normal-state resistivity of Nb-Ti or Nb_3Sn, and the ratio k/ρ_E is up to 6 orders of magnitude higher[1], therefore the presence of copper can promote the stability to a considerable extent. Furthermore, during a quench the copper carries the current producing lower Joule losses than normal-conducting Nb-Ti or Nb_3Sn, thus reducing the overheating and acting as a passive protection system. The normal-conducting material present in superconducting strands is therefore referred to as *stabilizer*, and it should be characterized

[1]See Appendix A for material properties of copper and superconducting materials.

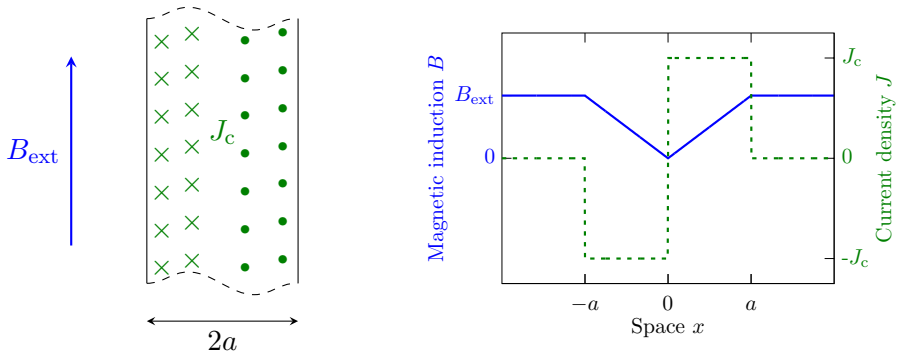

Figure 2.3: Superconducting slab subjected to an external field in critical state.

by a very low electrical resistivity at cryogenic temperatures. Its residual resistivity ratio RRR, that is the ratio between the resistivity at room temperature and at cryogenic temperatures[2], should therefore be very high. In the case of copper, typical values are around 100, that require a high purity material to be obtained.

Flux Jumping

The very fine subdivision of superconductor in filaments is mandatory due to the phenomenon of *flux jump*[3]. It can be explained considering for example a superconducting slab characterized by a width $2a$. If an external magnetic field parallel to the broad face is applied to the sample, opposite persistent currents flow on the surfaces of the specimen according to Faraday-Neumann-Lenz law to screen the magnetic field. However, if the field is strong enough, the current density required for the screening could be higher that the critical current density and the magnetic field can therefore penetrate in the slab. The limiting condition is when the field is fully penetrated and the sample is carrying opposite critical current densities in each half of the slab, as shown in Figure 2.3. This condition, called *critical state*, can be unstable, since a small disturbance can easily trigger a quench causing a collective flux unpinning. In particular, under adiabatic assumptions, it can be demonstrated [188] that an instability occurs in the slab if:

$$\frac{\mu_0 J_c^2 a^2}{\rho c_p (T_c - T_0)} > 3, \tag{2.2}$$

where μ_0 is the vacuum magnetic permeability and ρc_p is the volumetric heat capacity. The only geometrical parameter present in Eq. (2.2) is the slab half width a, and it is evident that its reduction can enhance the stability. The same principle applies also to the diameter of superconducting wires, therefore practical superconducting strands must be subdivided into a very large number of filaments, whose typical diameters are in the range of micrometers to avoid flux jumping.

[2]See Appendix A.3, page 192.
[3]See [188] chap. 7 for a very complete description of the phenomenon.

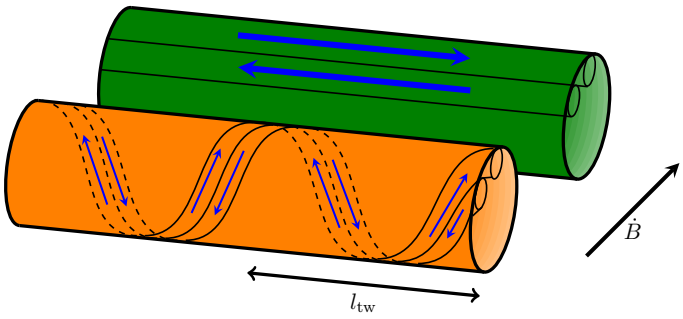

Figure 2.4: Sketch of the different behavior in transient fields of a non-twisted and a twisted wire. The blue arrows indicate the eddy current flow, that reverses every half twist pitch in the case of the twisted wire.

Inter-Filamentary Coupling

The subdivision and the normal-conducting matrix are effective in improving the strand stability, but if an external transient magnetic field is applied to the wire, eddy currents generate among the superconducting filaments flowing through the resistive matrix. This is undesirable, since AC losses are produced and the filaments become coupled together, reducing the effectiveness of the flux jump protection provided by subdivision. To solve this issue, the superconducting filaments are twisted with a pitch l_{tw}, since in this way the electric field generated by any external magnetic field variation reverses every half twist pitch, considerably decreasing the eddy currents and the coupling between filaments, as depicted in Figure 2.4. However, twisting is not effective in reducing the AC losses related to the strand self-field, that therefore sets a limit to the maximum wire diameter d_{st}, that should not be much greater than 1 mm, and to the maximum number of filaments, around 10^5 [189].

2.1.2 Nb-Ti

The niobium-titanium alloy was the first superconducting material to be engineered for mass industrial production, since 1960s [50], but the most remarkable achievements in its fabrication have been obtained in the 1980s, pushed by the requirements of particle accelerators and by the increasing demand for MRI magnets. Nowadays, Nb-Ti is still the most important industrial superconducting material for applications in the range $2 - 8$ T. It has indeed several advantages compared to other superconductors, in particular as regards the mechanical properties. It is very ductile but very strong at the same time: it is comparable to the stainless steel in terms of yield strength [15]. Moreover, these very good mechanical properties permit a cheaper fabrication process compared to Nb_3Sn or HTS superconductors. In Figure 2.5 some examples of Nb-Ti strand cross-sections are reported.

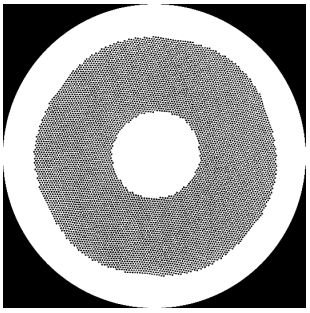

(a) SSC prototype strand (courtesy of Peter J. Lee, NHMFL-FSU).

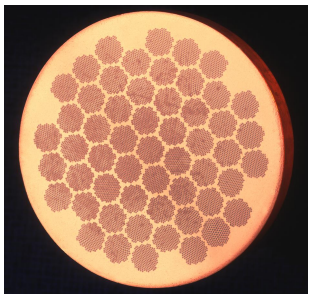

(b) LHC strand containing more than 8000 filaments (© CERN).

Figure 2.5: Cross-sections of Nb-Ti strands.

Fabrication Process

A typical fabrication process of a Nb-Ti strand follows the following steps [50] [188], depicted in Figure 2.6:

1. *Billet fabrication.* The first step is the creation of a cylindrical Nb-Ti billet with diameter of $200 - 600$ mm, that must be very homogeneous to obtain good mechanical and electrical properties. This is achieved through several processes like consumable-electrode arc melting, electron-beam melting, or plasma arc melting of pure metals. The level of impurities must be controlled very precisely to less than 200 ppm, except for oxygen and tantalum that have more relaxed specifications. The composition typically ranges between 44 and 50% of titanium in weight. At 44% in weight of titanium the maximum critical field of about 11 T at 4.2 K is achieved, whereas an higher titanium content can improve the critical temperature up to a 1:1 composition in weight.

2. *Monofilamentary extrusion.* The billet is put in a high-purity copper sheat and extruded to reduce its cross-section size by a factor ~ 20. The surfaces between the copper and the billet must be chemically clean to improve the creation of the bond between the filament and the stabilizer. A diffusion barrier, made with a niobium foil, is inserted between Nb-Ti and copper to prevent the formation of intermetallic components that may distort or even break the filaments.

3. *Multifilamentary extrusion.* In a second extrusion stage, several extruded monofilamentary billets are stacked together in a copper can and reduced to an overall diameter of $25 - 40$ mm. Before this stage, the monofilamentary billets are drawn in an hexagonal shape to better fit in the copper can. In the case of simple strands, like MRI wires that are characterized by only ~ 100 filaments, only this second extrusion process is necessary.

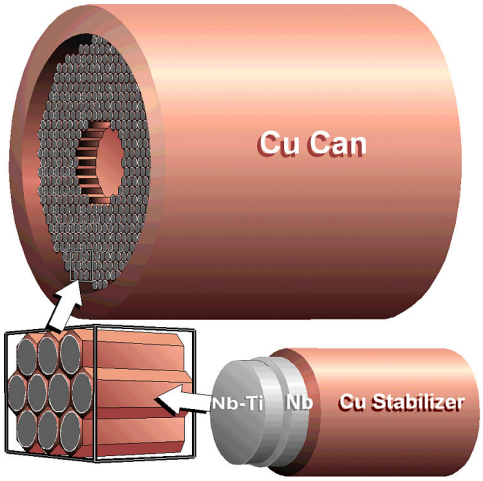

Figure 2.6: Fabrication of a Nb-Ti strand (courtesy of Peter J. Lee, NHMFL-FSU).

4. *Thermo-mechanical cycles.* To improve the critical current through flux pinning, the conductor should be subjected to several thermal cycles. Different strategies have been proposed along the years: common processes are composed by three heat treatments at 420℃ lasting for 80 hours each or 4-6 heat treatments at lower temperature ($\sim$ 375℃). Cold wire drawing is done before and after each thermal cycle, further reducing the conductor cross-section to the centimeter range.

5. *Final drawing and twisting.* The wire is brought to its final diameter, generally less than 1 mm, with a final cold work. Just before the final drawing, the wire is twisted with a pitch $10-20$ times larger than the diameter, in order to reduce the interfilamentary coupling currents in transient regime.

Wires with several thousands of filaments can be produced with this process. Aluminum instead than copper could be used as stabilizer. Other alloys like Cu-Ni or Cu-Mn are sometimes employed to increase the matrix resistivity, in particular when strong field variations are expected, in order to reduce AC losses and to decouple the superconducting filaments when they are very small, about some micrometers [178]. The n-index (Eq. 1.22) of Nb-Ti strands is generally high, as large as 50 [148]. Lower values are obtained if the filaments are smaller than $3\,\mu$m [189].

Critical Current Scaling Laws

The most common scaling law for Nb-Ti strands is the so-called *Bottura fit* [26]:

$$\frac{J_c(B,T)}{J_{c,\mathrm{ref}}} = \frac{C}{B}\left(\frac{B}{B_{c2}(T)}\right)^{\alpha}\left(1-\frac{B}{B_{c2}(T)}\right)^{\beta}\left[1-\left(\frac{T}{T_{c,0}}\right)^{n}\right]^{\gamma}, \tag{2.3}$$

where $J_{c,\mathrm{ref}}$ is a reference critical current density, typically measured at 5 T and 4.2 K, C is a *scaling constant* and α and β are the pinning exponents. The upper

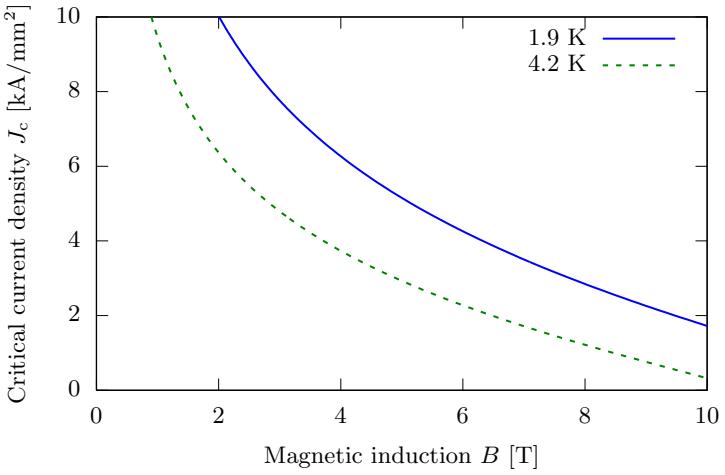

Figure 2.7: Magnetic field dependence of critical current in Nb-Ti typical LHC strands [26].

critical field is expressed by the formula:

$$B_{c2}(T) = B_{c2,0}\left[1 - \left(\frac{T}{T_{c,0}}\right)^n\right], \tag{2.4}$$

where n is generally equal to 1.7. Typical values for parameters are reported in Table 2.1. Figure 1.8a and Figure 2.7 have been obtained using this scaling law with the parameters reported in the last row of Table 2.1.

Table 2.1: Common ranges for Bottura fit parameters [26]. The typical values refer to LHC Nb-Ti strands.

	C [-]	α [-]	β [-]	γ [-]	n [-]	$T_{c,0}$ [K]	$B_{c,0}$ [T]	$J_{c,ref}$ [A/mm^2]
Range	24-38	0.57-0.89	0.75-1.10	1.76-2.30	1.7	8.5-9.35	14-14.5	$3 \cdot 10^3$
Typical	27.04	0.57	0.9	2.32		9.2	14.5	

Another scaling law sometimes used for Nb-Ti strands is the so-called *Bochvar fit* [95]:

$$J_c(B,T) = C[B_{c2}(T)]^{m-p}B^{p-1}\left(1 - \frac{B}{B_{c2}(T)}\right)^q, \tag{2.5}$$

with the following temperature dependence for the upper critical field:

$$B_{c2}(T) = B_{c2,0}\left[1 - \left(\frac{T}{T_{c,0}}\right)^2\right]\left(1 - c_1\frac{T}{T_{c,0}}\right). \tag{2.6}$$

The parameters are $B_{c2,0}$, $T_{c,0}$, the scaling constant C, $2 < m < 2.5$, $c_1 = 1.67$ and the pinning coefficients p and q, typically near respectively to 1 and 1.2.

2.1.3 Nb_3Sn

Niobium-tin belongs to the class of the *A15 phases*, which includes intermetallic compounds with the composition A_3B, where A is a transition metal and B can be any element. Further than Nb_3Sn, also Nb_3Ge, V_3Ga and V_3Si are notable superconducting compounds of this class. Differently from niobium-titanium alloy that exhibits a smooth variation of the superconducting properties with the composition, the correct stoichiometric composition is very important in these materials to achieve good critical parameters. Nb_3Sn is characterized by a quite peculiar crystallographic structure, with a body centered cubic lattice of tin atoms with two niobium atoms for each face of the cube (see Figure 1.4a). The pinning mechanism is in this case mainly due to the grain boundaries in the polycrystalline material.

Albeit superconductivity in Nb_3Sn has been discovered in 1954 [118], the large-scale industrial applications are relatively recent. The advantages of Nb_3Sn compared to Nb-Ti are the much higher critical parameters: $T_{c,0}$ is around 18.3 K and $B_{c2,0}$ is around 25 T [72]. Conversely, the mechanical properties are poorer: the material is very hard and brittle, and small elongations (about 0.3%) can irreversibly degradate the material or even fracture it. These limitations obviously affect the fabrication process, that must be different from that of Nb-Ti.

Fabrication Process

The first commercial Nb_3Sn conductors were made in the shape of thin tapes with a tiny layer of superconductor deposited on one face through chemical vapor deposition or surface diffusion [188]. In the 1970 the feasibility of the creation of multifilamentary composite like Nb-Ti strands was demonstrated through the so-called *bronze-route process* [90], described below.

The main difference between niobium-titanium and niobium-tin fabrication is that in the latter case the formation of the superconducting material from its precursors is done through an heat treatment that takes place after the strand has already reached its final diameter and usually after the coil winding. This is mandatory since the brittle Nb_3Sn would not tolerate the strong mechanical stresses needed to draw the material into a millimeter range wire, whereas the niobium and the tin separately are sufficiently ductile for such a process. Moreover, to reduce the mechanical stress provoked by the winding process, the so-called *react-and-wind* process employed for Nb-Ti is often replaced by the *wind-and-react* technique, in which the heat treatment is the final production step. The heat treatment is done at very high temperatures (around 650°C) lasting for ten days or more. Longer heat treatments facilitate the formation of the stoichiometric Nb_3Sn through diffusion, increasing the critical current but also causing a diffusion of pollutants in the stabilizer copper, that may result in a reduced RRR. The n-index is generally lower than Nb-Ti, up to 30-40.

Different processes have been elaborated and proposed along the years [72] (see also Figure 2.8):

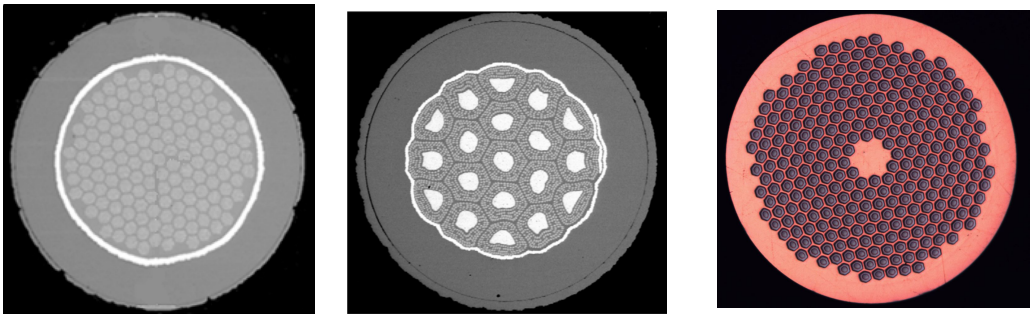

(a) Bronze (left) and IT (right) strands for ITER TF coil [168]. Both are 0.82 mm large.

(b) 1.25 mm PIT for the NED project [32] (© CERN).

Figure 2.8: Cross-section of Nb_3Sn strands made with different fabrication processes.

- *Bronze process.* It was the first method to be developed. Nb rods are inserted in a bronze matrix, surrounded by a stabilizing copper sheat. A diffusion barrier, typically made of tantalum, is interposed between the bronze and the copper to prevent the diffusion of the first in the second during the heat treatment, that would pollute the stabilizer and strongly increase its resistivity. The overall non-Cu area is employed for the formation of superconducting Nb_3Sn. Very fine filaments can be obtained ($\leq 5\,\mu$m), whereas the non-Cu critical current is relatively low, around 1 kA/mm^2 at 12 T and 4.2 K. It may be preferred in applications where strong field transients are expected.

- *Internal Tin (IT) process.* The strand contains a certain number of *subelements*, composed by a tin core surrounded by a composite of niobium and copper. In the case of a *Restacked Rod Process* (RRP) niobium filaments are embedded in a copper matrix, whereas in the *Modified Jelly Roll* (MJR) process a niobium mesh layered with copper is present. Differently from bronze process, the tin core area cannot be used for superconductor formation and the subelement acts as a quite large filament of about $50 - 150\,\mu$m. However, much higher non-Cu current density can be obtained, up to 3 kA/mm^2 at 12 T and 4.2 K [73].

- *Powder-In-Tube (PIT) process.* A tin-rich powder is embedded in niobium rods that are stacked into an high-purity matrix of copper. This process needs shorter heat treatments (some days) compared to the other methods, and it is able to obtain relatively small decoupled filaments of $30 - 50\,\mu$m. Non-Cu critical currents up to 2.7 kA/mm^2 at 12 T and 4.2 K [32] can be obtained, with large values for the n-index, up to two times compared to the other processes [104].

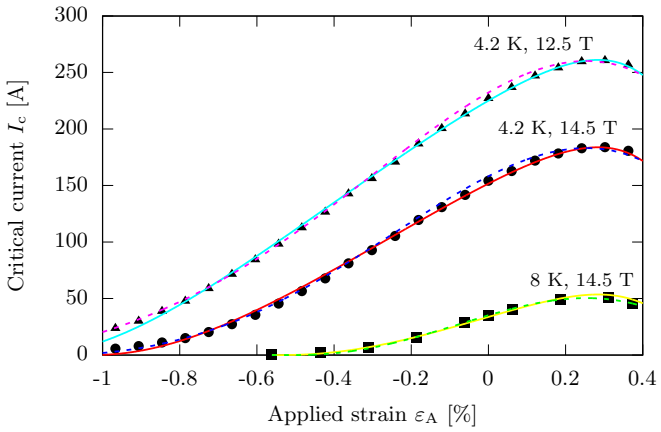

Figure 2.9: Critical current as a function of applied strain on a Nb_3Sn Internal-Tin strand for ITER TF production [168]. The solid lines represent ITER scaling law, the dotted ones Durham fit.

Critical Current Scaling Laws

In the last years a lot of effort has been put in the complete understanding of the pinning mechanism in the niobium-tin compound. This phenomenon is much complicated in niobium-tin than in niobium-titanium since the strain ε dependence cannot be neglected, as shown for example in Figure 2.9. One of the first empirical models regarding this aspect is the *Ekin model* [62]:

$$s(\varepsilon) = \frac{B_{c2}(\varepsilon)}{B_{c2,0}} = 1 - \alpha|\varepsilon_A + \varepsilon_m|^u, \tag{2.7}$$

where $s(\varepsilon)$ is the so-called *strain function*, $u \approx 1.7$ and:

$$\alpha \approx \begin{cases} 900, & \varepsilon_A < -\varepsilon_m, \\ 1250, & \varepsilon_A > -\varepsilon_m. \end{cases} \tag{2.8}$$

The strain can be expressed as $\varepsilon = \varepsilon_A + \varepsilon_m$, where ε_A is the *applied strain*, whereas ε_m is the *intrinsic strain*. The thermal contraction of copper at cryogenic temperatures is indeed higher than niobium-tin, therefore a thermal pre-compression acts on the superconductor even if no strain is applied. Critical field and current maxima can be therefore observed when this pre-compression is compensated at $\varepsilon_A = -\varepsilon_m$. For the critical temperature a typical correlation is:

$$\left[\frac{T_c(\varepsilon)}{T_{c,0}}\right]^w = s(\varepsilon), \tag{2.9}$$

with $w \approxeq 3$. A very common scaling law based on Ekin model is *Summers' fit* [160]:

$$J_{\mathrm{c}}(B,T) = \frac{C}{\sqrt{B}}\left(1-\frac{B}{B_{\mathrm{c2}}(T)}\right)^2\left[1-\left(\frac{T}{T_{\mathrm{c},0}}\right)^2\right]^2, \tag{2.10}$$

with the following empirical temperature dependence for upper critical field:

$$B_{\mathrm{c2}}(T) = B_{\mathrm{c2},0}\left[1-\left(\frac{T}{T_{\mathrm{c},0}}\right)^2\right]\left\{1-0.31\left(\frac{T}{T_{\mathrm{c},0}}\right)^2\left[1-1.77\,\log\left(\frac{T}{T_{\mathrm{c},0}}\right)\right]\right\}, \tag{2.11}$$

The strain dependence is introduced through the Ekin model just described (Eqs. 2.7 and 2.9) and with:

$$C = C_0[s(\varepsilon)]^{1/2}. \tag{2.12}$$

The critical surface is therefore characterized by four parameters: the maximum upper critical field $B_{\mathrm{c2},0}$, the maximum critical temperature $T_{\mathrm{c},0}$, the scaling constant C_0 and the strain constant α.

A more accurate description than Summers' fit has been proposed by Twente University [74]:

$$J_{\mathrm{c}}(B,T,\varepsilon) = \frac{C}{B}s(\varepsilon)\,\mathrm{MDG}\,(t)(1-t^2)b^p(1-b)^q, \tag{2.13}$$

where the *reduced field* b and the *reduced temperature* t are defined as:

$$b = \frac{B}{B_{\mathrm{c2}}(t,\varepsilon)} = \frac{B}{B_{\mathrm{c2},0}s(\varepsilon)\,\mathrm{MDG}(t)}, \tag{2.14}$$

$$t = \frac{T}{T_{\mathrm{c}}(\varepsilon)} = \frac{T}{T_{\mathrm{c},0}\,[s(\varepsilon)]^{1/w}}. \tag{2.15}$$

$\mathrm{MDG}(t)$ is the *Maki-De Gennes function*, an implicit microscopic model that describes the upper critical field dependence:

$$\log\left(\frac{T}{T_{\mathrm{c},0}}\right) = \Psi\left(\frac{1}{2}\right) - \Psi\left(\frac{1}{2}+\frac{\hbar D B_{\mathrm{c2}}(T)}{2\Phi_0 k_{\mathrm{B}} T}\right), \tag{2.16}$$

where D is the diffusion constant of the normal conducting electrons, $\hbar$ is the reduced Planck constant, Φ_0 is the flux quantum and k_{B} is the Boltzmann constant and $\Psi(x)$ is the *digamma* function, derivative of the logarithm of Gamma function $\Gamma(x)$:

$$\Psi(x) = \frac{\mathrm{d}}{\mathrm{d}x}\log\left[\Gamma(x)\right]. \tag{2.17}$$

In order to simplify the model, $\mathrm{MDG}(t)$ is generally approximated with the empirical formula:

$$\mathrm{MDG}(t) \approxeq 1 - t^{1.52}. \tag{2.18}$$

Table 2.2: Fit parameters for $\mathrm{MDG}(t) \cong 1 + \sum_{i=1}^{6} c_i t^i$.

c_1	c_2	c_3	c_4	c_5	c_6
0.00624582	−2.35233	2.85869	−2.54358	1.333669	−0.302699

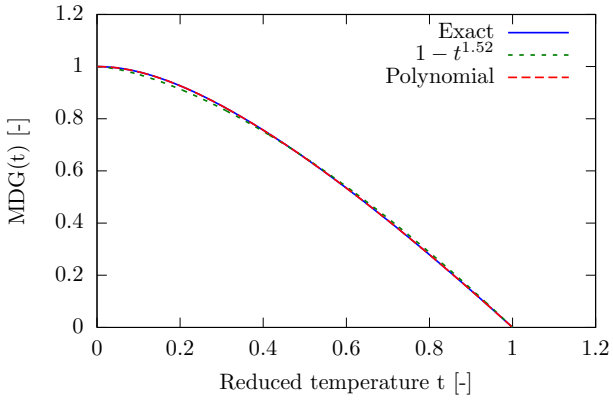

Figure 2.10: Maki-De Gennes function and its approximations.

A better fit can be obtained with the 6$^{\text{th}}$ order polynomial whose coefficients are reported in Table 2.2. $\mathrm{MDG}(t)$ and the two proposed fits are plotted in Figure 2.10.

The strain function $s(\varepsilon)$ is obtained through the so-called *deviatoric strain model* [72] and it results in:

$$s(\varepsilon) = 1 + \frac{1}{1 - C_{\mathrm{a},1}\varepsilon_{0,\mathrm{a}}} \left[C_{\mathrm{a},1} \left(\sqrt{\varepsilon_{\mathrm{sh}}^2 + \varepsilon_{0,\mathrm{a}}^2} - \sqrt{(\varepsilon - \varepsilon_{\mathrm{sh}})^2 + \varepsilon_{0,\mathrm{a}}^2} \right) - C_{\mathrm{a},2}\varepsilon \right], \tag{2.19}$$

$$\varepsilon_{\mathrm{sh}} = \frac{C_{\mathrm{a},2}\varepsilon_{0,\mathrm{a}}}{\sqrt{C_{\mathrm{a},1}^2 - C_{\mathrm{a},2}^2}}. \tag{2.20}$$

This scaling law has been adopted as official ITER parametrization for Nb_3Sn critical surface [27]. Five parameters are necessary: the maximum upper critical field $B_{\mathrm{c2},0}$, the maximum critical temperature $T_{\mathrm{c},0}$, the scaling constant C and the pinning force exponents p and q, that are respectively set to 0.5 and 2 in most common cases. Three more parameters, $C_{\mathrm{a},1}$, $C_{\mathrm{a},2}$ and $\varepsilon_{0,\mathrm{a}}$ are needed for the strain dependence. A selection of common values for the parameters is reported in Table 2.3.

A simplified and improved version of Eq. (2.13) has been proposed in [8]:

$$J_{\mathrm{c}}(B, T, \varepsilon) = C(1 - t^2)b^{p-1}(1 - b)^q. \tag{2.21}$$

The relations (2.14) and (2.15) are maintained, whereas an improved strain function is proposed:

$$s(\varepsilon) = \max\left\{0, \frac{1 - C_{\mathrm{a},1}\sqrt{\varepsilon^2 + \varepsilon_{0,\mathrm{a}}^2} - C_{\mathrm{a},2}\left[\varepsilon^3 - 3(\varepsilon_{0,\mathrm{a}})^2\varepsilon\right]}{1 - C_{\mathrm{a},1}\varepsilon_{0,\mathrm{a}}}\right\}. \tag{2.22}$$

Table 2.3: Some examples of parameters for Twente/ITER scaling law.

Type	p [-]	q [-]	C_{a1} [-]	C_{a2} [-]	$\varepsilon_{0,\mathrm{a}}$ [%]	ε_{m} [%]	$T_{\mathrm{c},0}$ [K]	$B_{\mathrm{c},0}$ [T]
PIT, SMC3 [107]	0.5	2	45.062	4.256	0.286	0.0	16.97	29.45
PIT, FRESCA II [24]	0.453	1.90	60	22	0.31	−0.15	16.3	30.2
IT, ITER TFPRO [83]	0.5	2	81.69	35.25	0.15	−0.057	16.21	34.02
IT, ITER TF [168]	0.746	2.335	79.94	45.04	0.207	−0.284	16.26	32.59
Bronze I, ITER TF [168]	0.525	1.547	404.87	386.71	0.139	−0.422	16.06	29.88
Bronze II, ITER TF [168]	0.489	1.618	226.93	203.86	0.187	−0.366	16.02	30.28

It must be noted that the number of the fit parameters and their symbols are the same than Eq. (2.13), but their meaning and their values are generally different.

Another fit function often used to describe niobium-tin critical surface is the *Durham scaling law* [162]:

$$J_{\mathrm{c}}(B,T,\varepsilon) = A(\varepsilon)[T_{\mathrm{c}}^{*}(\varepsilon)(1-t^2)]^2[B_{\mathrm{c2}}^{*}(T,\varepsilon)]^{n-3}b^{p-1}(1-b)^q. \tag{2.23}$$

where:

$$B_{\mathrm{c2}}^{*}(T,\varepsilon) = B_{c2,0}^{*}(\varepsilon)(1-t^{\nu}), \tag{2.24}$$

$$\frac{B_{c2,0}^{*}(\varepsilon)}{B_{c2,0}^{*}(0)} = 1 + c_2\varepsilon^2 + c_3\varepsilon^3 + c_4\varepsilon^4, \tag{2.25}$$

$$\left(\frac{A(\varepsilon)}{A(0)}\right)^{1/u} = \left(\frac{B_{\mathrm{c2},0}(\varepsilon)}{B_{\mathrm{c2},0}(0)}\right)^{1/w} = \frac{T_{\mathrm{c}}^{*}(\varepsilon)}{T_{\mathrm{c}}^{*}(0)}. \tag{2.26}$$

The model is very flexible since it features a lot of parameters (12, plus the pre-compression ε_{m}), although some of them are typically considered fixed, for example $u = 0$, $n = 2.5$, $\nu = 1.5$ and $w = 2.2$. In Table 2.4 some examples of parameters for ITER TF strands are reported.

Table 2.4: Some examples of parameters for Durham scaling law for ITER TF strands [168]. The applied strain must be inserted in the fit function as a percentage.

Type	p [-]	q [-]	c_2 [-]	c_3 [-]	c_4 [-]	ε_{m} [%]	$T_{\mathrm{c},0}$ [K]	$B_{\mathrm{c2},0}$ [T]
IT	0.963	2.310	−0.753	−0.606	−0.160	−0.254	16.73	30.76
Bronze I	1.056	2.099	−0.487	−0.263	−0.0420	−0.382	16.60	29.80
Bronze II	0.490	1.420	−0.435	−0.219	−0.0325	−0.369	16.36	28.75

Recently, a scaling law based on an exponential strain dependence has been proposed [169], leading to very accurate results both from a theoretical and from an experimental point of view.

Figure 2.11: LHC Rutherford cable (© CERN). In both images, the copper matrix of some strands is etched, showing the Nb-Ti filaments.

2.2 Superconducting Cables

Generally, superconducting strands are bundled together into cables rather than being used individually. High current cables have indeed many advantages in windings for high-field magnets [188] [189]. With high currents less turns are necessary, simplifying the magnet design and reducing its cost, at the same time improving the conductor ruggedness. Indeed, a reduced number of turns leads to a smaller impact of the turn-to-turn insulation on the winding fill factor, compacting the design. Furthermore, it leads to a decreased inductance, reducing the voltages during current ramps and allowing faster current discharges in the case of a quench. Moreover, the stability is enhanced, since current redistribution among parallel strands can help the recovering from local disturbances that can affect a single wire. The main drawbacks of large superconducting cables are the increased power dissipated by the current leads and joints and the high current power converters required, but their impact is more than compensated by the advantages [188].

An important characteristic of a cable design is the possibility of a full geometrical *transposition* of the strands, that means that every wire should exchange its position with each other one along the cable length, in order to obtain an uniform average position in the cable cross-section. In this way, the AC losses are significantly reduced and the strands are exposed to almost the same mean magnetic induction along the cable length. Transposition is different from twisting, since in a twisted cable a wire located in the center of the cable stays in the same position all along the cable length.

Several designs are available for superconducting cables. In the following, Rutherford cables and Cable-In-Conduit-Conductors (CICC) are described. The first is the most common design for magnets employed in particle accelerators, whereas the second will be widely used in fusion magnets like those of ITER.

2.2.1 Rutherford Cables

The Rutherford cable was developed in the beginning of 1970s in the Rutherford laboratory, from which it takes its name. This cable can be described as a flattened hollow twisted tube of strands, that form therefore two fully transposed layers [189].

It is characterized by a very large fill factor (between 80 and 90%) and it generally carries currents in the range $10 - 20$ kA with a number of strands N_{st} between about 10 and 50. The cabling scheme is the same of that of the Roebel cable bar commonly used in electric machines. Images of a LHC Nb-Ti Rutherford cable are reported in Figure 2.11.

In particle accelerators the field produced by magnets must be controlled very carefully. Considering a polar system of coordinates (r, ϕ), the ideal current distribution needed to produce a $2n$-polar magnetic field is proportional to $\cos(n\phi)$ [148]. Since such a distribution is not practically achievable, it is approximated by a suitable arrangement of coil blocks forming arc segments, as it can be seen in Figure 2.12. The Rutherford cables are the main conductor employed in these magnets, because of the very high engineering current density that can be achieved and the great geometrical precision they can offer. To permit a better positioning of the cables in the magnet cross-section, Rutherford cable cross-section is generally slightly trapezoidal rather than perfectly rectangular. This characteristic is called *keystoning*.

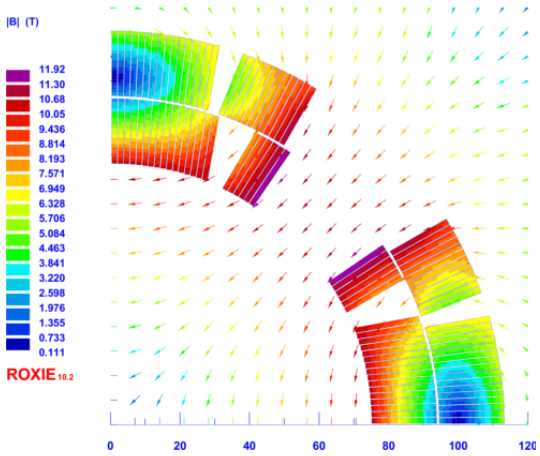

Figure 2.12: Field map on a quadrant of the cross-section of the MQXF quadrupole for the HiLumi upgrade of LHC [67]. The image and the field have been obtained with the ROXIE [148] numerical tool.

In Figure 2.13 images of a cabling machine for Rutherford cable are reported. As shown in Figure 2.13a, a large rotating disk is equipped with a certain number of spools with the strands to be cabled [53]. The number of rotations per cable unit length defines the *transposition pitch* l_{tr} of the cable. The rotation speed and the pulling force acting on wires is controlled in order to reduce their torsion and equalize the tension among them. The wires then pass in the middle of a set of four rollers that define the cable thickness w and height h, as shown in Figure 2.13b. The keystoning angle α can be obtained by tilting the top roller, but its amount is limited by the critical current degradation that is obtained if the narrow-edge packing factor is higher than 98% [148]. To reduce the inter-strand coupling currents among the two

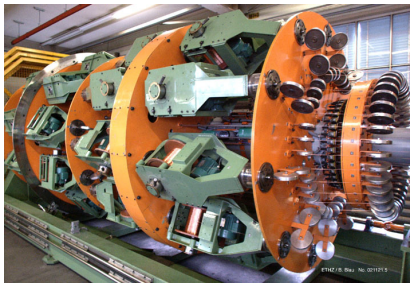

(a) The rotating spools.

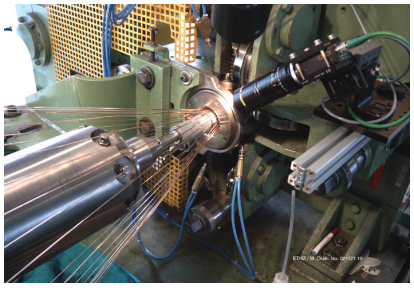

(b) The rollers acting on the wires.

Figure 2.13: Images of a Rutherford cabling machine (© CERN).

Table 2.5: Geometrical parameters of some selected Rutherford cables.

Magnet	N_{st}	d_{st} [mm]	h [mm]	w [mm]	α [degrees]	l_{tr} [mm]	w_{ins} [mm]	*Reference*
LHC main dipole	28	1.065	15.1	1.9	1.25	115	0.125	[148]
DISCORAP SIS300 dipole	36	0.825	15.1	1.48	0.9	100	0.125	[178]
HQ01e quadrupole	35	0.8	15.15	1.437	0.75	102	0.09	[182]
11 T dipole	40	0.7	14.70	1.269	0.79	110	0.150	[14]
SMC3 racetrack	14	1.25	10.0	2.2	0.0	60	0.1	[10]

cable layers, sometimes an annealed stainless steel strip, some tens of micrometers thick, is interposed between them to increase the contact resistance [178].

Rutherford cable insulation is done in different ways. Nb-Ti cables are generally wrapped with some layers of a thin polyimide sheet. For example, in the case of LHC cables three layers of polyimide with an overall thickness w_{ins} of 125 μm per cable face are employed [145]. Since it was discovered that leaving the cable porous to coolant can improve the conductor stability, a slight gap between turns of insulation is left [189]. In the case of Nb_3Sn cable, this insulation technique is not applicable, since polyimide cannot withstand the thermal cycle needed by the wind-and-react process. The cable is therefore insulated by means of glass fiber wraps, sleeves or braids. After the heat treatment, the winding is impregnated with epoxy resin to assure a better structural support to the fragile Nb_3Sn strands.

2.2.2 Cable-In-Conduit-Conductors

Fusion magnets like those of ITER project require currents up to 68 kA, much higher than accelerator magnets. Furthermore, the environment in which they are located is very noisy: ITER magnets are indeed designed to work in pulsed operation up to more than 1 T/s, more than two orders of magnitude larger than LHC nominal ramp rate. Moreover, the plasma itself can affect the coil performance in the case of instabilities or accidental disruptions. Conversely, the field quality specifications are generally relaxed compared to accelerator-grade cables. A more robust design with

improved cooling capabilities is therefore required for these working conditions. This is achieved in the so-called Cable-In-Conduit Conductors (CICC) thanks to *forced-flow cooling* by means of super-critical helium

CICCs are composed by a very large number of strands, up to about 1500. A multi-stage cabling scheme, sometimes called *rope-type cabling*, is adopted [55]. First of all, three strands are twisted together with a twist pitch t_1 to form the so-called *triplet*, that is generally the fundamental brick of a CICC. A group of triplets, e.g. three of them, are then twisted together with a pitch t_2 to form a 2^{nd} order bundle, in this case referred to as 3×3. Then, a certain number of these 2^{nd} order sub-cables, e.g. five of them, is twisted together to form a 3^{rd} order bundle called $3\times3\times5$ and so on, up to the last cabling stage. Suitable intermediate compaction is applied on the cables and the sub-cables to better control their shape and geometry. The twist pitches gradually increase with the cabling stage and are generally selected to be non-integer multiples to avoid trivial coupling current loops [54].

After cabling, the conductor is inserted in a resistive jacket, generally made of steel, to give mechanical stiffness to the conductor. Depending on the application the jacket cross-section can be circular, square, square with a circular hole for the conductor or rectangular. The jacket is oversized by a few millimeters on the diameter to enable the cable insertion, therefore it should be compacted onto the cable with a set of rollers to achieve its final dimensions. Finally, the conductor is spooled to facilitate transportation. A pair of images of CICCs from ITER production is shown in Figure 2.14.

(a) TF conductor. (b) CS conductor.

Figure 2.14: Images of ITER CICCs (courtesy of Carlos Sanabria, NHMFL-FSU).

With this design, the strands are fully transposed and a considerable void fraction f_{void}, around 30-40%, is available. These voids are employed for forced-flow cooling by means of super-critical helium. Often, the last cabling stage is twisted around a central stainless steel spiral to facilitate the helium circulation between the strands and to reduce its pressure drop between inlet and outlet [54]. This very porous design permits a much better heat exchange with the coolant compared to Rutherford cable, due to the larger wetted area and to the forced helium flow. However, an important drawback, in particular for Nb_3Sn wires, is that the strands have more freedom

Table 2.6: ITER conductors specifications [55]. TF and CS conductors rely on Nb_3Sn technology, whereas PF and CC conductors are made of Nb-Ti strands.

(a) $N_{\mathrm{st,SC}}$ is the number of SC strands in the cable. The symbol ◯ indicates a circular jacket, ⊡ a squared jacket with a circular hole and □ a squared jacket. The dimension reported is the external diameter in the first case, the external side in the other cases.

Type	Cable Layout	Triplet	Copper Core	$N_{\mathrm{st,SC}}$	Jacket [mm]
TF	$(3 \times 3 \times 5 \times 5 + \mathrm{C}) \times 6$	2 SC+1 Cu	3×4 Cu	900	◯ 43.7
CS	$3 \times 3 \times 4 \times 4 \times 6$	2 SC+1 Cu	-	576	⊡ 49.0
PF1,6	$3 \times 4 \times 4 \times 5 \times 6$	3 SC	-	1440	⊡ 53.8
PF2-4	$((3 \times 3 \times 4 + \mathrm{C_1}) \times 5 + \mathrm{C_2}) \times 6$	2 SC+1 Cu	1.2 mm ($\mathrm{C_1}$) 2.7 mm ($\mathrm{C_2}$)	720	⊡ 51.9
PF5	$(3 \times 4 \times 4 \times 4 + \mathrm{C}) \times 6$	3 SC	2.85 mm	1152	⊡ 51.9
CC	$3 \times 4 \times 5 \times 5$	3 SC	-	300	□ 19.2

(b) $d_{\mathrm{cable,i}}$ is the inner diameter of the cable after compaction, corresponding to the central spiral diameter (absent in the CC conductor). $d_{\mathrm{cable,e}}$ is the external diameter of the cable after compaction, except for CC conductor in which it is the side of the square.

Type	Twist pitches t_i [mm]					d_{st} [mm]	f_{void} [%]	$d_{\mathrm{cable,i}}$ [mm]	$d_{\mathrm{cable,e}}$ [mm]
TF	80	140	190	300	420	0.82	29.7	7.9-8.1	39.7
CS	20	45	80	150	450	0.83	33.5	6.8-7.2	32.6
PF1,6	45	85	145	250	450	0.73	34.3	9.8-10.2	37.7
PF2-4	45	85	145	250	450	0.73	34.1	9.8-10.2	35.3
PF5	45	85	145	250	450	0.73	34.1	9.8-10.2	35.3
CC	45	85	145	250	-	0.73	35.4	-	14.8

to displace compared to Rutherford impregnated cables, and this can be a serious concern in terms of performance degradation as the winding is subjected to several electromagnetic (and therefore mechanical) cycles.

To improve the overall cable performance in terms of stability and protection, in some CICCs a certain number of only copper strands, referred to as *segregated copper strands*, are added in the conductors. For example, one or even two of the strands of the triplet can be replaced with a copper strand. In some cases, like ITER TF and PF conductors, also entire normal-conducting *cores* are added in the central channel of high-order superconducting bundles.

The last stage sub-cables, referred to as *petals*, are generally partially wrapped with a thin stainless steel tape, to facilitate helium penetration into the petal and enabling inter-petal current redistribution in the case of a quench. The steel tape provides mechanical support and an increase of the inter-strand resistance to reduce the coupling currents and the AC losses [54]. The overall cable is wrapped with another thin stainless steel tape to provide protection during jacketing.

As an example of design parameters, in Table 2.6 the main specifications of the CICCs that will be employed in ITER magnets are reported.

Part II

Electromagnetic and Thermal Numerical Models for Superconducting Cables

Chapter 3

Coupled Thermal Electromagnetic THELMA Code

The analysis of the superconducting cables performances is a very complex task from an engineering point of view. Phenomena happening on different scales must indeed be considered, starting from the micrometric superconducting filaments carrying fractions of ampere to the largest CICCs carrying tens of kA in a cross-section of some centimeters. Also the time scale of the disturbances to be considered is very wide, ranging from interfilamentary coupling currents with time constants of milliseconds to eddy currents, lasting for several seconds, induced by plasma instabilities. A numerical approach to this problem is mandatory in many cases, due to the large number of unknowns, the very complex material behavior and geometry and the intrinsic coupling between thermal and electromagnetic properties. An accurate description of the conductor geometry is generally necessary, since phenomena like the coupling currents among strands are strongly dependent on it. Because of that, it is often difficult to employ general purpose finite-elements software, that would require a enormous number of mesh elements to describe efficiently the cable geometry. Thus, dedicated software is frequently developed in order to better fit the requirements of this kind of computation.

During this PhD activity, the coupled electromagnetic and thermal model THELMA for the analysis of superconducting cables has been used and further developed. The geometrical, electromagnetic and thermal modules are described in this chapter, with a particular focus on the brand-new parts implemented, regarding the Rutherford cables geometry, the brand-new thermal model and its coupling with the electromagnetic module.

3.1 Numerical Models for Superconducting Cables

The unsuitability of commercial finite-elements codes in describing the very complex geometry and the unconventional material properties of superconducting cables have encouraged the development of many dedicated numerical models to analyse the current and temperature distributions. Some of the most notable in the field of thermal and electromagnetic analysis are summarized in this section. Very often, these models are based on the generation of a lumped or distributed electrical network equivalent to the object under study. This permits to take advantage of the well-known techniques for the solution of the electrical network problems.

An early example of this kind of model was given for the computation of eddy currents in a flat metal-filled superconducting braid subjected on a uniform field along the cable [125]. A lumped electrical network, characterized by $N_{\mathrm{st}} - 1$ independent current loops, was proposed to overcome the difficulty in applying the Maxwell's equations in the anisotropic geometry of the conductor. Many authors have generalized this model with the concept of "columns" [6] or "calculation bands" [174] that permits to consider more complex magnetic field configurations. The well-known *CUDI* model [175], focused on Rutherford cables, is based on this approach. Its equivalent network defines the possible current paths in the cable and the possible inter-strand heat exchanges. The cable is discretized over the cross-section in $2N_{\mathrm{st}} - 2$ sections and in N_{st} bands for each cable transposition pitch. The code has demonstrated his effectiveness in studying and reproducing experimental data on the development of coupling currents [174] and on the minimum quench energies [187]. A modified version of CUDI, *CUDI-CICC* [130] has been developed by the University of Twente to extend the approach to CICCs, although describing only the last stage sub-cables.

Further models based on equivalent lumped networks obtain the solution thanks to the *node analysis* [46] rather than the concept of bands or current loops. The electromagnetic code developed by the University of Udine and included in the THELMA code is among them, and is described in detail in the following. The *JackPot-ACDC* code [172], developed by the University of Twente, is another member of this class. It is focused on the analysis and design of CICC cables and joints in both steady-state and transient regimes. The main advantage of this code is the MATLAB programming environment that, thanks to its efficiency, permits a very detailed description of the conductor, up to the individual strand, with a reasonable computational effort [143]. The code comprehends a thermal model computing the temperatures of helium, cable and joint along the conductor axis, representing the cable cross-section with six independent temperatures (one for each petal).

Several models are instead based on a distributed parameters network, like [153]. One of the most complete and general purpose is *THEA* [25], which can be used to model both Rutherford cables and CICCs [5] [29] and is able to describe the conductor in its electromagnetic, thermal and hydraulic aspects [30]. The model for the electrical current distribution is based on the hypothesis that the current can

flow continuously from each strand to all the other through distributed contacts. A system of parabolic differential equations is obtained in this way, and it can be solved numerically or even analytically under some assumptions [28]. These equations, with suitable arrangements or modifications, are the basis for several other codes, like [103] or the electromagnetic module, described in detail in the following, developed by the University of Bologna and implemented in the THELMA code.

All these models are normally intended for a description of a short cable segment, since they are generally too demanding and detailed for the simulation of an entire coil or magnet. Further dedicated codes are therefore generally employed for this task. For example, the software *ROXIE* by CERN [148] permits a detailed design of the electromagnetic performances of accelerator magnets. Codes for the analysis of the quench behavior at the magnet level are also available, like *QLASA* by INFN-LASA laboratory [146], or the thermal module based on a lumped network embedded in ROXIE [151].

3.1.1 THELMA Code

The THELMA code is divided into several independent modules, that are described in detail in the following sections. A part of the code, herein referred to as *geometrical model*, is devoted to the generation of the cable geometry starting from the superconducting strand and cable parameters. After this step, suitable equivalent networks are generated by the *electromagnetic* and the *thermal* models, that can be used together or separately. The electromagnetic model is composed of two modules:

- a *linear lumped parameters network* developed by the University of Udine [18], referred to as *Udine EM module*, capable to describe superconducting cables, joints and terminations far from the critical surface;

- a *non-linear distributed parameters network* developed by the University of Bologna [34], referred to as *Bologna EM module*, that features only an elementary model for joints and terminations, but is suitable to describe the superconductor in more general working conditions.

The two modules can also be used together, in particular when the termination or joint is described by Udine EM module and the remaining part of the cable is modeled by Bologna EM module. The *thermal model* is instead a non-linear lumped equivalent network, developed at the University of Udine during this PhD. Presently, it can be coupled only with the Bologna EM module. A *thermal-hydraulic* module developed by Politecnico di Torino [140], more focused on the helium behavior and its thermal stability in CICCs, is also available. Since this module has not been used in the present work, it will not be considered any further.

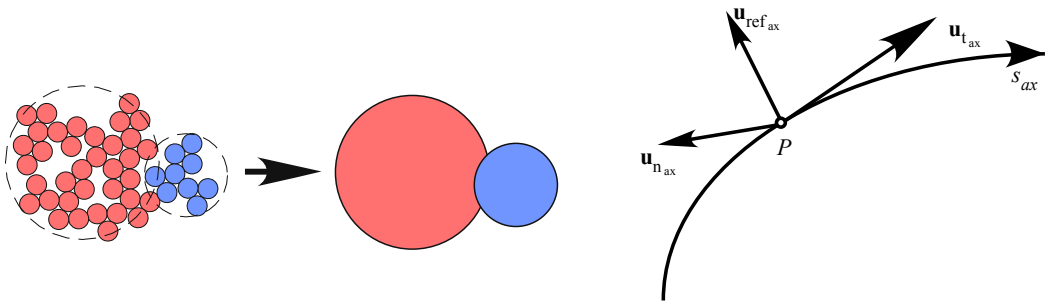

(a) Left: two bundles obtained by grouping several strands. Right: equivalent macrostrands.

(b) Local triad describing the cable axis as a function of s_{ax}.

Figure 3.1: THELMA geometrical model.

3.2 THELMA Geometrical Model

The sequence adopted for the superconductors geometry modeling is described in [19]. This phase is divided into three main steps:

1. *the definition of the cable cross-section.* To meet the requirements of complex cables like CICCs, a hierarchical model is employed for the cable-cross section. First, the material and geometrical properties of each individual strand are defined. Then, the cable cross-section geometry is generated following a *group-and-define strategy*: more and more complex bundles can be defined by grouping strands and bundles defined in the previous steps, as shown in Figure 3.1a. In order to facilitate the analyses of cables made of many strands, it is also possible to use equivalent *macrostrands* or *cable elements* in place of cable bundles, so that the number of model unknowns can be reduced;

2. *the definition of the cable axis 3D geometry.* This step makes use of some embedded primitives, describing rectilinear segments, helices, circles or circle arcs, or with an array of coordinates that is then interpolated by suitable cubic splines. In any case, a local triad $(\mathbf{u}_{\mathrm{t,ax}}, \mathbf{u}_{\mathrm{n,ax}}, \mathbf{u}_{\mathrm{ref,ax}})$ is obtained as a function of the curvilinear coordinate along the cable axis s_{ax}, as shown in Figure 3.1b;

3. *the computation of the geometry of each individual strand.* The geometry of each strand can be computed depending on the cabling scheme, starting from the information on the cable cross-section and the cable axis geometry, as reported in the following paragraphs.

3.2.1 Rutherford Cable

In this section the geometry of the strands of a Rutherford cable wound on a rectilinear axis is described first. In particular, the equations for the strand coordinates

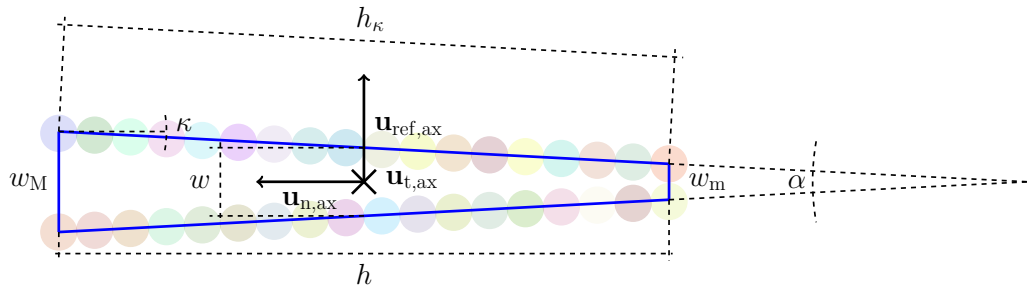

Figure 3.2: Sketch of the geometrical parameters on a Rutherford cable cross-section. The keystoning is exaggerated for clarity purposes.

$\mathbf{x} = (x_1, x_2, x_3)$ and the tangent unit vector to the strand axis $\mathbf{u}_\mathrm{t} = (u_{\mathrm{t},1}, u_{\mathrm{t},2}, u_{\mathrm{t},2})$ are presented, where:

$$\mathbf{u}_\mathrm{t} = \frac{\mathrm{d}\mathbf{x}}{\mathrm{d}s}, \tag{3.1}$$

and s is the curvilinear coordinate along the strand axis. The results are then extended for whatever curvilinear cable axis described by the triad $(\mathbf{u}_{\mathrm{t,ax}}, \mathbf{u}_{\mathrm{n,ax}}, \mathbf{u}_{\mathrm{ref,ax}})$ with the transformation:

$$\mathbf{x}^* = x_1\mathbf{u}_{\mathrm{t,ax}} + x_2\mathbf{u}_{\mathrm{n,ax}} + x_3\mathbf{u}_{\mathrm{ref,ax}} + \mathbf{x}_\mathrm{a}, \tag{3.2}$$

where $\mathbf{x}_\mathrm{a}$ is the cable axis point. In Figure 3.2 the main parameters of the cross-section are schematized, with a much exaggerated keystoning angle α for clarity purposes. The cable axis reference vector $\mathbf{u}_{\mathrm{ref,ax}}$ is parallel to the cable short-edge. Along the cable axis, the strands describe an isosceles trapezoid in the cross-section, represented with a solid blue line in the figure: w_m and w_M are respectively the minor and major bases and h is the height. The following relations can be written:

$$\kappa = \arctan\left(\frac{w_\mathrm{M} - w_\mathrm{m}}{2h}\right) = \frac{\alpha}{2}, \tag{3.3}$$

$$w = \frac{w_\mathrm{m} + w_\mathrm{M}}{2}, \tag{3.4}$$

$$h_\kappa = \frac{h}{\cos\kappa}. \tag{3.5}$$

Longitudinal views of the cable are shown in Figure 3.3. Considering a transposition pitch l_tr, the transposition angle φ, assumed constant along the cable axis and on all the cable faces, can be computed as:

$$\varphi = \arctan\left[\frac{l_\mathrm{tr}}{2(w + h_\kappa)}\right], \tag{3.6}$$

since in half transposition pitch the strand has moved along half of the trapezoid perimeter.

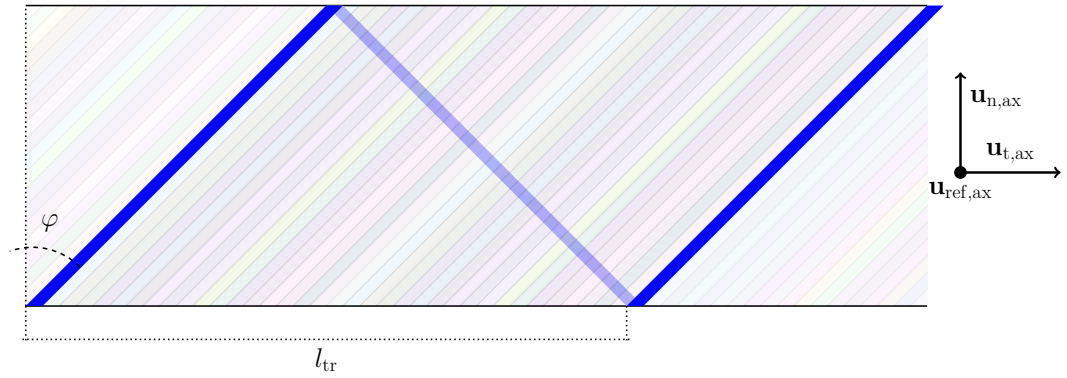

(a) Long-edge view.

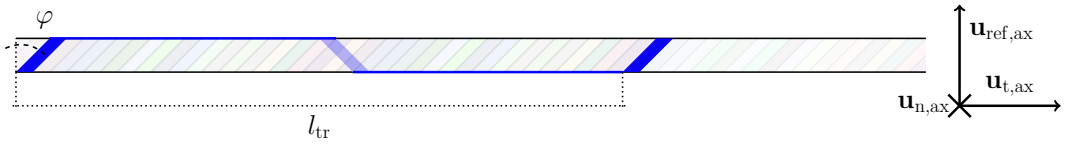

(b) Short-edge view.

Figure 3.3: Sketch of the strands transposition on the Rutherford cable faces.

Piece-Wise Linear Model

A preliminary simplified model for the geometry of each strand axis as a function of the cable axis curvilinear coordinate s_{ax} can be obtained with a piece-wise linear approximation. Even if the geometry is periodic with a space period equal to the transposition pitch l_{tr}, it suffices to consider the behavior in $s_{\mathrm{ax}} \in [0, l_{\mathrm{tr}}/2)$. To obtain the geometry of the second half-period, the following transformation is applied:

$$s_{\mathrm{ax}} \quad \Longrightarrow \quad s^*_{\mathrm{ax}} = \frac{l_{\mathrm{tr}}}{2} - s_{\mathrm{ax}}, \tag{3.7}$$

$$x_3 \quad \Longrightarrow \quad x^*_3 = -x_3, \tag{3.8}$$

$$u_{\mathrm{t},2} \quad \Longrightarrow \quad u^*_{\mathrm{t},2} = -u_{\mathrm{t},2}. \tag{3.9}$$

The cable transposition direction described in the following is left-handed, i.e. anti-clockwise. To obtain a right-handed transposition direction, it suffices to consider the transformation:

$$x_3 \quad \Longrightarrow \quad x^r_3 = -x_3, \tag{3.10}$$

$$u_{\mathrm{t},3} \quad \Longrightarrow \quad u^r_{\mathrm{t},3} = -u_{\mathrm{t},3}. \tag{3.11}$$

Three different regions for $s_{\mathrm{ax}} \in [0, l_{\mathrm{tr}}/2)$ are defined. Their boundaries along the cable axis curvilinear coordinate are:

$$s^a_{\mathrm{ax}} = \frac{w_{\mathrm{M}}}{2} \tan\varphi, \tag{3.12}$$

$$s^b_{\mathrm{ax}} = \left(\frac{w_{\mathrm{M}}}{2} + h_\kappa\right) \tan\varphi. \tag{3.13}$$

In any case the first coordinate of $\mathbf{x}$ and $\mathbf{u}_{\mathrm{t}}$ is:

$$x_1(s_{\mathrm{ax}}) = s_{\mathrm{ax}} \tag{3.14}$$

$$u_{\mathrm{t},1} = \sin\varphi, \tag{3.15}$$

since the curvilinear coordinate s along the strand axis can be expressed by:

$$s = \frac{s_{\mathrm{ax}}}{\sin\varphi}. \tag{3.16}$$

The equations for the other two coordinates depend on the curvilinear coordinate region and are the following:

- *Region a:* when the strand lays on the largest short-edge cable face, i.e. trapezoid major base w_{M}, the position is described by the following equations, valid for $s_{\mathrm{ax}} \in [0, s^a_{\mathrm{ax}}]$:

$$x^a_2(s_{\mathrm{ax}}) = \frac{h}{2}, \tag{3.17}$$

$$x^a_3(s_{\mathrm{ax}}) = -\frac{w_{\mathrm{M}}}{2} + \frac{s^a_{\mathrm{ax}} - s_{\mathrm{ax}}}{\tan\varphi}. \tag{3.18}$$

  The tangent unit vector to the strand axis $\mathbf{u}_{\mathrm{t}}$ is:

$$u^a_{\mathrm{t},2} = 0, \tag{3.19}$$

$$u^a_{\mathrm{t},3} = -\cos\varphi \tag{3.20}$$

- *Region b:* when the strand lays on the long-edge cable face, i.e. trapezoid side h_κ, the position is described by the following equations, valid for $s_{\mathrm{ax}} \in [s^a_{\mathrm{ax}}, s^b_{\mathrm{ax}}]$:

$$x^b_2(s_{\mathrm{ax}}) = -\frac{s_{\mathrm{ax}} - s^a_{\mathrm{ax}}}{\tan\varphi} \cos\kappa + \frac{h}{2}, \tag{3.21}$$

$$x^b_3(s_{\mathrm{ax}}) = \frac{s_{\mathrm{ax}} - s^a_{\mathrm{ax}}}{\tan\varphi} \sin\kappa - \frac{w_{\mathrm{M}}}{2}. \tag{3.22}$$

  The tangent unit vector to the strand axis $\mathbf{u}_{\mathrm{t}}$ is:

$$u^b_{\mathrm{t},2} = -\cos\varphi\cos\kappa, \tag{3.23}$$

$$u^b_{\mathrm{t},3} = \cos\varphi\sin\kappa \tag{3.24}$$

- *Region c:* when the strand lays on the smallest short-edge cable face, i.e. trapezoid minor base w_m, the position is described by the following equations, valid for for $s_\mathrm{ax} \in [s^b_\mathrm{ax}, l_\mathrm{tr}/2)$:

$$x^c_2(s_\mathrm{ax}) = -\frac{h}{2}, \tag{3.25}$$

$$x^c_3(s_\mathrm{ax}) = -\frac{w_\mathrm{m}}{2} + \frac{s_\mathrm{ax} - s^b_\mathrm{ax}}{\tan\varphi} \tag{3.26}$$

  The tangent unit vector to the strand axis $\mathbf{u}_\mathrm{t}$ is:

$$u^c_{\mathrm{t},2} = 0, \tag{3.27}$$

$$u^c_{\mathrm{t},3} = \cos\varphi \tag{3.28}$$

In Figure 3.4 an example of the long-edge and short-edge views of one strand axis of a keystoned Rutherford cable with 36 strands is reported. The geometry described above corresponds to the first strand of the cable, assumed with initial position in the middle of the largest cable thickness:

$$x_2(0) = \frac{h}{2}, \tag{3.29}$$

$$x_3(0) = 0. \tag{3.30}$$

From this geometry, the position of the i^th cable strand can be obtained by replacing in Eqs. (3.17)-(3.28) the axis curvilinear coordinate s_ax with $s^i_\mathrm{ax} = s_\mathrm{ax} + \gamma_i$, with:

$$\gamma_i = (i-1)\frac{l_\mathrm{tr}}{N_\mathrm{st}}. \tag{3.31}$$

A further *initial curvilinear phase* γ_0 can be added to all the strands to shift the first strand initial position.

Smoothed Model

The piece-wise model is simple, however it gives discontinuities in the tangent unit vector $\mathbf{u}_\mathrm{t}$ when passing from one region to the following, as shown in Figure 3.4c. To remove the discontinuities, the model has been *smoothed* around its discontinuities with suitable circle arcs like those shown in Figure 3.5, in order to obtain a continuous tangent unit vector[1]. These circle arcs correspond to the central angles Θ^a and Θ^b, that are respectively the angle between $\mathbf{u}^a_\mathrm{t}$ and $\mathbf{u}^b_\mathrm{t}$ and between $\mathbf{u}^b_\mathrm{t}$ and $\mathbf{u}^c_\mathrm{t}$:

$$\Theta^a = \arccos\left(\mathbf{u}^a_\mathrm{t} \cdot \mathbf{u}^b_\mathrm{t}\right) = \arccos\left(\sin^2\varphi - \cos^2\varphi\sin\kappa\right), \tag{3.32}$$

$$\Theta^b = \arccos\left(\mathbf{u}^b_\mathrm{t} \cdot \mathbf{u}^c_\mathrm{t}\right) = \arccos\left(\sin^2\varphi + \cos^2\varphi\sin\kappa\right). \tag{3.33}$$

[1]The proof of the equations described in this section is available in Appendix C.

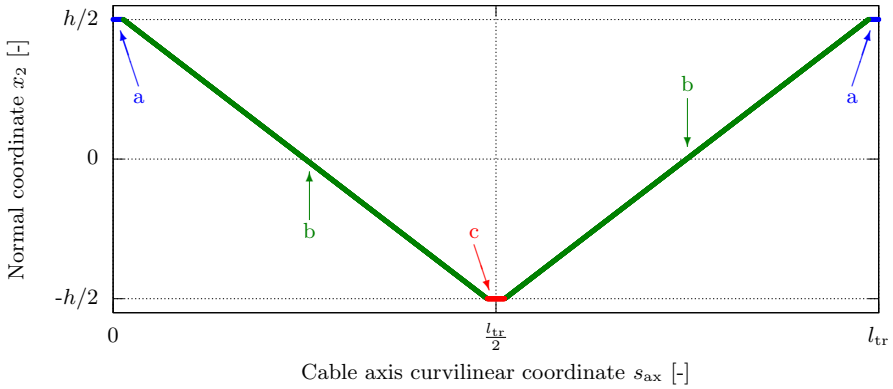

(a) Long-edge view.

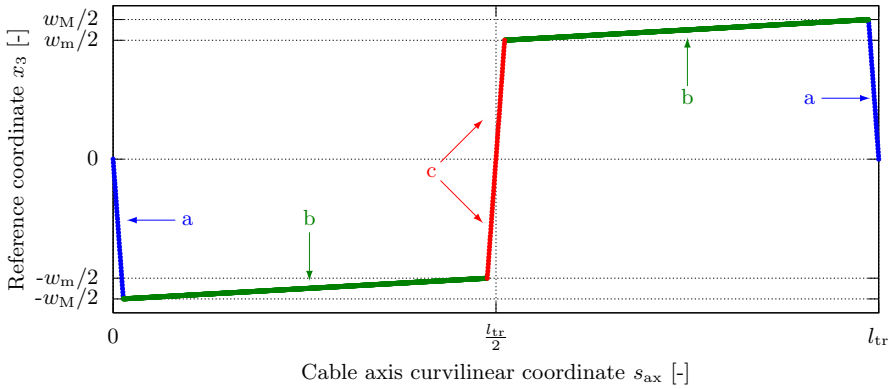

(b) Short-edge view.

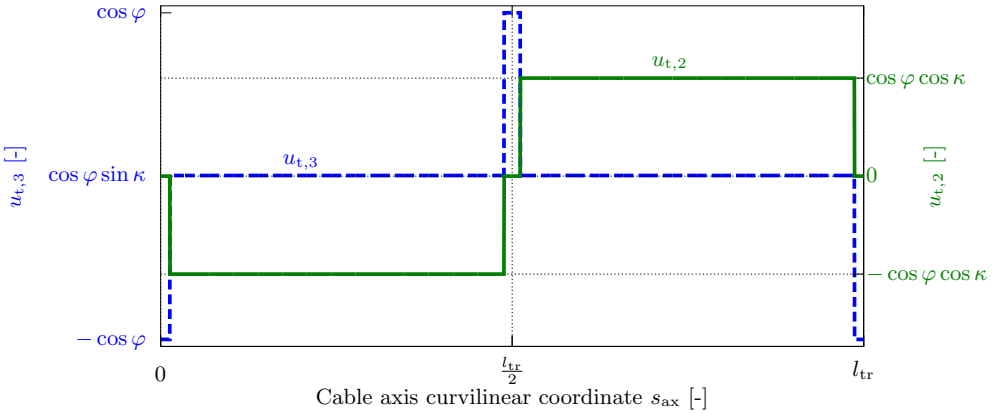

(c) Tangent unit vector components.

Figure 3.4: Piece-wise linear geometry for a 36 strand keystoned Rutherford cable.

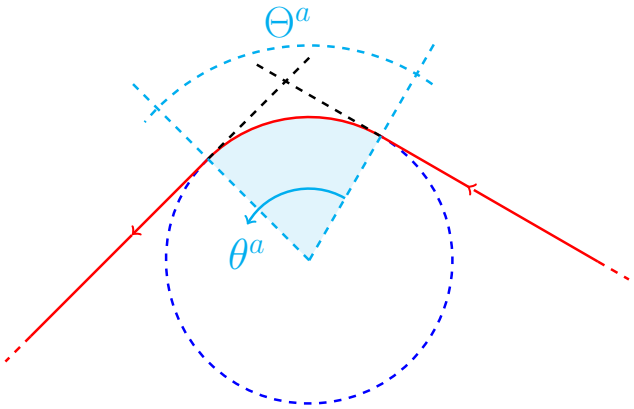

Figure 3.5: 2D view of the circle arc employed in the smoothed model for region a.

Two further regions are therefore defined astride s^a_{ax} and s^b_{ax}. The length of these transitions, named $s_{\mathrm{sm}} = \alpha_{\mathrm{sm}} w_{\mathrm{m}} \tan\varphi$ for both regions. The parameter $0 < \alpha_{\mathrm{sm}} \leq 1$ permits to adjust the smoothing intensity. If $\alpha_{\mathrm{sm}} = 0$ the piece-wise linear model is obtained, conversely if $\alpha_{\mathrm{sm}} = 1$ the region c), corresponding to the minor thickness of the Rutherford, is completely replaced by a circle arc.

It is easier to represent the strand position and its tangent unit vector as a function of the angular position θ along the circle arc, that can be computed as a function of the cable axis coordinate s_{ax} as:

$$\theta^a(s_{\mathrm{ax}}) = \arccos\left[\sin\Theta^a \sqrt{\frac{1}{2(1-\cos\Theta^a)} - (t^a)^2} + (\cos\Theta^a - 1)t^a\right], \tag{3.34}$$

where:

$$t^a = \frac{s_{\mathrm{ax}} - s^a_{\mathrm{ax}}}{s_{\mathrm{sm}}}. \tag{3.35}$$

Since $t^a \in [-1/2, 1/2]$, Eq. (3.34) is well-defined for any non-trivial value of Θ^a, i.e. $\Theta^a \neq 0$. Equations (3.34) and (3.35) are valid for the transition astride s^a_{ax}.

The equations for the two circle arcs are the following (Eq. 3.14 is still valid):

a1) When the strand is passing from the smallest short-edge cable face to the long-edge cable face, the position is described by the following equations, valid for $s_{\mathrm{ax}} \in [s^a_{\mathrm{ax}} - s_{\mathrm{sm}}/2, s^a_{\mathrm{ax}} + s_{\mathrm{sm}}/2]$, corresponding to $\theta^a \in [0, \Theta^a]$:

$$x_2^{a1}(\theta^a) = -\frac{s_{\mathrm{sm}}}{2}\frac{\cos\kappa}{\tan\varphi}\frac{1-\cos\theta^a}{1-\cos\Theta^a} + \frac{h}{2}, \tag{3.36}$$

$$x_3^{a1}(\theta^a) = \frac{s_{\mathrm{sm}}}{2}\frac{1}{\tan\varphi}\frac{\sin\kappa(1-\cos\theta^a) + 1 - \cos(\Theta^a - \theta)}{1-\cos\Theta^a} - \frac{w_{\mathrm{M}}}{2}. \tag{3.37}$$

The tangent unit vector to the strand axis $\mathbf{u}_\mathrm{t}$ is:

$$u^{a1}_{\mathrm{t},1}(\theta^a) = \sin\varphi\frac{\sin\theta^a + \sin\left(\Theta^a - \theta^a\right)}{\sin\Theta^a}, \tag{3.38}$$

$$u^{a1}_{\mathrm{t},2}(\theta^a) = -\cos\varphi\cos\kappa\frac{\sin\theta^a}{\sin\Theta^a}, \tag{3.39}$$

$$u^{a1}_{\mathrm{t},3}(\theta^a) = \cos\varphi\frac{\sin\kappa\sin\theta^a - \sin\left(\Theta^a - \theta\right)}{\sin\Theta^a} \tag{3.40}$$

b1) When the strand is passing from the long-edge cable face to the largest short-edge cable face, the position is described by the following equations, valid for $s_\mathrm{ax} \in [s^b_\mathrm{ax} - s_\mathrm{sm}/2, s^b_\mathrm{ax} + s_\mathrm{sm}/2]$, corresponding to $\theta^b \in [0, \Theta^b]$:

$$x^{b1}_2(\theta^b) = \frac{s_\mathrm{sm}}{2}\frac{\cos\kappa}{\tan\varphi}\frac{1-\cos\left(\Theta^b - \theta^b\right)}{1-\cos\Theta^b} - \frac{h}{2}, \tag{3.41}$$

$$x^{b1}_3(\theta^b) = \frac{s_\mathrm{sm}}{2}\frac{1}{\tan\varphi}\frac{\left[\cos\left(\Theta^b - \theta^b\right) - 1\right]\sin\kappa + 1 - \cos\theta^b}{1-\cos\Theta^b} - \frac{w_\mathrm{m}}{2}. \tag{3.42}$$

The tangent unit vector to the strand axis $\mathbf{u}_\mathrm{t}$ is:

$$u^{b1}_{\mathrm{t},1}(\theta^b) = \sin\varphi\frac{\sin\theta^b + \sin\left(\Theta^b - \theta^b\right)}{\sin\Theta^b}, \tag{3.43}$$

$$u^{b1}_{\mathrm{t},2}(\theta^b) = -\cos\varphi\cos\kappa\frac{\sin\left(\Theta^b - \theta^b\right)}{\sin\Theta^b}, \tag{3.44}$$

$$u^{b1}_{\mathrm{t},3}(\theta^b) = \cos\varphi\frac{\sin\kappa\sin\left(\Theta^b - \theta^b\right) + \sin\theta^b}{\sin\Theta^b} \tag{3.45}$$

In Figure 3.6 and 3.7 details of the smoothed model for three different values of α_sm are shown, in the case of the same Rutherford cable geometry reported in Figure 3.4. A 3D view of the same modeled geometry is reported in Figure 3.8a. Finally, in Figure 3.8b the 3D sketch of the model for a curved Rutherford cable segment is shown. The geometry is that of the 14 strands SMC3 non-keystoned Rutherford cable, as reported in Table 2.5.

3.2.2 Cable-In-Conduit-Conductors

In the case of CICC strands, a pseudo-analytical geometrical model is employed [19]. A reversed numbering sequence corresponding to the cabling stage is assumed for the subsequent bundle axes, which starts from 0 for the strand axis and ends to the number of stages n_st for the cable axis. The procedure starts with the generation of a set of simple helices around the cable axis. These helices correspond to the last-but-one cable bundles. A new set of *composite helices* is then generated around these curves, to obtain the axes of the last-but-two bundles. As shown in Figure 3.9, the points of $(k-1)^\mathrm{th}$ axis are found from the point of k^th axis as a function of the curvilinear coordinate along the k^th axis s_k as:

$$\mathbf{OP}_{k-1} = \mathbf{OP}_k + r_k\cos\left(\omega_k s_k + \theta_k\right)\mathbf{u}_{\mathrm{n}_k} + r_k\sin\left(\omega_k s_k + \theta_k\right)\mathbf{u}_{\mathrm{ref}_k}, \tag{3.46}$$

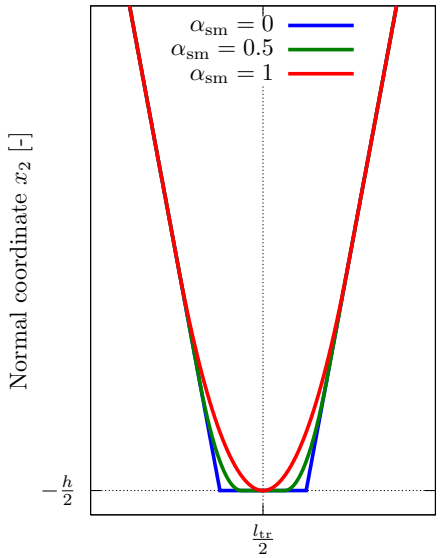

(a) Long-edge coordinate x_2.

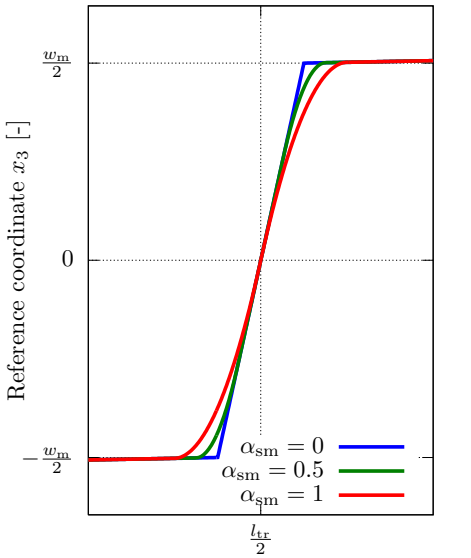

(b) Short-edge coordinate x_3.

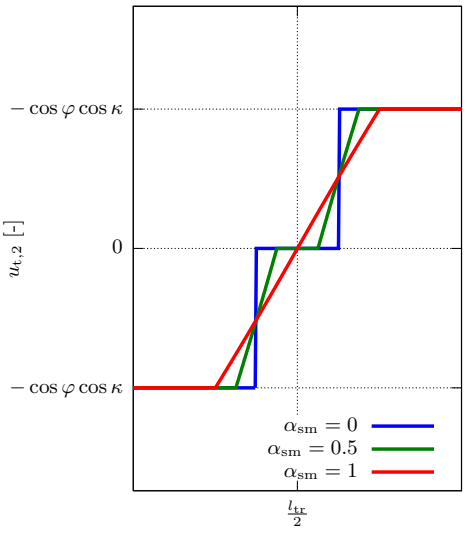

(c) Long-edge tangent unit vector $u_{\mathrm{t},2}$.

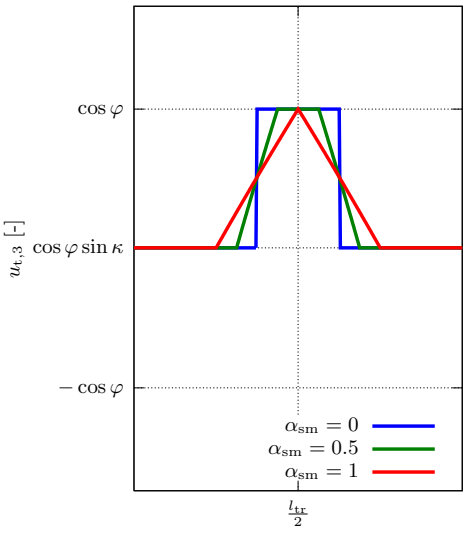

(d) Short-edge tangent unit vector $u_{\mathrm{t},3}$.

Figure 3.6: Details of the smoothed geometry for a 36 strand keystoned Rutherford cable.

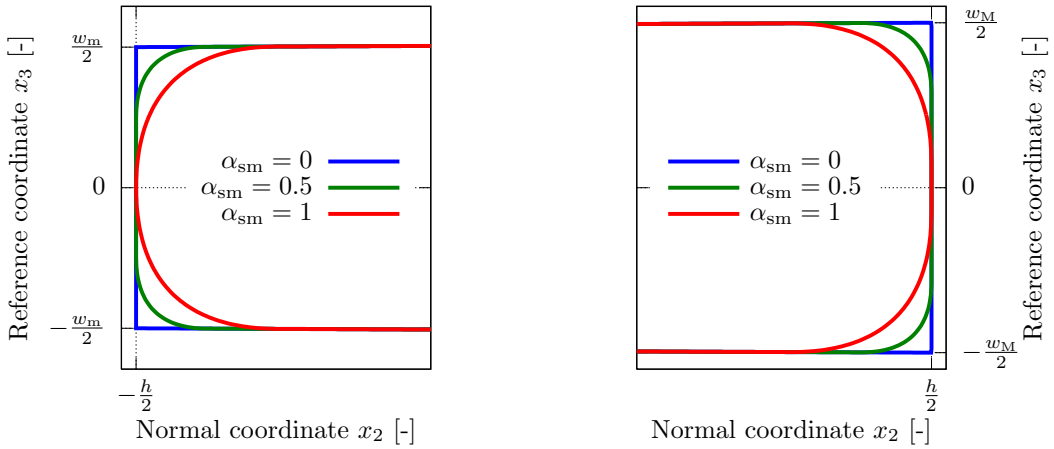

Figure 3.7: Details of a Rutherford cable cross-section with the smoothed model. Left: minor thickness. Right: major thickness.

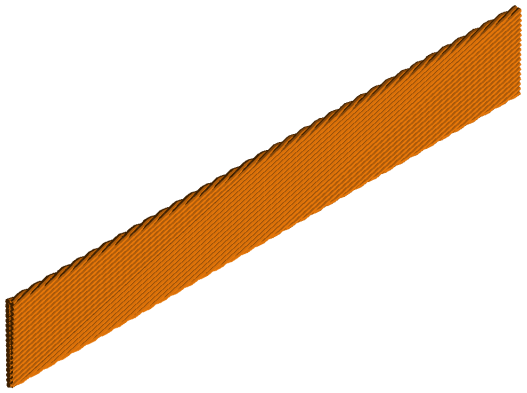

(a) Rectilinear segment of a 36 strands keystoned Rutherford cable.

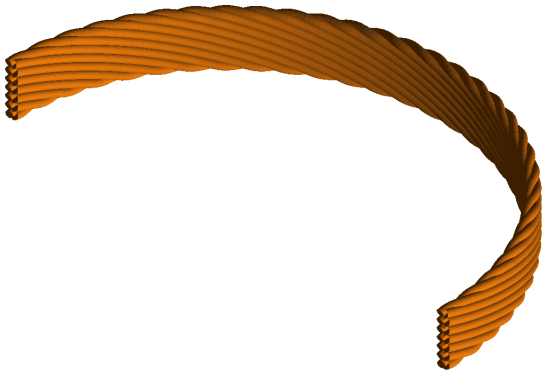

(b) Curved segment of a 14 strands non-keystoned Rutherford cable.

Figure 3.8: 3D views of modeled Rutherford cable segments.

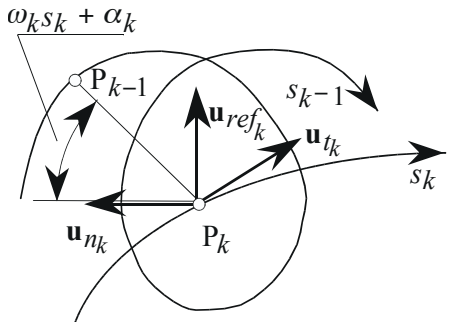

Figure 3.9: CICC geometry: generation of the $(k-1)^{\text{th}}$ axis from the k^{th} axis.

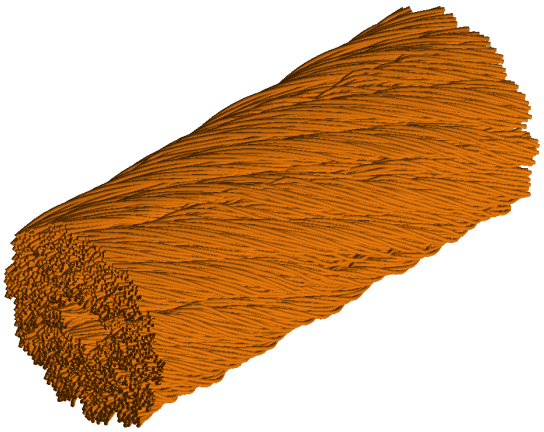

Figure 3.10: 3D view of a rectilinear segment of a ITER TF CICC.

with $k = 1, \ldots, n_{\text{st}}$. $\mathbf{OP}_{k-1}$ and $\mathbf{OP}_k$ are respectively the position vectors of the generic points of $(k-1)^{\text{th}}$ and the k^{th} axes, r_k is the k^{th} *twisting radius*, θ_k is the *initial angular phase* and:

$$\omega_k = \frac{2\pi}{p_k}, \tag{3.47}$$

where p_k is the k^{th} *twisting pitch*. The twisting radius and the twisting pitch can be computed from the cable geometrical parameters, whereas θ_k should be determined from the actual cable geometry, even though its value is generally unknown. Thus, θ_k is generally considered as a random variable during the analyses, in order to assess the typical cable parameters and characteristics, that should be almost independent on the actual initial angular phase. A pseudo-random array of initial angular phases $\boldsymbol{\Theta}$, called *phase set*, is generally employed to define the angular phases of all the cable bundles.

The iterative application of Eq. (3.46) requires the curvilinear coordinate to be computed for each axis point at each stage, but in general this cannot be done in an analytical way due to the non uniform curvature of the axis of a composite helix.

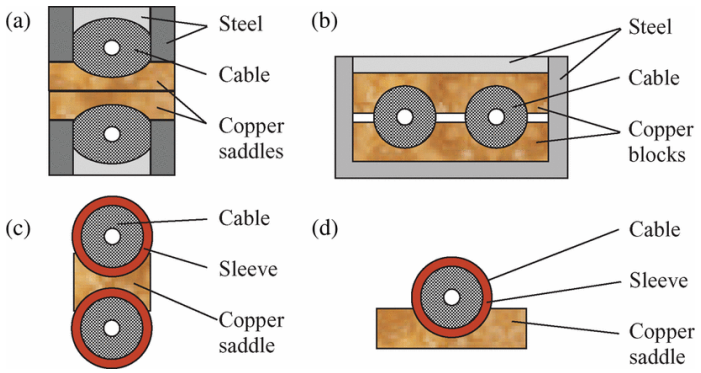

Figure 3.11: Examples of joint and termination cross-sections. (a) twin box joint; (b) segmented copper joint; (c) and (d) cylindrical sleeved joint and termination.

Thus, a spline-based description is adopted, in which first a set of $\mathbf{P}_{k-1}$ points is generated, whose coordinates are expressed as a function of the curvilinear coordinate s_k by means of Eq. (3.46), then a numerical computation of the curvilinear coordinate s_{k-1} is performed and the coordinates of points $\mathbf{P}_{k-1}$ are expressed as a function of s_{k-1}.

In Figure 3.10, a 3D view of the model for a short rectilinear segment of ITER TF CICC is reported. In this case, as in other full-size CICCs, a final compaction is applied to the conductor, so that the petals have a wedge-shaped cross-section. In the model, this is obtained through a suitable geometrical transformation of the bundle cross-section, so that the strand axes of each petal lay inside a circle sector.

3.2.3 CICC Joints and Terminations

Different types of CICC joints and terminations are foreseen in THELMA [17], as reported in Figure 3.11. In any case, a suitably shaped copper block, the *saddle*, is used to perform the electrical connection. In the magnet inlet and outlet terminations, the saddle is in direct contact with the feeding busbars. In a joint instead, a single good electrical contact between the two cables must be guaranteed, and it can be achieved in different ways. In a twin box joint, as in Figure 3.11a, two terminations are soldered together. In a segmented copper joint, as in Figure 3.11b, the cables are enclosed into a stack of two copper blocks. In the case of the cylindrical sleeved joint, as in Figure 3.11c, the electric connection is performed by a copper sleeve covering each cable and by a unique saddle.

In the Udine model for joints and terminations, the only objects considered are the cables and the saddle, since other components are made of materials with much higher resistivity like stainless steel. The saddle is represented by a 3D prismatic object, with one (in the case of a termination) or two curved saddle-shaped surfaces (in the case of the intermediate joint), which are in contact with the cable or the cables, as shown in Figure 3.12 for the termination.

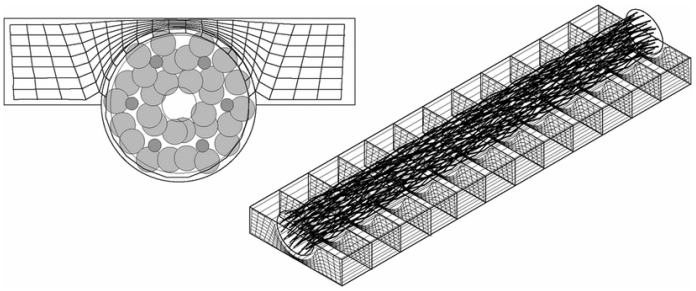

Figure 3.12: Example of a THELMA model for a termination [17]. Left: cross-section, showing the cable elements and the saddle mesh. Right: simplified 3D view.

3.3 THELMA Electromagnetic Model

In the analyses presented in this document, both Udine and Bologna EM modules have been used, depending on the type of analysis required. The Udine EM module has been used for all the steady-state linear analyses, being more detailed than Bologna EM module in terms of terminations and joints description and it is more suitable for the modeling of experiments like the inter-strand resistances measurements (see chapter 4). Instead, the Bologna EM module has been used for simulations in which the superconductor approaches the critical surface, and therefore the linear approximation foreseen by Udine EM module is longer valid. In the following the relevant aspects of both models are described.

The numerical efficiency of both modules has been enhanced during the PhD activity, allowing much detailed analyses than before. In steady-state, ITER CICC samples have been studied down to the individual strand, as reported in Section 4.5.2 and 4.5.3. In transient regime, detailed sensitivity analyses have been performed on a CICC cable discretized into more than 70 cable elements, corresponding to three complete cabling stages, as reported in Chapter 7.

3.3.1 Udine EM Module

Network Generation

When the cable geometry is defined in terms of strands or equivalent cable elements, the generation of the equivalent network is divided into these main phases [19]:

1. cable element equivalent network component creation;
2. cable element nodes and branches creation;
3. inter-strand resistances computation and network equivalent component creation;
4. inter-strand nodes and branches creation.

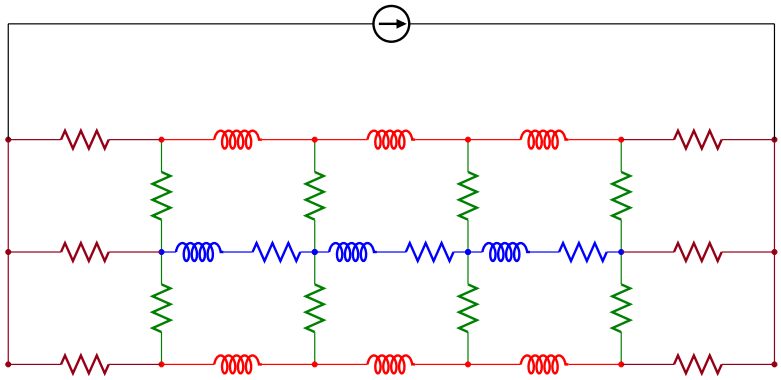

Figure 3.13: Simplified view of an equivalent electrical network. Two superconducting cable elements (in red), one resistive cable element (in blue), two joints (in magenta) and some of the inter-strand resistances (in green) are visible.

Each cable, with its cross-section modeled as a set of N_{ce} cable elements or strands, is divided into a suitable number N_{em} of equal segments along its axis, selected according to the space resolution level desired. The current density is assumed uniform in each of these segments. In the network, the superconducting cable elements are represented by purely inductive components, magnetically coupled to each other and with any external magnetic field source (which may be, for instance, a close coil). In the resistive cable elements, i.e. copper strands or cores, a suitable longitudinal resistance is added. In this way, a linear inductive network N-dipole is generated, whose self and mutual inductance coefficients are computed with an integral method starting from the cable element geometry. As regards the inter-strand resistances, their computation and the related parameters are extensively described in Section 4.4.

In the case of a joint, the same discretization along the cable longitudinal direction is used for both the saddle and the cable strands [18]. In the saddle, the current density is non uniform not only along the cable direction, but also in the cross-section, since the contacts between the strands and with the saddle are not evenly distributed. For this reason, the saddle sections are all discretized in the same way by means of a 2D structured grid, as shown in Figure 3.12. Starting from the mesh geometry, the joint discretization and the saddle material, a suitable set of transverse conductances is generated. To take into account also of the saddle longitudinal currents, the corresponding nodes of adjacent saddle sections are connected by longitudinal resistances. As a boundary condition, the terminations saddle surfaces in contact with the external feeding busbars are supposed to be equipotential.

A simplified view of the equivalent network is reported in Figure 3.13. One advantage of the Udine EM module is the possibility to insert additional components to the network, so that auxiliary objects, like power supplies, external resistors and so on can be installed.

Network Solution

The *modified node analysis method* has been adopted to solve the network in the time domain [46]. The unknowns are all the node potentials, but one, and all the currents in the current-driven components, in this case the inductive N-dipoles, any additional resistor and ideal e.m.f. generators. The following system can be written, applying the Kirchhoff's laws and the component voltage-current characteristics:

$$\begin{pmatrix} \mathbf{A}_\mathrm{r}^\mathrm{T} & \mathbf{R} \\ \mathbf{G} & \mathbf{A}_\mathrm{r} \end{pmatrix} \cdot \begin{pmatrix} \mathbf{V} \\ \mathbf{I} \end{pmatrix} + \begin{pmatrix} \mathbf{0} & \mathbf{M} \\ \mathbf{C} & \mathbf{0} \end{pmatrix} \cdot \frac{\mathrm{d}}{\mathrm{d}t} \begin{pmatrix} \mathbf{V} \\ \mathbf{I} \end{pmatrix} = \begin{pmatrix} \mathbf{E} \\ \mathbf{J} \end{pmatrix}, \tag{3.48}$$

where $\mathbf{E}$ and $\mathbf{J}$ are the arrays of the known impressed e.m.f.s and currents, $\mathbf{V}$ and $\mathbf{I}$ are the arrays of unknown potentials and currents, $\mathbf{A}_\mathrm{r}$ is the incidence matrix for the current-driven components, $\mathbf{R}$ and $\mathbf{G}$ are respectively the matrices of the self and mutual resistances and conductances and $\mathbf{M}$ is the matrix of the self and mutual inductances. $\mathbf{C}$ is the matrix of the capacitances, not used in these electromagnetic analyses.

Equation (3.48) is an algebraic-differential system, and the system unknowns can be state variables or simple unknown quantities. The system equations and unknowns are therefore sorted so that, in the system, the algebraic equations and the simple unknowns are considered first. The final form of the system is the following:

$$\underbrace{\begin{pmatrix} \mathbf{D}_{\mathrm{S}_{\mathrm{aa}}} & \mathbf{D}_{\mathrm{S}_{\mathrm{ad}}} \\ \mathbf{D}_{\mathrm{S}_{\mathrm{da}}} & \mathbf{D}_{\mathrm{S}_{\mathrm{dd}}} \end{pmatrix}}_{\mathbf{D}_\mathrm{S}} \cdot \underbrace{\begin{pmatrix} \mathbf{X}_{\mathrm{S}_\mathrm{a}} \\ \mathbf{X}_{\mathrm{S}_\mathrm{d}} \end{pmatrix}}_{\mathbf{X}_\mathrm{S}} + \underbrace{\begin{pmatrix} \mathbf{0} & \mathbf{0} \\ \mathbf{0} & \mathbf{F}_{\mathrm{S}_{\mathrm{dd}}} \end{pmatrix}}_{\mathbf{F}_\mathrm{S}} \cdot \frac{\mathrm{d}}{\mathrm{d}t} \begin{pmatrix} \mathbf{X}_{\mathrm{S}_\mathrm{a}} \\ \mathbf{X}_{\mathrm{S}_\mathrm{d}} \end{pmatrix} = \underbrace{\begin{pmatrix} \mathbf{Y}_{\mathrm{S}_\mathrm{a}} \\ \mathbf{Y}_{\mathrm{S}_\mathrm{d}} \end{pmatrix}}_{\mathbf{Y}_\mathrm{S}}. \tag{3.49}$$

In these matrices, $\mathbf{X}_\mathrm{S}$ is the array of the sorted unknowns, $\mathbf{Y}_\mathrm{S}$ is the array of the sorted known terms, $\mathbf{F}_\mathrm{S}$ and $\mathbf{D}_\mathrm{S}$ are the sorted matrices. In all these arrays and matrices, the first sub-subscript is "a" for the algebraic equations and "d" for the differential ones. The second sub-subscript is "d" for the unknown state variables, and "a" for the other case. If $\mathbf{X}_{\mathrm{S}_\mathrm{a}}$ is obtained from the algebraic equations and replaced in the differential ones, the result is:

$$\frac{\mathrm{d}\mathbf{X}_{\mathrm{S}_\mathrm{d}}}{\mathrm{d}t} = \mathbf{F}_{\mathrm{S}_{\mathrm{dd}}}^{-1} \left[\mathbf{Y}_{\mathrm{S}_\mathrm{d}} - \mathbf{D}_{\mathrm{S}_{\mathrm{da}}} \mathbf{D}_{\mathrm{S}_{\mathrm{aa}}}^{-1} \mathbf{Y}_{\mathrm{S}_\mathrm{a}} + (\mathbf{D}_{\mathrm{S}_{\mathrm{da}}} \mathbf{D}_{\mathrm{S}_{\mathrm{aa}}}^{-1} \mathbf{D}_{\mathrm{S}_{\mathrm{ad}}} - \mathbf{D}_{\mathrm{S}_{\mathrm{dd}}}) \mathbf{X}_{\mathrm{S}_\mathrm{d}} \right]. \tag{3.50}$$

Since all the equations are linear, the system matrices are constant with time. To enhance the solution efficiency, $\mathbf{D}_{\mathrm{s}_{\mathrm{aa}}}$ and $\mathbf{F}_{\mathrm{s}_{\mathrm{dd}}}$ can be inverted once, before the simulation, by means of LU matrix factorization. The system of ordinary differential equations is then numerically solved with a suitable Runge-Kutta method[2].

3.3.2 Bologna EM Module

The Bologna EM module [34] is a complete 3D non-linear electromagnetic model for the computation of the current distribution among the N_ce cable elements (CEs)

[2] See Appendix D, page 231, for a description of some common Runge-Kutta methods.

and of the currents and voltages on the jacket of CICCs. To describe the external conduit, the jacket cross-section is split into N_{je} jacket elements (JEs), similar to the CEs used to describe the cable. The geometry of the JEs is derived extruding the conduit initial cross-section along the cable axis, thus obtaining JEs parallel to the cable axis. The module can of course be used also in the case of Rutherford cables, omitting the resistive jacket modeling and providing the suitable geometry, as described in Section 3.2.1.

The complete derivation of the equations of this model is available in [34]. The magneto-quasi-static regime without magnetizable bodies is considered, therefore the electric field $\mathbf{E}$ can be derived from the scalar potential V and the magnetic vector potential $\mathbf{A}$, by means of the following equation:

$$\mathbf{E} = -\nabla V - \frac{\partial \mathbf{A}}{\partial t}. \tag{3.51}$$

The equation for the charge conservation:

$$\nabla \cdot \mathbf{J} = 0, \tag{3.52}$$

together with suitable constitutive relations should be added to correctly define the problem, whose unknowns are the currents and the voltages, both assumed uniformly distributed in the cross section of a given CE or JE.

Let $I_{\mathrm{c}}^k(s,t)$ be the current flowing in the k^{th} CE. In the present approach, the *difference currents* i_{c}^k are evaluated, given by the deviation of the current in a given cable element from an uniform current distribution among all strands:

$$i_{\mathrm{c}}^k(s,t) = I_{\mathrm{c}}^k(s,t) - \frac{N_k}{N_{\mathrm{st}}} I(t) \tag{3.53}$$

where N_k is the number of strands represented by the k^{th} CE, N_{st} is the total number of strands in the cable, $I(t)$ is the total transport current as a function of t, and s is the curvilinear coordinate along the cable axis. A first set of equations is derived along the axis of each CE and JE from Eq. (3.51):

$$\begin{aligned}\frac{\partial V_{\mathrm{c}}^k}{\partial s}(s,t) = & -\mathbf{E}_{\mathrm{c}}^k \cdot \frac{\mathrm{d}\mathbf{y}_{\mathrm{c}}^k}{\mathrm{d}s} - m_{\mathrm{uc}}^k(s)\frac{\mathrm{d}I}{\mathrm{d}t}(t) - \sum_{\beta=1}^{N_{\mathrm{ext}}} m_{\mathrm{ec}}^{k\beta}(s)\frac{\mathrm{d}I_{\mathrm{e}}^\beta}{\mathrm{d}t}(t) \\ & - \sum_{\alpha=1}^{N_{\mathrm{ce}}} \int_0^L m_{\mathrm{cc}}^{k\alpha}(s,s')\frac{\partial i_{\mathrm{c}}^\alpha}{\partial t}(s',t)\,ds', \qquad k = 1,\ldots,N_{\mathrm{ce}}, \end{aligned} \tag{3.54}$$

$$\begin{aligned}\frac{\partial V_{\mathrm{j}}^h}{\partial s}(s,t) = & -\mathbf{E}_{\mathrm{j}}^h \cdot \frac{\mathrm{d}\mathbf{y}_{\mathrm{j}}^h}{\mathrm{d}s} - m_{\mathrm{uj}}^h(s)\frac{\mathrm{d}I}{\mathrm{d}t}(t) - \sum_{\beta=1}^{N_{\mathrm{ext}}} m_{\mathrm{ej}}^{h\beta}(s)\frac{\mathrm{d}I_{\mathrm{e}}^\beta}{\mathrm{d}t}(t), \\ & h = 1,\ldots,N_{\mathrm{je}}, \end{aligned} \tag{3.55}$$

where voltages V_{c} and V_{j} indicate the potential on the axis of a CE or JE with respect to a nil reference point taken at infinite distance from the cable. Here only

the physical meaning of the model equations is described, refer to [34] for the exact definition of the parameters m_{uc}, m_{cc}, m_{uj}, m_{ec} and m_{ej}.

The longitudinal variation of the voltage along the axis line of a CE or JE, appearing in the first member of Eqs. (3.54) and (3.55), derives from several components of the voltage drop. The first term in the second member represents the electric field component along to the CE/JE axis, $\mathbf{E}_{\mathrm{c}}^{k}$ the electric field acting on the k^{th} CE, and $\mathbf{y}_{\mathrm{c}}^{k}$ the position vector of the axis of the same CE. $\mathbf{E}_{\mathrm{j}}^{h}$ and $\mathbf{y}_{\mathrm{j}}^{h}$ are the same quantities in the h^{th} JE. The electric field is correlated to the current density in each element through appropriate constitutive relations, depending on the local temperature, magnetic induction and applied strain. In the CEs, the constitutive relation derives from the numerical solution of the electrical parallel between the normal conductor of the matrix and the superconductor, described by the power law[3]. The constitutive electrical relationship for the JEs is simply $\mathbf{E} = \rho_{\mathrm{E}}\mathbf{J}$.

The second term in second member of Eqs. (3.54) and (3.55) represents the voltages induced by time variations of the self field generated by the transport current $I(t)$ flowing along the whole cable. In evaluating these voltages, the current distribution is assumed uniform among the strands. The third term of the second member represents the mutual inductive coupling of each CE or JE with the N_{ext} external coils possibly present in a given magnetic configuration, characterized by the currents I_{e}^{β}, for $\beta = 1, \ldots, N_{\mathrm{ext}}$. Finally, the last term of Eq. (3.54) represents the mutual inductive coupling between the different cable elements. The corresponding term in Eq. (3.55) is neglected since the resistivity of the jacket is large enough to make the electrical time constants in the jacket negligible with respect to the electrical time constants in the cable.

A second set of equations, deriving from Eq. (3.52), is needed to solve the problem. At a given position along the cable, the CE current changes due to the distributed contacts with the other CEs and the JEs. Considering the formulation Eq. (3.51) for the electric field, the following equations can be derived:

$$\begin{aligned}\frac{\partial i_{\mathrm{c}}^{k}}{\partial s}(s,t) = &-\sum_{i=1}^{N_{\mathrm{ce}}} \sigma_{\mathrm{cc}}^{ki}(s)\left[V_{\mathrm{c}}^{k}(s,t) - V_{\mathrm{c}}^{i}(s,t) - h_{\mathrm{ucc}}^{ki}(s)\frac{\mathrm{d}I}{\mathrm{d}t}(t) - \sum_{\lambda=1}^{N_{\mathrm{ext}}} h_{\mathrm{ecc}}^{\lambda ki}(s)\frac{\mathrm{d}I_{\mathrm{e}}^{\lambda}}{\mathrm{d}t}(t)\right] \\ &-\sum_{i=1}^{N_{\mathrm{je}}} \sigma_{\mathrm{cj}}^{ki}(s)\left[V_{\mathrm{c}}^{k}(s,t) - V_{\mathrm{j}}^{i}(s,t) - h_{\mathrm{ucj}}^{ki}(s)\frac{\mathrm{d}I}{\mathrm{d}t}(t) - \sum_{\lambda=1}^{N_{\mathrm{ext}}} h_{\mathrm{ecj}}^{\lambda ki}(s)\frac{\mathrm{d}I_{\mathrm{e}}^{\lambda}}{\mathrm{d}t}(t)\right], \\ &\qquad k = 1, \ldots, N_{\mathrm{ce}}, \qquad (3.56)\end{aligned}$$

[3] See Eq. (1.21), page 17. Details on the numerical solution can be found in Section 6.4.2, page 138.

$$\frac{\partial i_{\mathrm{j}}^{h}}{\partial s}(s,t) = -\sum_{i=1}^{N_{\mathrm{ce}}} \sigma_{\mathrm{cj}}^{ih}(s) \left[V_{\mathrm{j}}^{h}(s,t) - V_{\mathrm{c}}^{i}(s,t) + h_{\mathrm{ucj}}^{ih}(s) \frac{\mathrm{d}I}{\mathrm{d}t}(t) + \sum_{\lambda=1}^{N_{\mathrm{ext}}} h_{\mathrm{ecj}}^{\lambda ih}(s) \frac{\mathrm{d}I_{\mathrm{e}}^{\lambda}}{\mathrm{d}t}(t) \right] - \sum_{i=1}^{N_{\mathrm{je}}} \sigma_{\mathrm{jj}}^{hi}(s) \left[V_{\mathrm{j}}^{h}(s,t) - V_{\mathrm{j}}^{i}(s,t) - h_{\mathrm{ujj}}^{hi}(s) \frac{\mathrm{d}I}{\mathrm{d}t}(t) - \sum_{\lambda=1}^{N_{\mathrm{ext}}} h_{\mathrm{ejj}}^{\lambda hi}(s) \frac{\mathrm{d}I_{\mathrm{e}}^{\lambda}}{\mathrm{d}t}(t) \right], \quad h = 1, \ldots, N_{\mathrm{je}}. \tag{3.57}$$

Also in this case, only a general description of the physical meaning is reported, whereas the detailed definition of the parameters σ_{cc}, σ_{cj}, σ_{jj}, h_{ucc}, h_{ucj}, h_{ucj}, h_{ecc}, h_{ecj} and h_{ejj} can be found in [34].

The first sum at the second member of both equations represents the current exchanges between a given CE or JE, respectively, with all the other CEs, whereas the second sum accounts respectively for the current exchanges between a given CE or JE element with all the other JEs. The term between square brackets is the integral of the electric field along a geometric line connecting the centers of two different CEs or JEs. The difference between the potentials V_c and V_j corresponds to the integration of $-\nabla V$ in Eq. (3.51). The remaining part of the integral corresponds to the integration of the time derivative of $\mathbf{A}$ and accounts for the voltages induced by variations of the self magnetic field generated by the cable and of the magnetic fields generated by external coils.

The straightforward solution the complete system made of Eqs. (3.54)-(3.57) would require a remarkable computational effort, since the number of unknowns and equations is $2(N_{\mathrm{ce}} + N_{\mathrm{je}})$. However, with suitable algebraic arrangements, the number of equations and unknown functions can be reduced to $N_{\mathrm{ce}} + N_{\mathrm{je}} - 1$, corresponding to the difference currents in all the JEs and in all CEs but the last. The result is an algebraic-differential system of equations, that can be suitably discretized in space by means of finite-elements. The solution of the algebraic part can be obtained by means of LU factorization, whereas common Runge-Kutta methods are employed for the differential part. In particular, the explicit Cash-Karp 5^{th} order method or the implicit TRX2 2^{nd} order method are used[4].

3.4 THELMA Thermal Model

A significant part of this PhD activity has been devoted to the development of a brand-new general purpose thermal model to be coupled with the existing electromagnetic modules. An equivalent lumped network model has been adopted in order to exploit large part of the existing routines of the Udine EM module. On the other hand, the node analysis used for the network solution is particularly effective for the thermal equivalent network, as it is described in the following. Differently from the Udine EM module, the thermal module must account for the non-linear thermal properties which are typical at cryogenic temperature. In the following, first the ca-

[4] See respectively Appendices D.1.4 and D.2.2.

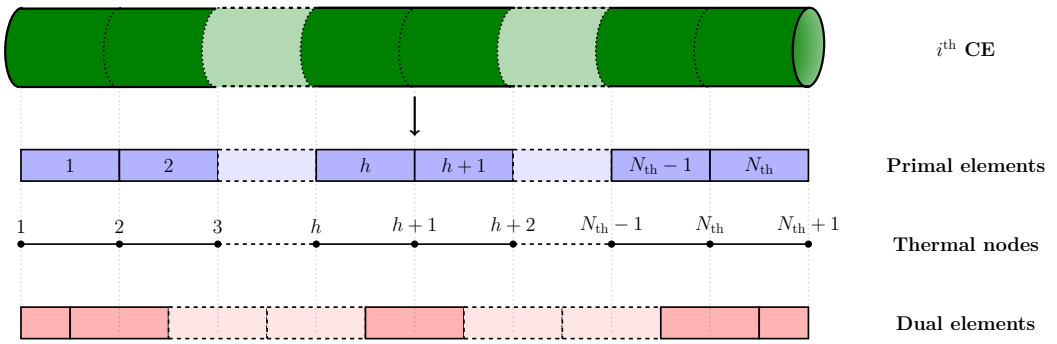

Figure 3.14: Sketch of the primal elements, thermal nodes and dual elements in a cable element.

ble equivalent network is described, then the model for the helium thermal network is summarized.

3.4.1 Cable Element Equivalent Network

Let a cable element (CE) be divided along the longitudinal cable axis coordinate s_{ax} into N_{th} *primal elements* [167], interleaved by $N_{\text{th}}+1$ *thermal nodes*. A *dual element* can be defined astride each thermal node, as shown in Figure 3.14. The following heat balance can be written at time t for each dual element h of the i^{th} CE, as sketched in Figure 3.15:

$$(\Delta U)_h^i = P_{h-1,h}^{\text{long},i} - P_{h,h+1}^{\text{long},i} + P_h^{\text{gen},i} - P_h^{i,\text{He}} + \sum_{\substack{j=1 \\ j\neq i}}^{N_{\text{ce}}} P_h^{ji}, \qquad h = 1,\dots,N_{\text{th}}+1, \quad (3.58)$$

where:

- $(\Delta U)_h^i$ is the *internal energy variation* of the h^{th} dual element of the i^{th} CE;
- $P_{h-1,h}^{\text{long},i}$ is the *longitudinal heat flow* from the $(h-1)^{\text{th}}$ to the h^{th} longitudinal dual element of the i^{th} CE. It is associated to each boundary between each dual element and the neighboring, therefore it corresponds to each primal element;
- $P_h^{\text{gen},i}$ is the *heat generated* inside the h^{th} longitudinal dual element of the i^{th} CE;
- $P_h^{i,\text{He}}$ is the *heat exchanged* between the h^{th} dual element of the i^{th} CE and the *helium*;
- P_h^{ji} is the *heat exchanged* between the h^{th} longitudinal dual elements of the j^{th} and of the i^{th} CE.

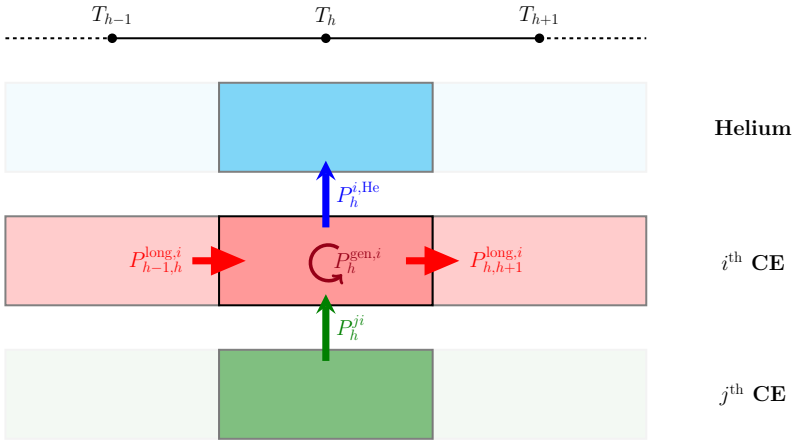

Figure 3.15: Sketch of the terms of the heat balance Eq. (3.58) for the h^{th} dual element of the i^{th} CE. For clarity purposes, only two CEs are represented.

If the length of each longitudinal element is sufficiently small, the temperature variation inside each dual element is small, therefore a uniform temperature T_h^i can be assigned to each dual element. In these conditions, the following expressions for the quantities present in Eq. (3.58) can be written:

- for the internal energy variation:

$$(\Delta U)_h^i = (\rho c_{\mathrm{p}})_h^i v_h^i \frac{\mathrm{d}T_h^i}{\mathrm{d}t} = C_h^i \frac{\mathrm{d}T_h^i}{\mathrm{d}t}, \tag{3.59}$$

  where v_h^i is the volume of the h^{th} longitudinal dual element of the i^{th} CE and $(\rho c_{\mathrm{p}})_h^i$ is its volumetric heat capacity. C_h^i is a suitable heat capacitance [J/K] representing the internal energy.

- For the longitudinal heat flow:

$$P_{h-1,h}^{\mathrm{long},i} = k_{h-1,h}^i \frac{A_{\mathrm{ce}}^i}{l_{h-1,h}^i}(T_{h-1}^i - T_h^i) = G_{h-1,h}^{\mathrm{long},i}(T_{h-1}^i - T_h^i), \tag{3.60}$$

  where $l_{h-1,h}^i$ is the distance along the CE axis between the neighboring thermal nodes $h-1$ and h, A_{ce}^i is the CE cross-section area, assumed constant along the cable length and $k_{h-1,h}^i$ is the thermal conductivity, defined for each primal element. $G_{h-1,h}^{\mathrm{long},i}$ is the equivalent thermal conductance [W/K] representing the longitudinal heat flow.

- The heat generated $P_h^{\mathrm{gen},i}$ is given by the total losses computed by the electromagnetic module, as explained in Section 3.5.

- For the heat exchanged with the helium:

$$P_h^{i,\mathrm{He}} = h_{\mathrm{c},h}^i A_h^{\mathrm{wet},i}(T_h^i - T_h^{\mathrm{He}}) = G_h^{i,\mathrm{He}}(T_h^i - T_h^{\mathrm{He}}), \tag{3.61}$$

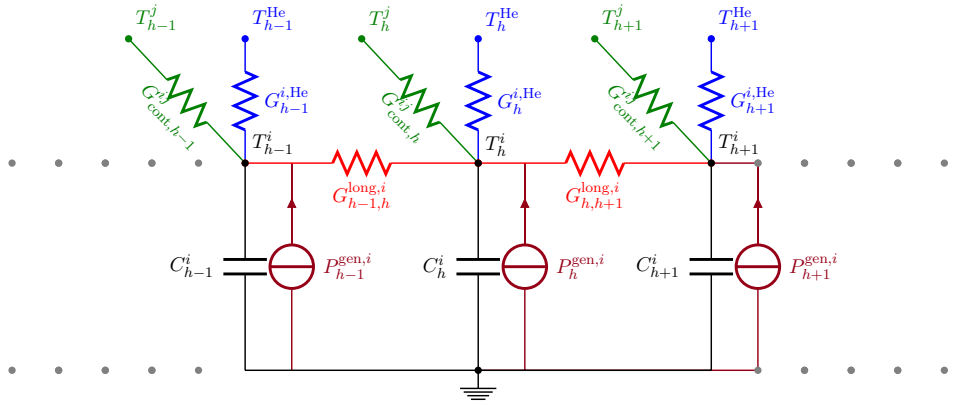

Figure 3.16: Equivalent thermal lumped network for the i^{th} CE. For clarity purposes, only the network components toward one further CE are represented.

where $h^i_{\mathrm{c},h}$ is the convective heat transfer coefficient and T^{He}_h is the temperature of the helium for the h^{th} longitudinal dual element. The wetted area $A^{\mathrm{wet},i}_h$ of the h^{th} longitudinal dual element of the i^{th} CE can be expressed by:

$$A^{\mathrm{wet},i}_h = l^i_h p^{\mathrm{wet},i}_h, \tag{3.62}$$

where l^i_h is the dual element length and $p^{\mathrm{wet},i}_h$ its wetted perimeter. $G^{i,\mathrm{He}}_h$ is the equivalent thermal conductance [W/K] representing the heat exchange with helium. In some cases, like the quench propagation in impregnated Rutherford cables (see chapter 6) an adiabatic assumption can be considered for the conductor, therefore this term can be neglected.

- For the heat exchanged among j^{th} and i^{th} CE, a suitable contact thermal conductance $G^{ji}_{\mathrm{cont},h}$ can be used:

$$P^{ji}_h = G^{ji}_{\mathrm{cont},h}(T^j_h - T^i_h). \tag{3.63}$$

The evaluation of these thermal contact conductances is explained, together with their electrical counterpart, in Section 4.4.

It must be noted that the network components described above can be written as the product between a *geometrical factor*, dependent only on the cable element geometry and discretization, and a *material property*. For example, in the case of the heat capacitance, the dual element volume is the geometrical factor and the volumetric heat capacity is the material property.

The heat balance (3.58) corresponds to an equivalent lumped network featuring thermal conductances, capacitors and heat flow generators, as shown in Figure 3.16. Since the material properties $(\rho c_{\mathrm{p}})^i_h$, $k^i_{h-1,h}$ and $G^{ji}_{\mathrm{cont},h}$ are far from being constant in the temperature range of interest[5], the equivalent network components are nonlinear. In particular, the following assumptions have been considered:

[5]See Appendix A, page 181.

- $(\rho c_\mathrm{p})_h^i$ are evaluated at the dual element temperature T_h^i;
- $k_{h-1,h}^i$ are evaluated at the primal element temperature, approximated as the mean temperature between neighboring dual elements:

$$T_{h-1,h}^i = \frac{T_{h-1}^i + T_h^i}{2}; \tag{3.64}$$

- the contact thermal conductances $G_{\mathrm{cont},h}^{ji}$ are evaluated at the mean temperature among the CEs in contact:

$$T_h^{ji} = \frac{T_h^j + T_h^i}{2}. \tag{3.65}$$

Moreover, the CEs are generally a composite material, a mixture of superconductor and copper. Their material properties are therefore computed as the weighted average of copper and superconductor properties according to the Cu/nCu cross-section areas ratio λ^i:

$$\lambda^i = \frac{A_{\mathrm{ce,Cu}}^i}{A_{\mathrm{ce,nCu}}^i}, \qquad A_{\mathrm{ce,Cu}}^i + A_{\mathrm{ce,nCu}}^i = A_{\mathrm{ce}}^i. \tag{3.66}$$

In particular:

$$(\rho c_\mathrm{p})^i = \frac{\lambda^i (\rho c_\mathrm{p})_\mathrm{Cu} + (\rho c_\mathrm{p})_\mathrm{SC}}{1+\lambda^i}, \tag{3.67}$$

$$k^i = \frac{\lambda^i k_\mathrm{Cu} + k_\mathrm{SC}}{1+\lambda^i} \approxeq \frac{\lambda^i}{1+\lambda^i} k_\mathrm{Cu} \tag{3.68}$$

The last approximation is valid since the thermal conductivity in superconducting materials is many orders of magnitude lower than in copper[5].

3.4.2 Helium Equivalent Network

A general model for the helium should consider the details of the fluid dynamics and of the different states on the phase diagram. However, the purpose of the present work is limited to a description of the helium temperature impact on the superconductor, neglecting phenomena such as pressure variations or changes of state that should be better studied with dedicated models like [30] [140]. The following assumptions are therefore considered:

- the helium channel along the cable axis is modeled as an additional *thermal CE*, subdivided into N_th primal elements by $N_\mathrm{th}+1$ thermal nodes at which the temperatures T_h^He are assigned, as done for the CEs. In principle, the extension of this model to multiple parallel helium channels, e.g. an helium channel for each petal in a CICC, poses no theoretical problems. However, in

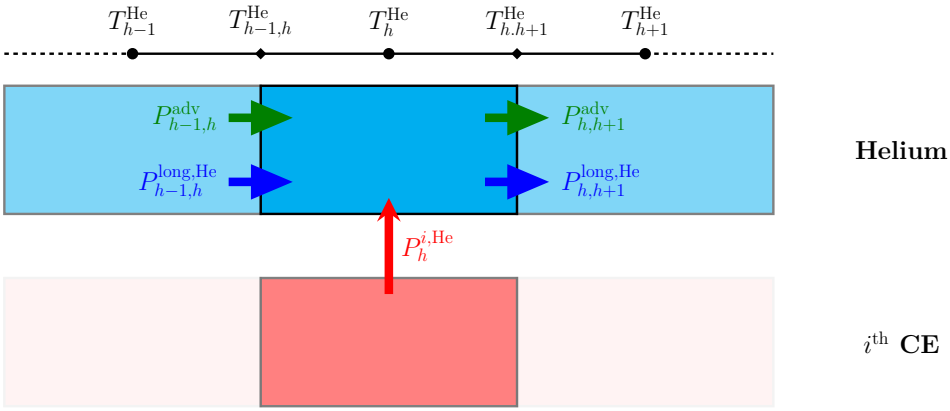

Figure 3.17: Sketch of heat fluxes and temperatures for the helium heat balance Eq. (3.69). For clarity purposes, only one CE is reported.

that case further assumptions should be made regarding the subdivision of the fluid mass among the helium parallel channels and on the heat flows among them. Since these phenomena are difficult to be evaluated experimentally, a single channel model has been considered;

- the helium material properties[6] depend not only on temperature, but also on pressure P_{He}. In the present work, P_{He} is considered an impressed quantity, i.e. an input parameter of the model;

- if forced-flow cooling is considered, like in CICCs, the mass flow rate $\dot{m}$ is assumed to be constant with time and uniform along the conductor length. Different assumptions require a detailed fluid dynamic description, that lies outside the limits of the present work;

- changes of state are not foreseen, i.e. no latent heat is considered.

Under these assumptions, the following heat balance, similar to Eq. (3.58) can be written for helium, as sketched in Figure 3.17:

$$(\Delta U)^{\mathrm{He}}_{h} = P^{\mathrm{long,He}}_{h-1,h} - P^{\mathrm{long,He}}_{h,h+1} + \sum_{i=1}^{N_{\mathrm{ce}}} P^{i,\mathrm{He}}_{h} + P^{\mathrm{adv}}_{h-1,h} - P^{\mathrm{adv}}_{h,h+1}, \qquad h = 1, \ldots, N_{\mathrm{th}} + 1. \tag{3.69}$$

[6] See Appendix A.5, page 204.

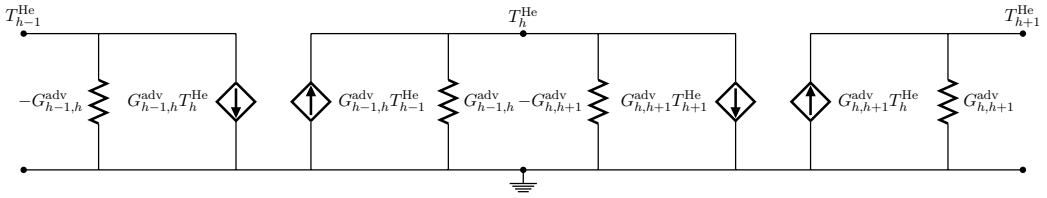

Figure 3.18: Equivalent network for the advective terms $P^{\mathrm{adv}}_{h-1,h}$ and $P^{\mathrm{adv}}_{h,h+1}$.

The meaning, the expression and the equivalent network components of $(\Delta U)^{\mathrm{He}}_h$, $P^{\mathrm{long,He}}_{h-1,h}$, $P^{\mathrm{long,He}}_{h,h+1}$ and $P^{i,\mathrm{He}}_h$ are the same of the corresponding terms of Eq. (3.58):

$$(\Delta U)^{\mathrm{He}}_h = (\rho c_{\mathrm{p}})^{\mathrm{He}}_h v^{\mathrm{He}}_h \frac{\mathrm{d}T^{\mathrm{He}}_h}{\mathrm{d}t} = C^{\mathrm{He}}_h \frac{\mathrm{d}T^{\mathrm{He}}_h}{\mathrm{d}t}, \tag{3.70}$$

$$P^{\mathrm{long,He}}_{h-1,h} = k^{\mathrm{He}}_{h-1,h} \frac{A^{\mathrm{He}}}{l^{\mathrm{He}}_{h-1,h}} (T^{\mathrm{He}}_{h-1} - T^{\mathrm{He}}_h) = G^{\mathrm{long,He}}_{h-1,h} (T^{\mathrm{He}}_{h-1} - T^{\mathrm{He}}_h), \tag{3.71}$$

$$P^{i,\mathrm{He}}_h = h^i_{\mathrm{c},h} A^{\mathrm{wet},i}_h (T^i_h - T^{\mathrm{He}}_h) = G^{i,\mathrm{He}}_h (T^i_h - T^{\mathrm{He}}_h), \tag{3.72}$$

where $l^{\mathrm{He}}_{h-1,h}$ is the distance between neighboring helium thermal nodes, v^{He}_h is the helium dual element volume, A^{He} its equivalent cross-section area computed on the basis of the conductor void fraction f_{void}, $(\rho c_{\mathrm{p}})^{\mathrm{He}}_h$ its volumetric heat capacity and $k^{\mathrm{He}}_{h-1,h}$ its thermal conductivity.

The remaining terms $P^{\mathrm{adv}}_{h-1,h}$ and $P^{\mathrm{adv}}_{h,h+1}$ represent the *advective heat flows*, evaluated respectively at the boundary between $h-1$ and h and between h and $h+1$ dual elements, as shown in Figure 3.17. These heat flows can be expressed by:

$$P^{\mathrm{adv}}_{h,h+1} = \dot{m} h^{\mathrm{He}}(T^{\mathrm{He}}_{h,h+1}), \tag{3.73}$$

where h^{He} is the helium specific enthalpy, computed at $T^{\mathrm{He}}_{h,h+1}$, that is the temperature at the boundary between h and $h+1$ dual elements. Provided that the temperature variation inside each dual element is small, $T^{\mathrm{He}}_{h,h+1}$ can be written as:

$$T^{\mathrm{He}}_{h,h+1} = \frac{T^{\mathrm{He}}_h + T^{\mathrm{He}}_{h+1}}{2}. \tag{3.74}$$

and the enthalpy can be approximated as:

$$h^{\mathrm{He}}(T^{\mathrm{He}}_{h,h+1}) \approxeq h^{\mathrm{He}}(T^{\mathrm{He}}_h) + (c^{\mathrm{He}}_{\mathrm{p}})_{h,h+1} \frac{T^{\mathrm{He}}_{h+1} - T^{\mathrm{He}}_h}{2}, \tag{3.75}$$

where $(c^{\mathrm{He}}_{\mathrm{p}})_{h,h+1}$ is the specific heat at constant pressure. A similar expression can be obtained for $P^{\mathrm{adv}}_{h-1,h}$:

$$P^{\mathrm{adv}}_{h-1,h} = \dot{m} h^{\mathrm{He}}(T^{\mathrm{He}}_{h-1,h}) \approxeq \dot{m} \left[h^{\mathrm{He}}(T^{\mathrm{He}}_h) - (c^{\mathrm{He}}_{\mathrm{p}})_{h-1,h} \frac{T^{\mathrm{He}}_h - T^{\mathrm{He}}_{h-1}}{2} \right], \tag{3.76}$$

therefore the net advective heat flow entering in the h^{th} dual element is:

$$P^{\text{adv}}_{h-1,h} - P^{\text{adv}}_{h,h+1} \approxeq \frac{\dot{m}(c_{\text{p}}^{\text{He}})_{h-1,h}}{2}(T^{\text{He}}_{h-1} - T^{\text{He}}_{h}) - \frac{\dot{m}(c_{\text{p}}^{\text{He}})_{h,h+1}}{2}(T^{\text{He}}_{h+1} - T^{\text{He}}_{h}) = \\ = G^{\text{adv}}_{h-1,h}(T^{\text{He}}_{h-1} - T^{\text{He}}_{h}) - G^{\text{adv}}_{h,h+1}(T^{\text{He}}_{h+1} - T^{\text{He}}_{h}). \tag{3.77}$$

Thus, the lumped network equivalent to the advective terms can be expressed by means of thermal conductances $\pm G^{\text{adv}}_{h,h+1}$ and controlled heat flow generators, as shown in Figure 3.18.

In general, the advective term must be considered with care, since it may involve numerical instabilities. Indeed, the equivalent lumped network described above is equivalent to the *central difference scheme* proposed in [137], based on the assumption of a piece-wise linear temperature profile along the longitudinal coordinate. However, this approximation is valid only for small values of the adimensional *Peclet number* Pe, defined as the ratio between the strengths of advective and diffusion terms, that in the case of an isolated helium channel is:

$$\text{Pe}_{h,h+1} = \frac{\dot{m} c_{\text{p}}^{\text{He}} l^{\text{He}}_{h,h+1}}{A^{\text{He}} k^{\text{He}}_{h,h+1}} = 2\frac{G^{\text{adv}}_{h,h+1}}{G^{\text{long,He}}_{h,h+1}} \tag{3.78}$$

If $|\,\text{Pe}_{h,h+1}\,| > 2$, the central difference scheme may become numerically unstable [137]. A trivial solution to the problem is the use of a finer discretization mesh, that reduces $l^{\text{He}}_{h,h+1}$ and the Pe number accordingly. Alternative possibilities exist, for example the use of an *upwind scheme*, that approximates $T^{\text{He}}_{h,h+1}$ with a relation based only on the temperatures of the upstream fluid. The simplest case is:

$$T^{\text{He}}_{h,h+1} = T^{\text{He}}_{h}, \tag{3.79}$$

Upwind schemes are numerically stable but introduce a spurious *numerical diffusivity* that can lead to inaccurate results, therefore they are not considered in the present case. More complex schemes also exists, based on the estimation of the effective Pe number of each element [137]. However, they are not feasible in the case of CICCs, since the diffusive term relies mainly on the thermal diffusion in the solid part of the conductor, making the estimation of the Pe number very complex. Nevertheless, the presence of the diffusive term along the solid part of the cable has a stabilizing effect, since the thermal conductivity of copper is many orders of magnitude larger than helium, and this results in a strongly reduced Pe number compared to the case of the isolated helium channel.

3.4.3 Network Completion and Solution

Similarly to the Udine EM module, further network components can be included to describe additional objects or conditions. For example, a network component equivalent to the e.m.f. generator used in the EM module can be added to model an

impressed temperature difference on a given surface. Conversely, heat flow generators can represent heat depositions due to natural disturbances or controlled heaters. With such choices, appropriate boundary conditions can be applied:

- if a *Dirichlet condition* should be considered, e.g. an assigned helium temperature, a *impressed temperature difference generator* can be used;
- a *general Neumann condition*, i.e. an assigned heat flow, can be modeled thanks to suitable *heat flow generators*;
- an *adiabatic Neumann condition*, i.e. no heat flow, is assumed if no additional network components are considered.

In variable regime, if only Neumann conditions are considered, all the thermal nodes correspond to differential unknowns, since a thermal capacitor is connected between each of them and the ground node. The n_{dir} nodes at which a Dirichlet condition is applied, i.e. a temperature is assigned, are instead algebraic unknowns.

Like in Udine EM module, the thermal network equations are built thanks to the modified node analysis method, resulting in a system of equations corresponding to Eq. (3.48), rearranged as in Eq. (3.50) and solved with a Runge-Kutta method. However, in the thermal case, the system matrices are not constant and are recomputed considering the material properties non-linearity. This applies to the system matrices $\mathbf{F}_{\mathrm{S}}$ and $\mathbf{D}_{\mathrm{S}}$ of Eq. (3.49) which are therefore written as the sum of their linear and non-linear components:

$$\mathbf{F}_{\mathrm{S}} = \mathbf{F}_{\mathrm{S,L}} + \mathbf{F}_{\mathrm{S,NL}}, \tag{3.80}$$

$$\mathbf{D}_{\mathrm{S}} = \mathbf{D}_{\mathrm{S,L}} + \mathbf{D}_{\mathrm{S,NL}}. \tag{3.81}$$

$\mathbf{F}_{\mathrm{S,L}}$ and $\mathbf{D}_{\mathrm{S,L}}$ are stored through all the computation, together with the *geometrical factors*, that are the constant parameters needed for the computation of $\mathbf{F}_{\mathrm{S,NL}}$ and $\mathbf{D}_{\mathrm{S,NL}}$, such as the element areas, volumes and lengths. The non-constant material properties depend on a set of *control variables*, that are either quantities internal to the thermal module, e.g. temperatures, or quantities given by external modules like the EM model, e.g. magnetic induction. The control variables are stored for each non-linear network component and suitably updated as the simulation progresses. At each time step of the Runge-Kutta method, the material properties are recomputed according to the last set of the control variables, and combined with the appropriate geometrical factors to obtain $\mathbf{F}_{\mathrm{S,NL}}$ and $\mathbf{D}_{\mathrm{S,NL}}$, that are then added to their linear counterpart to obtain the final matrices.

The computation of the non-linear terms can be very cumbersome if carried out without any suitably tailored criterion. In the case of the thermal model, the accuracy with which the material properties are known can be of some percent, therefore, a small fixed variation threshold δ_i has been defined for each control variable, to prevent unnecessary material properties recalculation when the maximum control variable change is lower than δ_i. For example, a threshold of 10^{-3} K is generally used for the temperature.

The inversion of matrices $\mathbf{D}_{\mathrm{S_{aa}}}$ and $\mathbf{F}_{\mathrm{S_{dd}}}$ must be performed at any matrix change to obtain the solution of Eq. (3.50), and this may generally require a huge amount of computational time. However, in the case of the thermal model this operation is particularly easy, since the differential matrix $\mathbf{F}_{\mathrm{S_{dd}}}$, which contains all the values of the thermal capacitors, is a diagonal matrix, since all the thermal capacitors are connected to ground node representing the absolute zero temperature:

$$\mathbf{C} = \begin{pmatrix} C_1 & 0 & \cdots & 0 & 0 \\ 0 & C_2 & \cdots & 0 & 0 \\ \vdots & \vdots & \ddots & \vdots & \vdots \\ 0 & 0 & \cdots & C_{n-1} & 0 \\ 0 & 0 & \cdots & 0 & C_n \end{pmatrix}, \tag{3.82}$$

On the other hand, matrix $\mathbf{D}_{\mathrm{S_{aa}}}$ is $2\,n_{\mathrm{dir}} \times 2\,n_{\mathrm{dir}}$, therefore it must be inverted only if Dirichlet conditions are applied. Moreover, n_{dir} is generally small, i.e. some units, therefore the computational effort required is negligible.

Thus, the modified node analysis method applied to the thermal lumped network leads to a differential system of equations that can be solved quite efficiently also in the non-linear case.

3.5 Thermal-Electromagnetic Coupling

To carry out the analyses performed during this PhD activity, the Bologna EM module and the lumped thermal network have been coupled together. No coupling between Udine EM module and lumped thermal network model was necessary. Presently, the coupling between EM and thermal (TH) models is *explicit*. This means that the two systems of differential-algebraic equations are solved independently with internal step-sizes, respectively h_{em} and h_{th}, and suitable information is exchanged between the two models when an additional step-size h_{exp} is passed. An *implicit* coupling, i.e. a combination of the two models into a single system of equations with a single step-size h_{imp}, adopted for example in [30], has not been considered for several reasons. First of all, it is less modular and flexible than several explicitly coupled models. Moreover, since the thermal and electromagnetic problems can be characterized by quite different time constants, the solution of a single model with a Runge-Kutta method would be affected by the smallest among all the time constants, being the integration step-size controlled by error estimation techniques[7]. As an example, a very tiny time constant resulting from the thermal equations can slow down also the solution of the EM equations and viceversa. With the explicit coupling, the internal step-sizes are completely independent and useless system solutions are avoided. The drawback of explicit coupling is the need to find a good method to decide the step-size h_{ext} necessary to obtain accurate results.

[7] See Appendix D, page 231.

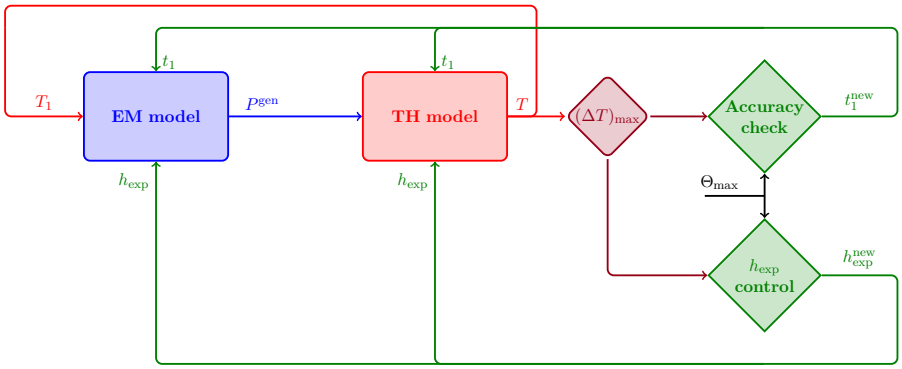

Figure 3.19: Conceptual scheme of the TH-EM models coupling.

The conceptual scheme of the coupling between the models is reported in Figure 3.19. The EM model can be considered as a black box that gives as output the cable losses, provided that the temperature distribution along the cable is given as input. The thermal model computes the temperature distribution along the cable considering as input the electromagnetic losses produced by the cable. The following steps are therefore suitably cycled:

1. *EM step*: starting from an initial temperature distribution T_1 at t_1, the EM module evolves for a duration h_{exp}. The electromagnetic losses P^{gen} along the cable are computed at t_1 and at $t_1 + h_{\text{exp}}$. These losses are exact with the assumption of a constant temperature in the interval $[t_1, t_1 + h_{\text{exp}}]$.

2. *TH step*: the losses, averaged thanks to a trapezoid rule during the step-size h_{exp}, are given to the thermal module. The temperature distribution evolution in the interval $[t_1, t_1 + h_{\text{exp}}]$ is then evaluated;

3. *Accuracy check*: the assumption of a quite constant temperature distribution for the solution of the EM module should be checked in order to assess the model self-consistency. The maximum temperature increase $(\Delta T)_{\max}$ during the step-size is therefore evaluated from the thermal model, and compared with a fixed threshold $\Theta_{\max}$, that is an input parameter of the code. Suitable values for $\Theta_{\max}$ are around $10^{-3} \div 10^{-2}$ K. If $(\Delta T)_{\max} > \Theta_{\max}$, the computed step is rejected and recalculated with a reduced step-size. Conversely, if $(\Delta T)_{\max} < \Theta_{\max}$, the temperature profile has not changed significantly and the EM step can be considered valid, therefore a new EM step starting at $t_1 + h_{\text{exp}}$ is considered.

4. *Step-size control*: both in case of rejection or acceptance of the computed results, the new step-size $h_{\text{exp}}^{\text{new}}$ is automatically computed thanks to the heuristic:

$$h_{\text{exp}}^{\text{new}} = 0.9\, h_{\text{exp}} \sqrt[4]{\frac{\Theta_{\max}}{(\Delta T)_{\max}}}, \tag{3.83}$$

that provides a very smooth control of the step-size in order to maintain an almost constant $(\Delta T)_{\max}$ in subsequent steps. Equation (3.83) is based on a similar formula for step-size control taken from [78].

Presently, the coupling works only with cables discretized into the same number of cable elements N_{ce} by the EM and TH models, whereas the numbers N_{em} and N_{th} of longitudinal segments of EM and TH modules can be different. If $N_{\mathrm{em}} \neq N_{\mathrm{th}}$, the temperature and losses along the cable are suitably linearly interpolated.

Chapter 4

Inter-Strand Resistances

The longitudinal electrical resistance of a superconducting cable far from the critical surface can be generally considered as null. However, the same assumption cannot be made for the transverse resistance, that is the resistance that the current experiences when transferring from a strand to a neighboring one. Indeed, several aspects can affect this phenomenon: the presence of thin oxide layers, coatings and solder can change the inter-strand resistance by orders of magnitude. Furthermore, all of these aspects are strongly dependent on the heat treatment applied, on the materials purity and on the mechanical forces the cable is subjected to.

Due to the complexity of the phenomenon, no satisfactory theoretical and general purpose model can be employed for inter-strand resistance estimation. Nevertheless, since the current and heat redistribution among strands are important aspects in terms of cable stability and losses, dedicated measurements are performed to evaluate the actual inter-strand resistances in superconducting cables. In this Chapter, the main experimental methods employed in Rutherford cables and CICCs for the inter-strand electrical resistances evaluation are summarized. The effectiveness of THELMA electromagnetic code in modeling such experimental procedures and in reproducing their results is then demonstrated by means of some case studies. These analyses were a necessary step to validate the code and to calibrate the inter-strand resistance parameters. The data used for all the model validation and calibrations have been taken from literature or given by researchers, as cited in detail in the relevant thesis sections.

4.1 General Aspects of the Inter-Strand Contact

The electrical and thermal inter-strand resistances have a significant impact on the superconducting cables performances. Indeed, very large values are unwanted, since they can avoid current and heat redistribution among neighboring strands in the case of a localized electromagnetic or thermal disturbance. Conversely, a very low electrical resistance value is also generally undesirable, since it promotes the flow of significant eddy currents in transient regime, leading to huge AC losses that can affect the thermal stability of the conductor. A detailed analysis of the inter-strand resistances is therefore needed for a correct design of a superconducting cable.

Many aspects affect the electrical and thermal inter-strand resistances in superconducting strands [187]:

- the *contact*: the actual area of contact between two surfaces is generally localized in a few discrete spots, even for very smooth surfaces [51]. This is confirmed by experimental results in which the conductance is dependent upon the applied force between the samples and not on the area of contact nor on the apparent contact pressure [149];
- the *oxidation*: the thin oxide layer present on the outermost surface of the strand has a remarkable role on the effective transverse resistance. The thickness of this layer is strongly dependent on the heat treatment, on the surface material and on the mechanical pressure applied. For example, a reduction of the inter-strand electrical resistance is observed if the heat treatment is performed under transverse pressure, since the oxygen may diffuse and dissolve in the metallic bulk [141]. Moreover, at low temperatures each oxide layer acts as an additional boundary resistance, and the Kapitza resistance due to the acoustic mismatch between the layers can be significant [149];
- the *strand coating*: since the natural oxidation of copper surface gives unpredictable results, a coating is generally applied to the strands to better control the oxidation growth. For example, in the case of LHC strands a SnAg alloy is used, since a controlled copper oxide layer can be grown with a suitable heat treatment [187]. Other materials employed for coatings are Ni, Cr and Al_2O_3 [150];
- the presence of *solder*: if very small values for inter-strand resistance should be achieved, partial or full soldering can be employed;
- the presence of additional bundle *cores or wrappings*: if large values of inter-strand resistances are needed, thin layers of resistive material can be employed to decouple neighboring strands. Generally, stainless steel foils $10 - 100\,\mu$m thick are used.

The electrical inter-strand resistance is generally dominated by the contribution of the oxide, whereas the main phenomenon affecting the thermal inter-strand resistance is the contact [187]. Different behaviors can be observed as a function of

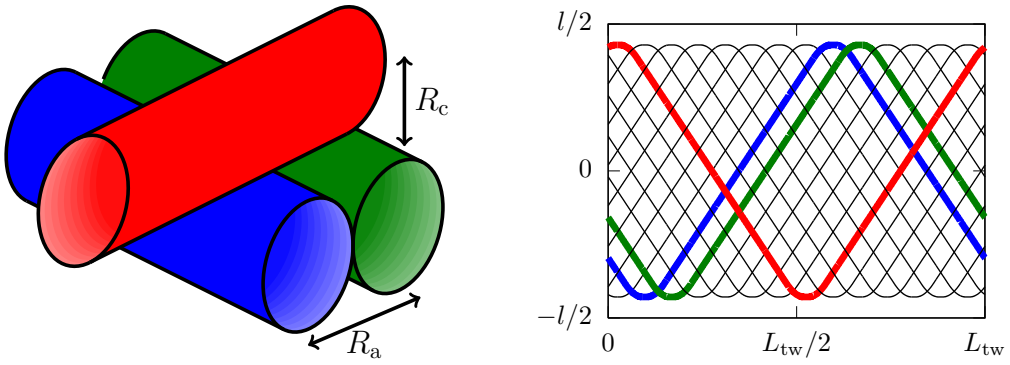

(a) 3D sketch.

(b) 2D sketch of a Rutherford cable.

Figure 4.1: Adjacent and cross-over resistances in Rutherford cables.

temperature for electrical and thermal inter-strand resistance. The first are not expected to vary in the temperature range of interest [101] [187], whereas a power law fit is typically considered for the thermal contact conductance per unit length [W/(K·m)]:

$$k_{\text{cont}}(T) = \alpha T^{\beta}, \tag{4.1}$$

where α and β are two fitting constants. Typical values for β are between 0.75 and 2.5 [149]. At temperatures higher than $20 - 30$ K, k_{cont} becomes linear with temperature and tends to a constant value above 200 K [84].

In the following, the common techniques adopted for inter-strand electrical resistance measurements in Rutherford cables and CICCs are summarized and discussed. Then, the THELMA model for the analysis of inter-strand resistance measurements is explained. Finally, some case studies of numerical analyses of the inter-strand resistances with THELMA are presented.

4.2 Rutherford Cables

Two different types of inter-strand resistances are generally defined in a Rutherford cable, as shown in Figure 4.1a:

- the *adjacent resistance* R_a [Ω], that is the resistance between neighboring strands on the same face of the cable;
- the *cross-over resistance* R_c [Ω], that is the resistance between strands laying on opposite faces of the cable.

Each type of inter-strand resistance is associated to a contact area which is defined conventionally. The contact area for R_c is defined as the shadow area of the cross-over, whereas the strand diameter multiplied for the cross-over length is generally

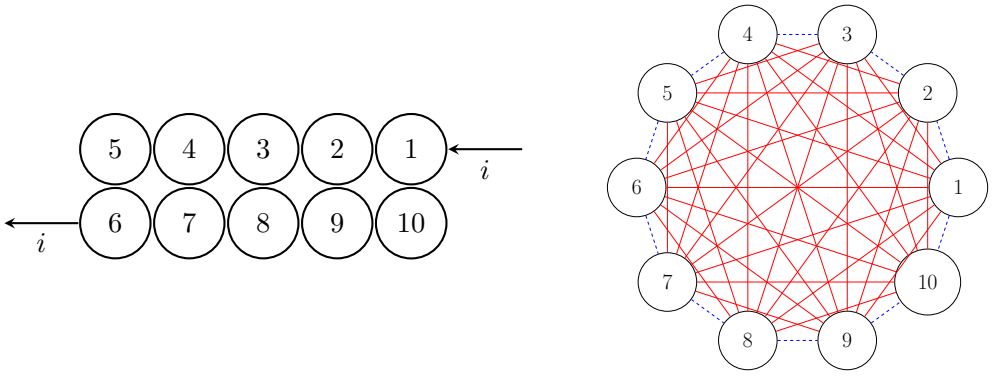

Figure 4.2: R_a and R_c measurement in a Rutherford cable with 10 strands. Left: principle of the measurement technique. Right: Fully-connected graph representing the equivalent network. Solid lines represent $G_{c,tot}$, dashed lines $G_{a,tot}$.

considered for R_a [189]. The contact surface resistivity is obtained from the measured resistance and this contact area. As shown in Figure 4.1b in a Rutherford cable, each couple of non-adjacent strands experiences two cross-over contacts along one transposition pitch. The overall contact between two adjacent strands along the same length can instead be represented as the parallel of $2\,N_{st}$ contacts with resistance R_a.

Due to the constraints on the geometrical parameters of Rutherford cables for accelerator magnets, the inter-strand coupling currents and their related losses are more sensitive to R_c than R_a [174], therefore high R_c values are desirable to reduce AC losses. On the other hand, very large values of both R_a and R_c can dramatically reduce the minimum energy needed to quench the cable [187]. Following these results, a desired feature is to obtain high value for R_c, to mitigate losses, and a much lower value for R_a to promote stability thanks to current redistribution among adjacent strands [189]. Nevertheless, the bare contact among strands generally gives R_a values up to an order of magnitude higher than R_c values due to the rolling applied to the broad face [187] [189], therefore a thin stainless steel core is often added between the cable layers to increase R_c. A wide compilation of R_a and R_c values is reported in [187]. Typical R_a values for non-cored cables are around $1 - 10\,\mu\Omega$, whereas R_c in cored cables can be larger than some mΩ.

The experimental evaluation of adjacent and cross-over resistances is generally performed with a direct ohmic method [141] [174]. A DC current I is injected between opposite strands in the cross-section and the voltage distribution v among the strands is measured, as schematized in Figure 4.2. In the case of uniform R_a and R_c along the sample, the measurements can be compared with simple theoretical results. Indeed, considering a sample as long as one transposition pitch, the equivalent electrical network can be easily represented as a fully connected mesh of

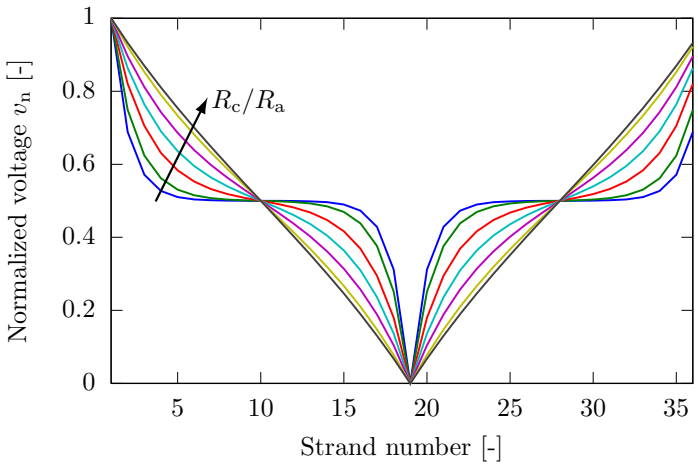

Figure 4.3: Analytical normalized voltage distribution in a 36 strands Rutherford cable during an inter-strand resistance measurement. In the graph, the values for $\delta = R_c/R_a$ are 1, 2, 5, 10, 20, 50 and 100.

conductances $G_{c,tot}$ and $G_{a,tot}$ [S]:

$$G_{c,tot} = \frac{2}{R_c}, \tag{4.2}$$

$$G_{a,tot} = \frac{2N_{st}}{R_a}. \tag{4.3}$$

In these conditions, the network solution can be described by means of the normalized voltage distribution $v_n = v/v_{max}$, that depends only on the ratio $\delta = R_c/R_a$ and it is symmetric as regards the strand taken as mass node, as shown in Figure 4.3. In particular, in the limit $\delta \gg 1$, that means $R_c \gg R_a$, the normalized voltage tends to a straight line. It can be easily demonstrated that in these conditions the measured voltage is proportional to R_a:

$$v = \frac{R_a I}{8}. \tag{4.4}$$

4.3 Cable-In-Conduit-Conductors

Several dedicated testing stations exist for the inter-strand resistances measurements in CICCs, such as the Twente cryogenic press [1], the VOFEX device [134] or the CRPP JORDI device [7], that is more focused on CICC terminations and joints. These tests are generally done by feeding in turns pairs of strands characterized by increasing different cabling stage, starting from strands of the same triplet, then of the same 2^{nd} order bundle and so on, up to consider couples of strands that belong to different cable petals. Differently from Rutherford cables, simple theoretical models

describing the inter-strand resistances tests are not feasible, due to the complexity and randomness of the conductor geometry. The equivalent contact resistance per unit length r_c [Ω·m] between two strands in the cable, is conventionally defined as [131]:

$$r_c = \frac{v}{I} L, \tag{4.5}$$

where v and I are respectively the measured voltage and current and L is the sample axial length, generally chosen close to the last stage twist pitch. It must be noted that in these measurements all the cable strands contribute to r_c to some extent, not only the two strands considered. A four-probe-method is generally used to improve the measurement accuracy [123] [131] [134]. For Ni-plated Nb-Ti strands, typical values for r_c are between some tenths and some hundreds of nΩ·m [129], whereas in the case of Nb_3Sn Cr-coated strands, typical values are $1 - 10$ nΩ·m for strands of the same triplet and 100 nΩ·m for strands of different higher order cabling stages [123] [131]. Inter-petal resistances are dominated by the stainless steel wrap, and they may be higher than 1 $\mu\Omega$·m. r_c is very sensitive to the applied force and the mechanical cycling load. In particular, it decreases with the applied load, since the strands are pressed one against the other, but mechanical hysteresis and relaxation phenomena can be observed [129] [131]. The inter-strand resistances generally reach a saturation value in loaded mechanical conditions after thousand of cycles [123] [129].

In the usual inter-strand resistance measurement, each superconducting strand is equipotential. Particular care in analyzing the measurements should be taken if copper strands are embedded in the conductor. Equation (4.5) indeed is no longer valid if one of the strands under test is normal-conducting, since the current diffusion between the normal-conducting and the superconducting strands spans approximately along a diffusion length[1]:

$$l_{\mathrm{diff}} = \sqrt{\frac{r_c A_{\mathrm{st}}}{2\rho_{\mathrm{E}}}}, \tag{4.6}$$

where A_{st} is the strand cross-section area and ρ_{E} is the electrical resistivity of normal-conducting strands. Typical values of l_{diff} can be estimated between some millimeters and one centimeter. In this case, the measured resistance between a superconducting and a normal-conducting strand can be expressed as:

$$R_{\mathrm{c,NC}} \propto \frac{r_c}{l_{\mathrm{diff}}}. \tag{4.7}$$

This result is in good agreement with available measurements of inter-strand resistances with copper strands, for example $9 - 25$ $\mu\Omega$·m [131].

[1] See Appendix E, page 237 for an analysis of this aspect in the case of an isolated CICC triplet.

4.4 Inter-Strand Resistances in the THELMA Code

The THELMA model is characterized by the following parameters representing inter-strand elementary electrical resistances [19]:

- the *strand spot contact resistance* $R_{\mathrm{st}}^{\mathrm{s}}$ [Ω]. It is used to model occasional contacts along the cable axis, like the R_{c} in Rutherford cables or the inter-strand resistances between strands belonging to different bundles in a CICC;
- the *strand distributed contact resistance* $R_{\mathrm{st}}^{\mathrm{d}}$ [Ω·m]. It models contacts that are supposed to be uniform along the cable axis, like the R_{a} in Rutherford cables or the distributed contact between strands of the same triplet in a CICC;
- the *stainless steel spot additional contact resistance* $R_{\mathrm{ss_a}}^{\mathrm{s}}$ [Ω], used to model the stainless steel cores in a Rutherford cable or the petal wrappings in a CICC.

These elementary resistances are a property of the individual strand, and their suitable combination gives rise to the inter-strand resistances measured in actual cables, that depend to some extent on all the cable strands. The same elementary resistance values are generally considered for superconducting and copper strands if their surface coating is the same. If a CICC termination or a joint is modeled, one additional parameter $R_{\mathrm{sdl}}^{\mathrm{s}}$ is used to describe the contact resistance between the cable and the saddle. In the absence of specific experimental data, it is usually assumed $R_{\mathrm{sdl}}^{\mathrm{s}} = R_{\mathrm{st}}^{\mathrm{s}}$, since it is expected that the saddle and strand contributions to the resistance have the same magnitude. The elementary parameters for inter-strand electrical resistances are generally calibrated through suitable numerical analyses, performed to reproduce experimental results on cable short samples, as extensively reported in the following section.

As regards the thermal inter-strand conductances, the following parameters are considered:

- the *strand spot contact conductance* $G_{\mathrm{st}}^{\mathrm{s}}$ [W/K], with the same meaning as the corresponding electrical resistance $R_{\mathrm{st}}^{\mathrm{s}}$;
- the *strand distributed contact resistance* $G_{\mathrm{st}}^{\mathrm{d}}$ [W/(K · m)], with the same meaning as the corresponding electrical resistance $R_{\mathrm{st}}^{\mathrm{d}}$.

Differently from the electrical case, few experimental data are available for the thermal inter-strand resistances. In this work, experimental data in the range $4 - 10$ K from [101] are considered as reference for $G_{\mathrm{st}}^{\mathrm{d}}$. Equation (4.1) has been employed to fit such data, for both coated and non-coated superconducting strands, as shown in Figure 4.4. In the first case, $\alpha = 0.545$ W/(K$^{1+\beta}$ · m) and $\beta = 1.54$ have been used, whereas in the second case $\alpha = 0.107$ W/(K$^{1+\beta}$ · m) and $\beta = 2.25$. $G_{\mathrm{st}}^{\mathrm{s}}$ is then obtained from $G_{\mathrm{st}}^{\mathrm{d}}$ by an estimation of the contact length.

After the set-up of the elementary parameters, the length of the distributed contacts and the locations of the spot contacts are automatically computed from

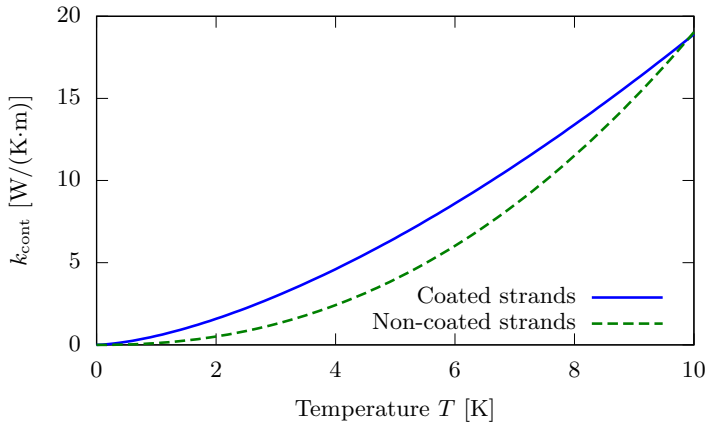

Figure 4.4: Eq. (4.1) for thermal contact conductivity k_{cont} fitted with data from [101].

the modeled strand geometries by a routine that evaluates the distance between one strand and all the others along all the cable axis, taking into account the presence of possible stainless steel wrappings. In this way, a set of contact points between strands is found, which correspond to concentrated or distributed conductances, as described in detail in [19]. In the equivalent network, these conductances are grouped into equivalent conductances connected to the network nodes that represent the strand.

4.5 Numerical Analysis of Inter-Strand Resistances Measurements

The electrical inter-strand measurements can be analyzed in the THELMA code by means of the Udine EM module described in Section 3.3.1, based on an equivalent lumped electrical network. Since no resistive transition is supposed to take place during such measurements, the superconducting strands are considered as zero longitudinal resistance elements, whereas the copper strands are characterized by a non-zero longitudinal resistance, computed on the basis of the material properties at cryogenic temperature[2]. If a CICC termination or a joint is modeled, the copper blocks, here collectively referred to as *saddle*, are represented by means of a suitable mesh of transverse and longitudinal resistances.

To simulate experimental measurements, suitable current generators are activated in turn and their corresponding voltages are computed to obtain the resulting resistance. Since these are steady-state measurements, the system of equations (3.48)

[2]See Appendix A.3, page 192 for the details.

simplifies into the following linear system:

$$\underbrace{\begin{pmatrix} \mathbf{A}_\mathrm{r}^\mathrm{T} & \mathbf{R} \\ \mathbf{G} & \mathbf{A}_\mathrm{r} \end{pmatrix}}_{\mathbf{S}} \cdot \begin{pmatrix} \mathbf{V} \\ \mathbf{I} \end{pmatrix} = \begin{pmatrix} \mathbf{E} \\ \mathbf{J} \end{pmatrix}. \tag{4.8}$$

The system matrix $\mathbf{S}$ can be quite large and it is very sparse. To reduce the number of unknowns, the nodes representing each superconducting strand can be merged together, resulting in only one unknown potential per strand. Moreover, all the resistances R, representing copper elements or inter-strand resistances, are modeled as conductances $G = 1/R$, since, in the modified node analysis solution method, each resistance adds two unknowns, being the resistor a current-driven component, whereas only one unknown is added in the case of a conductance. With these modifications, no current-driven component are present in the final network, and the system Eq. (4.8) becomes:

$$\mathbf{GV} = \mathbf{J}, \tag{4.9}$$

whose solution can be obtained by LU decomposition or iterative methods like Bi-CGStab [171].

In the following, some examples of inter-strand resistances analyses done with the THELMA code are reported. The first is related to a Rutherford cable, the second to a CICC sample and the third to a CICC termination.

4.5.1 DISCORAP Rutherford Cable

Extensive inter-strand resistances measurements had been performed at INFN Milano, laboratorio LASA, on samples of the DISCORAP Rutherford cable [178]. A view of the cable is shown in Figure 4.5a, whereas its main data are reported in Table 2.5. This conductor is employed in the 3.9 m curved dipole model developed by INFN for the SIS300 synchrotron of the FAIR facility [177], designed for very high ramp rate cycling, up to 1 T/s. To limit the huge AC losses due to from such

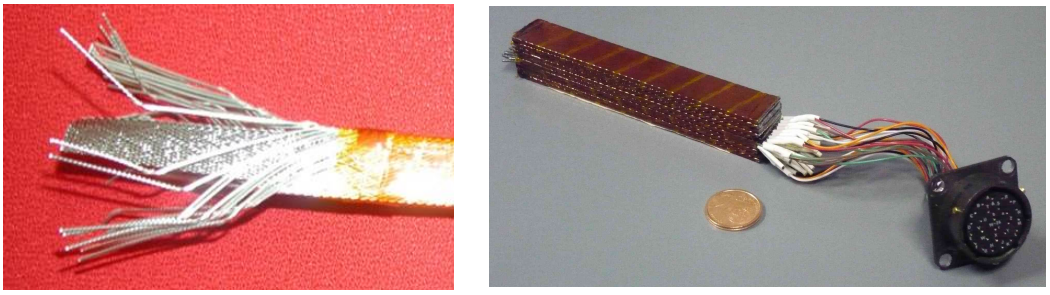

(a) View of the cable. (b) Sample for inter-strand resistances tests.

Figure 4.5: DISCORAP Rutherford cable (courtesy of Giovanni Volpini, INFN Milano, laboratorio LASA).

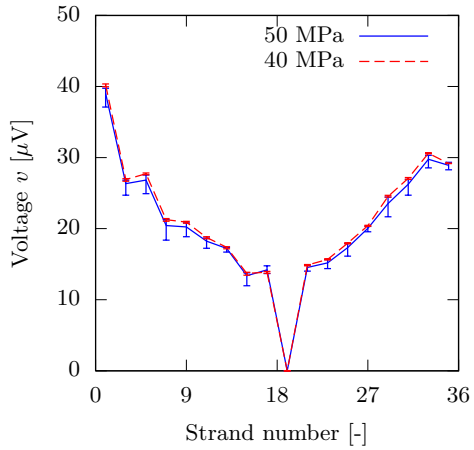

(a) Measured voltages at different applied pressures.

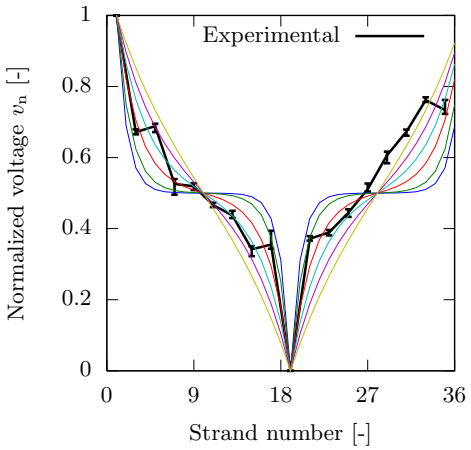

(b) Comparison between measured (bold) and computed normalized voltages.

Figure 4.6: DISCORAP Rutherford cable inter-strand resistance measurements.

large field variations, the cable has been subjected to a special heat treatment in oxidizing atmosphere to increase R_a. Moreover, a stainless steel core, about 13 mm width and 25 μm thick, is employed to enhance R_c.

The measurements were performed by means of the direct ohmic method for Rutherford cables previously described in this Chapter. Ten cable pieces one transposition pitch long (10 cm) were stacked together and cured following the same procedure adopted for magnet coil construction, as shown in Figure 4.5b. After this preparation, the sample was inserted in a cryogenic mechanical test machine to apply variable pressure on the stack, in order to provide accurate and reproducible stress conditions and to study the sample during cycling. In the case of the measurements considered for this analysis, the cool-down was performed applying a constant pressure of 50 MPa and then the sample was subjected to some thousands of mechanical cycles between 40 and 50 MPa. The voltages were measured on one every two strands of one cable piece. Both positive and negative DC currents have been employed, showing only negligible differences, therefore in the following the voltages are presented as normalized for an unitary DC current. In Figure 4.6a the measured voltages at 40 MPa and 50 MPa are reported as a function of the strand number. No clear signs of performance degradation with cycling have been found. For this reason, the variation with pressure, being quite limited in the present case, is not considered any further.

The experimental data described above give an important opportunity to apply the new THELMA code Rutherford cable model. To model these measurements with the THELMA code, the normalized voltages have been compared with the characteristics reported in Figure 4.3, as shown in Figure 4.6b, in order to obtain a first guess for the parameter δ. It can be noticed that the measured normalized

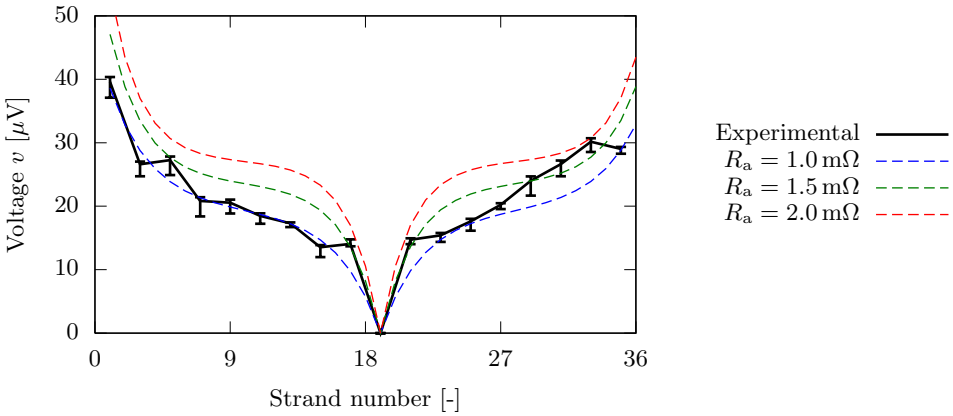

(a) Uniform model. $R_c = 8\,m\Omega$, different values of R_a.

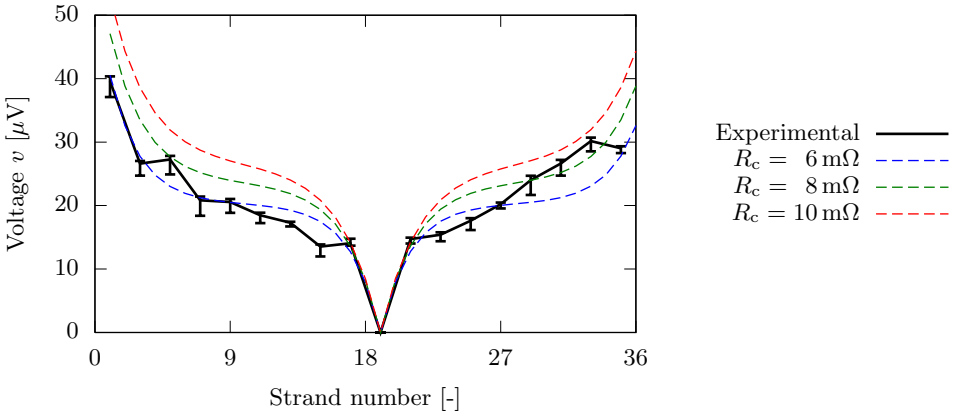

(b) Uniform model. $R_a = 1.5\,m\Omega$, different values of R_c.

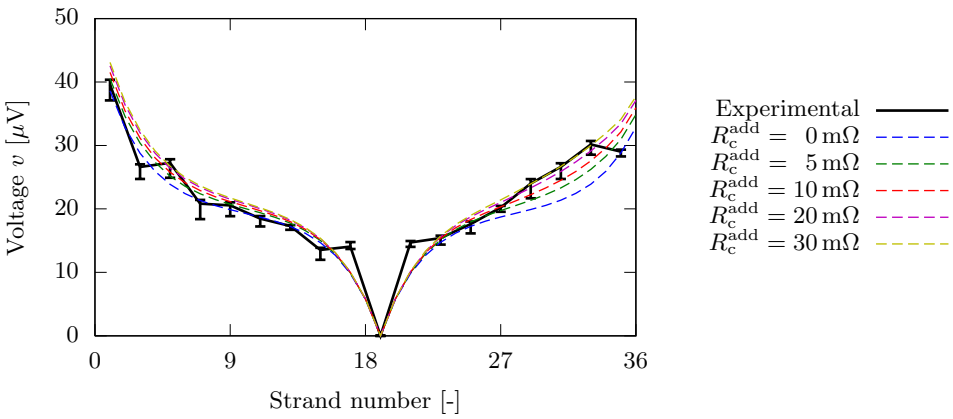

(c) Defective model. $R_c = 8\,m\Omega$, $R_a = 1\,m\Omega$, different R_c^{add}.

Figure 4.7: Comparison between measurements on DISCORAP Rutherford cable and THELMA simulations.

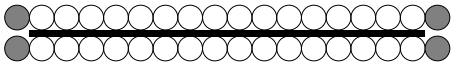

(a) Core width 100% of the internal contact length.

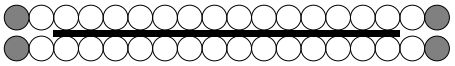

(b) Core width 93% of the internal contact length, centered placement.

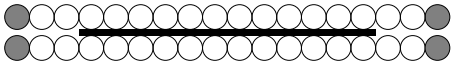

(c) Core width 86% of the internal contact length, centered placement.

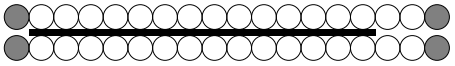

(d) Core width 93% of the internal contact length, off-centered placement.

Figure 4.8: Sketch of the different models for the core width and placement. It must be noted that the grey-filled strands are not covered by the core since they are in adjacent contact.

voltages of the strands between number 28 and number 34 lay in an area where no data is expected, even for very large values of δ. This means that such values are affected by systematic errors or by sample inhomogeneities localized in those strands, thus they should be considered with care.

In a first THELMA model, uniform R_c and R_a along the sample have been employed, whose values have been optimized comparing the simulations with the measured voltages, as shown in Figure 4.7a and Figure 4.7b. Values of R_a between 1 and 2 mΩ and values of R_c between 6 and 10 mΩ lead to reasonable fits of the experimental data, but they cannot describe the larger voltages measured on the strands between 28 and 34. A possible explanation for this feature is the presence of a *defect* localized in those strands. In particular, the impact of an additional cross-over resistance R_c^{add} acting only on such strands has been checked, with values ranging between 5 to 30 mΩ. It must be noted that, lacking any independent evidence of such a local defect, it must be considered only as a working hypothesis. The results in the case $R_a = 1\,\text{m}\Omega$ and $R_c = 8\,\text{m}\Omega$ are reported in Figure 4.7c, showing that this defective model can reasonably explain an asymmetric distribution of voltages and the larger voltages measured in some localized strands.

In another set of THELMA simulations, the impact of a further inhomogeneity has been analyzed. The stainless steel core width is indeed around 90% of the internal cable width, therefore some strands may be in direct contact along the sample, without any core contribution, and this may strongly affect the inter-strand resistances and AC losses [49]. Since this phenomenon tends to reduce the measured voltages in an inter-strand resistances test, the reference case has been chosen as $R_a = 1.5\,\text{m}\Omega$ and $R_c = 8\,\text{m}\Omega$, since it leads to slightly (about 10%) overestimated voltages, as shown in Figure 4.7a. For clarity purposes and to better outline the role of the core width and placement, no defects have been added, i.e. $R_c^{add} = 0\,\text{m}\Omega$. Four case studies have been considered, as shown in Figure 4.8:

a) a core covering 100% of the internal cable width (reference case, see Figure 4.7a and 4.7b);

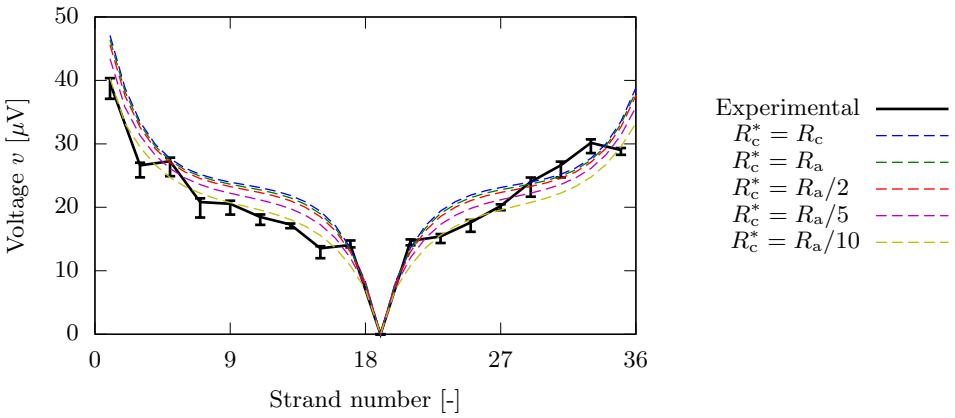

(a) Core width 93% of the internal contact length, centered placement.

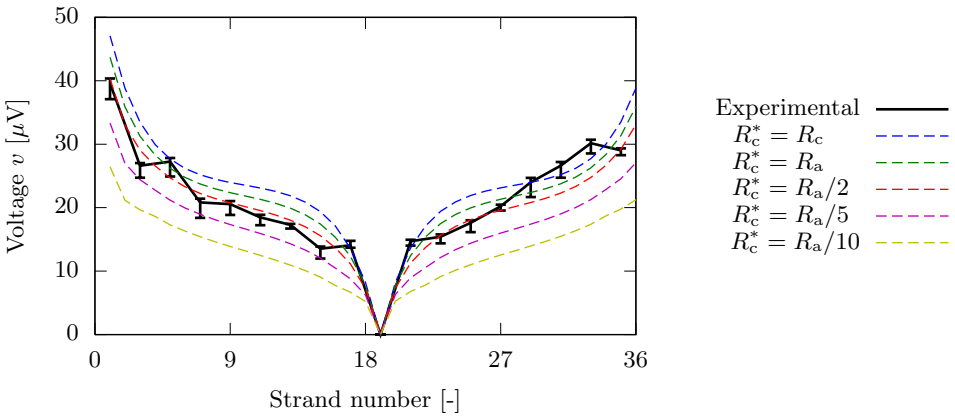

(b) Core width 86% of the internal contact length, centered placement.

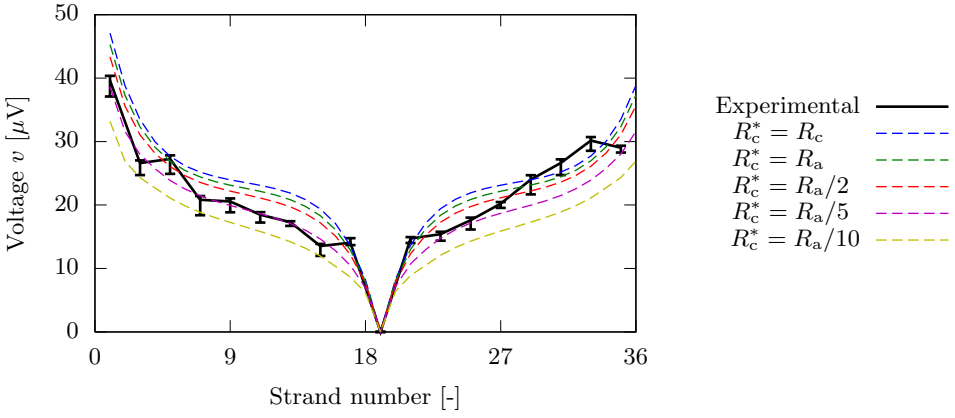

(c) Core width 93% internal contact length, asymmetric placement.

Figure 4.9: Comparison between measurements on DISCORAP Rutherford cable and THELMA simulations with different core widths and placements. Reference values for inter-strand resistances are $R_a = 1.5\,\mathrm{m\Omega}$ and $R_c = 8\,\mathrm{m\Omega}$.

b) a core covering 93% of the internal cable width, corresponding to one direct cross-contact per cable edge;

c) a core covering 86% of the internal width width, corresponding to two direct cross-contacts per cable edge;

d) a core covering 93% of the internal cable width but with an asymmetric placement (shifted to one cable edge).

The results are reported in Figure 4.9. A further parameter, the cross-over resistance in the absence of core, R_c^*, must be added: values between $R_a/10$ and R_a have been considered in the sensitivity analysis. Limited voltage dependance on R_c^* is shown in the case b). Nevertheless, even in this case the incomplete covering results in a 10% voltage reduction compared to the reference case, provided that R_c^* is one order of magnitude lower than R_a. In cases c) and d), larger voltage drops can be obtained, respectively up to 35% and 20%. In these cases, a 10% reduction compared to the reference case can be obtained for much larger values for R_c^*, respectively one half and one fifth of R_a, in good agreement with the values proposed in [187] for the cross-contact resistance in absence of core, between one half and one eighth of R_a.

In conclusion, reasonable values for the inter-strand resistances in the DISCORAP Rutherford sample considered are in the range $1 - 2\,\mathrm{m\Omega}$ for R_a and $6 - 10\,\mathrm{m\Omega}$ for R_c. More precise values cannot presently be assessed because of the uncertainties on the core width and placement and on the cross-over resistance in the absence of core. In any case, the model gives a possible explanation for the observable asymmetries in some strand voltages in terms of the presence of a localized defect, i.e. a bad contact or an inhomogeneity in the stainless steel core, resulting in a local much higher value for the cross-over resistance.

4.5.2 CICC Sample EUTF3-EAS

The EUTF3-EAS sample is a 40 cm CICC segment, whose inter-strand resistances r_c for each cabling stage have been measured by Twente University both in the presence and the absence of mechanical load [123]. In the following, the values measured at maximum load after 10000 loading cycles are considered. The main characteristics of this sample are reported in Table 4.1. A view of the cable cross-section together with the modeled geometry is shown in Figure 4.10.

The elementary resistance optimization strategy in complex cables like CICCs is carried out on these steps, suitably iterated:

1. the stainless steel spot additional contact resistance $R_{ss_a}^s$ is adjusted starting from the measured values taken from strands of different petals;

2. being the strands of the same triplet in a nominally distributed contact, the strand distributed contact resistance R_{st}^d is the dominating parameter as regards the intra-triplet resistances, therefore it is adjusted starting from the measured values taken from strands of the same triplet;

Table 4.1: EUTF3-EAS conductor main data.

No. of strands N_{st}	900 (SC) + 522 (Cu)
Strand diameter d_{st}	0.81 mm
Cabling scheme	((2 SC + 1 Cu) $\times 3 \times 5 \times 5+$ core) $\times 6$
Core scheme	3×4 Cu
Twisting pitches t_i	80 / 140 / 190 / 300 / 420 mm
Sub-cable SS wrapping covered surface	50%
Conductor void fraction	28%

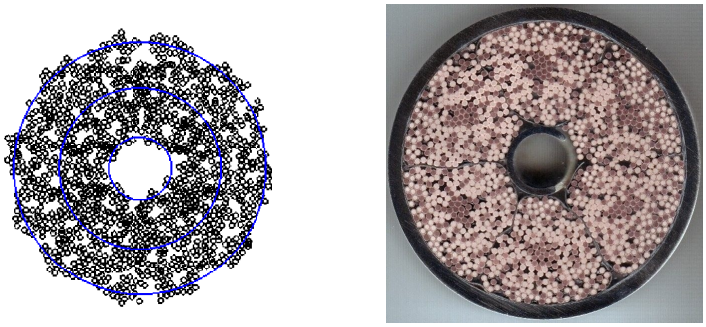

Figure 4.10: View of EUTF3-EAS sample model discretization and cross-section of a TF CICC (courtesy of ITER organization).

3. The strand spot contact resistance R_{st}^{s} is dominant in the case of contacts between strands of different triplets, thus it is adjusted starting from the measured values taken from strands of different triplets and larger bundles.

In the case of CICCs, the model can consider a wide set of combinations of strand pairs, which give different resistance values depending, among the other factors, on the cable bundles initial phase set. In a CICC the angular phases array[3] $\boldsymbol{\Theta}$ is indeed not known, however it may affect the measurements, since in a sample characterized by a different $\boldsymbol{\Theta}$, different values of resistances are measured for the same strand combinations, due to the slightly different geometries determined by the bundles initial phases. For the measures corresponding to each cabling stage, a histogram of inter-strand resistance distribution can therefore obtained with the numerical model, in which the position of the measured value is evaluated in relationship with the histogram. The plausibility of the numerical results should be therefore assessed comparing the measured values with the overall distribution of resistances rather than with a single computed value.

In the present case, the entire sampling of 1st and 2nd stage inter-strand resistances between superconducting strands has been computed, corresponding respectively to 450 and 1800 values. For the high-order cabling stages, a number

[3] See Section 3.2.2, page 61.

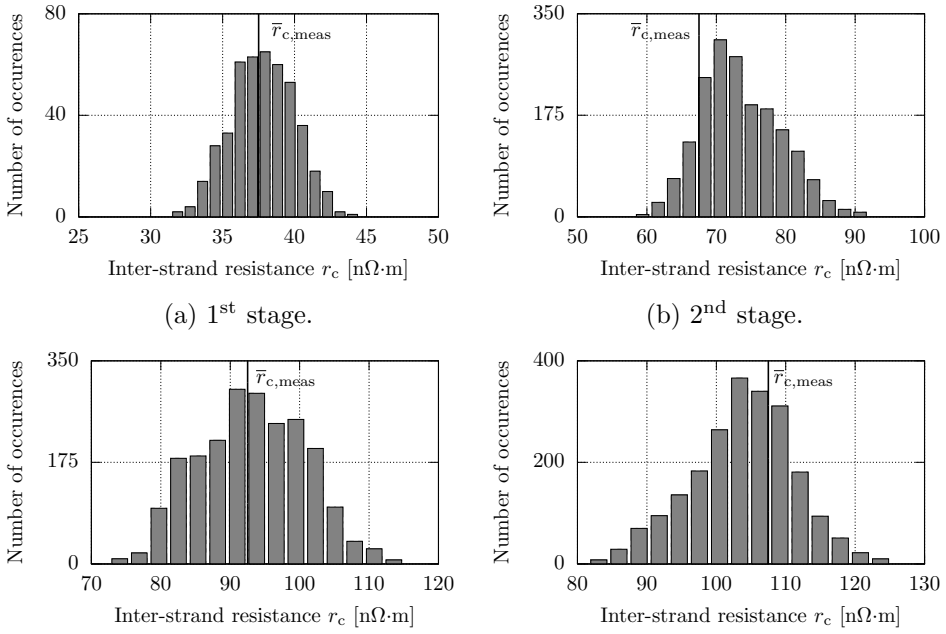

(a) 1st stage.

(b) 2nd stage.

(c) 3rd stage.

(d) 4th stage.

Figure 4.11: EUTF3-EAS sample, histograms of the computed contact resistances compared with the measured mean value.

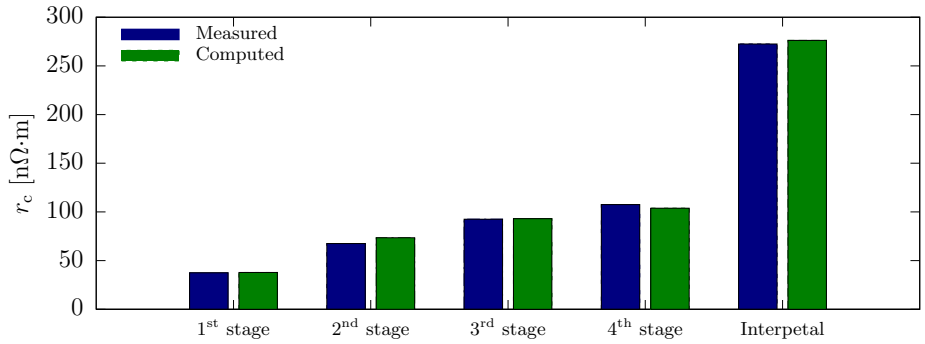

Figure 4.12: EUTF3-EAS sample, comparison between the measured and the computed inter-strand resistances

of 1500 samples for each stage has been chosen to limit the computational effort. These latter samples have been chosen randomly across the cable cross-section to be representative of the overall conductor behavior. The computed histograms of the inter-strand resistances of EUTF3-EAS sample are reported in Figure 4.11 for the measures of different cabling stages. In each histogram, the measured value is reported as a reference, showing that this value is well within the standard gaussian dispersion. A direct comparison between the measured resistances and the average value of the computed ones, is presented in Figure 4.12.

Since no measured values for the inter-strand resistances with normal-conducting strands were available, no computation of them has been made, even though their contribute to the inter-strand resistances of the superconducting strands has been accurately taken into account. If a cable were made of superconducting strands only, the model results would indeed be independent on the cable discretization into longitudinal cable elements because superconducting strands can be modeled with short circuits. Since this is not the case of EUTF3-EAS, the discretization of the cable into a finite number of longitudinal elements gives rise to a discretization error, due to the fact that, in the model, all the contacts on the cable sections between two adjacent longitudinal elements are grouped into an equivalent conductance, as shown in Figure 4.13.

Thus, a sensitivity analysis has been carried out to check the effect of the cable longitudinal discretization. To this purpose, the cable has been divided into an increasing number of longitudinal elements Δz long, to check the variation of the computed inter-strand resistance. Figure 4.14 reports the average inter-strand resistance as a function of the length of the cable longitudinal elements. The resistances are reported as normalized values, by referring them to the value computed at the minimum length Δz. The dependence of the average resistance on the longitudinal length is weak for the first stage and stronger for the fourth stage, in agreement with the fact that the first stage resistances rely mainly on the direct contact between superconducting strands and therefore are dominated by far by the distributed contact resistance value $R_{\mathrm{st}}^{\mathrm{d}}$. As it can be seen, the error is within 5% even if a very rough discretization is adopted ($\Delta z = 0.04$ m, corresponding to 10 longitudinal elements). The figure also shows that this error tends asymptotically to zero as the length of the longitudinal elements is comparable with the diffusion length l_{diff} (Eq. 4.6), that in the present case is about 10 mm considering RRR = 100 for the copper.

4.5.3 CICC Termination RF33

An extensive numerical analysis [21] has been performed on a CICC termination built with the ITER-type CICC RF33 [154], used to manufacture the Russian RFTF1 SULTAN sample [43] and tested in 2009 in the JORDI device [45]. In such device, the termination sample is tested at liquid helium temperature in the absence of background magnetic field and mechanical load. A set of shunt resistors in the cryostat permits to feed individual cable strands and/or bundles of strands (*channels*) with controlled currents, while other *measurement channels* take the voltage signals

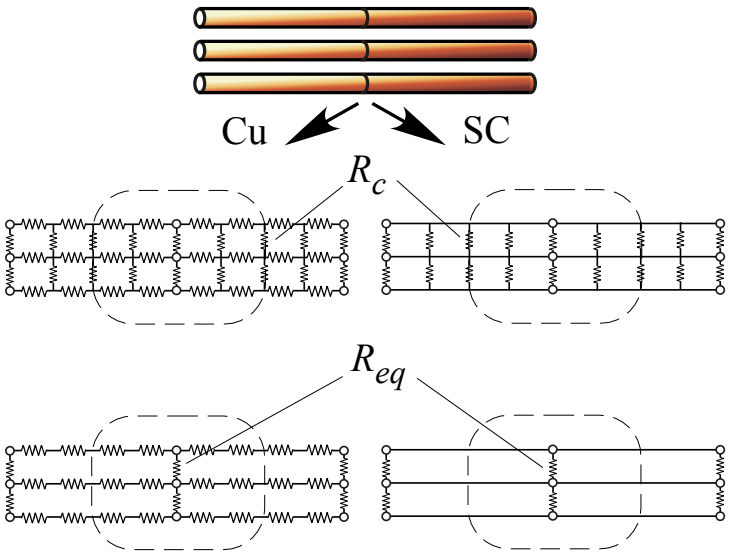

Figure 4.13: Discretization of a cable segment into a finite number of longitudinal elements. Top: view of three Cu or SC strands divided into two longitudinal elements. Centre: sketch of part of the equivalent lumped network (in steady-state). Bottom: the transverse contact resistances across each cable section are grouped into an equivalent resistance R_{eq}.

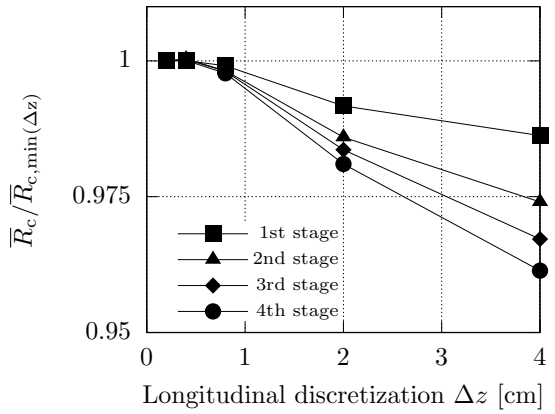

Figure 4.14: EUTF3-EAS sample. Average adimensional inter-strand resistance as a function of the length of each cable longitudinal element.

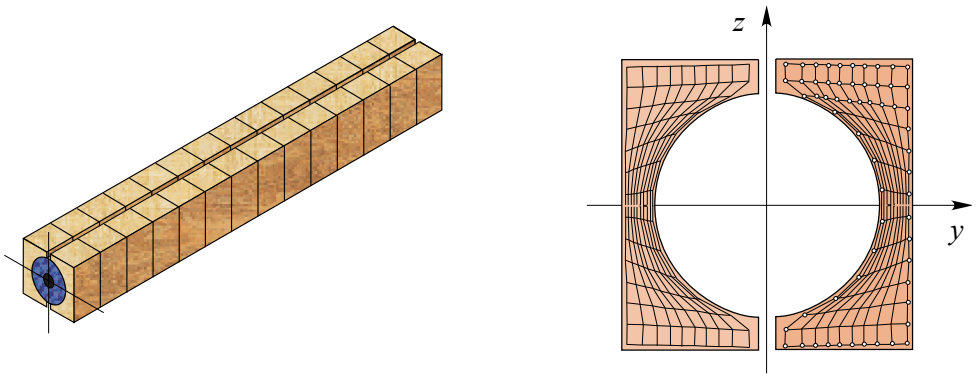

(a) Pictorial view. (b) Mesh of the saddle cross-section.

Figure 4.15: RF33 cable JORDI sample.

which are then used to obtain the resistances.

RF33 conductor parameters are the same as EUTF3-EAS sample (see Table 4.1). The JORDI sample was produced using a virgin unreacted RF33 cable segment. Before the heat treatment, at one end the cable bundles were opened and $N_{\mathrm{ch}} = 150$ channels were created, each corresponding to a 2^{nd} stage bundle, characterized by the cabling scheme $(2\,\mathrm{SC} + 1\,\mathrm{Cu}) \times 3$. After the heat treatment, the jacket and the stainless steel wraps on the cable outer surface only were removed, together with the strand Cr coating. The termination saddle was made of an array of 14 pairs of copper blocks with an overall length of 391 mm with intermediate insulating layers, as shown in Figure 4.15a. The external sizes of the cross-section of each block are 25 and 51 mm, whereas the seat diameter is 39.5 mm. In Figure 4.15b a sketch of the equivalent network mesh of the saddle is reported, showing only the network transverse branches. The external surface of the saddle was coated with SnPbBi low melting superconducting alloy, to create a reference equipotential surface.

Two types of measurements were taken by CRPP on this sample: the *inter-strand resistances* and the *channel equivalent resistances*.

Inter-Strand Resistance Measurement

The inter-strand resistances were taken on a selection of 10 cable strands, chosen on the basis of their cabling stage and identified by a letter corresponding to the petal (A to F), and a number, corresponding to the third stage bundle (1 to 5), as shown in Figure 4.16. The resistances were measured by selecting one of these strands, identified by D1, as common return lead for all measurements and feeding in turn the other ones. In this way, a 9×9 self and mutual resistance matrix $\mathbf{R} = (R_{i,j})$ was obtained, as shown in Table 4.2a. The strand combinations give rise to to four *classes* $\mathcal{S}_k$, $k = 1 \ldots 4$, of topologically equivalent measurements:

1. strands in the same petal, in adjacent third stages (D1D2),

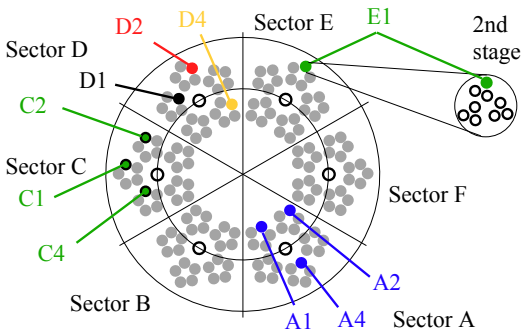

Figure 4.16: Sketch of the location of the 2nd stage bundles whose strands have been selected for the inter-strand resistance measurement. Each sector corresponds to a cable petal.

Table 4.2: Interstrand resistances measurement: resistance matrices (nΩ).

(a) Measured resistances $R_{i,j_{\text{meas}}}$.

	A1	A2	A4	C1	C2	C4	D2	D4	E1
A1	8.45	5.13	5.88	4.29	3.90	3.97	3.11	3.31	3.84
A2	5.29	9.06	5.79	4.10	3.90	3.98	3.18	3.13	3.83
A4	5.18	5.44	9.21	3.92	3.88	4.00	3.10	3.36	3.85
C1	3.84	3.91	4.25	7.93	4.35	4.29	3.10	3.10	3.40
C2	2.90	3.86	4.22	4.44	7.98	4.42	3.21	3.23	3.30
C4	3.43	3.87	4.06	4.19	4.35	8.42	3.10	3.23	3.43
D2	3.08	3.11	3.39	3.15	3.14	3.22	6.62	3.08	3.10
D4	3.28	3.23	3.60	3.16	3.25	3.31	2.98	6.72	3.16
E1	3.72	3.66	4.16	3.28	3.26	3.34	3.05	3.18	7.99

(b) Mean value of computed resistances.

	A1	A2	A4	C1	C2	C4	D2	D4	E1
A1	8.30	4.79	4.66	3.94	3.94	3.93	3.09	3.41	3.94
A2	4.79	8.26	4.66	3.94	3.94	3.93	3.09	3.41	3.94
A4	4.66	4.66	8.31	3.94	3.94	3.93	3.09	3.41	3.94
C1	3.94	3.94	3.94	7.79	4.36	4.17	3.09	3.41	3.70
C2	3.94	3.94	3.94	4.36	7.81	4.18	3.09	3.41	3.70
C4	3.93	3.93	3.93	4.17	4.18	7.80	3.09	3.41	3.69
D2	3.10	3.10	3.10	3.12	3.12	3.11	6.27	3.12	3.08
D4	3.41	3.41	3.41	3.41	3.41	3.41	3.09	6.82	3.41
E1	3.94	3.94	3.94	3.70	3.70	3.69	3.09	3.41	7.77

2. strands in the same petal, in not adjacent (opposite) third stages (D1D4),

3. strands in adjacent petals (D1C1, D1C2, D1C4 and D1E1) and

4. strands in not adjacent petals (opposite) (D1A1, D1A2 and D1A4).

Since different values of resistances $R_{i,j}$ are measured also among strands of the same class $\mathcal{S}_k$, due to the different geometries determined by the bundles initial angular phases, a Montecarlo numerical approach has been adopted, simulating a set of $N_{\text{ph}} = 50$ identical terminations differing from each other only as regards their variable initial phases $\boldsymbol{\Theta}_n$, with each array entry randomly generated to be uniformly distributed in $]-\pi;\pi]$. The mean value of the computed resistance matrix is reported in Table 4.2b. The agreement between measured and computed values can be considered very good, taking into account the measurement accuracy ($\leq 1\,\text{n}\Omega$ [45]) and the magnitude of the antisymmetric component of the measured matrix, whose entries are up to 13%, while they should be ideally zero.

The optimization strategy and the results assessment has been done considering the classes $\mathcal{S}_i$, rather than the whole resistance matrix $\mathbf{R}$. The assumption is that, considering a large set of terminations, the mean values of the self and mutual resistances $R_{i,j}$ tend to common limits depending only on the classes the strands i

Table 4.3: Measured class resistances matrices.

(a) Class resistances $R^c_{k,s_{meas}}$ [nΩ].

Class	1	2	3	4
1	6.62	3.03	3.13	3.16
2	3.03	6.72	3.20	3.32
3	3.13	3.20	8.08	3.89
4	3.16	3.32	3.89	8.91

(b) Class data range $\Delta R^c_{k,s_{meas}}$ [%].

Class	1	2	3	4
1	0.0	3.3	5.4	9.8
2	3.3	0.0	6.6	14.2
3	5.4	6.6	6.1	35.7
4	9.8	14.2	35.7	8.5

and j belong to:

$$\lim_{N_{\mathrm{ph}}\to\infty} \mathrm{mean}(R_{i,j}) = R^{\mathrm{c}}_{k,s};\ \forall i \in \mathcal{S}_k \text{ and } \forall j \in \mathcal{S}_s, \tag{4.10}$$

since, on the average, the mean distance and the number of contacts between couples of strands belonging to the same class is the same. Therefore, it is possible to define a matrix of the self and mutual resistances between classes $\mathbf{R}^{\mathrm{c}} = \left(R^{\mathrm{c}}_{k,s}\right)$ for both the computed and the measured values.

To evaluate the range of variation of the measured samples, the *measured data class range* $\Delta R^{\mathrm{c}}_{k,s_{\mathrm{meas}}}$ is defined:

$$\Delta R^{\mathrm{c}}_{k,s_{\mathrm{meas}}} = 100 \cdot \frac{\max(R_{i,j_{\mathrm{meas}}}) - \min(R_{i,j_{\mathrm{meas}}})}{R^{\mathrm{c}}_{k,s_{\mathrm{meas}}}}, \tag{4.11}$$

where $R^{\mathrm{c}}_{k,s_{\mathrm{meas}}}$ is the mean of the measured samples $R_{i,j}$ in which $i \in \mathcal{S}_k$ and $\forall j \in \mathcal{S}_s$. $\Delta R^{\mathrm{c}}_{k,s_{\mathrm{meas}}}$ is related to the dispersion of measured values that should be equal on the average: large values of it mean measured data relatively unreliable to be compared with the average computed data. Table 4.3 reports the measured values $R^{\mathrm{c}}_{k,s_{\mathrm{meas}}}$ between the strands of the different classes and the corresponding measured class ranges: values about few percent or ten percent are present, with the exception of mutual resistances between strands of class 4 and 3, for which 35.7% is reached. A null value indicates that only one measured sample was available for such class.

The elementary inter-strand resistances have been optimized minimizing a second parameter, the *computed data class error* $\Delta R^{\mathrm{c}}_{k,s_\sigma}$:

$$\Delta R^{\mathrm{c}}_{k,s_\sigma} = 100 \cdot \frac{R^{\mathrm{c}}_{k,s_{\mathrm{mean}}} - R^{\mathrm{c}}_{k,s_{\mathrm{meas}}}}{\sigma_{k,s}}, \tag{4.12}$$

in which $\sigma_{k,s}$ is the standard deviation of the computed samples $R_{i,j}$ in which $i \in \mathcal{S}_k$ and $\forall j \in \mathcal{S}_s$. $\Delta R^{\mathrm{c}}_{k,s_\sigma}$ is related to the probability that a given measured value has to be computed considering the random array $\boldsymbol{\Theta}$. This probability depends on the type of statistical distribution of the computed data, however its value is expected to be high when the measured value is close to the average computed one. As an example, in the presence of a gaussian distribution, a measured value

Table 4.4: Computed class resistances matrices optimized minimizing the computed data class error $\Delta R^{\mathrm{c}}_{k,s_\sigma}$.

(a) Class resistances $R^{\mathrm{c}}_{k,s_{\mathrm{comp}}}$ [nΩ].

Class	1	2	3	4
1	6.22	3.09	3.09	3.09
2	3.09	6.82	3.41	3.41
3	3.09	3.41	7.79	3.94
4	3.09	3.41	3.94	8.29

(b) Class data error $\Delta R^{\mathrm{c}}_{k,s_\sigma}$ [%].

Class	1	2	3	4
1	112	-27	21	34
2	-27	-42	-105	-46
3	21	-105	100	-25
4	34	-46	-25	210

Table 4.5: Computed class resistances matrices optimized fitting the results of an individual termination.

(a) Class resistances $R^{\mathrm{c}}_{k,s_{\mathrm{comp}}}$ [nΩ].

Class	1	2	3	4
1	6.81	3.38	3.39	3.39
2	3.38	7.46	3.73	3.73
3	3.39	3.73	8.46	4.28
4	3.39	3.73	4.28	8.98

(b) Class data error $\Delta R^{\mathrm{c}}_{k,s_\sigma}$ [%].

Class	1	2	3	4
1	-49	-152	-113	-100
2	-152	-288	-249	-192
3	-113	-249	-123	-178
4	-100	-192	-178	-22

corresponding to $\Delta R^{\mathrm{c}}_{k,s_\sigma} \geq 200$ has a probability to be computed of 2.25%. Table 4.4 reports the computed resistances $R^{\mathrm{c}}_{k,s_{\mathrm{comp}}}$ and the class error $\Delta R^{\mathrm{c}}_{k,s_\sigma}$ obtained after the optimization of the elementary inter-strand resistances. The histograms of the computed class inter-resistances are reported in Figure 4.17. In any case the the measured mean values are within the estimated variation of the resistances given by the Montecarlo simulation.

The effectiveness of the Montecarlo approach can be demonstrated also considering the results of another Montecarlo simulation reported in Table 4.5. In this case, The elementary inter-strand resistances optimization in this case has been performed to better fit the results of an individual termination, corresponding to a given $\boldsymbol{\Theta}$ value. The elementary contact resistances have been optimized by minimizing the RMS error between the computed and measured diagonal entries of the resistance matrix $\mathbf{R}$. With this second set of parameters, the top value of $|\Delta R^{\mathrm{c}}_{k,s_\sigma}|$ is increased, and the average $|\Delta R^{\mathrm{c}}_{k,s_\sigma}|$ value passes from 61% up to 153%, which means that the previous model parameters give results that can be measured with larger probability.

Channel Equivalent Resistances

Further with respect to similar measurements on CICC samples, in the present case the resistances towards the termination resistive saddle were also measured. To this

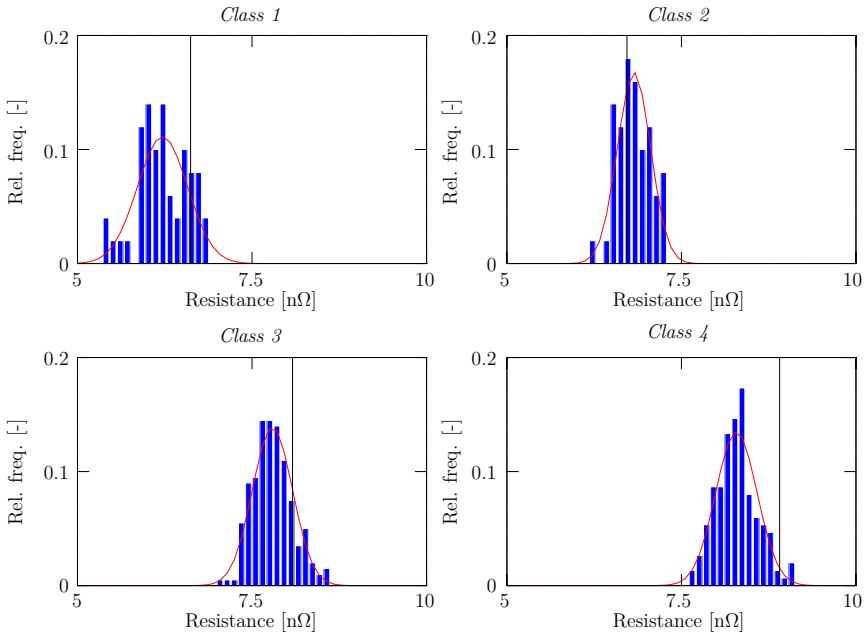

(a) Self resistances.

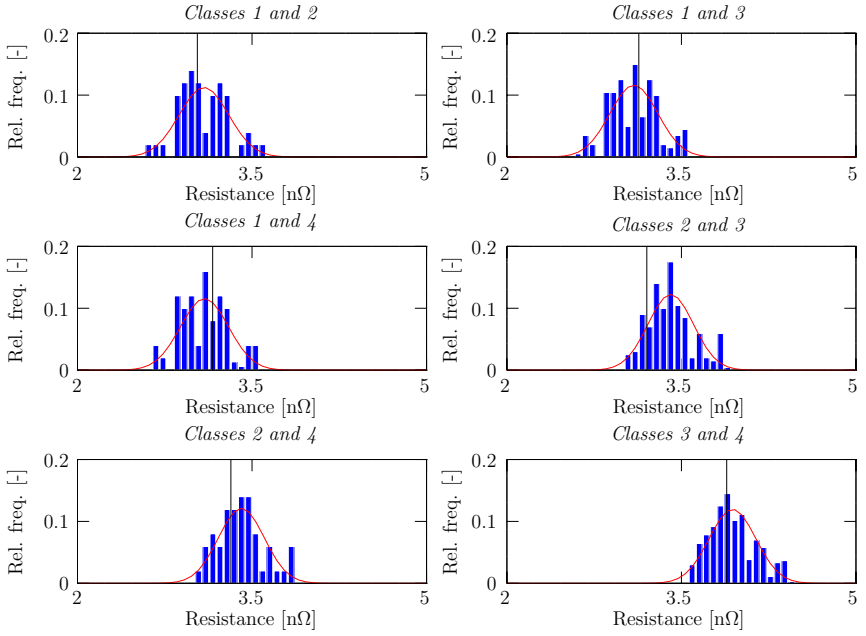

(b) Mutual resistances.

Figure 4.17: Computed resistances histograms and comparison with the measured values, marked by a vertical line.

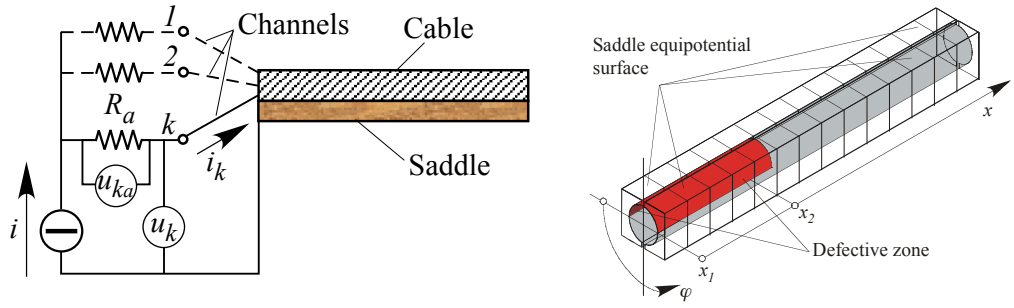

(a) Schematic of the electric circuit used.

(b) Sketch of the assumed defect.

Figure 4.18: Channel equivalent resistances analysis.

purpose, all the channels were simultaneously fed with nominally identical currents i_k, thanks to a set of calibrated additional resistances in series between the power supply and the channels leads. The voltage across the relevant additional resistance was used to measure the k^{th} channel current; the voltage u_k between the channel lead and the saddle gave the equivalent resistance. The schematic of this measurement circuit is reported in Figure 4.18a.

Considering the termination under test as an equivalent linear resistive network N_{ch}-dipole, having the saddle as common return node for all its ports, the relation between the arrays of channel currents $\mathbf{I}$ and voltages $\mathbf{U}$ can be expressed as:

$$\mathbf{U} = \mathbf{R}^* \cdot \mathbf{I}, \tag{4.13}$$

where $\mathbf{R}^* = \left(R^*_{k,s}\right)$ is the matrix of the self and mutual resistances between channels. In the presence of all equal currents i_k the channel equivalent resistance can therefore be expressed as:

$$R_{\text{ch}_k} = \sum_{s=1}^{N_{\text{ch}}} R^*_{ks}, \tag{4.14}$$

where R^*_{ks} is the generic entry of the N_{ch}-dipole resistance matrix $\mathbf{R}^*$.

The same elementary inter-strand resistances determined with the previous Montecarlo simulation are used to model the channel equivalent resistances, although in this case such statistical approach is not necessary. The channel equivalent resistances indeed depend significantly only on θ_1, the first entry of $\boldsymbol{\Theta}$. θ_1 is the initial angular phase of the petal and it affects directly the angular relative positions between all the petals and the saddle. Its value has been adjusted to fit the measured channel resistance distribution. The impact of θ_1 on the inter-strand resistances statistical distributions described in the previous section is negligible.

The distribution of the measured R_{ch_k} is shown in Figure 4.19a, where it is compared with the computed values. In the present case, each petal corresponds to 25 channels. As it can be seen, the computed channel resistances match well the lower

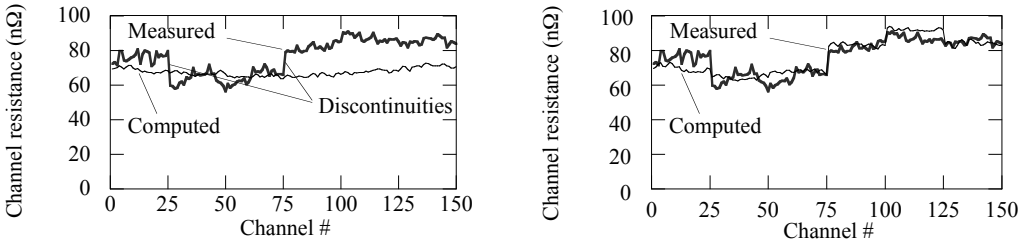

(a) Standard model.

(b) Model with one defect.

Figure 4.19: Measured channel equivalent resistances as a function of the channel number and computed values.

measured values, however the measured values show discontinuities for channels 25 and 75, corresponding to petals 2 and 3, not reproduced by this model. With the THELMA standard model, in which a uniform saddle-strand contact resistance was present and $R^{\mathrm{s}}_{\mathrm{st}} = R^{\mathrm{s}}_{\mathrm{sdl}}$, there was no way to get a distribution of channel resistances showing these discontinuities.

An alternative hypothesis is to consider $R^{\mathrm{s}}_{\mathrm{st}}$ independent from $R^{\mathrm{s}}_{\mathrm{sdl}}$ and to admit a non uniform saddle-strand contact resistance, from here on referred to as *defect* [17]. It must be clear that this assumption is only a functional hypothesis based on the THELMA model: any extrapolation of the quality of the saddle-strand contact in the real termination should be verified with further electrical tests and visual inspections. On the other hand, similar features of the measured data may be due also to other unknown characteristics of the measurement circuit or the sample, e.g. a non perfectly equipotential saddle surface.

In THELMA, a defect of the saddle surface is represented in terms of one or more saddle additional resistances $R^{\mathrm{s}}_{\mathrm{sdl_a k}}$ associated to rectangular domains $\mathcal{D}_k$ of the saddle seat surface. These resistances are independent on the $R^{\mathrm{s}}_{\mathrm{sdl}}$ parameter, which is considered uniform for any contact at the saddle surface. Each domain is limited by its lower and upper longitudinal coordinates x_{1_k}, x_{2_k} and angular coordinates around the saddle seat, φ_{1_k} and φ_{2_k}. With this feature, five new degrees of freedom are therefore added to the model per each new defective zone. Since the target of this analysis is only to give one possible interpretation of the experimental results a model as simple as possible has been considered, in which a single defective zone is present at the contact surface with $x_1 = 0$, $x_2 = 151$ mm, $\varphi_1 = \pi$, $\varphi_2 = 2\pi$ rad, as shown in Figure 4.18b. The resulting channel resistances are plotted in Figure 4.19b. The adopted value of additional resistance $R^{\mathrm{s}}_{\mathrm{sdl_a k}}$ is so high that, in the zone, a negligible conductance existed between saddle and strands. As it can be seen, discontinuities are now present also among the computed resistances and the two curves are much closer to each other. This defect lead to only negligible variations to the inter-strand resistance measurements described previously, since the impact of the saddle surface defect is negligible in such case.

Part III

Case Studies

Chapter 5

Analysis of the Voltage-Temperature Characteristic of a CICC sample

The performance characterization in complex cables like CICC samples is typically done through the measurement of voltage-current or voltage-temperature characteristics. However, in some cases the understanding of the experimental results is not an easy task. The voltages are generally measured on the steel jacket outer surface, but the relationship between them and the actual voltages acting on the superconducting strands is not trivial. Scattered positive and negative voltages are indeed measured on the jacket even if no resistive transition has occurred in the superconducting sample. Moreover, when transport current is ramped, both positive and negative voltage drifts can be measured, depending on the voltage tap location.

In this Chapter, the experimental data of a voltage-temperature characteristic measured on a ITER TF CICC sample is analyzed as a validation of the coupled thermal-electromagnetic THELMA code. First, the mechanism producing the scattered jacket voltages is described thorough a revised electromagnetic-only modeling of the conductor. Then, the coupled thermal-electromagnetic modeling is used to reproduce both electrical and thermal measurements, showing a very good agreement.

5.1 The SULTAN Facility

The analyses presented in this Chapter are based on measurements performed at the SULTAN facility in Villigen (CH) [39], where ITER CICC samples are tested and characterized. A typical SULTAN sample is made of two flanked straight CICC segments, called *legs*, connected in series by a joint and to the power supply by two terminations. The overall sample length is about 3.6 m. Since the cooling helium flows from the joint to the terminations in both legs, the flow is counter-current in one leg and concurrent in the other, with respect to the transport current. The background magnetic induction is provided by three pairs of superconducting coils, that generate a maximum induction of about 11 T along the sample 450 mm long *high-field zone*. A transport current up to 100 kA is supplied to the sample by a superconducting transformer.

One of the typical performance evaluations done in SULTAN is the measurement of the *voltage-temperature characteristic*. At a given electromagnetic operating condition, i.e. given magnetic field and transport current, the voltage along the cable is measured at different levels of forced-flow helium temperature, in order to assess the so-called *current-sharing temperature* T_{cs}, defined as the temperature at which the voltage along the cable reaches a threshold value. This threshold is conventionally set to $10\,\mu$V/m, similarly to the voltage-current characteristic measurements in the individual superconducting strands (see Section 1.4). To better evaluate the voltage distribution along the jacket outer surface, in SULTAN several groups of voltage taps referred to as *crowns* or *stars* are placed at given locations along the sample [42]. Each crown is composed by six independent voltage taps equally spaced around the outer jacket surface. In addition, Cernox sensors are placed in given locations along the jacket outer surface to perform a calorimetric estimation of T_{cs} [42].

5.2 Sample and Test Description

In the following, the analysis of TFPRO2 conductor re-test is presented [43]. The conductors OST1 and OST2, both made by internal-tin Nb_3Sn superconducting strands, form respectively the right and left leg of the sample. The complete sample is sketched in Figure 5.1 together with the electrical and thermal instrumentation. The *free cable* length, that is the length of the sample except the terminations and the joint, is about 2.6 m. Considering both legs, 22 temperature sensors and 38 voltage taps are present [42]. The voltage taps includes 14 voltage pairs and four crowns, two of them at the ends of the free cable of each leg ($S_{\mathrm{c},1}-S_{\mathrm{c},3}$ and $S_{\mathrm{c},2}-S_{\mathrm{c},4}$) and two located astride the high field zones ($S_{\mathrm{j},1}-S_{\mathrm{j},3}$ and $S_{\mathrm{j},2}-S_{\mathrm{j},4}$). Five couples of temperature sensors per leg are present, plus one sensor at each pipe inlet. The discrepancy among each couple of sensors placed in the same leg at the same location is < 10 mK in the worst case [42]. The signals of sensors T_1 and T_7 on the left leg have been discarded because of their erratic behavior, probably because the adhesive tape bonding to the jacket/pipe became loose [42].

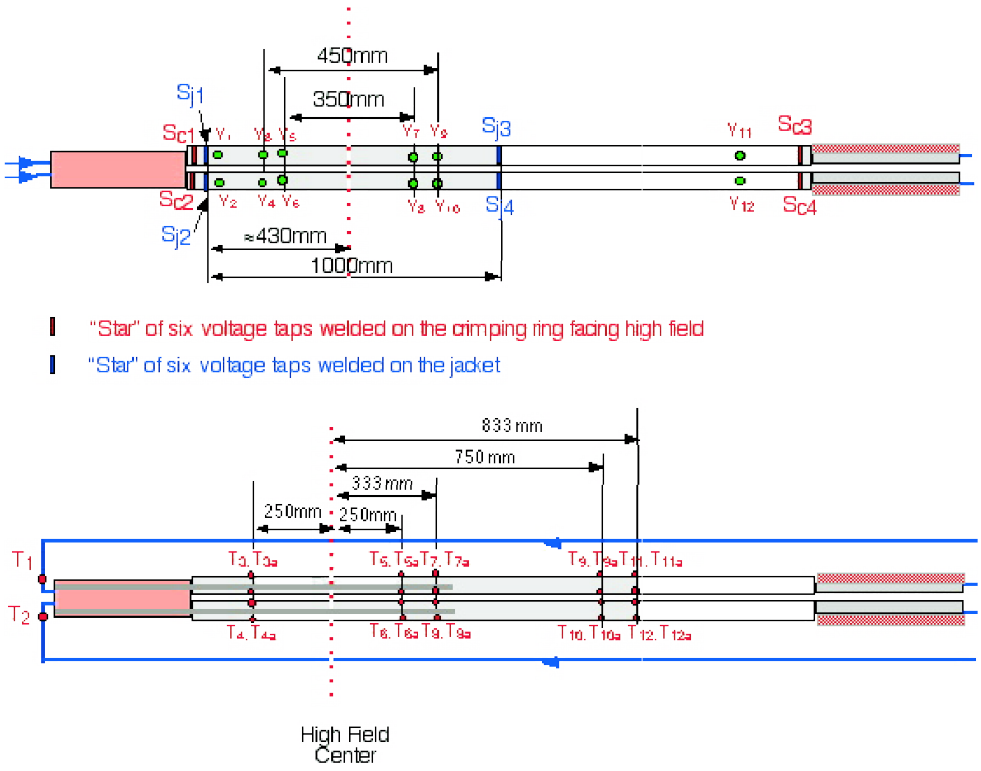

Figure 5.1: Sketch of the SULTAN sample and its instrumentation, courtesy of Denis Bessette, ITER/IO.

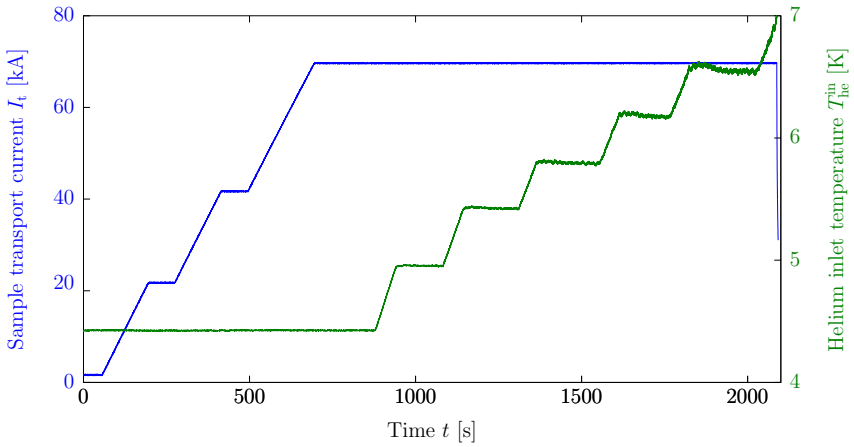

Figure 5.2: Sample transport current I_t and helium inlet temperature T_{he}^{in} as a function of time during the T_{cs} test TFPRO2D111005.

The central channel of the CICC is plugged by a 1.5 m long steel rod which extends into the high field region to force the flow in the strand bundle and reduce the temperature and mass flow rate gradients over the cable cross section [43]. A local heater[1], installed on the left leg (OST2) at a distance of one cm after the joint, is used to unbalance the temperature among the legs and hence allow reaching high voltage in OST2. In these conditions, larger discrepancies, up to 50 mK, can be found between the couples of sensors of T_3 vs. $T_{3,\mathrm{a}}$ and T_5 vs. $T_{5,\mathrm{a}}$, probably due to an uneven heat deposition in the sample outer surface by the heater [42].

During the test considered for the present analysis, the transport current is ramped to the nominal value of 68 kA with intermediate steps at 20 and 40 kA, as reported in Figure 5.2. As shown in the same graph, the helium inlet temperature is varied through subsequent steps after the electromagnetic conditions are stabilized. The local heater on the left leg has been switched on, bringing the initial temperature in OST2 up to about 6 K, compared to the initial temperature of about 4.425 K at the helium inlet and on the right leg.

5.3 Electromagnetic Modeling

The electromagnetic-only modeling of TFPRO2 had already been performed with an old version of the THELMA code and presented in [35]. In that version, a good fit between measured and computed electrical quantities was found with an excessively large value of the steel jacket longitudinal electrical resistivity. The validation of the THELMA new thermal model gave the opportunity to review the model parameters with the coupled thermal-electromagnetic analysis, presented in the following section.

The left leg, exposed to the highest temperature due to the local heater, is modeled along the complete free cable length, with a discretization of about 0.9 cm per longitudinal elements, corresponding to 300 elements. The cross-section is represented with the six petals and with 12 jacket elements (JE), suitably inductively coupled as explained in Section 3.3.2. As boundary conditions, the joint and the termination are represented by an equivalent lumped network computed on the basis of the joint/termination geometry. The network representing the jacket-joint termination is a star of resistors R_{JT}, connecting each JE to a reference node of the joint/termination lumped network, as shown in Figure 5.3. The background field and the inductive coupling exerted by the right leg and by the superconducting coils have been taken into account thanks to suitable current loops. It must be highlighted that the choice of a resistive-only lumped network to represent the joint/termination and the discretization in six petals rather than in smaller cable elements may lead to an inaccurate modeling of some inductive phenomena acting during the transport current ramps. However, the present analysis is more focused on the validation of the coupled thermal-electromagnetic model in particular during

[1] Polyimide heater, model Minco HK5162R52.3L12F [42].

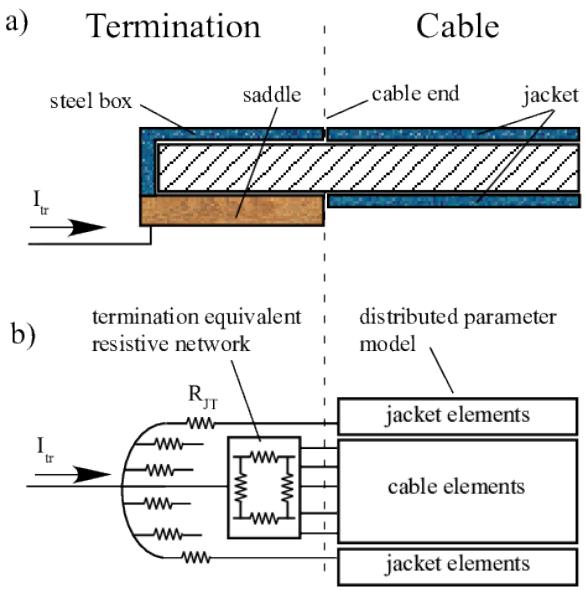

Figure 5.3: Electromagnetic modeling. a) Topology of the cable + jacket - termination interface. b) Equivalent networks to model the boundary conditions.

the helium temperature increase, therefore the level of detail used is accurate enough for such purposes.

The critical surface of the OST2 strand is described with the Twente/ITER scaling law [83] with the parameters reported in Table 2.3. A uniform value of the uniaxial strain $\varepsilon = -0.46\%$ has been assumed, obtained as a fitting parameter comparing the simulation results with experimental data. The n-index has been assumed correlated to the critical current with:

$$n = 1 + 3.535 \cdot I_{\mathrm{c}}^{0.339}, \tag{5.1}$$

as reported in [83], valid for $T > 6$ K. In the bare electromagnetic modeling, the conductor temperatures have been set considering the experimental data measured by the Cernox sensors.

As a reference value, the inter-petal resistance per unit length $r_{\mathrm{c}}^{\mathrm{pet}}$ has been set to about $1\,\mu\Omega$·m, in the range of the typical inter-petal resistance in the case of wrapped bundles [82]. As regards the jacket-petal resistance per unit length $r_{\mathrm{c}}^{\mathrm{jck-pet}}$, a reference value of about $2\,\mu\Omega$·m has been chosen, slightly larger than the values proposed in [82]. A sensitivity analysis on both parameters has been performed, as reported in the following.

5.3.1 Results

In Figure 5.4 and 5.5 the experimental and computed voltages between respectively the couple of crowns $S_{\mathrm{c},1}$ and $S_{\mathrm{c},3}$ and $S_{\mathrm{j},1}$ and $S_{\mathrm{j},3}$ are reported. The measured voltages have been smoothed with a moving average to reduce the experimental noise.

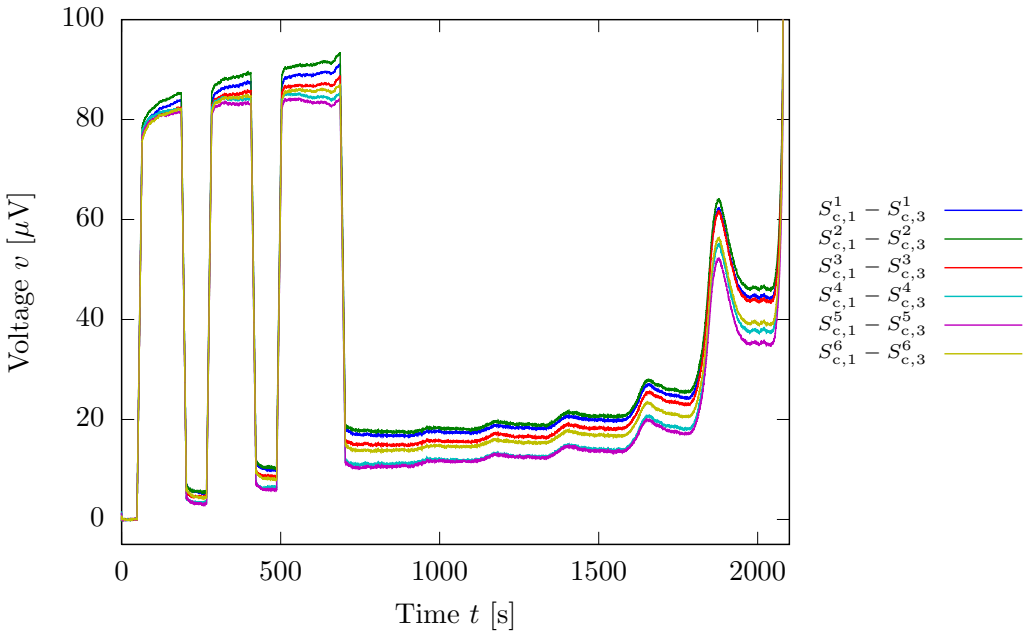

(a) Experimental.

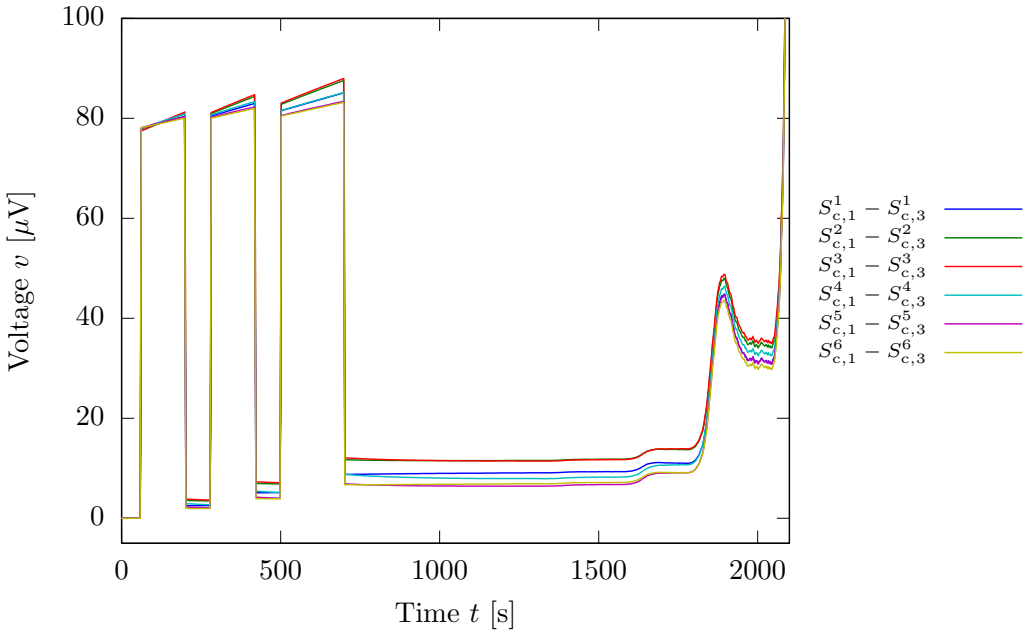

(b) Simulated.

Figure 5.4: Voltages between the six couples of taps of crowns $S_{c,1}$ and $S_{c,3}$ (whole sample), test TFPRO2D111005.

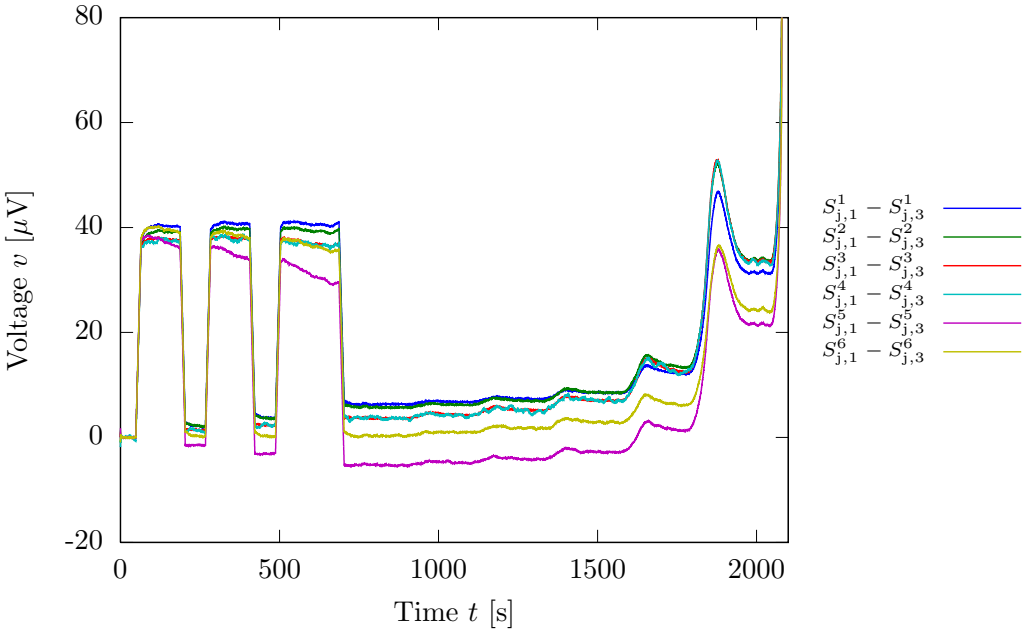

(a) Experimental.

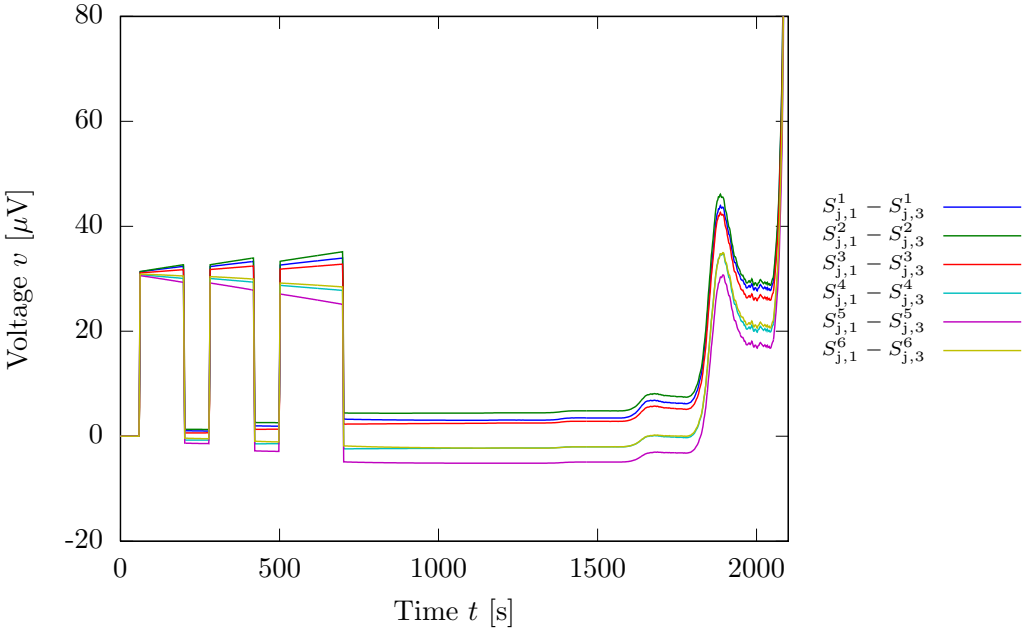

(b) Simulated.

Figure 5.5: Voltages between the six couples of taps of crowns $S_{j,1}$ and $S_{j,3}$ (high field zone), test TFPRO2D111005.

A post-processing has been instead applied on the computed voltages, to include the effect of the spurious inductive voltages acting on the voltage taps connections during the transport current ramps, as described in [139]. The computed voltages are in very good agreement with the experimental data, from both the qualitative and the quantitative point of view. The numerical model foresees a slightly uneven current distribution among the petals, with maximum variations of 7-8% compared to the petal average current.

Some sensitivity analyses have been performed to check the results correctness. For example, a sample with a different phase set has also been studied, showing only negligible differences. More detailed studies have been performed regarding the numerical convergence of the results and the jacket voltages dispersion.

Numerical Convergence

To test the numerical stability of the results, discretizations in 150 and 600 longitudinal elements have also been considered. In particular, both the cable computed losses and voltages have been analyzed. Indeed, the cable losses are the input of the thermal model, and a check of their correctness and numerical stability should be performed before considering the coupled THELMA code, as explained in the following section.

As regards the cable losses, only negligible differences can be found, since the mean relative differences among the reference case with 300 elements and the cases with 150 and 600 elements are in any case less than 0.1%. The same conclusion applies to the computed voltages astride the high field zone (crowns S_{j}), since the maximum difference between the different discretizations is in any case lower than $0.1\,\mu$V, less than the experimental accuracy. As regards the computed voltages on the crowns S_{c}, minor differences are visible, as reported in Figure 5.6a, since the discretization with 150 elements introduces an overestimation on all the voltages. However, it must be noted that the S_{c} signals, being measured near the joint and the termination, are affected by the boundary conditions, in particular on the value of R_{JT}, as shown in Figure 5.6b in the case of the model with 300 elements. Since no experimental data are available and simple analytical estimations cannot be performed on R_{JT}, it has been chosen equal $30\,\mu\Omega$ to better fit the measured voltages.

In conclusion, since a proper value for R_{JT} cannot be assessed a priori and because the qualitative behavior of the experimental signals is reproduced in any case, the results can be considered sufficiently stable with the discretization.

Jacket Voltages Dispersion

As already reported in [35], the voltage scattering among the signals of the couple of crowns S_{c} and S_{j} is very sensitive to the ratio between the distance among the voltage taps L_{taps} and the petal twist pitch t_{pet}. The voltage dispersion δv, defined as the maximum voltage difference between voltage taps of the same couple of crowns,

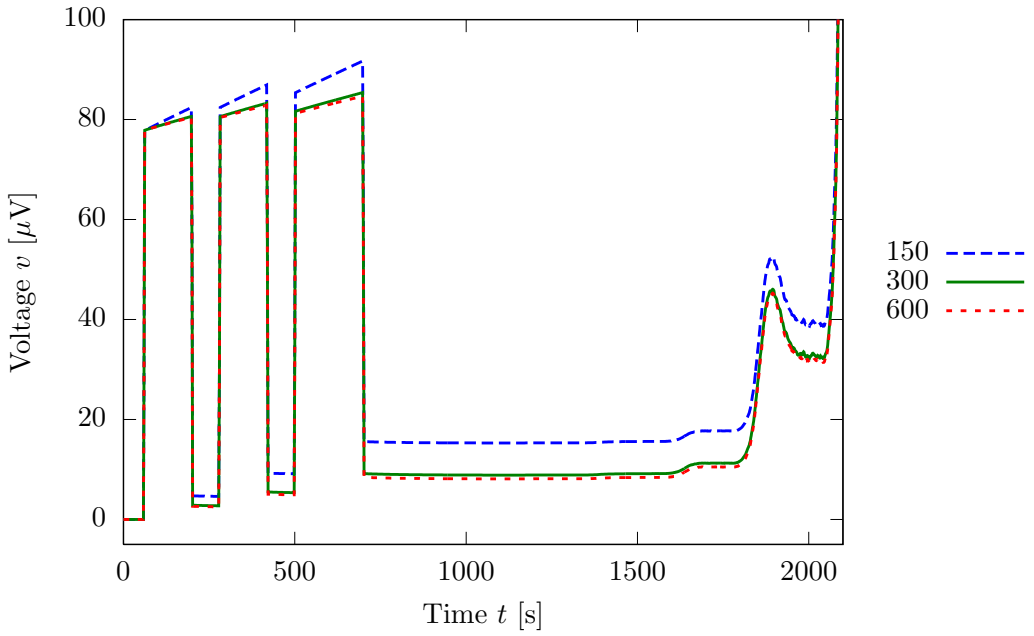

(a) Different cable longitudinal discretizations.

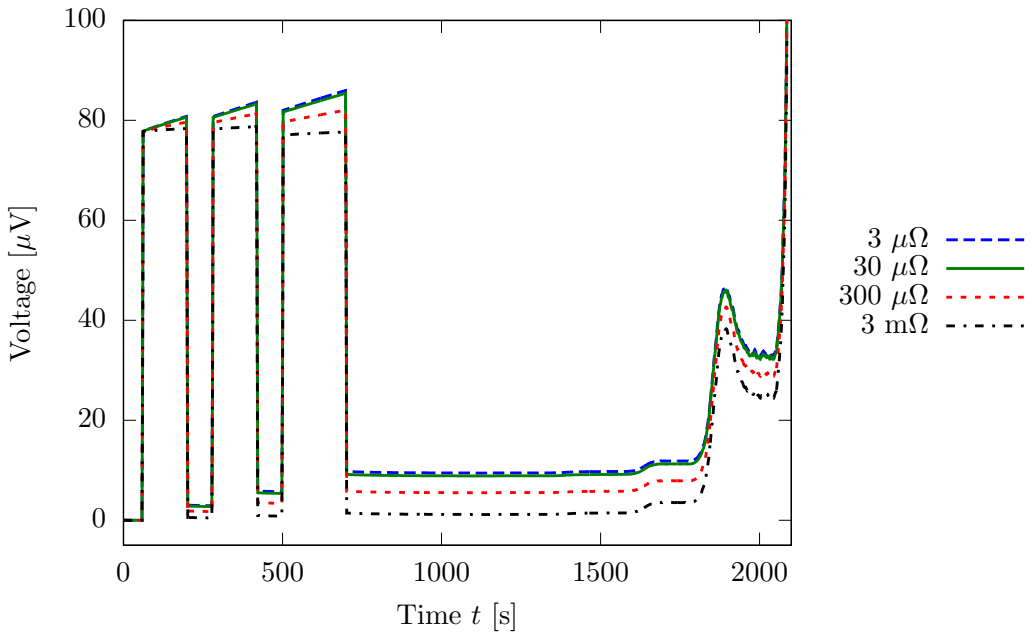

(b) Different values for jacket-joint/termination resistance R_{JT}.

Figure 5.6: Sensitivity analyses on the mean value of the computed voltages among the six couples of taps of crowns $S_{\mathrm{c},1}$ and $S_{\mathrm{c},3}$.

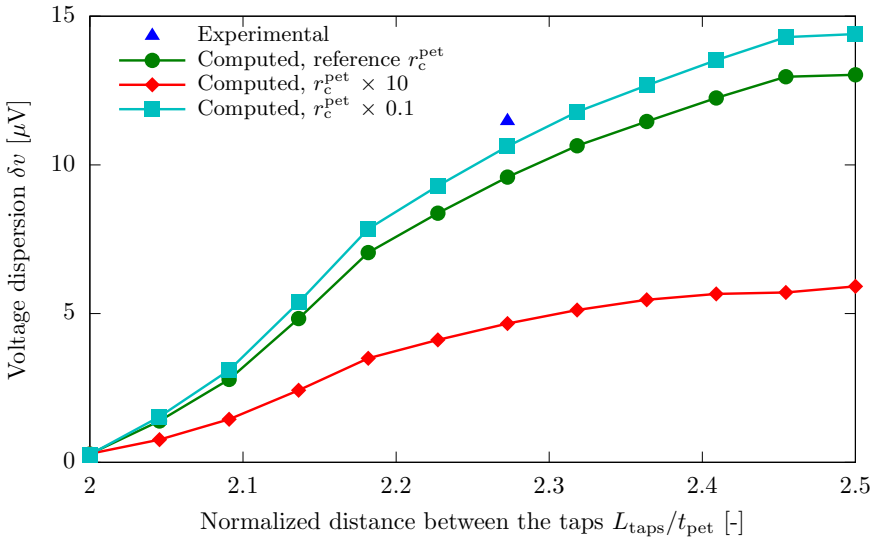

Figure 5.7: Voltage dispersion δv of the crown S_j as a function of the voltage taps distance L_{taps} compared to the petal twist pitch t_{pet}, in the case of different choices for the inter-petal resistance r_c^{pet}.

is shown in Figure 5.7 in the case of the signals S_j. δv is almost zero if:

$$L_{taps} = k\, t_{pet}, \quad k \in \mathbb{N}, \tag{5.2}$$

whereas the peak value is obtained for a distance:

$$L_{taps} = \left(k + \frac{1}{2}\right) t_{pet}, \qquad k \in \mathbb{N}. \tag{5.3}$$

In the present case, the nominal distance between $S_{j,1}$ and $S_{j,3}$ is 1 m and t_{pet} is 44 cm, thus an intermediate value for the voltage dispersion is obtained, in quite good agreement with the experimental value. Similar features can be found analyzing the crowns S_c.

In Figure 5.7 the dependence of δv on the inter-petal resistance per unit length r_c^{pet} is also shown. Large values of r_c^{pet} result in a much reduced voltage dispersion compared to experimental data, whereas only minor differences compared to the reference case can be found in the case of smaller r_c^{pet}. Similar features can be observed also varying the jacket-petal resistance per unit length $r_c^{jck-pet}$ instead of r_c^{pet}.

5.4 Coupled Thermal-Electromagnetic Analysis

The target of the coupled thermal-electromagnetic analysis is to reproduce not only the measured voltages, but also the temperature distribution along the sample. The

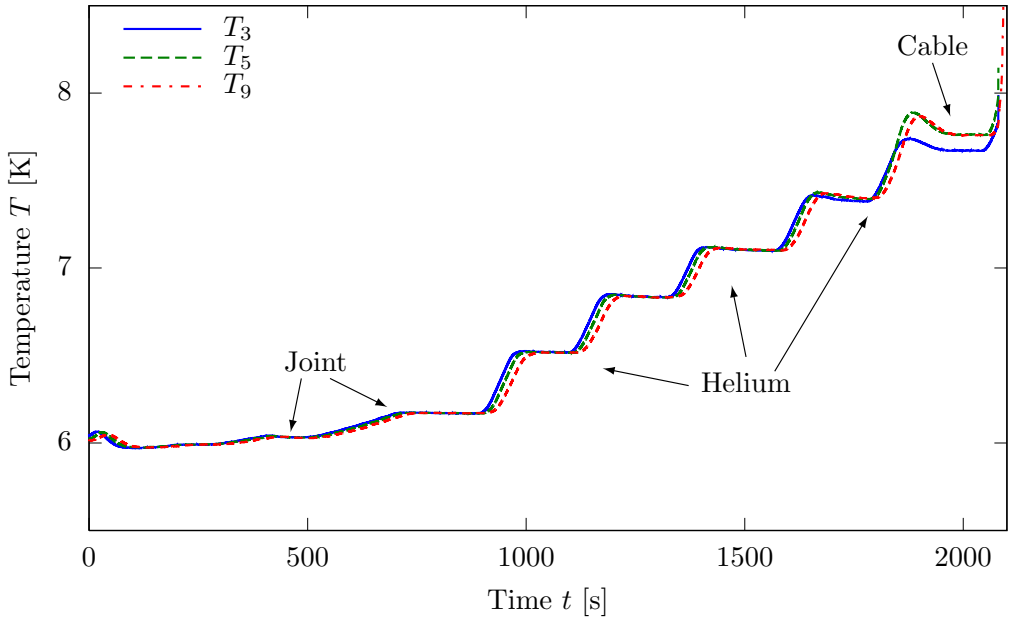

(a) Experimental from the Cernox sensors.

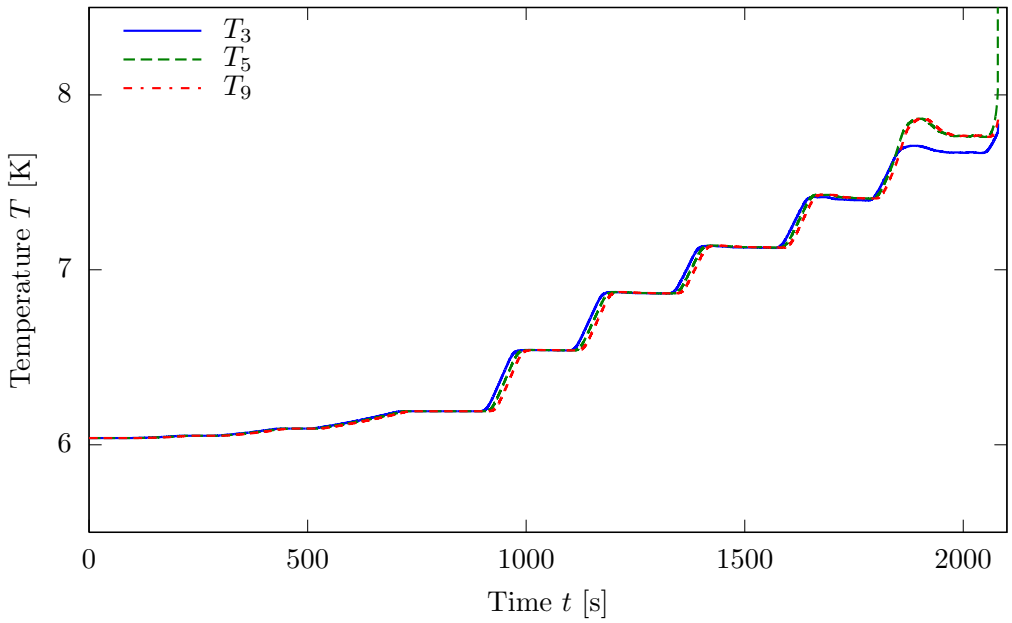

(b) Mean value of the computed cable temperatures at the Cernox sensors locations.

Figure 5.8: Temperatures on the left leg, test TFPRO2D111005.

temperatures measured on the left leg during the T_{cs} test by the Cernox sensors are reported in Figure 5.8a. Since two sensors are available at the same location along the sample, their mean value has been considered. Considering the helium flow direction, that is counter-current compared to the transport current, T_3 is measured just before the high field zone, T_5 just after it and T_9 at half meter from T_5, as shown in Figure 5.1. T_7 and T_{11} are not reported here, being very similar respectively to T_5 and T_9. The measured pressure of the inlet/outlet helium is 1.034 MPa, constant during the test. The mass-flow rate $\dot{m}$ ranges between 2.55 g/s before the transport current ramps and 2.2 g/s at the end of the test, with a mean value of 2.4 g/s that has been adopted for the numerical analyses. As described in the following, the impact of mass-flow rate on the simulation results has been checked with a sensitivity analysis. Since the central channel of the CICC is plugged for the large part of the sample length, the only void fraction internal to the petals has been taken into account for the helium channel cross-section area.

The free cable length has been discretized into six petals and 300 longitudinal elements, as it is in the electromagnetic model. Considering Figure 5.8a, four main heat sources can be identified:

1. the difference between T_{He}^{in} (Figure 5.2) and the temperature measured in the left leg is due to the heat deposited by the local heater placed close to the joint on the jacket outer surface. Since presently a thermal description for the jacket is not foreseen, a simplified model has been adopted. The Joule power produced by the DC heater current of 0.55 A on the heater resistance of 52.3 Ω has been evenly distributed on the six cable petals, with suitable heat-flow generators. Multiple generators have been used for each petal in order to correctly reproduce the heater length and position.

2. The first temperature increases, visible on all the sensors before 800 s, are not related a variation of the helium inlet temperature, but to the DC Joule losses produced by the transport current in the joint, that cause a small helium temperature increase that affects the sample downstream. To model this effect in the thermal network, the six petals have been extended also in the joint region. Since a thermal model for the copper blocks in the joint is not foreseen yet, a description similar to the heater has been adopted. The Joule losses produced by the time-depending transport current on the joint resistance modeled in the electromagnetic module have been evenly distributed both along the joint length and among the six petals with equivalent heat-flow generators.

3. The steps produced by the inlet helium temperature variation have been modeled thanks to a time-dependent temperature generator connected at the inlet helium thermal node. This network component represents the only Dirichlet condition applied;

4. When the sample approaches high temperature and voltage, significant losses are produced in the cable, almost completely located in the high-field zone,

characterized by a lower temperature margin. The effect on the measured temperatures is the difference visible in the last two temperature steps between T_3 (upstream the high-field zone) and T_5 and T_9 (downstream). This phenomenon is already accounted by the coupling between the thermal and electromagnetic module[2]. Small losses are produced also in the jacket, but their amount is negligible compared to the cable losses.

5.4.1 Results

In Figure 5.8b the mean temperature of the cable computed by the coupled thermal-electromagnetic analyses at the Cernox sensors locations is reported, showing a very good agreement with measurements. The computed voltages of the crowns S_c and S_j are very similar to the ones obtained with the electromagnetic-only model (see Figure 5.4 and 5.5), thus in good agreement with experimental data. The computed temperature distribution along the sample is quite uniform among the petals and very close to the computed helium temperature. The only exceptions are the region astride the local heater and the high-field zone, as reported in Figure 5.10. In this Figure, that shows the computed temperature distribution at $t = 2000\,\mathrm{s}$, the temperature increases due to the DC cable losses in the high-field zone and due to the local heater are noticeable.

Also in this case, some parametric analyses have been performed to assess the results validity of the coupled modeling.

Numerical Convergence

The numerical convergence has been analyzed in the same way as the electromagnetic model. Longitudinal discretizations into 150 and 600 elements have been studied together with the reference case with 300 elements, comparing the results in terms of both computed voltages and temperatures. This analysis has been performed also to check the existence of possible numerical instabilities due to the advective term in the thermal network[3], but no evidences of this issue have been found.

The result of the analysis is that the discretization with 300 longitudinal elements is enough accurate for a detailed description of the sample. Comparing the discretizations with 300 and 600 longitudinal elements, the maximum difference in the computed temperatures is less than 5 mK, except in the small region covered by the heater, where it is slightly larger ($\approx$ 30 mK) but in any case comparable or lower than the measurement accuracy. The effect of such temperature difference is a relative difference of less than 2% in the computed voltages, corresponding to a maximum error lower than $0.8\,\mu\mathrm{V}$. On the other hand, the discretization with 150 elements shows much larger discrepancies compared to the reference case, some tenths of mK in temperature and up to some μV in voltage.

[2] See Section 3.5, page 80.
[3] See Section 3.4.2, page 75.

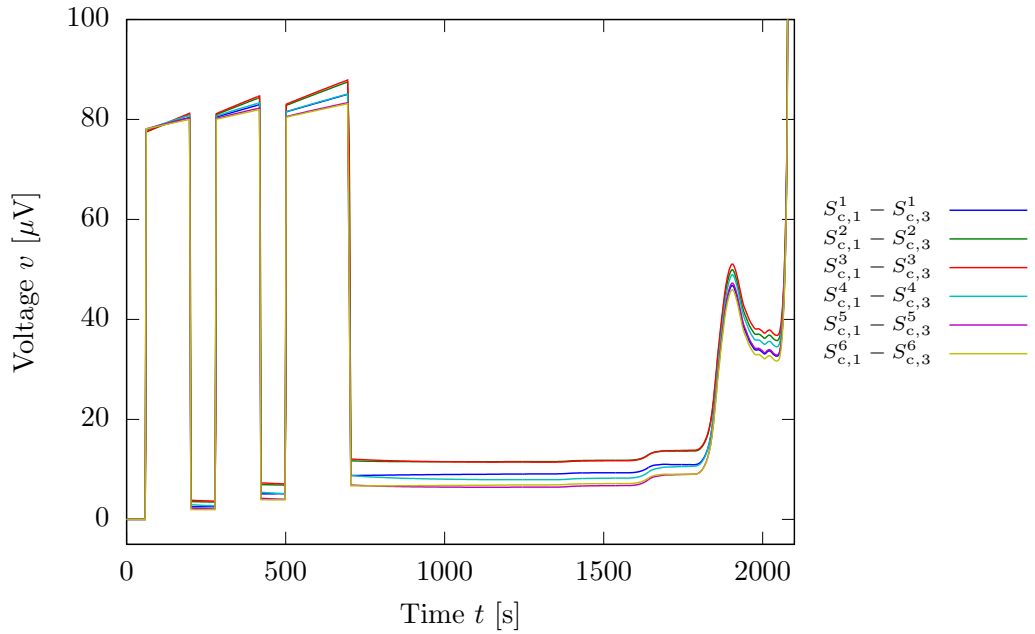

(a) Crowns S_c.

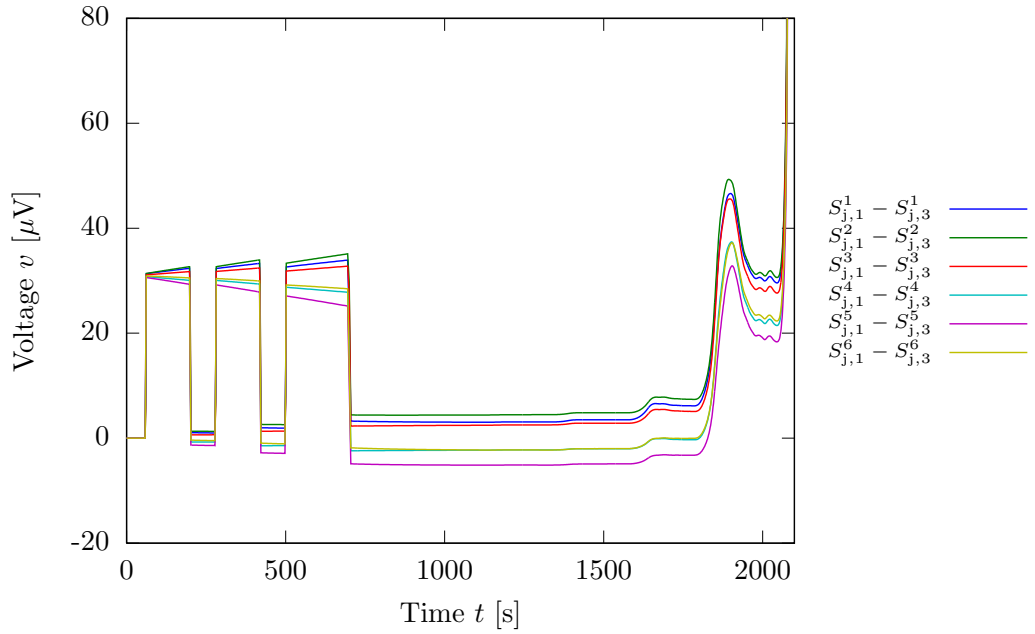

(b) Crowns S_j.

Figure 5.9: Voltages computed by the coupled thermal-electromagnetic model between the crowns S_c and S_j, test TFPRO2D111005 (to be compared with Figure 5.4 and 5.5).

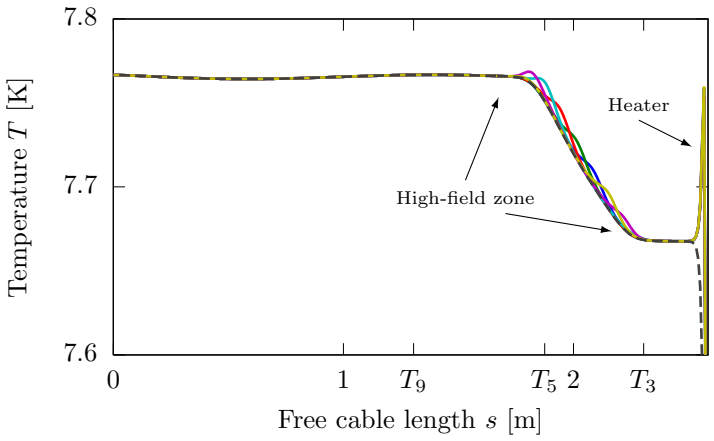

Figure 5.10: Computed temperature distribution along the free cable length in the six petals (solid lines) and helium channel (dashed line), $t = 2000\,\mathrm{s}$. The locations along the free cable length of the sensors T_3, T_5 and T_9 are indicated.

The results presented above have been obtained using $\Theta_{\max} = 10^{-2}\,\mathrm{K}$ as a threshold for the coupling among thermal and electromagnetic models[4]. Simulations with reduced thresholds down to $10^{-3}\,\mathrm{K}$ show only negligible differences, proving the correctness of the results concerning this aspect.

Impact of Helium Parameters

According to the commonly used correlations[5], in the present case the convective heat transfer coefficient h_c varies in the interval $[200; 350]\ \mathrm{W/(m^2{\cdot}K)}$ through the temperature range of interest. Values for h_c equal to 200, 275 and 350 $\mathrm{W/(m^2{\cdot}K)}$, constant and uniform along the sample, have been considered. Maximum differences up to 0.1 K can be found on the computed temperatures, that result in slightly different computed voltages only when approaching the resistive transition, as reported in Figure 5.11.

A much larger sensitivity is instead observed on the mass flow rate $\dot{m}$, as shown in Figure 5.12a. A value of 2.3 g/s, more suitable for the description of the last part of the measured data, results in a much anticipated resistive transition compared to the reference case of 2.4 g/s. However, it must be noted that all of these analyses have been performed with the same value of uniaxial strain $\varepsilon = -0.46\%$, that is a fitting parameter in the absence of further information. The code is able in any case to reproduce the experimental data, provided that ε is varied accordingly. In Figure 5.12b the computed voltages of the crowns S_j are reported for different choices for $\dot{m}$, but in this case also the uniaxial strain has been trimmed in order to better fit the measurements. Only minor discrepancies both in the computed temperatures

[4] See Section 3.5, page 80.
[5] See Appendix A.5.1, page 205.

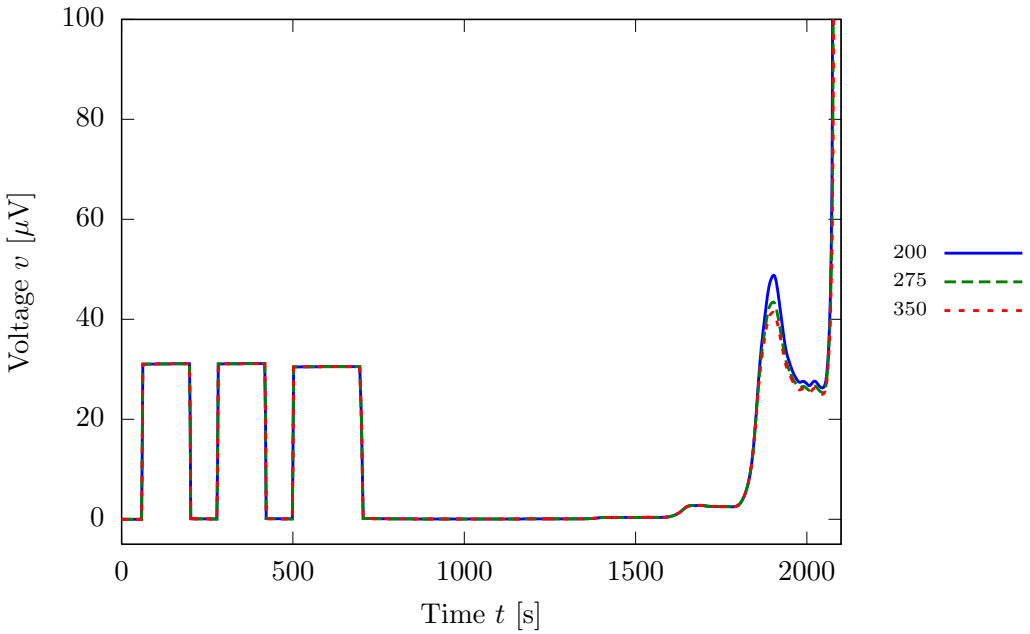

Figure 5.11: Impact of different convective heat transfer coefficients h_c on the mean computed voltages between the crowns $S_{j,1}$ and $S_{j,3}$. Values of h_c in W/(m^2·K).

($\approx$ 50 mK) and voltages are visible in this case, even if very small changes of ε have been used. Thus, presently more accurate numerical results cannot be assessed, in the absence of precise data regarding the strain and because of the limitations of the model in terms of the description of the helium fluid dynamics.

5.5 Conclusions

The capability of the coupled thermal-electromagnetic THELMA code in reproducing both electrical and thermal measurements on a CICC sample during a voltage-temperature test has been demonstrated. A small set of parameters is necessary for this kind of computation. In particular, the brand-new thermal model is able to reproduce experimental data imposing only the helium inlet temperature and mass-flow rate, whereas a bare electromagnetic modeling needs experimental data from temperature sensors all along the sample to correctly evaluate the current distributions and the DC losses. The petal twist pitch, the distance among the taps and the contact parameters, i.e. the inter-petal and jacket-petal resistances, have an important role as regards the reproduction of the voltage dispersion measured on the jacket outer surface. The uniaxial strain and the mass-flow rate have instead a paramount importance as regards the resistive transition of the sample, both in terms of temperatures and voltages.

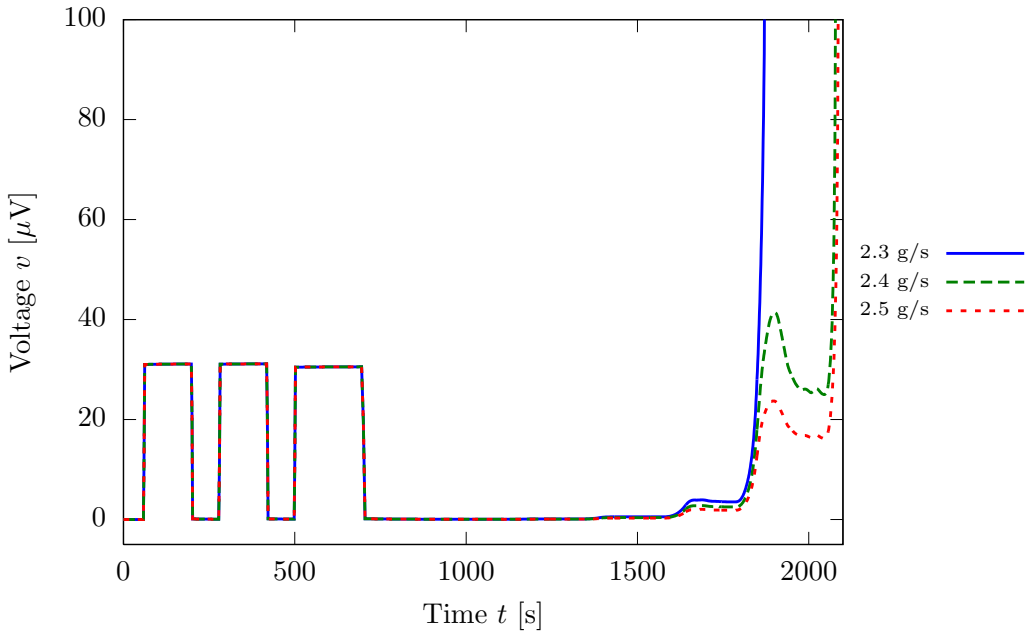

(a) Constant uniaxial strain $\varepsilon = -0.46\%$.

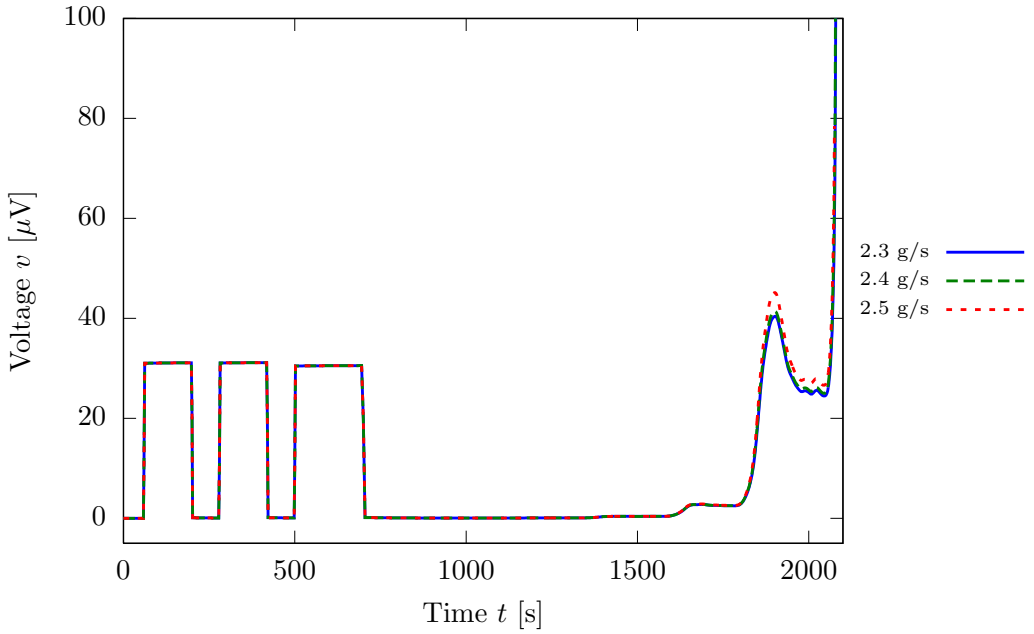

(b) Varied uniaxial strain: -0.4525% at 2.3 g/s, -0.46% at 2.4 g/s and -0.4675% at 2.5 g/s.

Figure 5.12: Impact of mass flow rate $\dot{m}$ on the mean computed voltages between the crowns $S_{\mathrm{j},1}$ and $S_{\mathrm{j},3}$ with different choices for the uniaxial strain.

Chapter 6

Quench Longitudinal Propagation in Impregnated Coils

The quench detection systems employed in superconducting magnets are generally based on resistive voltage measurements along the coil. Indeed, as a quench propagates along the conductor from the initial starting point, an electrical resistance increasing with time is developed. It is well known, both experimentally and theoretically, that the propagation of the normal-conducting zone occurs with a rather constant longitudinal velocity, after the initial transients have decayed. This quench longitudinal propagation velocity v_{lq} *is therefore an important parameter, since the magnet resistance growth and therefore the time needed to detect a quench are strongly related to it.*

The focus of this Chapter is the analysis of the quench longitudinal propagation in impregnated coils. The case study is the Short Model Coil, a small racetrack magnet wound with a Nb_3Sn *Rutherford cable, produced and tested at CERN, Geneva (CH). In the following, experimental, theoretical and numerical results are presented. Some important aspects of superconducting cables modeling are described in detail. Different analytical and numerical models for the transition from superconducting to normal-state are summarized, introducing the generation function, that models the losses produced by the cable in so-called current-sharing regime.*

6.1 Short Model Coil

The *Short Model Coil* (SMC) project is aimed at the design, production and test of Nb_3Sn racetrack sub-scale coils in a dipole configuration in order to reach magnetic fields at least of 12 T on the conductor [10]. The assembly and the cross-section of one of these magnets are shown in Figure 6.1a and 6.1b. The design foresees one or two coils, mounted in a shell-based structure employing the so-called *bladders and keys* technique to control the assembly mechanical pre-load [138]. Each coil is composed by two layers, each featuring N_t turns, in the so-called *double pancake* design. The turns are packed to each other and suitably distanced with two spacers at the coil ends to achieve the maximum magnetic field in the 15 cm long straight part of the turn [114]. In this way, the turns form three groups at the coil ends, as shown in Figure 6.1c and 6.2. An iron yoke covers the central straight part of the windings to concentrate the flux lines in this region [114].

In the following, the SMC3 version of the magnet is considered, which has reached a maximum field on the conductor of about 12.5 T at a cooling temperature of 1.9 K [10]. The coil and conductor data are summarized in Table 6.1. SMC3 is composed by two coils with 21 turns on each layer, wound with a Rutherford cable featuring 14 strands (see Figure 6.1d). The superconducting strand has been produced with the PIT process, with a non-Cu critical current density of about 2.4 kA/mm^2 at 12 T and 4.2 K and a RRR ranging between 70 and 80. The analyses of this work[1] are focused on the quench longitudinal propagation velocity measured during several tests both at a cooling temperature of 1.9 and 4.2 K.

6.1.1 Magnet Instrumentation

Each coil layer is equipped with eight voltage taps. One is located at the coil inlet/outlet, two in the low-field zone, one just after the innermost spacer and four in the high-field zone. The voltages are measured between couples of neighboring voltage taps, in this way collecting 15 signals for each coil. Table 6.2 summarizes the voltage taps of one coil of SMC3, whereas in Figure 6.2 a sketch of the voltage taps is reported. The measuring equipment embedded in each coil is completed by other devices that are not relevant for the present work, like strain gauges, Hall probes and spot heaters.

The first part of the connections with the voltage taps lays on printed circuits called *traces*, visible in the coil top view shown in Figure 6.1c. They are made of stainless steel strips, glued and pressed on top of a 25 μm polymide sheet [10]. The stainless steel sheet is then coated by metallization with a 20 μm layer of copper and the traces are printed and engraved.

[1]The research leading to these results has received funding from the European Commission under the Transnational Access activity of the FP7 Research Infrastructures project EUCARD-2, grant agreement no. 312453.

Table 6.1: Summary of the main features of SMC3.

Number of turns per layer N_t		21
Number of turns for each group		17/2/2
Straight section length L	[mm]	150
Pole half width r_{int}	[mm]	40
Interlayer insulation thickness t_{int}	[mm]	0.2
Mid-plane insulation thickness t_{mid}	[mm]	1.6
Bare cable width w_c	[mm]	10
Bare cable thickness t_c	[mm]	2.2
Cable insulation thickness t_{ins}	[mm]	0.1
Cable transposition pitch l_{tr}	[mm]	60
Strand diameter d_{st}	[mm]	1.25
Number of cable strands N_{st}		14
Short sample current I_{ss} @4.2 K	[kA]	14
Peak field @I_{ss}, 4.2 K	[T]	12.5 – 13

(a) Magnet assembly.

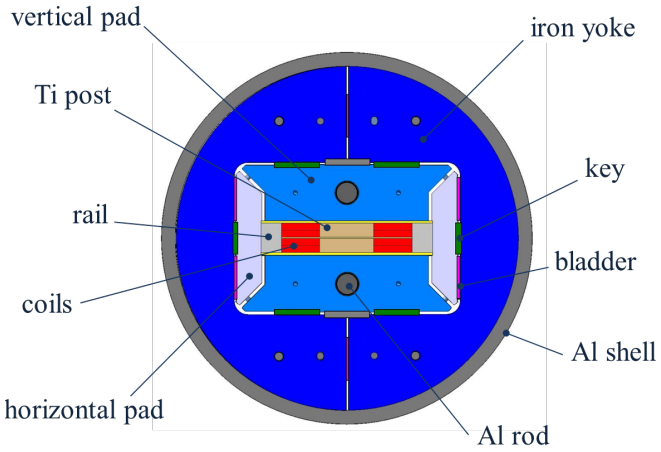

(b) Magnet cross-section.

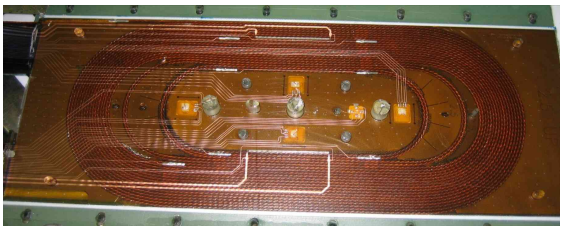

(c) Coil top view.

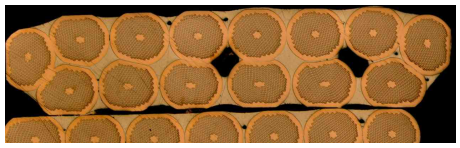

(d) Cable cross-section.

Figure 6.1: SMC3 magnet (courtesy of CERN).

Table 6.2: Summary of the voltage taps signals for one coil of SMC3.

Coil part	Signal name		No. of turns
	Upper Layer	Lower Layer	
Outermost turns	162-32	31-161	8
Straight low field section	32-42	41-31	-
Remaining outer turns	42-112	111-41	8.5
Middle and inner groups	112-52	51-111	3.5
Straight high field section	52-62	61-51	-
Pole turn	62-102	101-61	-
Straight high field section	102-72	71-101	-
Layer jump	72-71		-

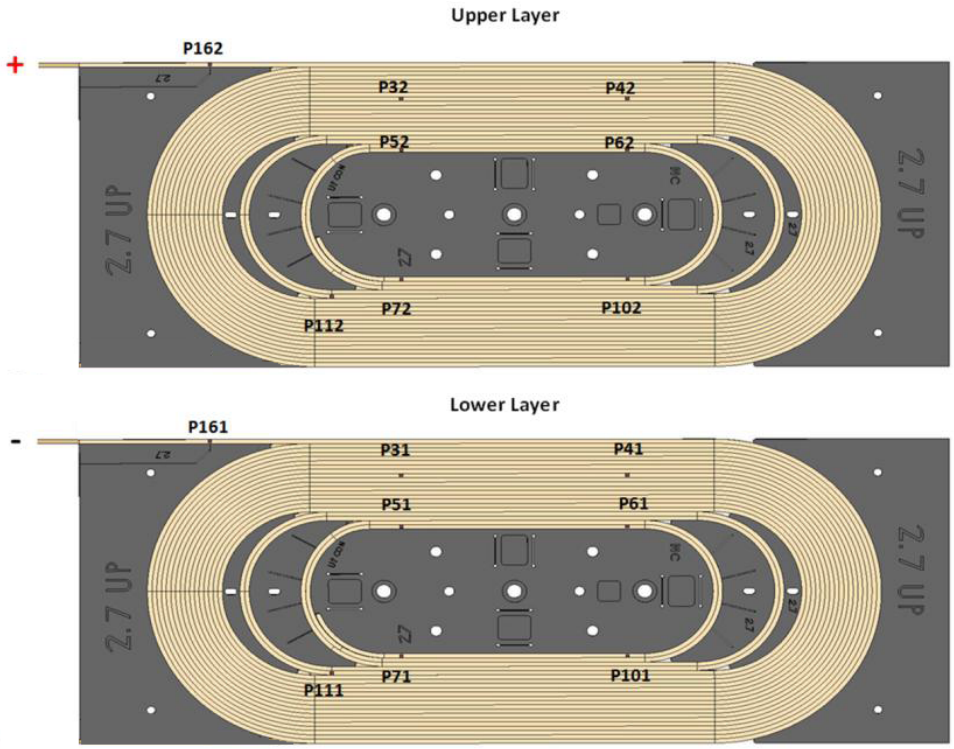

Figure 6.2: Sketch of the SMC3 voltage taps.

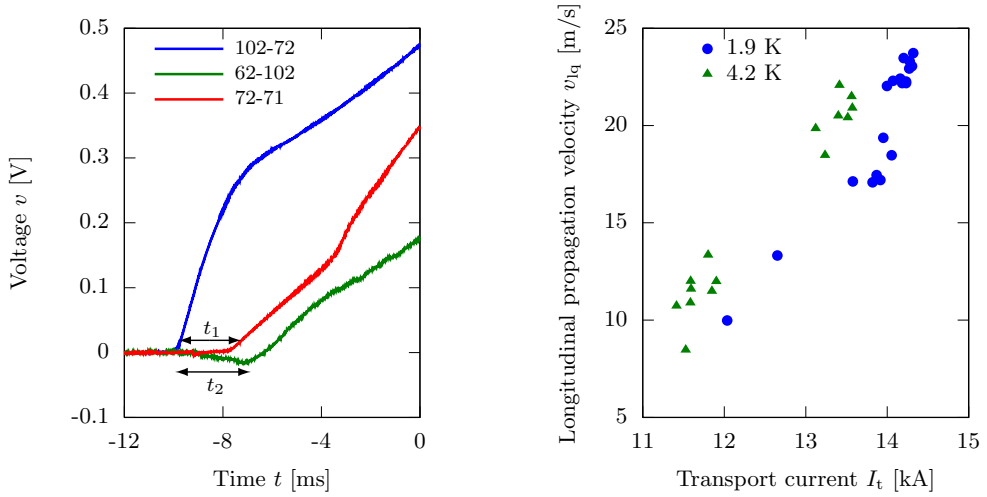

(a) Voltages during a quench at 14053 A. (b) Measured v_{lq} through the ToF method.

Figure 6.3: Time of Flight method in SMC3 magnet.

6.2 Experimental Evaluation

Experimental data from several quenches are available for SMC3, at different levels of magnet current ranging from 11 to 14 kA. The large majority of the quenches (75%) start in the high field zone in the straight part of coil 1, in particular most of them are located in the coil section named 102-72 [10]. From the voltage taps it is possible to estimate the quench longitudinal propagation velocity v_{lq} thanks to the *Time of Flight* (ToF) method. As shown in Figure 6.3a, a resistive voltage is developed in adjacent sections of the coil as the quench propagates longitudinally. The ToF method is based on the estimation of the delays t_1 and t_2 between the voltage growth in neighboring coil sections, since the distance d_{taps} between the taps is known (in the present case 13 cm):

$$v_{lq}^{ToF} = \frac{d_{taps}}{t_1 + t_2}. \tag{6.1}$$

The delays are computed considering a fixed voltage threshold for the signals, i.e. some mV. The measured v_{lq}^{ToF} are reported in Figure 6.3b as a function of the magnet current for tests at 1.9 K and 4.2 K. The values range between 10 and 25 m/s, showing a clear temperature dependence due to the different *temperature margin*, that is the difference between the bath temperature and the temperature at which the conductor starts to generate DC losses. The velocity increases with the magnet current, mainly due to the larger Joule losses produced, but also as a consequence the reduced temperature margin as the magnetic induction is increased. The accuracy of the measurements can be assessed considering a spread of about 1-2 m/s for quenches at similar magnet current and same temperature.

6.3 Analytical Models

Several analytical models for the quench longitudinal propagation velocity v_{lq} are available in literature, for example [58] [185] [188]. All of these theories are based on a 1D model of the conductor, in which the material properties are suitably averaged according to the relevant cross-section fractions. Generally, the only contribution of the copper-superconductor composite is considered, i.e. insulating materials are neglected. Indeed, the time constants of heat diffusion are inversely proportional to the material *thermal diffusivity* D_{th}, that is the ratio between thermal conductivity k and volumetric heat capacity ρc_{p}:

$$D_{\mathrm{th}} = \frac{k}{\rho c_{\mathrm{p}}}. \tag{6.2}$$

In the case of copper, the order of magnitude of D_{th} is around 1 m^2/s, i.e. many orders of magnitude larger than the value of common insulating materials like polyimide, G10 and epoxy resin[2], in which the thermal diffusivity is lower than 10^{-4} m^2/s. Thus, it is generally assumed that the heat does not diffuse appreciably into the insulation during quench front traveling [146] [188].

Since the following study is focused on impregnated coils, the heat exchange with helium can be neglected. Thus, the following heat balance equation can be written:

$$\frac{\partial}{\partial x}\left(k\frac{\partial T}{\partial x}\right) - \rho c_{\mathrm{p}}\frac{\partial T}{\partial t} + G(T) = 0, \tag{6.3}$$

where $G(T)$ is the so-called *generation function* [W/m^3], that models the heat produced by the conductor when passing from superconducting to normal-conducting state. This function is generally approximated as:

$$G(T) = \begin{cases} \rho_{\mathrm{E}} J_{\mathrm{t}}^2, & T > T_{\mathrm{tr}}, \\ 0, & T < T_{\mathrm{tr}}, \end{cases} \tag{6.4}$$

where ρ_{E} is the equivalent electrical resistivity of the conductor (by far dominated by copper), J_{t} is the engineering transport current density and T_{tr} is a suitable *transition temperature*, intermediate between the bath temperature T_0 and the critical temperature T_{c}. Detailed discussion on the choice of T_{tr} can be found in the following. Since only the metallic components of the conductor are considered, Wiedemann-Franz law $\rho_{\mathrm{E}} k = L_0 T$ is employed[2], being well verified in the range of temperature of interest of this analysis.

Quench propagation models are based on the assumption that the temperature profile propagates along the cable with a velocity v_{lq} without changing its shape. In these conditions, Eq. (6.3) can be rewritten with a change of variables $z = x - v_{\mathrm{lq}} t$:

$$\frac{\mathrm{d}}{\mathrm{d}z}\left(k\frac{\mathrm{d}T}{\mathrm{d}z}\right) + v_{\mathrm{lq}}\rho c_{\mathrm{p}}\frac{\mathrm{d}T}{\mathrm{d}z} + G(T) = 0, \tag{6.5}$$

[2]See Appendix A for details.

that leads to:

$$k\frac{\mathrm{d}^2T}{\mathrm{d}z^2} + \frac{\mathrm{d}k}{\mathrm{d}T}\left(\frac{\mathrm{d}T}{\mathrm{d}z}\right)^2 + v_{\mathrm{lq}}\rho c_{\mathrm{p}}\frac{\mathrm{d}T}{\mathrm{d}z} + G(T) = 0, \tag{6.6}$$

The coordinate $z = 0$ represents the traveling boundary between the superconducting and the normal-conducting zone. With the approximation (6.4), Eq. (6.3) can be solved separately in the normal-conducting and superconducting zone, imposing the boundary condition:

$$\left(\frac{\mathrm{d}T}{\mathrm{d}z}\right)_{z=0^+} = \left(\frac{\mathrm{d}T}{\mathrm{d}z}\right)_{z=0^-} \tag{6.7}$$

In an early work, *Whetstone and Roos* solved Eq. (6.6) with the following approximation in the normal-conducting zone [185]:

$$k\frac{\mathrm{d}^2T}{\mathrm{d}z^2} \ll \frac{\mathrm{d}k}{\mathrm{d}T}\left(\frac{\mathrm{d}T}{\mathrm{d}z}\right)^2, \tag{6.8}$$

that corresponds to assume an almost linear temperature profile in that region. In these conditions the propagation velocity can be computed as:

$$v_{\mathrm{lq}}^{\mathrm{WR}} = J_{\mathrm{t}}\sqrt{\frac{L_0T_{\mathrm{tr}}}{C_{\mathrm{int}}\left[C_{\mathrm{T_{tr}}} - \dfrac{C_{\mathrm{int}}}{T_{\mathrm{tr}}}\right]}}, \tag{6.9}$$

where C_{int} is the integral of the volumetric heat capacity between T_0 and T_{tr}:

$$C_{\mathrm{int}} = \int_{T_0}^{T_{\mathrm{tr}}} \rho c_{\mathrm{p}}(T^{'})dT^{'}, \tag{6.10}$$

and $C_{\mathrm{T_{tr}}}$ is the volumetric heat capacity at T_{tr} in normal-conducting state. *Dresner* proposed a slightly different formula [58]:

$$v_{\mathrm{lq}}^{\mathrm{D}} = J_{\mathrm{t}}\sqrt{\frac{L_0T_{\mathrm{tr}}}{C_{\mathrm{int}}C_{\mathrm{T_{tr}}}}}, \tag{6.11}$$

in which the contribution of $C_{\mathrm{int}}/T_{\mathrm{tr}}$ vanishes. However, the most common model for propagation velocity is the *Wilson model* [188]:

$$v_{\mathrm{lq}}^{\mathrm{W}} = \frac{J_{\mathrm{t}}}{C_{\mathrm{T_{tr}}}}\sqrt{\frac{L_0T_{\mathrm{tr}}}{T_{\mathrm{tr}} - T_0}}. \tag{6.12}$$

This solution is obtained with the assumption of constant material properties with temperature, and it is easy to demonstrate that with these assumptions Eq. (6.11) leads directly to Eq. (6.12). Since the approximation of constant material properties is very crude, Wilson suggests to replace $C_{\mathrm{T_{tr}}}$ with a suitable average C_{avg}

of the volumetric heat capacity in the range of the transition between T_0 and T_{tr}. Considering for example an integral average:

$$C_{\mathrm{avg}} = \frac{C_{\mathrm{int}}}{T_{\mathrm{tr}} - T_0}, \tag{6.13}$$

Eq. (6.12) becomes:

$$v_{\mathrm{lq}}^{\mathrm{W}} = \frac{J_{\mathrm{t}}}{C_{\mathrm{int}}} \sqrt{L_0 T_{\mathrm{tr}} (T_{\mathrm{tr}} - T_0)}. \tag{6.14}$$

Examples of propagation velocity computed with these expressions are given in the next section and plotted in Figure 6.6.

6.4 Generation Function

The most questionable approximation in the analytical methods is the model for the generation function (Eq. 6.4), with its abrupt transition at T_{tr}. Such an assumption is necessary to permit an analytical computation, but it neglects a possible *current-sharing regime*, in which the current can be partially shunted in the normal-conducting matrix. This regime ranges between two limits. The conductor losses start at the so-called *generation temperature* T_{g}[3], defined as the temperature at which the critical current is exceeded by the conductor transport current. This is valid for a sharp transition from superconducting to normal-conducting state, i.e. quite large values of the n-index, conversely non negligible losses can be obtained also at lower temperature. The maximum value of $G(T)$ is instead achieved at T_{c}, when the superconductor is no almost unable to carry any current. T_{c} depends only on magnetic induction and strain in the conductor, whereas T_{g} depends also on the transport current.

6.4.1 Choice of the Transition Temperature

If $T_{\mathrm{c}} \approxeq T_{\mathrm{g}}$, the shape of $G(T)$ obviously does not affect the quench propagation, and Eq. (6.4) can be considered a good approximation. This is applicable for example at the lowest values of the transport current, or in Nb-Ti, that is characterized by a reduced critical temperature and largest n-index compared to other materials. However, in other cases like in Nb_3Sn conductors at high levels of transport current, the current-sharing regime can span over several degrees, resulting in a non-trivial choice of the transition temperature T_{tr}. As an example, the critical temperature and the generation temperature are reported in Figure 6.4 as a function of the magnet current, in the case of the SMC3 conductor subjected to the highest magnetic field.

To take into account this aspect in the analytical models, different values for the transition temperature T_{tr} can be chosen. Wilson assumes a linear variation of

[3]Sometimes this temperature is called T_{cs}, current sharing temperature. Since this can be misleading with the definition of T_{cs} given in chapter 5 in the field of performance evaluation in CICCs, the symbol T_{g} is preferred.

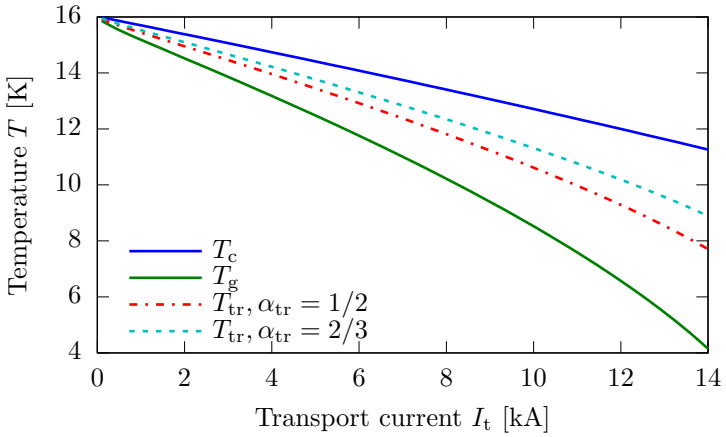

Figure 6.4: Computed critical temperature T_c and generation temperature T_g for SMC3 conductor. The transition temperatures corresponding to a linear and a quadratic approximation for the generation function are also reported.

the generation function from T_g to T_c [188]. Therefore, considering a principle of equal-area among the linear generation function and the approximated Eq. (6.4) (see Figure 6.5), the transition temperature can be chosen as:

$$T_{tr} = T_g + \frac{1}{2}(T_c - T_g). \tag{6.15}$$

An alternative approach is to consider the current in the copper, rather than the generation function, linear with the temperature in current-sharing regime [88]. This assumption leads to a quadratic generation function with temperature, that results in this transition temperature according to the equal-area principle:

$$T_{tr} = T_g + \frac{2}{3}(T_c - T_g). \tag{6.16}$$

In general, the transition temperature can be described by:

$$T_{tr} = T_g + \alpha_{tr}(T_c - T_g), \tag{6.17}$$

In Figure 6.5 the different choices for the $G(T)$ and the T_{tr} are schematized in terms of *normalized generation function* $g = G(T)/G(T_c)$.

The parameter $0 \leq \alpha_{tr} \leq 1$ considerably affects the results of the analytical models. In particular, lower values for α_{tr} result in larger v_{lq}, since the integral (6.10) is strongly reduced, being the volumetric heat capacity proportional to T^3 in this temperature range. In Figure 6.6, the computed longitudinal propagation velocities with the models (6.9), (6.11) and (6.14) are plotted as a function of the magnet current in the case of SMC3 conductor, together with the experimental data. Two data sets have been taken, the first at 1.9 K and the second at 4.2 K. The

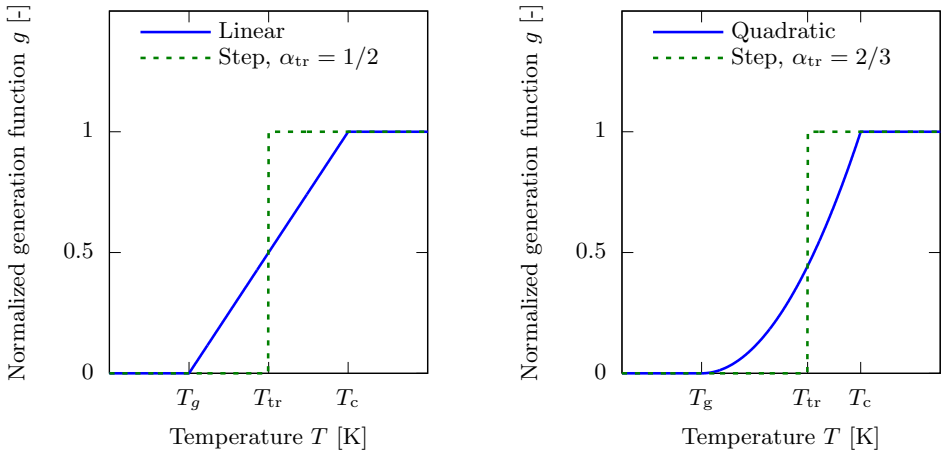

Figure 6.5: Normalized generation function $g = G(T)/G(T_c)$ as a function of temperature with different assumptions.

magnet field employed in the calculations is the highest field in the winding computed from the magnet load line. Important differences between the case $\alpha_{tr} = 1/2$ and $\alpha_{tr} = 2/3$ are visible. Wilson model (Eq. 6.14) leads always to the highest velocities, Whetstone-Roos equation (Eq. 6.9) to intermediate values and Dresner equation (Eq. 6.11) to the lowest. This latter model gives the best fit in the present case, in particular if $\alpha_{tr} = 2/3$ is considered.

6.4.2 Numerical Models

In numerical tools, more complex models can be used to compute the generation function in a superconductor carrying the transport current I_t.

- The *Stekly model* [157] is a very common assumption, implemented in several numerical tools for quench simulation like QLASA [146] and ROXIE [148]. According to this model, all the transport current exceeding the critical current is carried by the normal-conducting matrix, up to the critical temperature at which no more current flows in the superconductor. Thus, according to this model, at any $T > T_g$ the superconductor carries its critical current. The equivalent circuit of such a model is the parallel between an ideal current generator carrying the minimum current between I_t and $I_c(T)$ and a resistance per unit length r_{nm} representing the normal-conducting matrix, as shown in Figure 6.7a. The generation function $G(T)$ produced by such a circuit is simply:
$$G(T) = r_{nm}(I_t - I_c)J_t. \tag{6.18}$$
- A more detailed model can be obtained considering the equivalent circuit in Figure 6.7b representing the conductor. In this case the superconductor is

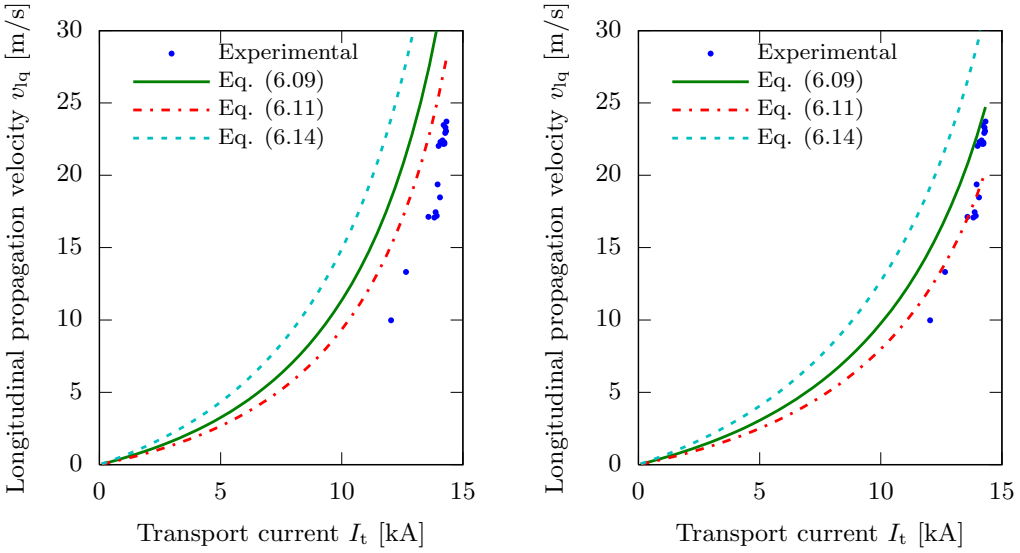

(a) Bath temperature $T_0 = 1.9$ K.

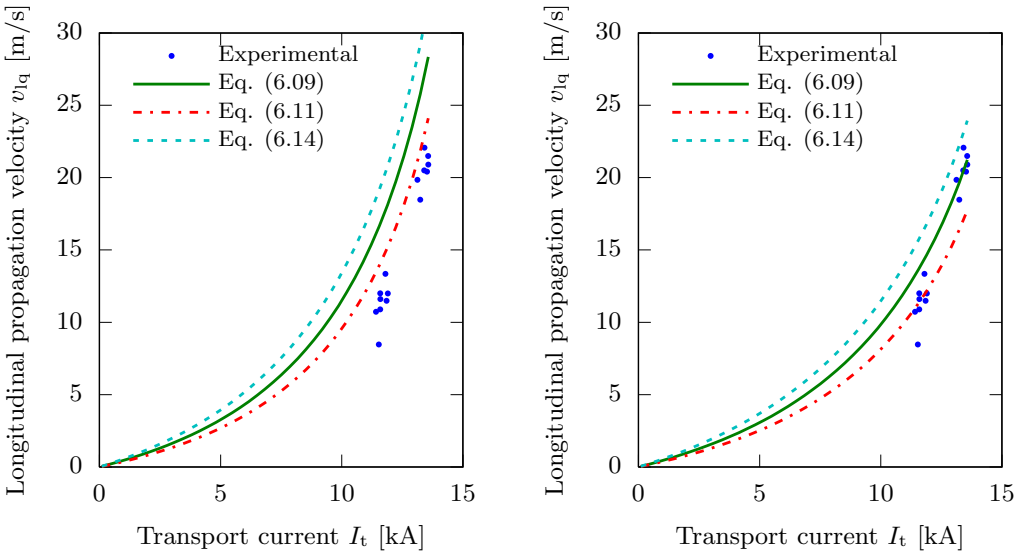

(b) Bath temperature $T_0 = 4.2$ K.

Figure 6.6: Quench longitudinal propagation velocity as a function of transport current with the analytical models, SMC3. The left plots represent the case $\alpha_{tr} = 1/2$, the right ones $\alpha_{tr} = 2/3$.

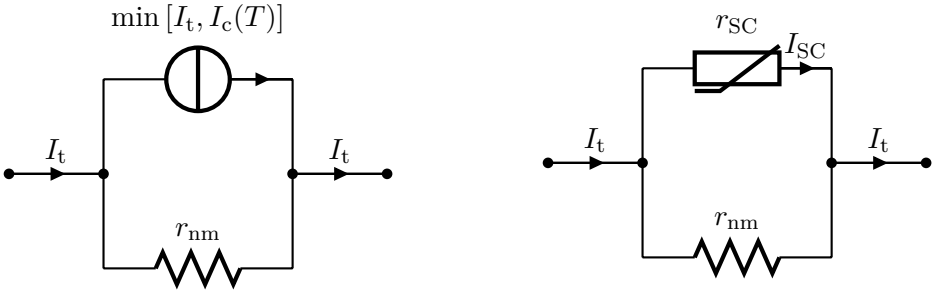

(a) Stekly model. (b) n-index model.

Figure 6.7: Equivalent circuits for the numerical generation function models.

represented as a non-linear resistor r_{SC} controlled by the power law[4] with a constant n-index. The following equation can be written:

$$E_c \left(\frac{I_{SC}}{I_c} \right)^n = r_{nm}(I_t - I_{SC}), \tag{6.19}$$

where I_{SC} is the current flowing in the superconducting branch of the circuit in Figure 6.7b. Equation (6.19) can be solved at each temperature as a function of I_{SC} by means of an iterative method like Newton-Raphson. The generation function can be computed as:

$$G(T) = J_t E_c \left(\frac{I_{SC}}{I_c} \right)^n. \tag{6.20}$$

This approach is used for example in the Bologna EM module, although the n-index can be varied with critical current, as explained below. In Figure 6.8, Eq. (6.20) is plotted in the case of SMC3 conductor at two different levels of the magnet current and for different values of the n-index. Also in this case the magnetic induction is computed by means of the magnet load line for the maximum field.

- The previous model can be extended considering also the n-index correlation with critical current that it is often observed experimentally[5]:

$$n = 1 + r\, I_c^s. \tag{6.21}$$

In the present case, measured values for the n-index are not available for SMC3 conductor, therefore two different correlations have been considered, as shown in Figure 6.9a:

$$n^h = 1 + 2.20\, I_c^{0.47}, \tag{6.22}$$

$$n^l = 1 + 1.32\, I_c^{0.45}. \tag{6.23}$$

[4] See Eq. (1.21), page 17.
[5] See Eq. (1.23), page 17

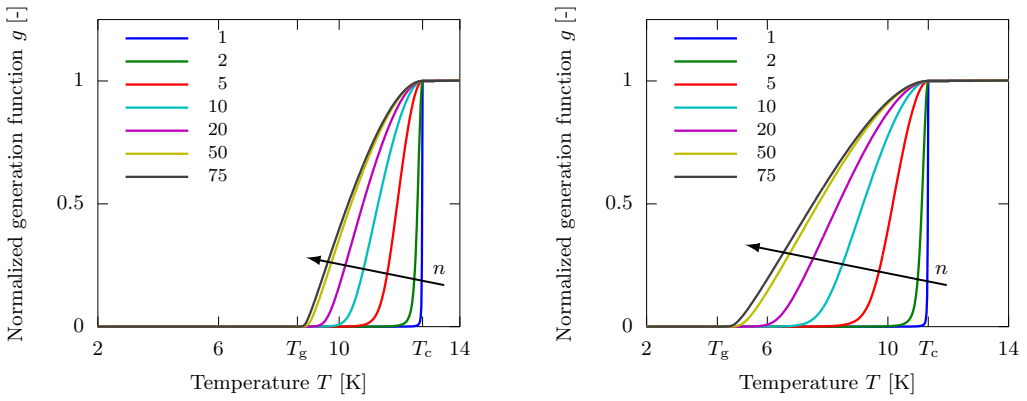

(a) $I_t = 10$ kA. (b) $I_t = 14$ kA.

Figure 6.8: Normalized generation function $g = G(T)/G(T_c)$ as a function of temperature with different n-indexes.

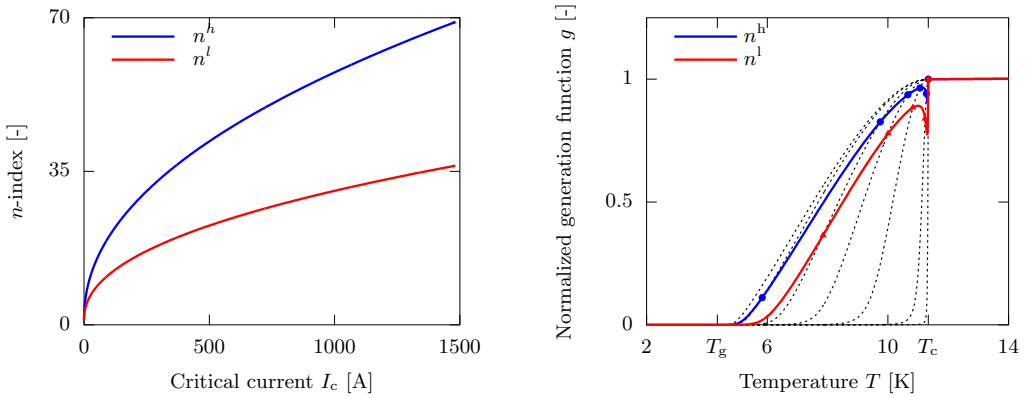

(a) n-index as a function of critical current. (b) Generation function at $I_t = 14$ kA.

Figure 6.9: Model with n-index dependent on the critical current.

The first correlation, that can be considered as the reference, leads to larger values for the n-index (up to more than 60) and comes from measurements on another PIT strand [104]. This strand is characterized by a critical current density similar to that of SMC3 (2450 A/mm^2 at 4.2 K and 12 T) but with a reduced diameter (0.81 mm instead of 1.25 mm). Since Eq. (6.21) is based on critical current rather than critical current density, the r coefficient has been scaled according to the different superconductor area, in order to obtain the same level of n-index at the same critical current density. The second correlation leads to n-indexes up to about 35 as measured on an internal-tin strand [168]. In Figure 6.9b the generation function at 14 kA for the two proposed correlations is reported. To obtain it, the n-index as a function of

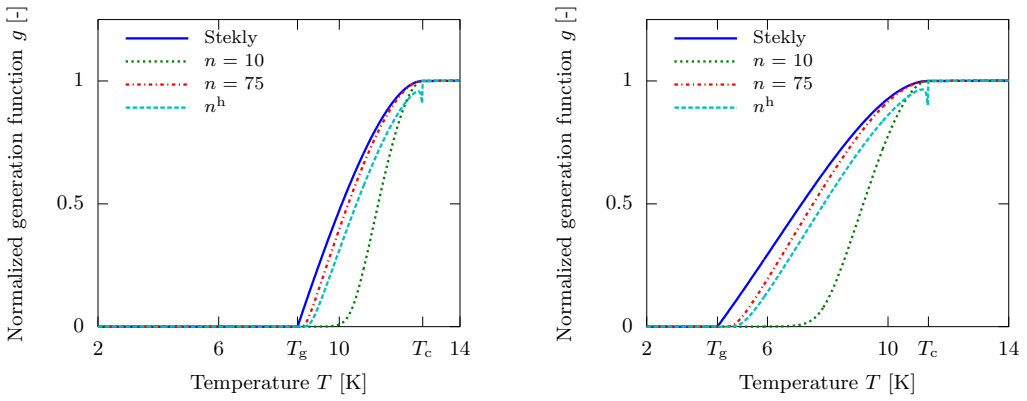

(a) $I_{\mathrm{t}} = 10$ kA. (b) $I_{\mathrm{t}} = 14$ kA.

Figure 6.10: Summary of the normalized generation functions $g = G(T)/G(T_{\mathrm{c}})$ as a function of temperature.

temperature must be computed combining Eq. (6.22) and Eq. (6.23) with the critical current scaling law. Then, at each temperature the value of $G(T)$ from Figure 6.8 is considered from the curve at the corresponding n-index.

As a summary, the generation functions obtained with the different models just discussed are plotted in Figure 6.10. It is evident that the Stekly model can be considered an approximation of the case of an infinite n-index. Because of that, in the following Stekly model is not considered anymore.

Although all of these models are based on commonly accepted theories, none of them can be directly validated experimentally, since the current-sharing regime is a thermally unstable state. In addition, deviations from the power-law are described in literature at low electric fields, and statistical approaches demonstrate that the power-law is a property of the whole composite strand, rather than of the superconductor only[6]. This is in contradiction with the basic assumption of all the models presented above, that consider the conductor as the parallel of two components, one representing the normal-conducting material and one representing the superconductor. However, such models for voltage-current characteristic require several statistical parameters taken on the very type of strand used in the Rutherford cable. These data are not available, moreover their temperature dependance is completely unknown, thus in the following they will not be considered. The large uncertainties in the generation function have therefore been analyzed by suitable parametric numerical simulations.

[6]For details see Appendix B, page 211.

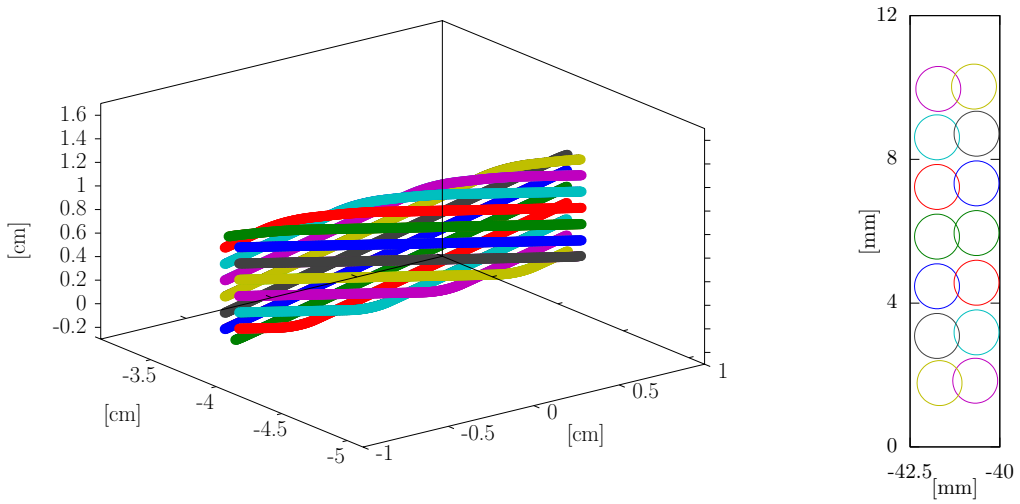

(a) Detail of the 3D view.

(b) Cross-section.

Figure 6.11: Images of the modeled SMC3 Rutherford cable.

6.5 Simulations with THELMA

The 15 cm long high-field section 102-72 where the majority of the SMC3 quenches happened has been modeled with THELMA to numerically evaluate the longitudinal propagation velocity as a function of the magnet current I_t and the conductor initial temperature T_0. Two different estimates for v_{lq} have been considered, one based on the ToF method (Section 6.2) applied to the computed voltages, the other on the temperature distribution evolution. A detailed sensitivity analysis has been performed to check some assumptions made and to better understand the role of generation function.

6.5.1 Model Description

The 14 strands of the Rutherford cable have been modeled with a longitudinal discretization of 1 mm, chosen to guarantee the convergence of the results and comply with the contact length between cross-over strands, that is of the order of $1-2$ mm. The geometrical parameters used to model the cable are reported in Table 6.1 and some views of the modeled geometry are shown in Figure 6.11. The Twente/ITER scaling law has been used to describe the strand critical current, with the parameters reported in Table 2.3, page 42. A critical current degradation of 16.3% due to cabling has been assumed, together with an applied axial strain $\varepsilon = -0.2\%$ [107]. As a reference, the n-index is assumed to vary according to the correlation reported in Eq. (6.22). The RRR has been assumed equal to 75 considering the measured range of $70-80$. The adopted electrical inter-strand resistances values are $R_c = 1\,\mathrm{m\Omega}$ and $R_a = 9.4\,\mu\Omega$ [53].

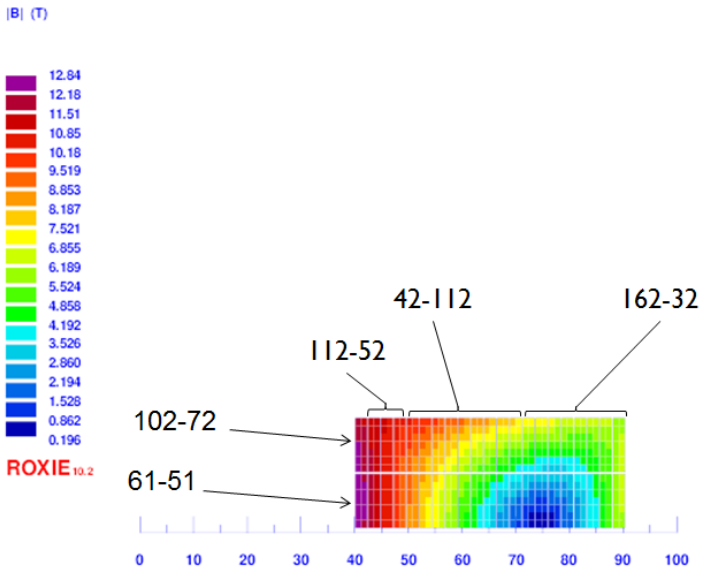

Figure 6.12: 2D field map of the cross-section of SMC3 computed with ROXIE indicating the location of some coil sections.

The modeling of the magnetic induction produced by the magnet is a critical aspect, since ferromagnetic materials are not foreseen in THELMA model, whereas the SMC3 iron yoke contributes with a non-negligible field of about 2 T. The following approximation has been made. The iron field on the magnet cross-section has been computed with ROXIE code [148] with a 2D model, in principle valid only for a long magnet. This field has been superposed to the field generated by all the SMC3 conductors except 102-72, whose self-field is already included in the model. To comply with the 2D iron model, the approximation of an arbitrary long magnet has been considered. The field map in the winding at a magnet current of 14 kA computed with ROXIE is reported in Figure 6.12. The resulting peak field on the conductor is about 12.8 T, in very good agreement with the value of 12.9 T computed with more accurate 3D tools [114]. Nevertheless, with the 2D approximation the field is almost constant along the 102-72 section, whereas 3D models foresee a reduction of about 0.5 T from the center of the magnet to the coil ends. To better assess the validity of the results, the impact of the magnetic field on v_{lq} has been checked through a parametric analysis.

In the simulation, the quench is triggered with the deposition of a suitable perturbation energy E_{p} in a single strand, midway between 102-72 section ends. Values between 0.1 and some mJ have been impressed depending on the temperature margin. Insulating materials material properties and heat exchange with helium have not been included in the model, following the adiabatic assumption justified in Section 6.3 by the low thermal diffusivity of the insulating materials.

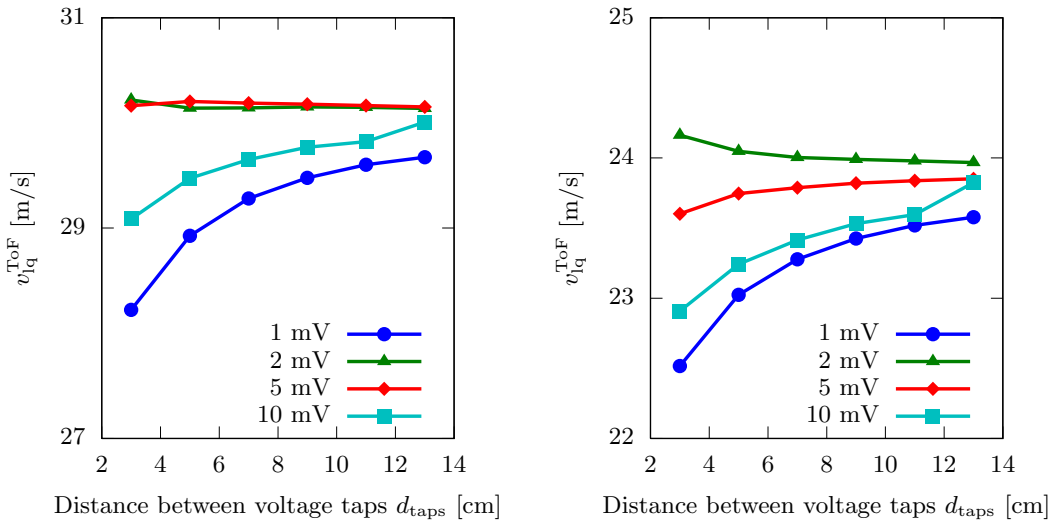

(a) $T_0 = 1.9$ K, $I_{\mathrm{t}} = 15$ kA.

(b) $T_0 = 4.2$ K, $I_{\mathrm{t}} = 14$ kA.

Figure 6.13: Computed $v_{\mathrm{lq}}^{\mathrm{ToF}}$ as a function of voltage taps distance d_{taps}.

6.5.2 Velocity Estimation

The quench longitudinal propagation velocity has been estimated from the simulations in two different ways. To comply with the available experimental data, the ToF method (Eq. 6.1) has been applied to the computed voltages. The delays t_1 and t_2 have been measured considering several voltage thresholds between 1 mV and 10 mV to check possible differences. Moreover, the voltage has been evaluated not only at the nominal distance between the taps (13 cm), but also at lower distances, down to 3 cm. This has been done to check if the quench propagation velocity is really constant at the nominal distance, i.e. the initial transients have already decayed. This check is meaningful only with the assumption of a 2D magnetic field, otherwise a slight change of the velocity is expected in proximity of the coil ends, due to the magnetic field reduction. In the following, the symbol $v_{\mathrm{lq}}^{\mathrm{ToF}}$ is used to refer to this estimation of the propagation velocity. In Figure 6.13 $v_{\mathrm{lq}}^{\mathrm{ToF}}$ is reported as a function of the taps distance d_{taps} for two simulations at different I_{t} and T_0. An example of the computed voltage taps is instead reported in Figure 6.14a.

At the nominal $d_{\mathrm{taps}} = 13$ cm the threshold affects the results by less than 1 m/s, in agreement with the experimental accuracy of $1 - 2$ m/s. For lower values of d_{taps}, larger variations up to about 2 m/s can be found, in any case comparable with the experimental accuracy. The quite weak dependence of $v_{\mathrm{lq}}^{\mathrm{ToF}}$ on d_{taps} confirms the assumption of a normal-conducting front traveling at an almost constant velocity. Thus in the following, when referring to $v_{\mathrm{lq}}^{\mathrm{ToF}}$, the value obtained at the nominal d_{taps} averaged among the different voltage thresholds is considered.

Another possible approach for the estimation of v_{lq} is based on the evolution of

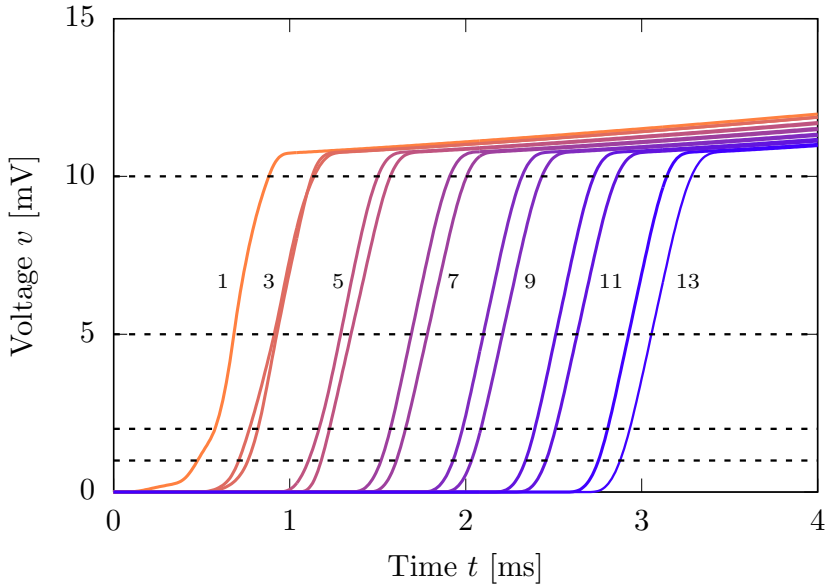

(a) Simulated voltages. The dashed lines represent the voltage thresholds considered. Each couple of solid lines refers to the left and right voltage tap at different values of d_{taps}, reported in cm near the curves.

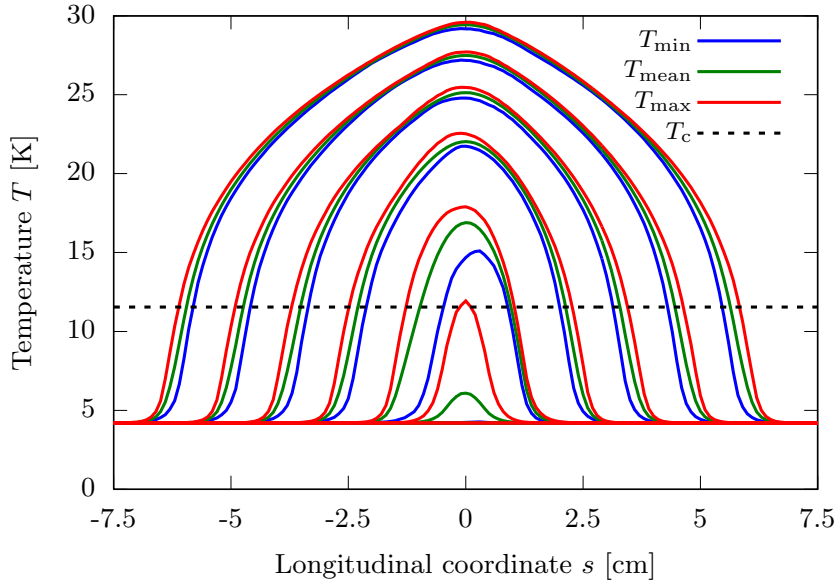

(b) Simulated temperature profile along the cable. Minimum, mean and maximum temperature at each longitudinal coordinate are reported together with T_{c} as a reference. The time step between two corresponding curves is 0.5 ms.

Figure 6.14: Simulated voltages and temperature profiles as a function of time during a quench, $T_0 = 4.2$ K, $I_{\text{t}} = 14$ kA.

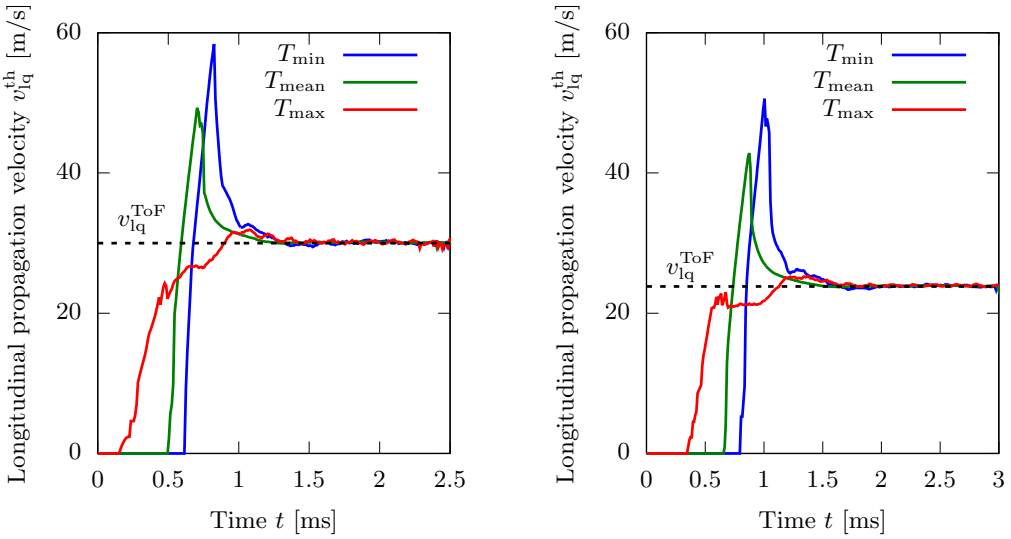

(a) $T_0 = 1.9$ K, $I_t = 15$ kA.

(b) $T_0 = 4.2$ K, $I_t = 14$ kA.

Figure 6.15: Estimated v_{lq}^{th} in the case of the minimum, mean and maximum temperature, compared with ToF method.

the computed temperature distribution of the conductor, considering the velocity at which a reference temperature, e.g. the critical temperature T_c, is moving along the conductor. The symbol v_{lq}^{th} is used to refer to this estimation, since it complies with the quench propagation velocity definition given by the theory presented in Section 6.3. However, being the temperature not exactly uniform among parallel strands, different criteria can be chosen, such as considering the minimum, maximum or mean temperature at each longitudinal coordinate, as shown in Figure 6.14b. Figure 6.15 compares the computed v_{lq}^{th} for T_{min}, T_{mean} and T_{max} as a function of time for a pair of simulations. From this figure it is evident that the different criteria affect the results only during the initial transient of about 1 ms, in which the quench propagates transversely among the strands, whereas a constant value is achieved when all the strands have become normal-conducting. As shown in the plot, this value is in good agreement with the ToF method, therefore in the following the symbol v_{lq} is used to refer to the propagation velocity, whatever method is employed for its estimation.

6.5.3 Current Distribution

In Figure 6.16 a typical current distribution pattern during the quench evolution is reported. In those plots the current is normalized to the ideal share of transport current for each strand, 1 kA in the referred case.

Before the disturbance, all the strands carry the same amount of current. Then, the perturbation occurs on an individual strand, thus its current is heavily reduced and quickly redistributed on the adjacent strands, as shown in Figure 6.16a. The

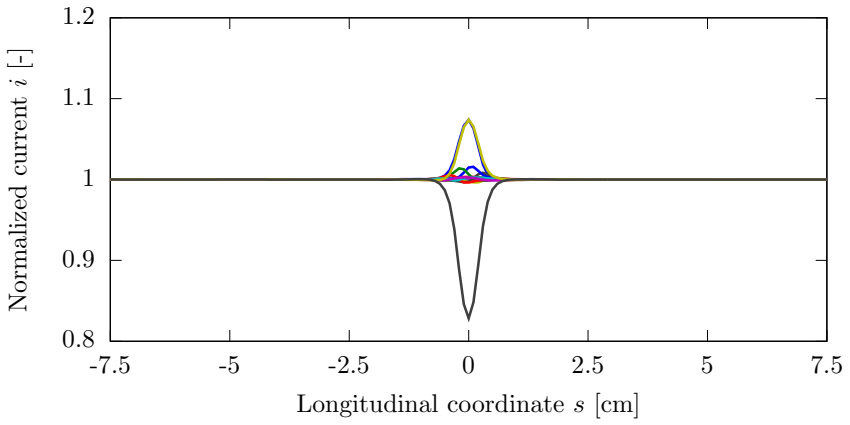

(a) 0.3 ms after the disturbance.

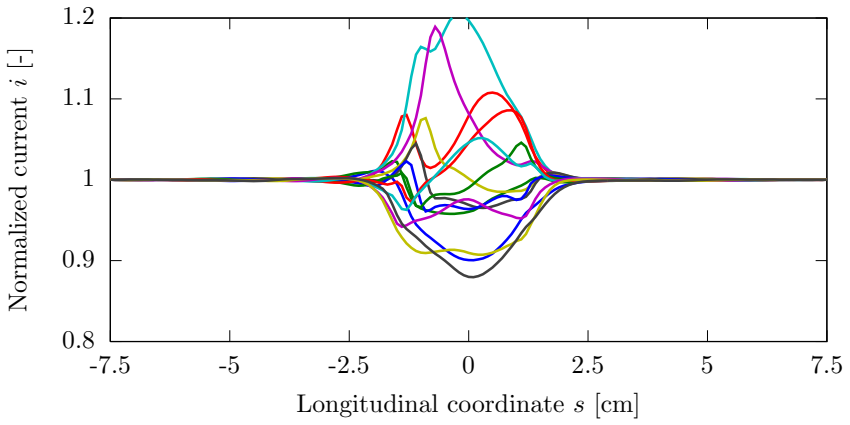

(b) 1 ms after the disturbance.

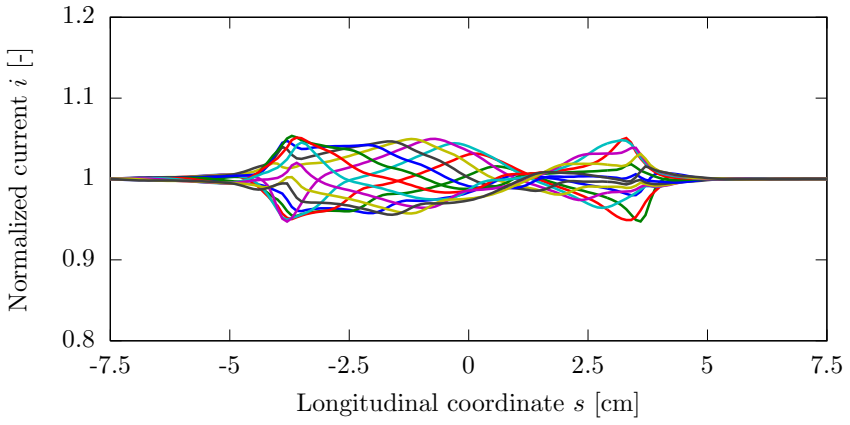

(c) 2 ms after the disturbance.

Figure 6.16: Computed current distribution among the strands, $T_0 = 4.2$ K, $I_t = 14$ kA. The current is normalized to the ideal share of transport current for each strand, 1 kA in this case.

combined effect of the current unbalances and of the temperature increase makes the perturbation propagate on other strands. Thus, a further increase of the current load on the remaining superconducting strands can be observed, as reported in Figure 6.16b, leading to current unbalances up to 30% of the ideal share of transport current. Finally, about $1-2$ ms after the perturbation, when all the strands have become resistive at the hot spot location, the quench propagates longitudinally and the current unbalances among the strands are strongly reduced to less than 10% of the ideal share of transport current (Figure 6.16c). This behavior is consistent with the previous analysis of the propagation velocity by means of the temperature distribution (Figure 6.15), since the velocity estimations made with the mean, maximum and minimum cable temperature lead to the same result $1-2$ ms after the perturbation, indicating that after this interval the cable is behaving similarly to a monolithic conductor.

6.5.4 Results and Parametric Analyses

In Figure 6.17 the computed v_{lq} is reported as a function of I_{t} and T_0 and compared with the experimental data. The model parameters used in these simulations are the reference values described in Section 6.5.1, therefore no further tuning parameter has been employed to better fit data. Nevertheless, the agreement among simulations and measurements is very good. A detailed sensitivity analysis has been performed to check the impact of some uncertain model parameters.

n-index and Generation Function

Figure 6.17 has been obtained assuming Eq. (6.22) as correlation between n-index and I_{c}. The correlation Eq. (6.23) has been also tested to check the impact of a reduced n-index on the resulting v_{lq}. As shown in Figure 6.18, v_{lq} is affected by the n-index only if the magnet current is very high, due to the larger current sharing regime, as explained in Section 6.4. The decreased n-index provided by Eq. (6.23) leads to v_{lq} reductions between 10% and 25% from 11 to 15 kA. The results at lower magnet current are very similar and thus not reported. The experimental data are closer to the simulations with larger values for the n-index, and this is reasonable since the PIT process is reported to achieve larger values of n-index compared to other manufacturing techniques [104]. Further simulations have been performed to check the v_{lq} sensitivity with generation function, taking as reference case $v_{\mathrm{lq}}^{\mathrm{ref}} = 20.6$ m/s computed at $T_0^{\mathrm{ref}} = 1.9$ K and $I_{\mathrm{t}}^{\mathrm{ref}} = 14$ kA. Such a large I_{t} value has has been chosen to enhance the sensitivity of v_{lq} with the generation function.

In a first set of simulations, different levels of applied strain ε between -0.4% and 0% have been considered, since the critical current variation with strain affects the generation temperature T_{g}. In the reference case is $T_{\mathrm{g}}^{\mathrm{ref}} \approx 4.6$ K for the 102-72 section, but it reduces down to ≈ 3.3 K with an increased compressive strain. The reference n-index correlation Eq. (6.22) has been employed. As shown in Figure

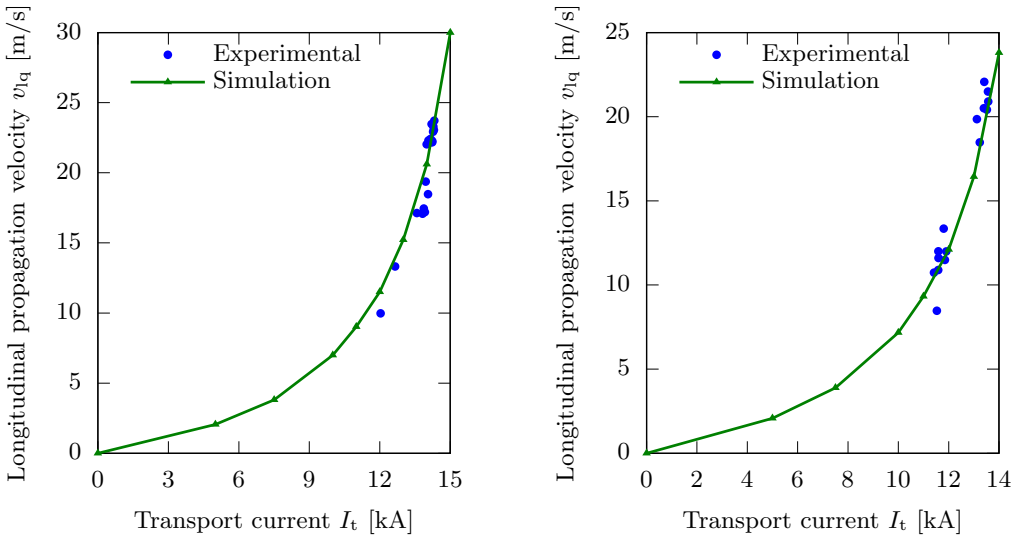

(a) $T_0 = 1.9$ K. (b) $T_0 = 4.2$ K.

Figure 6.17: Comparison between experimental data and THELMA simulations.

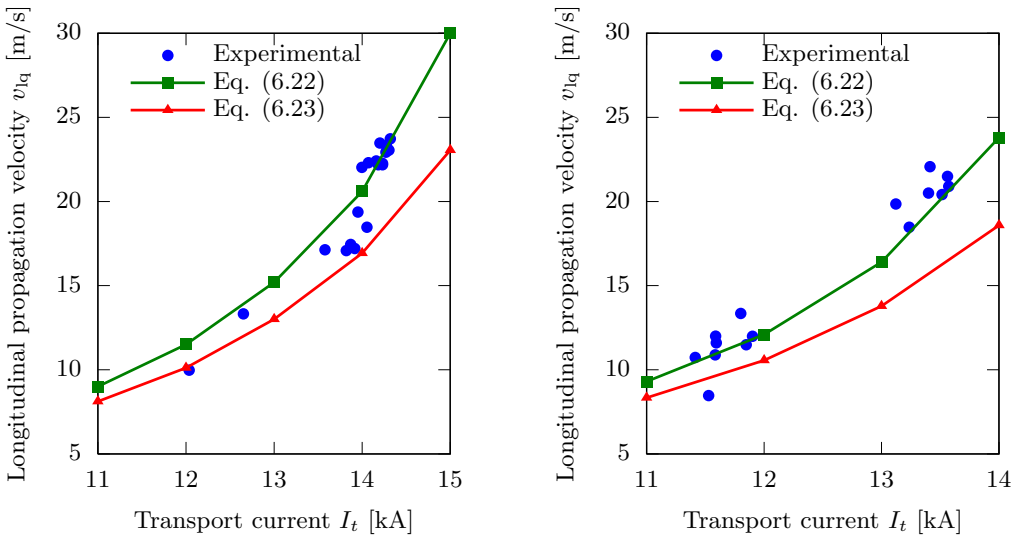

(a) $I_0 = 1.9$ K. (b) $I_0 = 4.2$ K.

Figure 6.18: Computed v_{lq} as a function of I_t and T_0 with different choices for the n-index correlation.

6.19a, the result is an increase in the worst case of more than 40% in v_{lq}, confirming the paramount role of the generation function in these computations.

In a second set of simulations, shown in Figure 6.19b, the applied strain has been set to its reference value but, instead than the correlation Eq. (6.22) several constant values of n-index ranging from 10 to 100 have been employed, to better outline the v_{lq} dependence with n-index. v_{lq} monotonically increases with n-index, with variations respectively of -35% and $+15\%$ at the minimum and maximum values considered, confirming the trend already shown by the previous results.

Magnetic Induction

The computed magnetic induction in the simulated 102-72 section has a peak value of about 12.6 T and a mean value of about 12 T at 14 kA. To assess how much v_{lq} is sensitive to the magnetic induction, other two neighboring magnet sections have been considered: the straight high-field section 61-51 and the straight part of the innermost turn of the section 112-52 (see Figure 6.12). The section 61-51 is the conductor zone exposed to the largest magnetic induction, with a peak value of about 12.8 T and a mean value of 12.5 T at 14 kA, about 0.5 T larger than 102-72. Conversely, a reduction of about 1 T can be estimated in the innermost turn of 112-52, since it is exposed to a peak value of 11.6 T and a mean value of 11.2 T.

The results of these further models are compared with the reference simulations and experimental data in Figure 6.20. As in the case of n-index sensitivity analyses, differences can be observed at large values of magnet current, whereas all the simulations lead to similar results as the current is decreased. The effect of a reduced magnetic induction (case 112-52) is very similar in magnitude to the effect of the reduced n-index described in the previous section, whereas the results of the 61-51 section are very close to the reference case (less than 5% difference).

Also in this case these results can be interpreted in terms of generation temperature, since T_{g} is affected by magnetic induction. At 14 kA, T_{g} can be estimated around 4.3 K in 61-51 section whereas it increases up to about 5.7 K in 112-52 innermost turn.

Other Analyses

Further parametric analyses have been performed to confirm the insensitivity of the propagation velocity to some parameters:

- *Perturbation energy* E_{p}. The reference case at T_0^{ref} and $I_{\mathrm{t}}^{\mathrm{ref}}$ has been examined with increasing levels of deposited energy between 0.1 mJ and 2 mJ. Only negligible differences (up to 1%) have been found on v_{lq}. Also the unlikely case of a simultaneous quench in all the 14 strands has been considered, leading to a insignificant velocity variation of 4%;

- *RRR.* Since, according to the theoretical models (6.9), (6.11) and (6.14), v_{lq} should not explicitly depend on k or ρ_{E}, RRR is not expected to be a sensitive

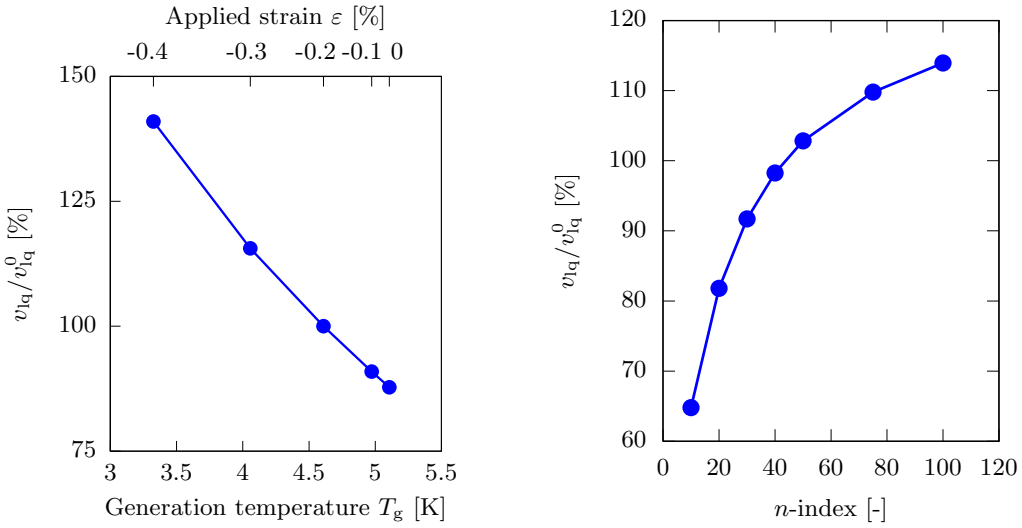

(a) Applied strain / T_g dependance. (b) Constant n-index dependance.

Figure 6.19: Parametric analyses regarding generation function, $T_0 = 1.9$ K and $I_t = 14$ kA.

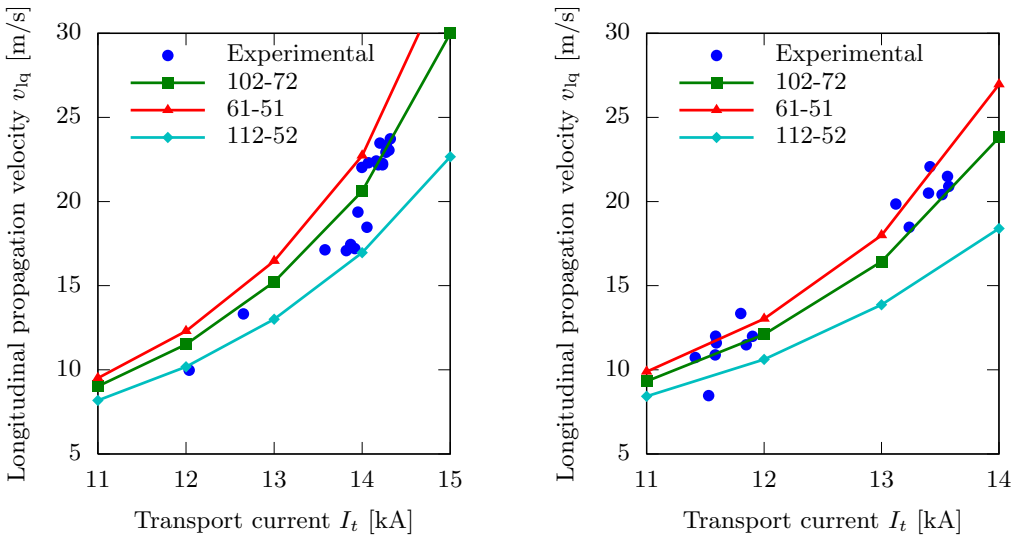

(a) $I_0 = 1.9$ K. (b) $I_0 = 4.2$ K.

Figure 6.20: Computed v_{lq} as a function of I_t and T_0 considering different quench location on the coil and therefore different background magnetic fields.

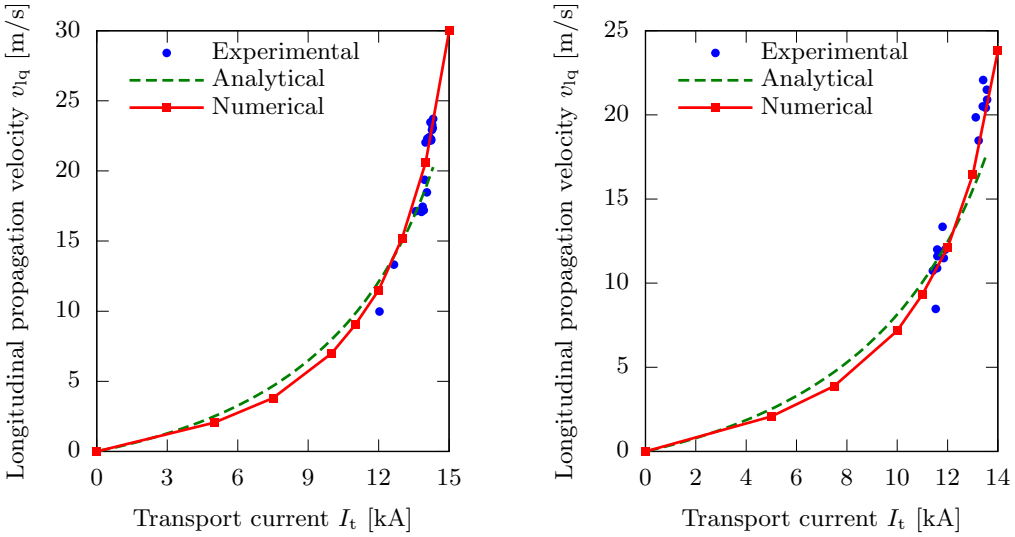

(a) $I_0 = 1.9$ K. (b) $I_0 = 4.2$ K.

Figure 6.21: Summary of experimental, analytical and numerical propagation velocity as a function of I_t and T_0.

parameter in this analysis. The model confirms this assumption, since differences less than 1% can be found if a RRR half and double of the reference value is considered;

- *Inter-strand resistances*. Alternative sets of electrical inter-strand resistances have been considered. The initial transient and the perturbation energy needed to quench the conductor may change with different assumptions, but the impact on v_{lq} is very small also with large variations of R_c and R_a, up to one or two orders of magnitude. The same conclusion applies also for different thermal inter-strand conductances fit functions.

6.6 Conclusions

The phenomenon of longitudinal quench propagation in impregnated coils has been widely studied. Experimental results from a small Nb_3Sn magnet have been analyzed in terms of propagation velocity by means of theoretical models and have been compared with numerical results obtained with the coupled electromagnetic-thermal THELMA code, as shown in Figure 6.21. In all these analyses the role of insulating materials has been discarded, justified by the very low thermal diffusivity of these materials compared to metals. Among the theoretical models, Dresner formula (Eq. 6.11) leads to the best fit, but in any case these models are less accurate in describing the experimental results in the complete available range and they are very

sensitive to the transition temperature T_{tr}. In numerical analyses, a similar large sensitivity can be found considering different models for the generation function, that is affected by both external causes, like the magnetic induction and applied strain, and intrinsic parameters, like the n-index of the strand. Nevertheless, the results of the numerical analyses with THELMA code are very close to experimental data if verisimilar assumptions are considered for some uncertain parameters.

Chapter 7

Current Distribution and Losses in a CICC Magnet

Superconducting cables can carry large amounts of current with insignificant losses in steady state regime. Nevertheless, AC losses can arise in the conductor when the magnetic field is varying. Several dissipative phenomena indeed affect superconducting cables in transient regime. First of all, coupling currents among adjacent strands can arise in varying fields, sometimes induced by the boundary conditions. Their flow is promoted by small inter-strand resistances, and they can lead to a significant heat load. In addition, these coupling currents can arrange in highly uneven current distributions among the strands, producing undesirable over-currents. Furthermore, eddy currents can arise also among different filaments of the same strand and in other metallic components like the CICC steel jacket.

In this Chapter the transient computation of the current distribution and the electromagnetic losses in a CICC through the THELMA code is presented, referring to a turn of the superconducting solenoid NAFASSY. A wide parametric analysis has been performed to assess the magnet stability in the nominal working conditions and to better understand some details of the numerical modeling of CICC. Some original results in terms of current periodicity, boundary conditions and inter-strand resistances modeling are described.

7.1 The NAFASSY Project

The *NAtional FAcility for Superconducting SYstems* (NAFASSY) project aims at setting up a facility at the University of Salerno where full-size superconducting devices and cables will be tested [52]. The core of the project is a 8 T solenoid, characterized by a very large bore diameter of more than 1 m (see Figure 7.1). The main data of the NAFASSY solenoid and conductor are reported in Table 7.1. The CICC is made of 96 Oxford Superconducting Technology (OST) internal-tin Nb_3Sn and 120 copper strands, cladded with a steel jacket to form a rectangular conductor. As shown in Figure 7.2, the cable features two different kinds of triplets: 24 are composed by two superconducting (SC) strands and one copper (Cu) strand, the remaining 48 by two Cu strands and one SC strand. The conductor is cooled by forced-flow helium with a mass-flow rate of 1 g/s, at an inlet temperature of 4.5 K and a pressure of 0.7 MPa.

Table 7.1: NAFASSY magnet and conductor main data.

Inner and outer radii R_i / R_o	0.572 / 0.736 m
Axial length h	1.276 m
No. of cylindrical layers N_r	10
No. of turns per layer N_z	47
No. of strands N_st	96 (SC) + 120 (Cu)
Strand diameter d_st	0.82 mm
Cu/non Cu ratio λ	≈ 1
Cabling scheme	$3 \times 3 \times 4 \times 6$
Twisting pitches t_i	80 / 110 / 135 / 160 mm
Jacket inner sizes	9.2×18.5 mm
Jacket thickness s_j	2.1 mm
Conductor void fraction	29%

NAFASSY will be fed by a power supply capable to deliver up to 20 kA, with maximum voltages +25/-20 V. In nominal conditions, the magnet will produce a peak field in the middle of the bore of about 6.7 T, whereas the maximum field on the conductor will be around 8 T (see Figure 7.3). Since the estimated magnet inductance is 188 mH, because of the limitations in the power supply voltage, the maximum current ramp rate is about 133 A/s, corresponding to a field ramp rate of about 53 mT/s.

In this Chapter the electromagnetic cable losses at different ramp rates and coolant temperatures have been evaluated to assess the magnet stability[1].

[1]Work supported by ENEA with contract "Analisi delle prestazioni del magnete Nafassy mediante il codice THELMA", under grant agreement PON NAFASSY, PONa3_00007. The results are widely reported in [20] and published in [111].

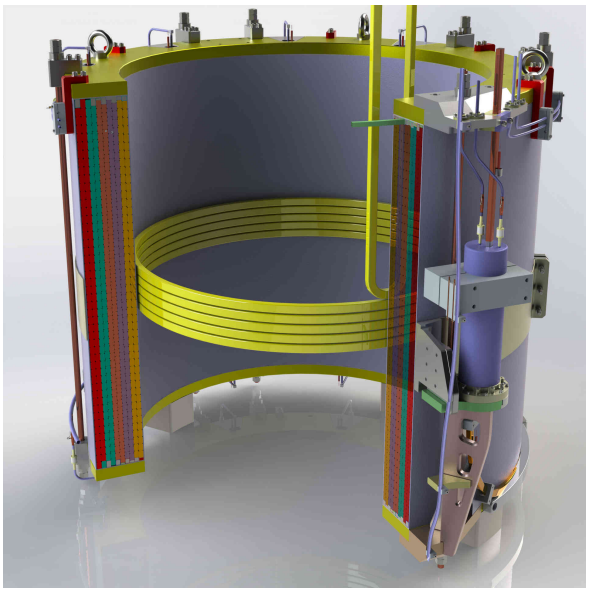

Figure 7.1: Artist view of the NAFASSY magnet [52].

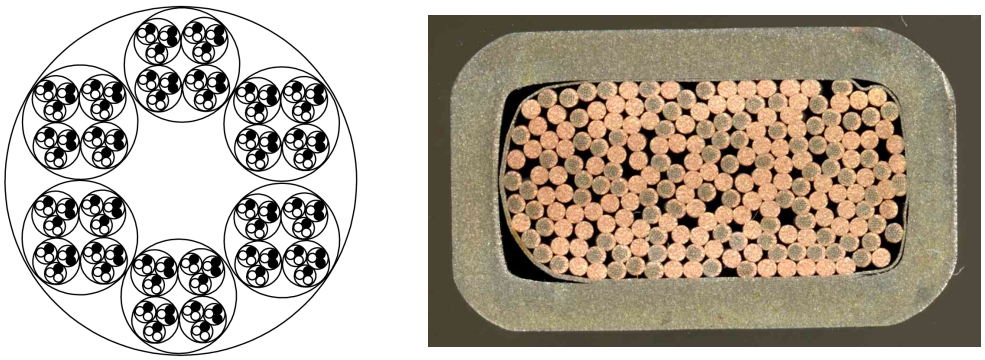

Figure 7.2: NAFASSY conductor [52]. Left: cable layout. Black circles are Nb_3Sn strands. Right: cable cross-section.

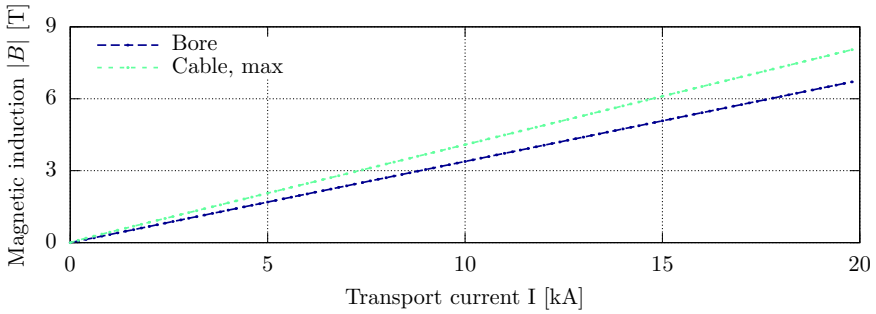

Figure 7.3: Peak magnetic induction module at the bore and in the conductor as a function of transport current.

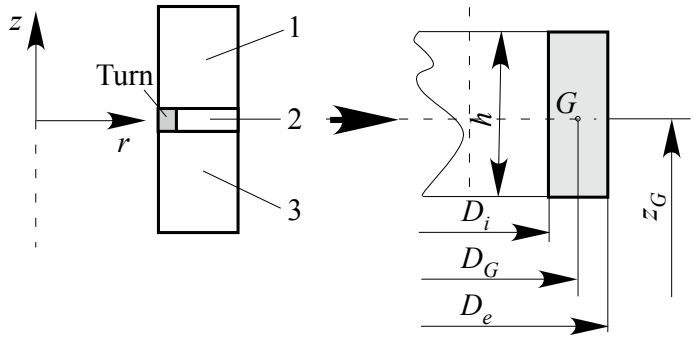

Figure 7.4: NAFASSY magnet model for field computation. Left: magnet cross-section (not in scale), showing the three equivalent sub-solenoids and the modeled turn. Right: geometrical quantities characterizing each sub-solenoid or turn.

Table 7.2: Geometrical parameters for NAFASSY magnet discretization into three sub-solenoids and one individual turn.

Sub-solenoid	Diameter (m) inner D_i	centre D_G	outer D_e	Axial length (m) h	Centre axial coord. z (m) z_G	N. of turns
1	1.150	1.3040	1.458	0.5681	0.2964	230
2	1.1808	1.3194	1.458	0.0247	0.00	9
3	1.150	1.3040	1.458	0.5681	−0.2964	230
Turn	1.150	1.1654	1.1808	0.0247	0.00	1

7.2 Model Description

To limit the computational effort required by the simulation, presently only one turn of NAFASSY is modeled, which is representative of the worst operating conditions in terms of magnetic field. This turn, about 3.7 m long, is located in the innermost cylindrical layer at the magnet middle plane and is fed with a ramped current waveform from 0 to 20 kA. As shown in Figure 7.4, the background field and the inductive coupling with the remaining 469 turns have been computed by means of three equivalent sub-solenoids fed with the same ramped current. Their geometry is described by the parameters reported in Table 7.2.

In the present analysis, a uniform and constant helium temperature is assumed along the cable. The heat exchange between helium and the cable is represented by advective thermal conductances G_{i,He_h}, computed considering the wetted perimeter of the individual CEs and the typical correlations used for the heat exchange in CICCs[2]. For example, at 4.5 K the heat exchange coefficient can be estimated

[2]See Section A.5.1, page, 205.

around $h_c = 550$ W/(m^2·K) [52]. The assumption that the helium temperature is uniform along the cable is a simplification, albeit a minor one, as it has been carefully checked and reported in Section 7.3.5. The GANDALF code [31] has been indeed preliminary used to estimate the magnet maximum helium temperature, without considering electromagnetic losses. This temperature, increased by a suitable safety margin, has then been used in the THELMA code to conservatively compute the electromagnetic losses. Finally, the impact of these losses on the helium temperature has been evaluated by an *a posteriori* analysis, so as to check that the corresponding temperature increase never exceeds the assumed safety margin.

7.2.1 Cable Model

Since a model for the rectangular cross-section geometry is presently not available, an equivalent cable with circular cross-section with the same void fraction has been considered. Different models of the NAFASSY cable cross-section have been used, to describe the cable with increasing levels of detail, as shown in Figure 7.5. Equivalent cable-elements are considered, whose electrical and thermal properties are computed on the basis of the represented strands. The material is modeled as an homogenous medium, whose properties are calculated through a weighted mean of copper and superconductor fractions according to the Cu/non Cu ratio λ. To keep the computational cost under reasonable limits, the discretizations into 6 CEs (last cabling stage), 24 CEs (last-two stages) and 72 CEs (last-three stages) have been considered. If not explicitly mentioned, the results will refer to the most detailed discretization model (72 CEs). In Figure 7.6 and 7.7 the computed magnetic induction along one of the 72 CEs discretization is reported, showing a variation of more than 1 T depending on the CE position.

The cable-elements have been discretized into the same number of thermal and electromagnetic longitudinal elements, with an length of about 2 cm, to have at least 4 elements per minimum twist pitch, on the basis of experience gained on similar analyses on CICCs [47].

The strand critical current has been modeled with the Durham scaling law and the commonly used n-index correlation with critical current has been assumed[3], with parameters $r = 2.8$ and $s = 0.45$ [168]. A total axial strain $\varepsilon = -0.70\%$, including the intrinsic thermal pre-compression has been assumed. This value is conservative compared to the typical performance degradation when passing from the individual strand to the jacketed cable [179].

7.2.2 Inter-Strand Resistances Calibration

The inter-strand resistance is a crucial parameter in the analysis of current distribution and losses of a CICC. In the case of NAFASSY no measurements of the

[3] The parameters for the scaling law are reported in Table 2.4, page 42, as regards the internal-tin strand. The correlation between n-index and critical current (Eq. 1.23) for this internal-tin strand is reported in Figure 1.12, page 18.

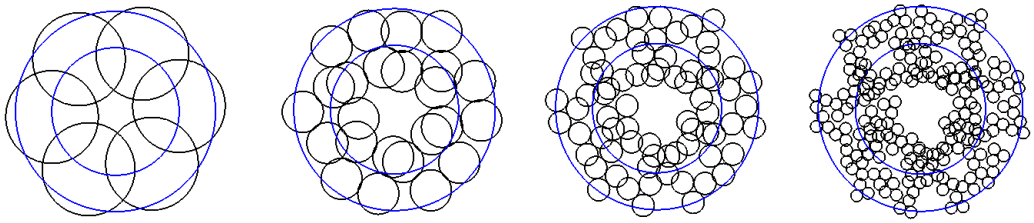

(a) 6 CEs. (b) 24 CEs. (c) 72 CEs. (d) 216 CEs.

Figure 7.5: Different discretizations for the NAFASSY magnet conductor.

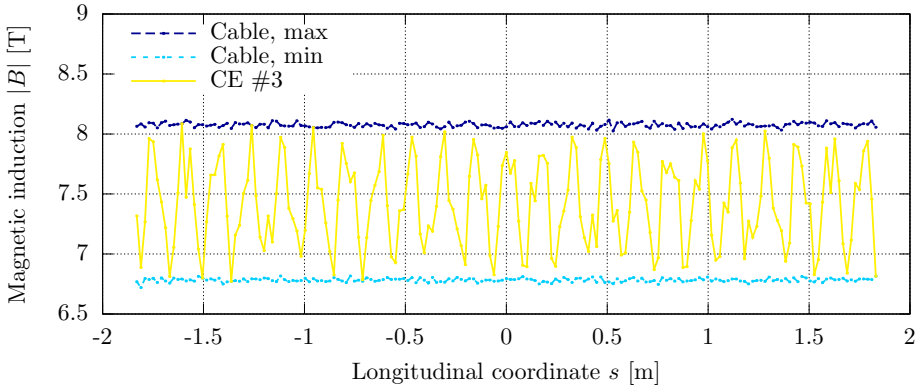

Figure 7.6: Computed magnetic induction module along the longitudinal coordinate of the modeled turn at a transport current of 20 kA. The maximum and minimum values are represented together with the field along one of the cable elements of the 72 CEs discretization.

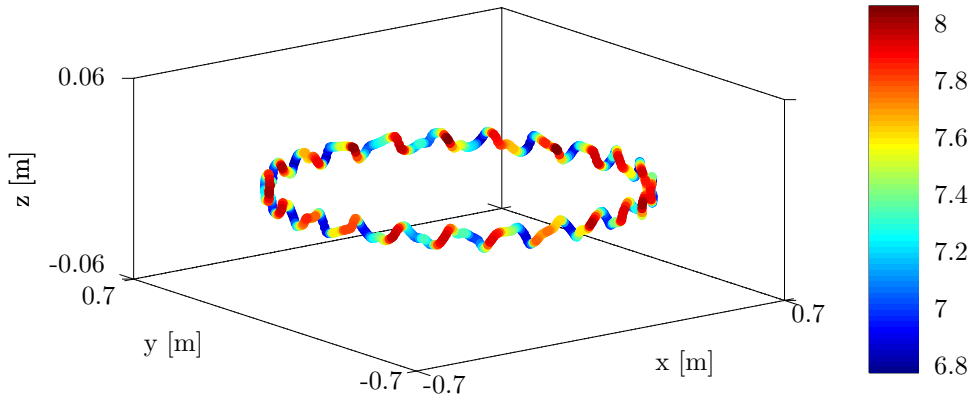

Figure 7.7: Computed magnetic induction module along one cable-element of the 72CEs discretization in the modeled turn at a transport current of 20 kA. The cable-element cross section is not in scale.

inter-strand resistances are available for the adopted cable, therefore the elementary strand contact resistances have been determined considering a 40 cm sample of the ITER EUTF3-EAS cable[4]. This sample has been chosen since its strand is characterized by a similar diameter (0.81 mm, [40]) and the cable has a similar void fraction (28%, [123]). As a conservative approach, the values measured at the maximum mechanical load have been considered, since the resistances are reported to decrease with increasing applied load, enhancing coupling losses.

After the model calibration, the computation of the NAFASSY inter-strand resistances has been performed. When the strands are grouped into equivalent cable-elements, their contact resistance should take into account the contribution of all the represented strands. To guarantee the geometrical congruence between different cable discretizations, a detailed cable model with all 216 NAFASSY strands has been created, in which the EUTF3-EAS strand elementary contact resistance has been assigned to both SC and Cu strands. The inter-strand resistances between each couple of strands of the complete NAFASSY cable have been therefore computed. Finally, the contact resistance between two cable-elements has been estimated for each NAFASSY discretization considering the parallel of the contact resistances between the strands represented by these cable-elements. A sketch of this procedure is reported in Figure 7.8.

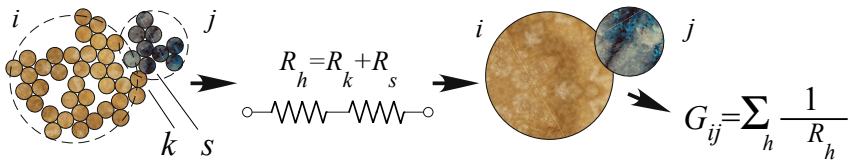

Figure 7.8: Sketch of the contact resistance computation for NAFASSY.

This approach is thorough for the contacts between two SC strands, since their longitudinal resistance is negligible and they can be effectively considered in parallel. An underestimation of the contact resistance is instead introduced for the Cu strands, since the current may experience also a part of their longitudinal resistance, as discussed in Section 4.3 and Appendix E. This aspect will be discussed in one of the following parametric analyses.

7.3 Results

7.3.1 Current Distribution Among the Cable Elements

In the following, the currents along the cable-elements are represented in terms of *adimensional currents* $i_k^{\mathrm{a}}(s,t)$, defined as:

$$i_k^{\mathrm{a}}(s,t) = \frac{i_k(s,t)}{i_k^{\mathrm{id}}(t)}, \tag{7.1}$$

[4]See Section 4.5.2, page 96 for the details of this analysis.

where $i_k(s,t)$ is the current in the k^{th} cable element at the curvilinear coordinate s along the cable and time t, and $i_k^{\text{id}}(t)$ is the ideal share of cable transport current, supposed uniform among each cable-element. In the absence of current redistribution i_k^{a} are constant. It must be noted that the conservative assumptions considered for the electric inter-strand resistances (see Section 7.2.2) enhance the non-uniformity in the current distribution among the cable elements.

In Figure 7.9 the computed i_k^{a} along the magnet turn at the 90% of a 133 A/s ramp are reported for the three cross-section discretizations. As expected, in Figure 7.9a the 6 CEs discretization shows local over-currents characterized by a space period equal to the fourth stage twist pitch, 160 mm, due to the periodic distribution of the mutual inductances with respect to the whole magnet.

A different current pattern can be observed in Figure 7.9b, that refers to the 24 CEs discretisation. The current distribution periodicity is evident in Figure 7.10a, that shows also the consistency between the current in a 24 CEs cable-element and the sum of the currents of the corresponding sub-bundles of the 72 CEs discretization, demonstrating the stability of the simulation results with discretization. The current pattern obtained is indeed not a simulation artifact, being related to the periodicity of the inter-strand contacts, already reported in other cases [61]. For two strands in adjacent bundles in a cable with two stages only, the space period p_{cont} of the contact along the cable axis can be found zeroing the function $\Phi_{1,2}$:

$$\Phi_{1,2}(x) = \frac{s_2(x)}{t_1} - \frac{x}{t_2} - k, \tag{7.2}$$

where t_i are the twisting pitches, $k \in \mathbb{N}$ and $s_2(x)$ is the length of the second stage at cable axis coordinate x, that can be computed as the length of a circular helix with radius r_2:

$$s_2(x) = x\sqrt{1 + \left(\frac{2\pi r_2}{t_2}\right)^2} = \gamma_2 x. \tag{7.3}$$

When $\Phi_{1,2} = 0$ the phase difference between stages 1 and 2 is zero: this means that the geometry is periodic with a periodicity p_{cont} that is:

$$p_{\text{cont}} = \frac{t_2 t_1}{\gamma_2 t_1 - t_2}. \tag{7.4}$$

The current loops tend to close their path in sections spaced by this periodicity since, at these locations, the cable geometry gives a similar contacts pattern. In the present case, for the 24 CEs discretization a periodicity $p_{\text{cont}} \approx 0.8$ m is obtained, clearly visible in Figure 7.10a.

In the case of three or more stages, a possible periodicity can be found by imposing for each couple of adjacent stages $(i,\, i+1)$ the functions $\Phi_{i,i+1}$:

$$\Phi_{i,i+1}(x) = \frac{s_{i+1}(x)}{t_i} - \frac{s_{i+2}(x)}{t_{i+1}} - k_{i,i+1}, \quad i = 1, 2, \ldots n_{\text{st}} - 1 \tag{7.5}$$

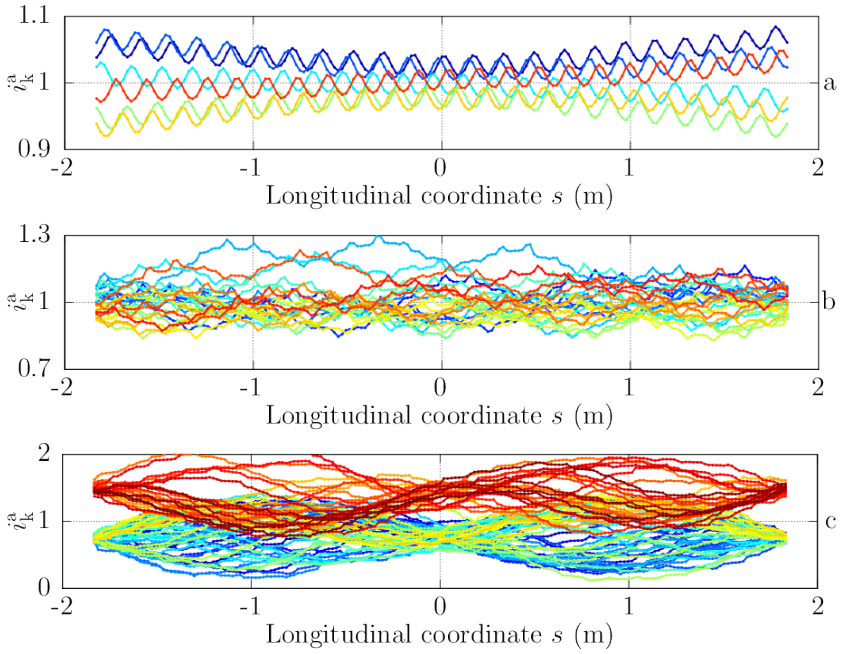

Figure 7.9: Current distribution along cable elements at 90% of the ramp for 6 (a), 24 (b) and 72 (c) CEs discretizations. In the last case, on average, the triplets corresponding to two SC strands (hot colors) carry twice the current carried by the triplets corresponding to one SC strand (cold colors).

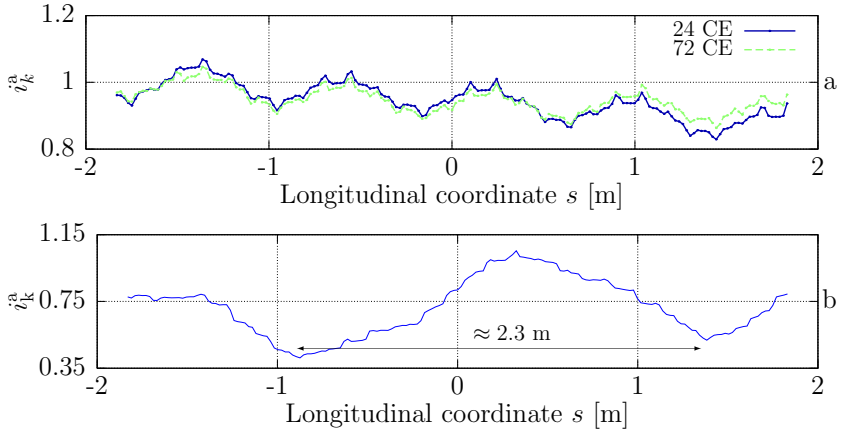

Figure 7.10: Currents distribution at the 90% of the ramp. Above: one cable element of the 24 CEs discretization compared with the sum of the currents of the corresponding sub-bundles of the 72 CEs discretizations. Below: one cable element of the 72 CEs discretization, showing the quasi-periodicity of 2.3 m.

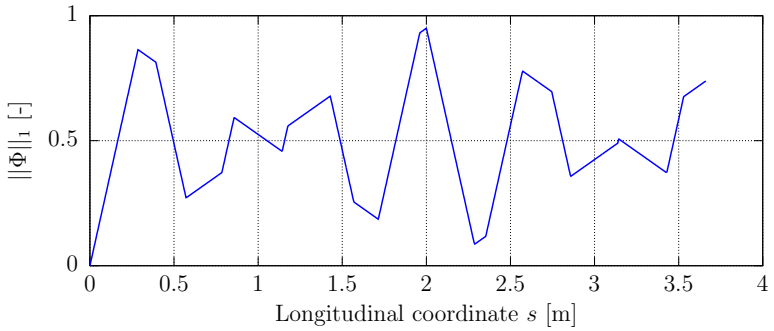

Figure 7.11: Function $||\Phi||_1$ describing quasi-periodicity of the contact patterns.

where n_{st} is the number of cabling stages and $s_i(x)$ is the length of the i^{th} stage at cable axis coordinate x. In particular, $s_{n_{\text{st}}+1}(x)$ is the length of the cable axis, equal to x. $k_{i,i+1}$ are suitable integers representing the number of cycles of difference between stage i and $i+1$. As an example, in the case of three stages the following system is obtained:

$$\Phi_{1,2}(x) = \frac{s_2(x)}{t_1} - \frac{\gamma_3 x}{t_2} - k_{1,2}, \tag{7.6}$$

$$\Phi_{2,3}(x) = \frac{\gamma_3 x}{t_2} - \frac{x}{t_3} - k_{2,3}. \tag{7.7}$$

For a cable with n_{st} stages, the exact geometry periodicity at coordinate p_{cont} could be found if:

$$\Phi_{i,i+1}(p_{\text{cont}}) = 0, \qquad \forall i = 1, 2, \ldots n_{\text{st}} - 1 \tag{7.8}$$

However, for $n_{\text{st}} > 2$ the system hardly has solutions for $k_{i,i+1} \in \mathbb{N}$. Furthermore, $s_i(x)$ can be easily expressed only for the last stage, being the lower order stages geometry not a simple helix.

Actually, considering the cable geometrical tolerances and the contact geometry, the problem of the periodicity could be cast in a less stringent way considering a *quasi-periodicity*, in which Eq. (7.8) are not zero, but sufficiently small. In this case, two strands in contact at a given section may be sufficiently close to each other after a quasi-period so that very few inter-strand contacts are necessary for the current to pass from one to the other. In this way the resistance between these two strands becomes negligible and a current loop can carry non-negligible currents. A reasonable indicator of this quasi-periodicity is therefore the l_1 norm:

$$||\Phi||_1 = \sum_{i=1}^{n_{\text{st}}-1} |\Phi_{i,i+1}| \tag{7.9}$$

Applying this approach to the 72 CEs discretisation, Figure 7.11 can be obtained. A local minimum of $||\Phi||_1$ at about 2.3 m can be noticed, and this quasi-periodicity is visible in the current distribution of several cable elements, like in Figure 7.10b.

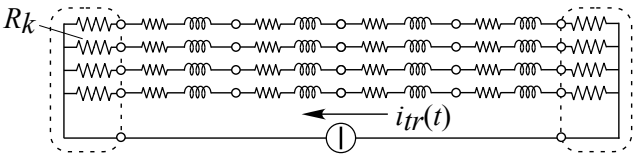

Figure 7.12: Equivalent circuit representing the boundary conditions.

Although no simulation has been performed with all 216 CEs, different current distributions along the cable are not expected in this case, since the first stage twist pitch is exactly the half of the last stage one, thus the contact pattern quasi-periodicity is conserved, as demonstrated by the computation of $||\Phi||_1$ considering all the four stages. Further similar minima can also be found for distances much larger than the turn length, but they are expected to have a minor effect on the magnet performance, being characterized by much larger time constants and subjected to a reduced magnetic field variation, extending on more than one turn.

7.3.2 Choice of the Boundary Conditions

When a part of a coil is modeled, in the present case a single turn, a Neumann boundary condition, that is a uniform current distribution, has been frequently assumed among the strands at the model boundaries, e.g. see [144]. For the NAFASSY magnet a parametric model has been adopted, in which the cable elements are connected at their ends to two suitable stars of resistors, as shown in Figure 7.12. These resistors must also be representative of the magnet terminations.

As a reference, the resistance $R_{\mathrm{term}} \approx 0.5\ n\Omega$ of a typical ITER Nb_3Sn sample termination [41] has been chosen. This termination can be considered as the parallel of about 1000 SC strands, so that an elementary strand-termination contact resistance $R_{\mathrm{term-str}} = 0.5\ \mu\Omega$ is estimated per each superconducting strand of this cable. The waveforms reported in Figure 7.9 have been obtained adopting this value. In addition to this reference case, the following cases have been studied:

a) $R_{\mathrm{term-str}}$ ten times bigger, that leads to a *quasi-Neumann* boundary condition in which the current is almost equally distributed among the SC part of the cable elements;

b) $R_{\mathrm{term-str}}$ ten times smaller, that leads to a *quasi-Dirichlet* boundary condition in which the cable ends are nearly two equipotential surfaces;

c) the case of a random distribution of resistances $R_{\mathrm{term-str}}$, obtained with a gaussian random perturbation of the reference value with a standard deviation $\sigma = R_{\mathrm{term,str}}/3$, as shown in Figure 7.13.

Figure 7.14 reports i_k^{a} along the magnet turn at the 90% of a 133 A/s ramp for the different boundary conditions. The case b) (quasi-Dirichlet) leads to the highest inhomogeneities. On the other hand, in the case a) (quasi-Neumann) the current

imbalances are quite similar to the reference case of Figure 7.9c. Higher current imbalances can be observed all along the turn also with a random distribution of the boundary resistances (case c). Since the actual distribution of currents at the turn ends cannot be predicted, a parametric evaluation of this type should always be carried out when the magnet terminations are not explicitly included in the model.

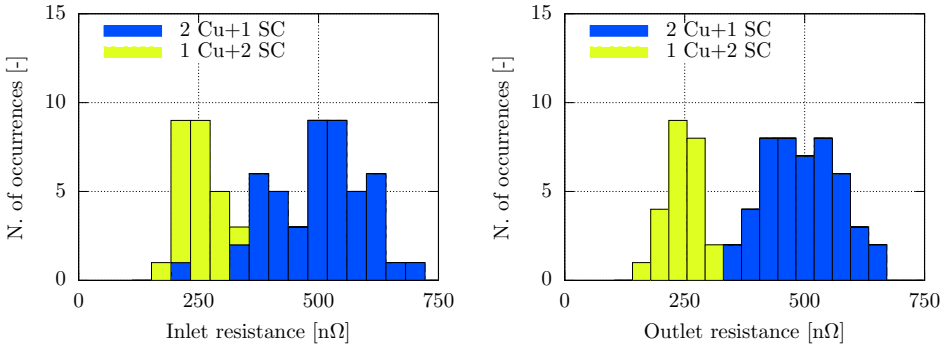

Figure 7.13: Inlet and outlet resistances histograms for the two triplet types.

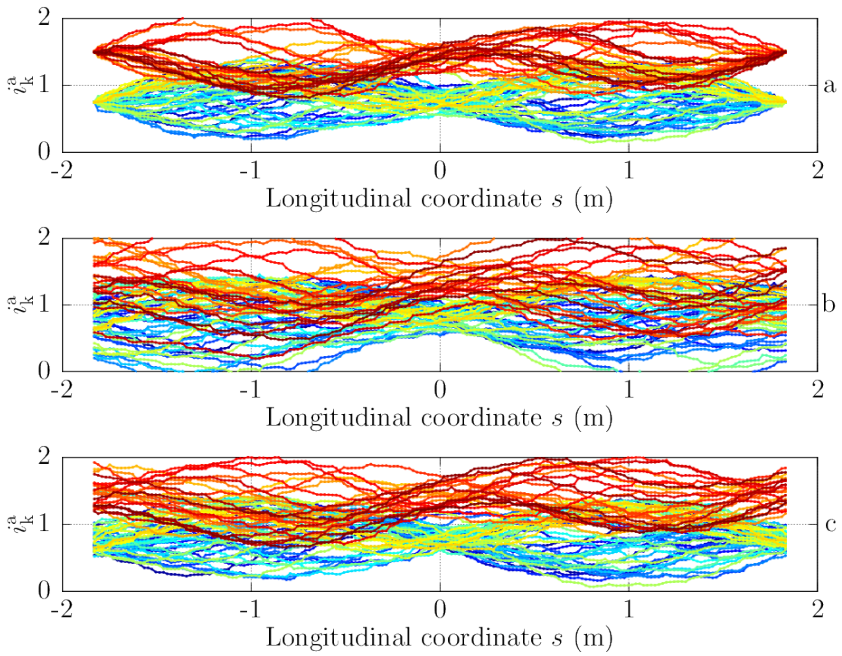

Figure 7.14: 72 CEs discretization, current distribution at 90% of the ramp for low (a), high (b) and randomly distributed (c) boundary resistances. See Figure 7.10c for the reference case.

7.3.3 Computed Losses

The cable losses analysis has been performed considering both *AC coupling losses*, due to the current redistribution among the cable elements through the contact resistances, and *DC losses*, due to the local current redistribution between the superconducting and the resistive zones of the cable elements.

AC losses depend on the square of the ramp rate and are almost independent on the coolant temperature. Simulations at different ramp rates (80, 100 and 133 A/s) have therefore been performed. A comparison of the current distributions at different ramp rates at the 90% of the ramp is reported in Figure 7.15, in which the ramp rate dependance of the uneven current distribution is evident. In Figure 7.16a the AC losses are reported as a function of the transport current for the three different values of ramp rate. These losses become constant with the transport current after a certain settling time for the coupling currents.

The over-currents also lead to DC losses, since the cable elements carrying more current can locally approach the critical current density, and this causes a longitudinal electric field according to the power-law[5]. This can be seen in Figure 7.17 in terms of *current margin* defined as:

$$i_k^{cm}(s,t) = 1 - \frac{i_k(s,t)}{i_k^c(B,T,\varepsilon)}, \tag{7.10}$$

where $i_k^c(B,T,\varepsilon)$ is the k^{th} cable element critical current, computed as a function of magnetic induction, temperature and strain at curvilinear coordinate s and time t. In some cable elements representing the triplets with only one SC strand, a current margin close to zero or even slightly negative is visible, since the transition between the superconducting state and the normal-state is not sharp. When the ramp ends (after 150 s, Figure 7.17c) the coupling currents decay and a large current margin is obtained again. DC losses are temperature dependent, therefore simulations at different coolant temperatures between 4.5 and 6 K have been performed. In Figure 7.16b the DC losses are reported as a function of transport current at the maximum ramp rate for three different values of coolant temperature. In the present case the DC losses are much smaller than AC losses, since they develop only in the very last part of the ramp and with a lower peak value, thus the corresponding delivered energy is smaller.

In any case, the magnitude of the total computed losses is not large enough to trigger an instability in the conductor, since the corresponding computed cable temperature increase is very small in any case (less than 10^{-2} K).

With the most detailed discretization (72 CEs) each triplet is represented as a single cable-element, thus the intra-triplet AC losses, associated with current loops entirely laying along the triplet strands, are not considered. However, these losses should have a minor impact, since the intra-triplet loops are characterized by a much smaller area compared with the loops between strands of different cabling stages.

[5] See Eq. (1.21), page 17.

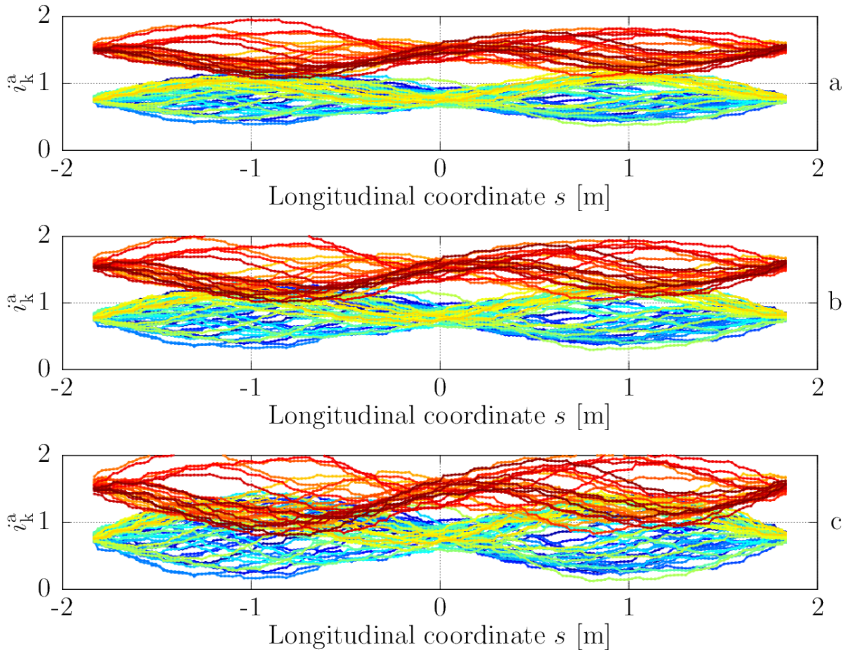

Figure 7.15: Adimensional currents along the curvilinear coordinate at 90% of the ramp, 80 A/s (a), 100, A/s (b), 133 A/s (c).

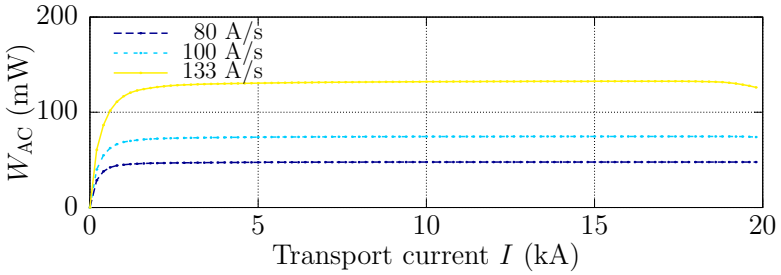

(a) AC coupling losses at three different ramp rates.

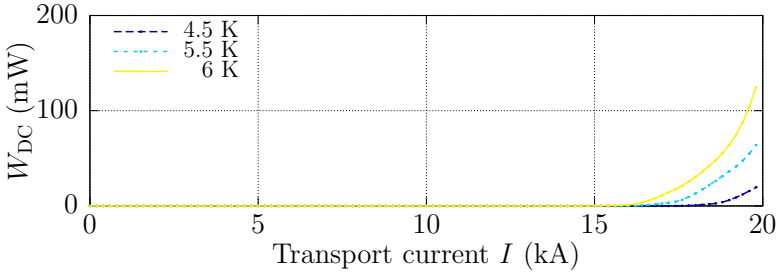

(b) DC losses at three different cooling helium temperatures.

Figure 7.16: Cable losses as a function of transport current.

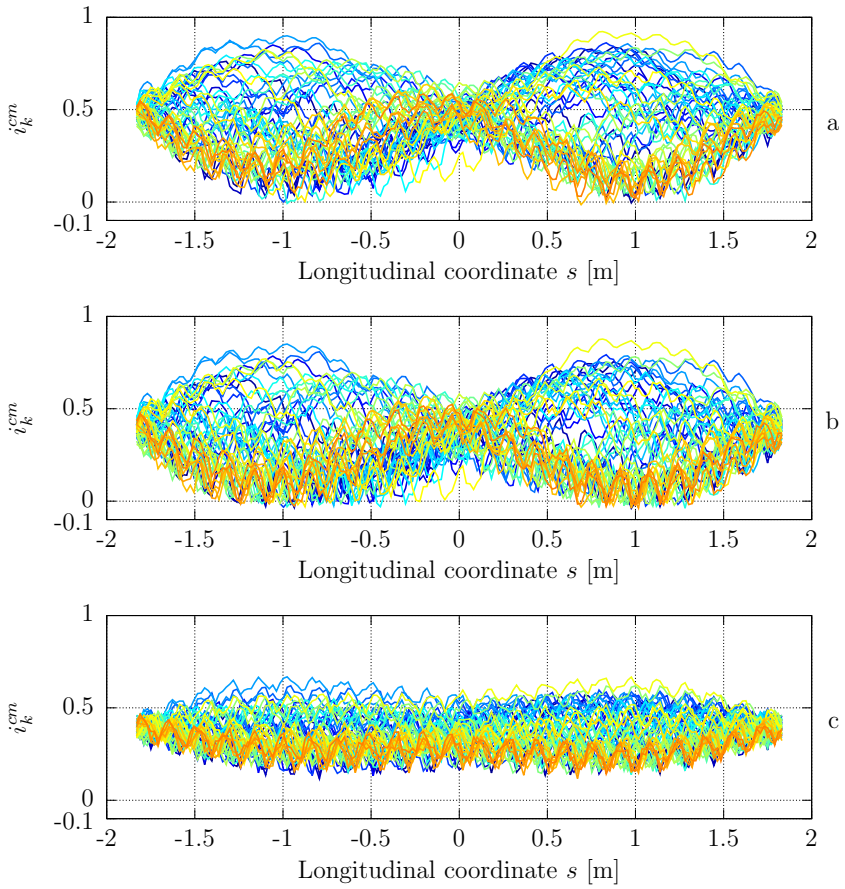

Figure 7.17: Current margin at 4.5 K, 133 A/s, triplets with 2 Cu strands and 1 SC strand at 140 (a), 150 (b) and 155 s (c).

The induced e.m.f. and the resulting losses should accordingly be much smaller. Moreover, the two thirds of the triplets include only one superconducting strand: any current loop internal to these triplets should lay along at least one copper strand with consequent very high loop resistances and negligible currents and losses.

7.3.4 Further Parametric Analyses

The accuracy of model assumptions and unknown parameters has been checked by means of some parametric analyses.

The Cu strand longitudinal resistance causes an underestimation of the contact resistances, as already explained in Section 7.2.2, and this involves an overestimation of the coupling losses. The significance of this aspect has been assessed by means of two further simulations. In a first case, all the contacts with Cu strands have been neglected, leading to a strong reduction of coupling currents, obtaining a dramatic losses reduction by about 75%. In a second case, the Cu contact resistances

have been considered again but with a suitable resistance added in series to the Cu strand elementary contact resistance. This additional term could represent the contribution of a possible short longitudinal path along the Cu strand. The length of this path is consistent with the diffusion length between one normal-conducting and one superconducting strand in contact, as estimated by Eq. (E.20). In this case the losses are reduced by 25% compared to the nominal case. The contacts with Cu strands cannot be therefore neglected to obtain a conservative estimation of the coupling losses.

The effect of the boundary conditions on the losses has also been considered, but substantial differences have not been found. Even in the unrealistic quasi-Dirichlet boundary assumption, the losses are only 10% higher than the nominal ones, whereas in the other cases the difference is less than 4%.

The performances of a similar cable with a smaller void fraction, 24% instead than 29% have been also analyzed. In principle, this should lead to higher coupling losses due to the increased number of contacts between strands. This is confirmed by the model which gave an increase of the AC losses by about 25%, however, with a still acceptable cable temperature increase.

Finally, some further checks have been performed. Different cable bundles initial angular phases[6] have been considered, but only minor differences have been found (less than 1%). Also different choices for contact thermal conductances between strands and a heat exchange coefficient h_c reduced by 50% did not affect the results appreciably.

7.3.5 Overall Magnet Stability

Assuming the inlet He temperature of 4.5 K, the magnet maximum helium temperature computed by the GANDALF code is 5.7 K [52]. To estimate the contribution of the EM losses, the following heat balance has been considered:

$$\dot{m}\Delta h = \int_0^l p_{\mathrm{EM}}(x) d\, x \tag{7.11}$$

where $\dot{m}$ is the mass-flow rate (kg/s), assumed constant, Δh is the helium specific enthalpy[7] variation (J/kg) and p_{EM} are the EM losses per unit length, averaged along the ramp. The upper integration bound l is estimated on the basis of the distance covered by the helium at the nominal $\dot{m}$ during the ramp ($l \approx 25{-}30$ m). To compute Eq. (7.11), it is assumed a uniform p_{EM}, obtained from the total losses (AC+DC) at 6 K computed in the magnet mid-plane turn, just described in Section 7.3.3. These are conservative assumptions, since the losses mitigate in the other turns due to the lower magnetic induction and He temperature. Following this approach, the He maximum temperature can be estimated to rise up to 5.85 K for the cable with the nominal void fraction, and to about 5.9 K for the one with lower void fraction.

[6] See Section 3.2.2, page 61.
[7] See Figure A.18, page 207.

Since no instability was found in the modeled turn and the maximum temperature is smaller than the temperature used for the losses computation, the conclusion that the magnet can operate safely up to the maximum ramp rate provided by the power supply.

7.4 Conclusions

The current distribution and losses in a CICC turn of NAFASSY magnet subjected to current and field ramps have been studied with the coupled THELMA model. The results of the simulations confirm the magnet safe design at the maximum current ramp rate deliverable by the power supply, even in very conservative assumptions. Furthermore, the analyses have highlighted some interesting aspects of the CICC behavior to be taken into account when modeling this type of objects.

In particular, the possibility of quasi-periodic current distributions along the cable elements has been demonstrated. This phenomenon is related to the periodicity of the inter-strand contact pattern and it is due to the interaction between subsequent twist pitches, that can create favorable paths for the current.

The influence of the boundary conditions on the model results has been checked, showing that they can affect the current distribution not only along a limited length but all along the conductor. However, in NAFASSY this does not affect remarkably the losses, even in the case of an unrealistic Dirichlet-like assumption.

Finally, the role of contacts with the Cu strands has been analyzed, showing that these contacts should not be neglected, since this may result in an unacceptable underestimation of the AC coupling losses.

It must be noted that the results presented in this Chapter should be experimentally validated through a comparison of the computed AC losses with the measured values, in order to check if the qualitative behavior is well represented by the numerical model and to assess if the hypotheses made in these analyses, in particular on the inter-strand resistances, are adequate.

Chapter 8

Conclusions

The aim of the present work was the development and application of the numerical code THELMA, capable to deal with a large class of problems in the field of superconducting cables research. The purpose of the THELMA code is to analyze in detail the very complex physics of superconducting cables, to grasp all the available information from experimental data, that are generally neither simple to understand nor completely exhaustive. These results can then be used in predictive analyses for the design and the definition of the operative limits of future projects.

The conclusive discussion is split into three parts. The first is devoted on the main aspects regarding the numerical modeling from the point of view of the analysis tool development. The second part is instead more focused on the effective results regarding the behavior of superconducting cables that the numerical analyses have pointed out during the PhD activity. Finally, possible future developments for this research are discussed.

Numerical Modeling

During this PhD activity, the original part of the THELMA code has been improved significantly, both in terms of available features, results accuracy and computational efficiency. The development of the two brand-new modules for the description of the *Rutherford cable* and for the *thermal analysis*, coupled with the pre-existing electromagnetic modules, has indeed enabled numerical analyses previously not feasible, reagarding the cables for accelerator magnets, as reported in chapter 6. In addition, as demonstrated for example by the analysis described in chapter 5, the coupled model is able to reproduce experimental data with a reduced number of given input parameters compared to the electromagnetic model alone.

As regards the thermal model, the *equivalent lumped network* has demonstrated his effectiveness. The most important strengths of this approach are its *flexibility* and *modularity*. The thermal model can indeed deal with very different problems, such as adiabatic cases or forced-flow cooling, with only simple and automatic modifications to the network. Moreover, the addition of further new features or special-

purpose modelings is very simple, since it suffices to define an adequate equivalent network component to be added to the model. Furthermore, the resulting system of differential equations can be solved quite efficiently even in a completely non-linear network, thanks to the *modified node analysis method*.

The choice of an *explicit coupling* among thermal and electromagnetic models has greatly supported the development of efficient, general-purpose and reusable software, taking advantage of the modularity of such an approach. The proposed heuristic for the switching between thermal and electromagnetic models, based on the evaluation of the maximum temperature increase in the step-size as reported in Section 3.5, leads to accurate results with an acceptable and easy-to-control computational effort.

In each of the case studies reported in the present work, a *detailed sensitivity analysis* of the most critical parameters has been accurately performed. This is *absolutely mandatory* in any case, in particular in applied superconductivity, where the number of uncertain or even unknown parameters is huge and a dramatic variation of the results with even tiny modifications in the input data may derive from the strongly non-linear and unstable behavior of materials. Moreover, this parametric approach leads to an in-deep comprehension of the problem analyzed and to a synthesis of the fundamental information embedded in the available experimental data. The increase in the numerical efficiency of the code, that has been a significant part of the PhD activity, was thus fundamental.

Discussion of the Results

Several numerical analyses have been performed during this PhD activity, both in the field of Rutherford cables and CICCs. Three main aspects are discussed here: the inter-strand resistances, the quench propagation in Nb_3Sn Rutherford cables and the current distribution in CICCs during transients.

Inter-Strand Resistances

Numerical analyses on experimental measurements on electrical inter-strand resistances have been performed for both Rutherford cables and CICCs, as reported in chapter 4. Completely different approaches must be considered in the two cases.

In the first case, the commonly used volt-amperometric techniques for the inter-strand resistances measurement are quite useful to estimate the parameters in the case of large cross-over resistances compared to the adjacent ones ($R_c \gg R_a$), but the presence of inhomogeneities such as asymmetries in the core placement and incomplete coverings can significantly complicate the task. In such cases, the numerical analyses are very useful to assess the order of magnitude of the parameters and the most important dependencies. However, more accurate results can be determined only in the presence of further experimental findings. For example, an accurate inspection of the measured sample can give information about the actual *core position*

and width, whereas a comparison with measurements on non-cored cable samples subjected to the same heat treatment and mechanical load can better outline the role of the core in the overall cable behavior. From the point of view of the numerical modeling, being the Rutherford cable geometry very well controlled and known, a *deterministic approach* based on the role of inhomogeneities, such as the core width and placement or localized defects, must be addressed.

In the case of CICCs, completely different criteria should be applied. The complexity and randomness of CICC geometry can be accurately analyzed only thanks to a *statistical approach*, that is fundamental from both an experimental and a numerical point of view. On one hand, the number of experimental samples taken must be representative of the statistical dispersion of the resistances, on the other hand numerical analyses must be performed considering a large number of different geometry configurations in order to infer general properties of the object analyzed. In any case, it must be recalled that *all the strands contribute* in a inter-strand resistance measurement in a CICC cable, not only the couple of strands under test. The presence of normal-conducting segregated strands must be accurately considered, since their contribute to the current exchange and therefore to the AC losses is not negligible, due to the phenomenon of the current diffusion between normal-conducting and superconducting strands.

Quench Propagation in Nb_3Sn Rutherford Cables

The longitudinal quench propagation in Nb_3Sn Rutherford cables has been widely studied, comparing experimental data with both analytical and numerical tools, as described in chapter 6. The *analytical models* for the quench longitudinal propagation velocity, such as the Wilson or Dresner formulas, can outline the functional dependance of some physical quantities such as the transport current density, but have some important drawbacks. Such estimates indeed neglect the current-sharing regime, since are based on the hypothesis of an abrupt transition from superconducting to normal-conducting state at a *transition temperature* T_t. The *generation function*, i.e. the power generated by the superconducting cable as a function of the temperature, is therefore represented as a step function. This can be a reasonable assumption for Nb-Ti or even for Nb_3Sn at low values of transport current, but it is not verified as the transport current density becomes a considerable percentage of the critical current density. In these conditions, the analytical models fail in reproducing the experimental data and become very sensitive on the value used as transition temperature.

Numerical analyses offer a more accurate description of the *current-sharing regime*, resulting in a good agreement between simulations and experimental data also at very large transport currents. Nevertheless, even in this case several uncertainties can affect the estimates. The generation function depends indeed on the cable *voltage-current characteristic*, that is affected by several external causes, such as the background magnetic field or the applied strain, and by intrinsic effects, such as the *n-index* and its correlation with the other superconducting parameters. In ad-

dition, the knowledge of the voltage-current characteristic in superconducting wires is yet incomplete and it should be therefore further investigated, as demonstrated by the statistical approach presented in Appendix B.

It must be noted that all these considerations should apply also to the high-temperature superconductors (HTS), perhaps even emphasized, since in that case the current-sharing regime spans over a broader temperature range. Since in HTS the longitudinal propagation velocity is much smaller than in niobium compounds, being therefore a serious concern for the quench protection systems, a more in-deep knowledge of the current-sharing mechanism is probably required for future improved designs.

Transient Current Distribution in CICCs Samples

The numerical analyses on a CICC magnet turn in transient regime, presented in chapter 7, have shown quite *uneven current distributions* among the cable strands in some cases. This phenomenon results from two main causes: the contact pattern periodicity and the boundary conditions.

The numerical analyses, confirmed by also an analytical model based on the twist pitches values, have demonstrated the possible existence of *quasi-periodic contact patterns* among couples of strands or small bundles, that can create favorable paths for current loops and therefore significant AC losses. Such quasi-periodicity happens when the distance between a couple of strands is locally so small that their inter-strand resistance becomes negligible and a current loop can close. Nevertheless, it must be noted that these results have been obtained during a predictive analysis, assuming low values for the inter-strand resistances for conservative purposes. This approach may have enhanced the entity of this phenomenon, that should therefore be further validated through comparisons with experimental data on the AC losses measured on the real conductor.

The analyses of a conductor segment with different *boundary conditions* have demonstrated that an uneven current distribution at the cable ends can affect the conductor behavior not only in their proximity, since it can diffuse all along a magnet thanks to the superconductive nature of the conductors. When modeling a part of a large coil, a parametric analysis of the boundary conditions is therefore required, since the assumption of a even distribution of currents at the ends, i.e. Neumann condition, cannot be assessed a priori.

Further Developments

Superconducting cables are very complex objects, therefore it is not easy to model each aspect of their physics in a completely satisfactory way. Some features that should be added in the THELMA code in future to increase its accuracy are the following:

- the *thermal modeling of an external jacket for the cable*: it could be used either to describe a resistive jacket (as in CICCs) or an external insulation layer (as in Rutherford cables), enabling a more advanced and accurate modeling of heaters and turn-to-turn heat propagation in magnets.

- A *more advanced thermal model for helium*, taking into account possible parallel helium channels, variations in its fluid dynamics and states. The present model has demonstrated his effectiveness in simple analyses, but several cases could hardly be properly described, e.g. a complete quench evolution in a forced-flow cooled cable.

- A *more accurate model for the geometry of CICCs*. The present model for the strands geometry in CICCs, although it has demonstrated his effectiveness in several analyses, is characterized by a large number of local overlaps among adjacent strands, and this may reduce its accuracy in representing the contact patterns and thus the current minor loops activated during transients. Furthermore, the model presently describes only CICCs with circular cross-sections, therefore its accuracy is reduced in alternative cases, such as rectangular or square cross-sections. The development of a geometrical model capable to reduce the overlaps with an iterative approach and to force the cross-section to any assumed shape should therefore be addressed.

- A *model for contribute of the ferromagnetic materials to the magnetic field*. The absence of this model in the THELMA code descends to the limited interest for this feature in ITER CICC magnets, whereas its contribute cannot be neglected in accelerator magnets and it must be properly modeled.

Part IV

Appendices

Appendix A

Material Properties

In this Appendix, a database of several material properties useful for superconducting materials modeling is reported. Some of the contents are included also in CERN technical note [109]. Several references have been considered for this compilation. Among them, the most important are:

- *MATPRO*: it is a collection of cryogenic material properties from Università degli Studi di Milano and Istituto Nazionale di Fisica Nucleare (INFN) [113];
- *NIST*: the official website of the National Institute of Standard and Technology [133] contains a database of cryogenic material properties;
- *EFDA*: a material data compilation for superconductor simulation has been published by the European Fusion Development Agreement [15];
- *CUDI*: the user manual of this software for Rutherford cable modeling [175] reports some useful material properties.

The temperature range of interest for superconductors numerical simulations is very large. It spans from near absolute zero to temperatures up to 400 K for quench protection studies. Unfortunately, for some materials data are available only between 4 K to 300 K, therefore extrapolation of experimental points is needed in some cases. It is important to notice that large uncertainties exist for the material properties, in particular at very low temperatures. Commonly, a range of uncertainty of $10-20\%$ can be considered plausible. In addition, differences often exist between samples of the same material, due, for instance, to material impurities, mechanical working and so on.

In this wide range of temperature, strong variations in almost all the interesting material properties can be found. Two fit functions among the others will be employed to describe their behavior; the first is the NIST typical log-log polynomial interpolation:

$$\log_{10} x = \sum_{n=0}^{N} a_n (\log_{10} T)^n, \tag{A.1}$$

where x is the computed material property and N is usually equal to 7 (only in one case there is an 8-th order polynomial). Another kind of fit function, used in particular in CUDI datasets is the piece-wise polynomial:

$$x(T) = \sum_{n=0}^{4} a_n T^n, \qquad T_{\min,i} < T < T_{\max,i}, \tag{A.2}$$

where the coefficients a_n are defined as constants for several temperature ranges $[T_{\min,i}; T_{\max,i}]$. Further fit functions will be presented in some particular cases.

The materials considered for this compilation are copper, Nb-Ti, Nb_3Sn and commonly used insulating materials like polyimide, epoxy resin and G10, that is a composite material made by fiberglass impregnated in epoxy resin. Finally, a review of some helium properties is reported.

A.1 Mass Density

The *mass density* ρ is defined as the mass per unit volume and it is measured in units of kg/m^3. In Table A.1 a list of typical values of ρ at room temperature is reported for several materials of interest in applied superconductivity. The change in mass

Material	ρ [kg/m^3]	*References and notes*
Cu	8920	[175]
	8960	[15] [113] [151]
Nb-Ti	5600	[113]
	6000	[15] [151]
	6630	[119], 46.5% wt of Ti
Nb_3Sn	8040	[15]
	8400	[151]
	8900	[113]
	8976	[77]
Polyimide	*1420*	[113] [151]
G10	1740-1780	[180], 38-42% vol. resin
	1830	[86], 36.4% vol. resin
	1900	[113]
	1948	[133]
Epoxy resin	*1180*	[65]
	1200	[113]
	1100-1300	[148]

Table A.1: Mass density of some materials commonly used in applied superconductivity. The most trustworthy value is reported in italics.

density at low temperatures due to thermal expansion is generally neglected, since it is a quite small effect and furthermore it is not well documented for all materials. As an example, in the case of copper the mass density increases between room and cryogenic temperatures of about 1.33% [86], an effect much smaller than the typical accuracy of material properties. Nb-Ti and Nb_3Sn probably exhibit smaller changes, since they are characterized by weaker thermal expansion than copper [15]. Very scattered values can be found in mass density of composites like G10 and Nb-Ti, probably due to different compositions. In the case of niobium-tin, the value of 8976 kg/m^3 [77] has been computed from the reported gram atom mass of 99.5 g and volume of 11.085 cm^3.

A.2 Heat Capacity

The *heat capacity* C, measured in J/K, is the amount of energy needed to increase (or decrease) the temperature of a specimen by one degree. According to thermodynamics, it can be defined as the temperature derivative of the internal energy U, at constant pressure P or at constant volume V:

$$C_\mathrm{P} = \left(\frac{\partial U}{\partial T}\right)_{P=\mathrm{const}}, \qquad C_\mathrm{V} = \left(\frac{\partial U}{\partial T}\right)_{V=\mathrm{const}}. \tag{A.3}$$

In solids, the heat capacity at constant pressure is generally considered and it is expressed in terms of normalized quantities:

- the *specific heat capacity* or *specific heat* c_p, that is the heat capacity per unit mass, measured in J/(K·kg);
- the *volumetric heat capacity* (VHC), that is the heat capacity per unit volume, measured in J/(K·m^3);
- the *molar heat capacity*, that is the heat capacity per mole, measured in J/(K·mol).

No specific symbol is generally used for VHC, that is generally referred to as ρc_p since it can be obtained multiplying the specific heat for the mass density. The molar heat capacity can instead obtained from specific heat multiplying it for the molar mass m_mol.

In the following paragraph, the general theoretical model for the specific heat is summarized together with the specific heat jump in superconducting materials. Then, the most important empirical fit functions available for copper, Nb-Ti, Nb_3Sn and some insulating materials are reported.

A.2.1 Theoretical Models

The specific heat of solids generally consists of two terms, the *lattice specific heat* and the *electronic specific heat* [58]. A good approximation for the first term is the

Debye formula:

$$\frac{c_\mathrm{p} m_\mathrm{mol}}{rR} = 12\left[\frac{3}{z^3}\int_0^z \frac{t^3}{(e^t-1)}\,dt\right] - \frac{9z}{e^z-1}, \tag{A.4}$$

where m_mol is the molar mass in kg, $R = 8.317$ J/(mol·K) is the universal gas constant, r is the number of atoms per molecule and $z = \theta_\mathrm{D}/T$, with T temperature and θ_D the so-called *Debye temperature*, an empirical parameter related to the phonon spectrum of the solid. Equation (A.4) can be approximated as:

$$c_\mathrm{p} m_\mathrm{mol} = \begin{cases} \dfrac{12\pi^4}{5} rR\left(\dfrac{T}{\theta_\mathrm{D}}\right)^3, & T \ll \theta_\mathrm{D}, \\ 3rR, & T \gg \theta_D. \end{cases} \tag{A.5}$$

A good fit between these asymptotic limits is:

$$c_\mathrm{p} = (c_\mathrm{p,low}^{-n} + c_\mathrm{p,high}^{-n})^{-1/n}, \tag{A.6}$$

with $n = 0.85$. In Figure A.1 Eqs. (A.4) and (A.5) are compared in the case of copper ($\theta_\mathrm{D} = 343$ K and $m_\mathrm{mol} = 63.54$ g).

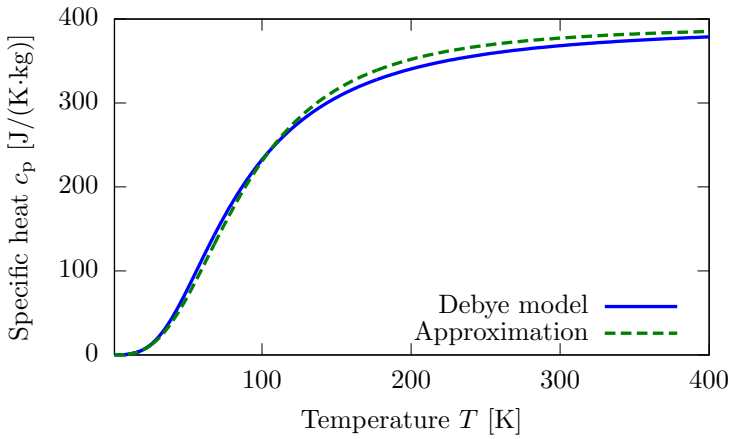

Figure A.1: Copper specific heat according to Debye model.

In metals, at low temperatures (a few kelvins) there is another contribution to the specific heat due to the conduction electrons, that obey to Fermi-Dirac statistics. Because the temperatures of interest are lower than Fermi temperature, the electrons are referred to as a degenerate Fermi gas, that has a simple linear temperature dependence for specific heat:

$$c_\mathrm{p,el} \cong \gamma T, \tag{A.7}$$

where γ is the *electronic specific heat constant* (sometimes called Sommerfeld constant) and it is proportional to the density of states at the Fermi surface.

In many normal conducting metals such as Ag, Al, Cu, both lattice and electronic specific heat give relevant contributions at low temperatures, therefore the specific heat is generally approximated by:

$$c_{\mathrm{p}} = \beta T^3 + \gamma T, \tag{A.8}$$

where β is a constant proportional to Debye temperature. In Table A.2 typical values for θ_{D} and γ are reported for some metals.

Table A.2: Typical values for θ_{D} and γ [91].

Material	θ_{D} K	γ mJ/(K^2·mol)	**Material**	θ_{D} K	γ mJ/(K^2·mol)
Li	335	1.63	Au	162.4	0.729
Na	156	1.38	Al	428	1.35
K	91.1	2.08	Sn	199	1.78
Cu	343	0.695	Ti	428	3.35
Ag	226.2	0.646	Nb	275	7.79

The specific heat changes smoothly with temperature for normal-conducting materials, whereas superconducting materials exhibit a discontinuity Δc_{p} in specific heat in occurrence to the transition at T_{c}. Starting from Eq. (A.8) it is possible to calculate for superconducting state [58]:

$$c_{\mathrm{p,s}} = \left(\beta + \frac{3\gamma}{T_{\mathrm{c,0}}^2}\right) T^3 + \gamma T \frac{B}{B_{\mathrm{c2,0}}}, \tag{A.9}$$

where $T_{\mathrm{c,0}}$ and $B_{\mathrm{c2,0}}$ are respectively critical temperature at 0 T and upper critical field at 0 K. Thus, the heat capacity in superconducting materials depends also on the applied magnetic induction. The discontinuity in specific heat at T_{c} is:

$$\Delta c_{\mathrm{p}} = \gamma T_{\mathrm{c}} \left(\frac{3T_{\mathrm{c}}^2}{T_{\mathrm{c,0}}^2} + \frac{B_{\mathrm{c2}}}{B_{\mathrm{c2,0}}} - 1\right) = 2\gamma T_{\mathrm{c}} \left(\frac{T_{\mathrm{c}}}{T_{\mathrm{c,0}}}\right)^2, \tag{A.10}$$

where $B_{\mathrm{c2}}/B_{\mathrm{c2,0}}$ is replaced[1] with $(1 - t^2)$. Thus at zero field ($T_{\mathrm{c}} = T_{\mathrm{c,0}}$):

$$\frac{\Delta c_{\mathrm{p}}}{\gamma T_{\mathrm{c}}} = 2. \tag{A.11}$$

A more precise model based on BCS theory gives instead:

$$\frac{\Delta c_{\mathrm{p}}}{\gamma T_{\mathrm{c}}} = 1.43. \tag{A.12}$$

With these models the electronic specific heat coefficient γ can be estimated in superconducting materials.

[1] See Eq. 1.12, page 11.

A.2.2 Copper

A high accuracy compilation of copper specific heat data as a function of temperature can be found in [186]. Two different interpolating functions are proposed. Between 0.3 and 25 K an odd-only 11th order polynomial is proposed (see Table A.3). Between 25 and 1300 K a cubic spline is instead reported:

$$\sum_{i=0}^{3} a_i \left(\frac{T - T_{\min,i}}{100} \right)^i, \qquad T_{\min,i} < T < T_{\max,i}, \tag{A.13}$$

with the coefficients and breaks reported in Table A.4. The coefficients of both Table A.3 and A.4 refer to molar heat capacity, therefore the material property should be divided by the molar mass of copper $m_{\text{mol}} = 63.54$ g to obtain the specific heat c_{p}.

Table A.3: Low temperature polynomial coefficients $\sum_{i=1}^{11} c_i T^i$ for copper molar heat capacity [J/(K·mol)]. The even coefficients are null.

c_1	c_3	c_5	c_7	c_9	c_{11}
$6.9434 \cdot 10^{-4}$	$4.7548 \cdot 10^{-5}$	$1.6314 \cdot 10^{-9}$	$9.4786 \cdot 10^{-11}$	$-1.3639 \cdot 10^{-13}$	$5.3898 \cdot 10^{-17}$

Table A.4: Cubic spline parameters for copper molar heat capacity [J/(K·mol)], temperature between 25 and 1300 K.

$T_{\min}$ [K]	$T_{\max}$ [K]	a_3	a_2	a_1	a_0
25	29	64.762 60	39.904 50	12.4259	0.962 97
29	44.73	−89.748 40	47.676 00	15.9290	1.528
44.73	69.20	−29.051 00	5.323 70	24.2660	4.864
69.20	139.46	5.242 50	−16.003 00	21.6530	10.695
139.46	200	1.873 60	−4.952 40	6.9300	19.827
200	330	0.372 40	−1.549 60	2.9936	22.623
330	1237.5	0.008 73	−0.097 37	0.8526	24.714
1237.5	1300	1.508 00	0.140 40	1.2433	30.960

Several further fit functions are available in literature. Three of them, often used in applied superconductivity, are described herein and plotted in Figure A.2 together with the high accuracy data just described. The maximum difference between the datasets is about 10%.

NIST

A polynomial interpolation based on Eq. (A.1) is proposed. The fit parameters are reported in Table A.5. The range of validity of this fit is between 4 K and 300 K.

Table A.5: Fit parameters for NIST copper specific heat.

a_0	a_1	a_2	a_3	a_4	a_5	a_6	a_7
−1.91844	−0.15973	8.61013	−18.996	21.9661	−12.7328	3.54322	−0.3797

MATPRO

The original reference is [86], that proposes a relation similar to Eq. (A.8) under 10 K:

$$c_{\mathrm{p}}(T) = 30.6 \cdot 10^3 \left(\frac{T}{344.5}\right)^3 + 10.8 \cdot 10^{-3}\ T, \tag{A.14}$$

in which the contributions of the electronic specific heat (proportional to T) and the lattice specific heat (proportional to T^3) are evident. From 10 K to 300 K, a piece-wise linear interpolation on tabulated values from [86] is used. Very close values are reported also in the user manual of the 2D/3D ANSYS quench simulation from Fermilab [115]. The value at 500 K from [186] has been used to extrapolate the behavior at higher temperatures.

CUDI

A piece-wise polynomial function between 0 K and 1000 K is proposed (see Eq. A.2), in terms of volumetric heat capacity. The fit parameters for each temperature range are reported in Table A.6.

Table A.6: Fit parameters for CUDI copper volumetric heat capacity [J/(K·m^3)].

T_{min} [K]	T_{max} [K]	a_4	a_3	a_2	a_1	a_0
0	9.441	$-3.08 \cdot 10^{-2}$	7.229	−2.1286	$1.0189 \cdot 10^2$	2.5631
9.441	31.134	$-3.045 \cdot 10^{-1}$	$2.9871 \cdot 10^1$	$-4.5561 \cdot 10^2$	$3.4695 \cdot 10^3$	$-8.2503 \cdot 10^3$
31.134	123.34	$4.19 \cdot 10^{-2}$	$-1.4024 \cdot 10^1$	$1.5089 \cdot 10^3$	$-3.1595 \cdot 10^4$	$1.784\,32 \cdot 10^5$
123.34	306.12	$-8.48 \cdot 10^{-4}$	$8.419 \cdot 10^{-1}$	$-3.2552 \cdot 10^2$	$6.0590 \cdot 10^4$	$-1.2851 \cdot 10^6$
306.12	498.15	$-4.80 \cdot 10^{-5}$	$9.173 \cdot 10^{-2}$	$-6.412 \cdot 10^1$	$2.0363 \cdot 10^4$	$1.028 \cdot 10^6$
498.15	1000	0	$1.2 \cdot 10^{-4}$	$-2.1486 \cdot 10^{-1}$	$1.003\,84 \cdot 10^3$	$3.1823 \cdot 10^6$

A.2.3 Nb-Ti

Larger uncertainties than in copper are present in the heat capacity of superconductors. Two commonly used fit functions are reported and plotted in Figure A.3.

MATPRO

The original reference for normal conducting Nb-Ti is [86], with low temperature values extrapolated and fitted with Eqs. (A.8) and (A.9). Data are linearly extrapolated over 310 K.

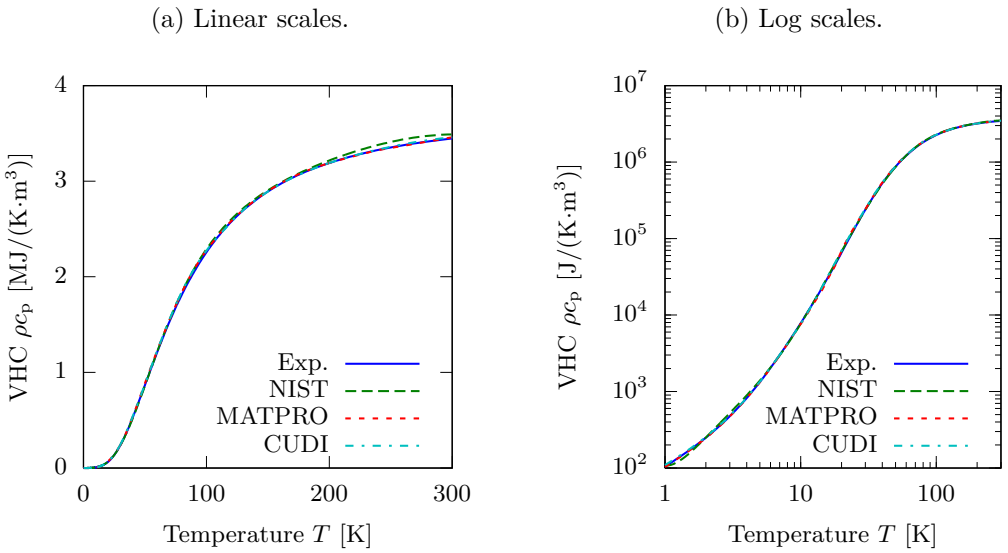

Figure A.2: Copper volumetric heat capacity according to experimental data of [186] and commonly used fit functions.

CUDI

As in the case of copper, a piece-wise polynomial function (Eq. A.2) for the VHC between 0 and 1000 K is proposed, but with a linear magnetic induction dependence under T_c for superconducting state. The fit parameters for each temperature range are reported in Table A.7.

Table A.7: Fit parameters for CUDI Nb-Ti volumetric heat capacity.

T_{min} [K]	T_{max} [K]	a_4	a_3	a_2	a_1	a_0
0	$T_c(B)$	0	$4.91 \cdot 10^1$	0	$64 \cdot B$	0
$T_c(B)$	28.358	0	$1.624 \cdot 10^1$	0	$9.28 \cdot 10^2$	0
28.358	50.99	$-2.177 \cdot 10^{-1}$	$1.198\,38 \cdot 10^1$	$5.5371 \cdot 10^2$	$-7.8461 \cdot 10^3$	$4.1383 \cdot 10^4$
50.99	165.8	$-4.82 \cdot 10^{-3}$	2.976	$-7.163 \cdot 10^2$	$8.3022 \cdot 10^4$	$-1.53 \cdot 10^6$
165.8	496.54	$-6.29 \cdot 10^{-5}$	$9.296 \cdot 10^{-2}$	$-5.166 \cdot 10^1$	$1.3706 \cdot 10^4$	$1.24 \cdot 10^6$
496.54	1000	0	0	$-2.57 \cdot 10^{-1}$	$9.555 \cdot 10^2$	$2.45 \cdot 10^6$

A.2.4 Nb_3Sn

An extensive comparison of experimental results on niobium-tin specific heat can be found in [108]. In the following, two quite common fit functions are reported and plotted in Figure A.4.

(a) Normal conducting. (b) Superconducting.

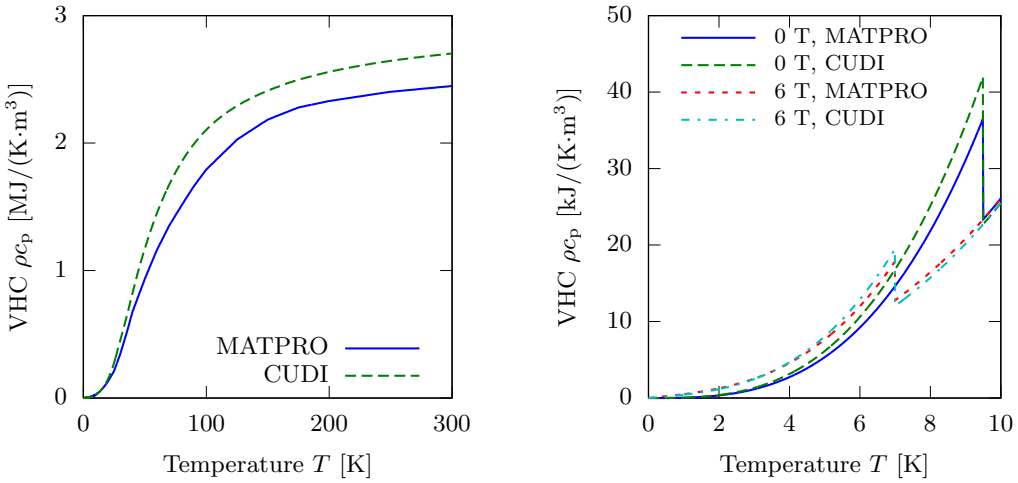

Figure A.3: Nb-Ti volumetric heat capacity according to MATPRO and CUDI.

MATPRO

Over 20 K, a NIST log-log polynomial fit (Eq. A.1) with the parameters reported in Table A.8 is proposed for specific heat. The original experimental values come from [92], the maximum fit error is about 5%, and the range of validity is [20; 400] K. From 400 to 500 K the fuction has been linearly extrapolated.

Table A.8: Fit parameters for MATPRO Nb_3Sn specific heat over 20 K.

a_0	a_1	a_2	a_3	a_4	a_5	a_6	a_7
79.78547	−247.44839	305.01434	−186.90995	57.48133	−6.3977	−0.6827738	0.1662252

Under 20 K, Eq. (A.9) for the superconducting state and Eq. (A.8) for the normal conducting state are used. For the electronic specific heat coefficient γ a value of 0.138 J/(K^2·kg) is used [77], whereas $\beta = 1.241$ mJ/(K^4·kg) has been considered in order to obtain a smooth behavior between the fit at high and low temperatures. Typical values for $T_{c,0}$ and $B_{c2,0}$ are respectively 18 K and 25 T [72].

CUDI

Also in this case, a piece-wise polynomial function (Eq. A.2) for VHC between 0 and 1000 K is proposed. The magnetic induction dependence is more complicated than Nb-Ti fit, because all the parameters of superconducting specific heat depend

on magnetic induction:

$$a_1(B) = 207 - 3.83 \cdot B + 2.86 \cdot B^2, \tag{A.15}$$
$$a_2(B) = -110 \cdot e^{-0.434 \cdot B}, \tag{A.16}$$
$$a_3(B) = 38.8 - 1.8 \cdot B + 0.0634 \cdot B^2. \tag{A.17}$$

The fit parameters for each temperature range are reported in Table A.9.

Table A.9: Fit parameters for CUDI Nb_3Sn volumetric heat capacity.

T_{min} [K]	T_{max} [K]	a_4	a_3	a_2	a_1	a_0
0	$T_c(B)$	0	$a_3(B)$	$a_2(B)$	$a_1(B)$	0
$T_c(B)$	26.113	0	7.42	0	1522	0
26.113	169.416	0	0	−61.635	19 902	−305 807
169.416	300	0	0	−7.4636	4411	763 801
300	-	0	0	0	0	1 415 377

(a) Normal conducting.

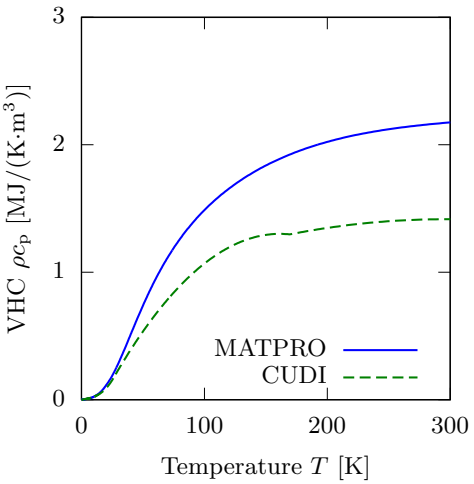

(b) Superconducting.

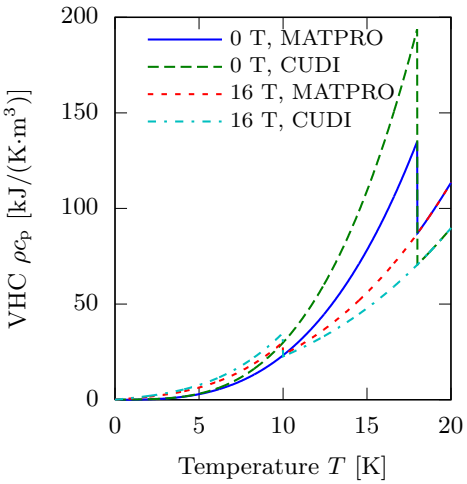

Figure A.4: Nb_3Sn volumetric heat capacity according to MATPRO and CUDI.

A.2.5 Polyimide

A polynomial interpolation from NIST is proposed for specific heat, based on Eq. (A.1). The range of validity is between 4 and 300 K and the reported curve fit error to data is 3%. The fit parameters are listed in Table A.10 and the dataset is plotted in Figure A.5. The same fit function is used also in MATPRO.

Table A.10: Fit parameters for NIST polyimide specific heat.

a_0	a_1	a_2	a_3	a_4	a_5	a_6	a_7
−1.3684	0.65892	2.8719	0.42651	−3.0088	1.9558	−0.51998	0.051574

A.2.6 Glass-Epoxy Resin

As shown in Figure A.5, in G10 large uncertainties are present on the material properties, since the behavior of these composite materials strongly depends on the composition and on the particular type of epoxy resin and fiberglass used.

NIST

The NIST polynomial function (Eq. A.1) is used, with the parameters reported in following table. The range of validity is $[4, 300]$ K with a reported fit error of about 2%. The same fit function is used also in MATPRO.

Table A.11: Fit parameters for NIST G10 specific heat.

a_0	a_1	a_2	a_3	a_4	a_5	a_6	a_7
−2.4083	7.6006	−8.2982	7.3301	−4.2386	1.4294	−0.24396	0.015236

Fermilab

A dataset of G10 specific heat is reported in [115]. The dataset has been fitted with the NIST polynomial function (Eq. A.1). The range of validity is also in this case $[1, 300]$ K and the maximum fit error on original data is about 4%.

Table A.12: Fit parameters for Fermilab G10 specific heat.

a_0	a_1	a_2	a_3	a_4	a_5	a_6	a_7
−2.22174	4.12105	−8.92637	21.26366	−22.41854	11.76922	−3.07216	0.31938

A.2.7 Epoxy Resin

In MATPRO a dataset regarding epoxy resin specific heat is present and it is shown in Figure A.5. It is a linear interpolation of data from [86] (under 100 K) and from [65] (between 100 and 300 K). Over 300 K the values have been linearly extrapolated.

(a) Linear scales. (b) Log scales.

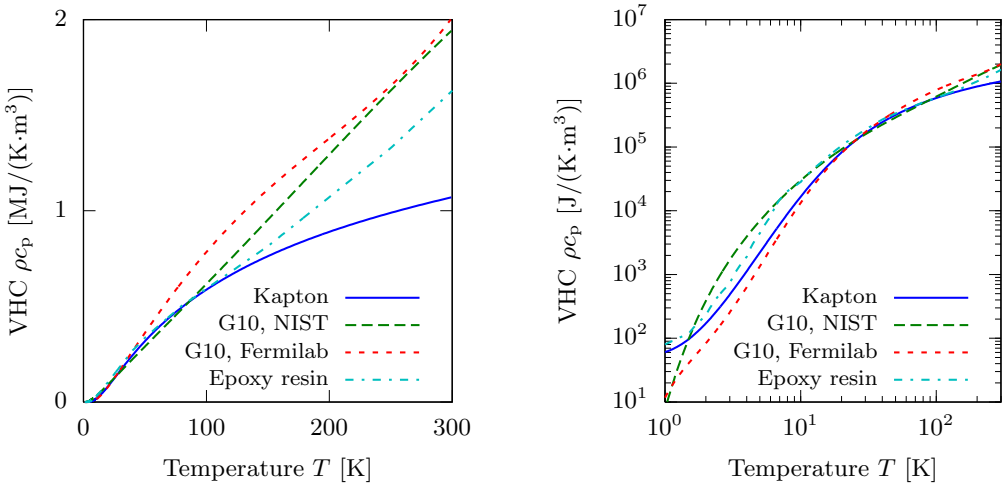

Figure A.5: Volumetric heat capacity of some insulating materials.

A.3 Electrical Resistivity

The *electrical resistivity* ρ_E is the constitutive material property that relates the electric field $\mathbf{E}$ with the current density $\mathbf{J}$:

$$\mathbf{E} = \rho_E \mathbf{J}, \tag{A.18}$$

and it is measured in Ω·m. In metals, the electrical resistivity can be generally expressed by the so-called *Matthiessen's rule* as the sum of two components:

$$\rho_E = \rho_{E,0} + \rho_{E,i}, \tag{A.19}$$

where $\rho_{E,0}$ is the contribution of crystal lattice and $\rho_{E,i}$ is the contribution of impurities and inhomogeneities in real metals. $\rho_{E,0}$ is the consequence of the scattering of electrons due the thermal motion of lattice ions, thus it tends to zero as the temperature tends to absolute zero. $\rho_{E,i}$ is instead temperature independent and it is therefore called *residual resistivity* since it is the remaining contribution at very low temperatures, when $\rho_{E,0}$ becomes negligible. Since residual resistivity is due to crystal inhomogeneities, it is often used as an indicator of the sample purity through the *residual resistivity ratio* RRR, defined as:

$$\mathrm{RRR} = \frac{\rho_E(T_h)}{\rho_E(T_l)}, \tag{A.20}$$

where T_h and T_l are respectively two arbitrary high and low temperatures. In Table A.13 some typical values for T_l and T_h.

Table A.13: Temperatures used for the RRR definition.

Model	T_l [K]	T_h [K]
NIST	4	273
MATPRO	4.2	295
CUDI	4	290

The temperature dependence of $\rho_{\mathrm{E},0}$ is well described [91] by the empirical *Grüneisen formula* that is $\rho_{\mathrm{E},0} \propto TG(\theta_\mathrm{R}/T)$, where:

$$G(x) = x^{-4} \int_0^x \frac{s^5 \mathrm{d}s}{(e^s - 1)(1 - e^{-s})}, \tag{A.21}$$

and θ_R is a reference temperature, typically very near to Debye temperature for specific heat. At very low and very high temperatures Eq. (A.21) can be approximated with:

$$\rho_{\mathrm{E},0} \propto \begin{cases} T, & T \gg \theta_\mathrm{R}, \\ T^5, & T \ll \theta_\mathrm{R}, \end{cases} \tag{A.22}$$

although deviations at low temperatures are common. In Figure A.6 Eq. (A.21) is plotted in terms of temperature and resistivity normalized to their value at θ_R.

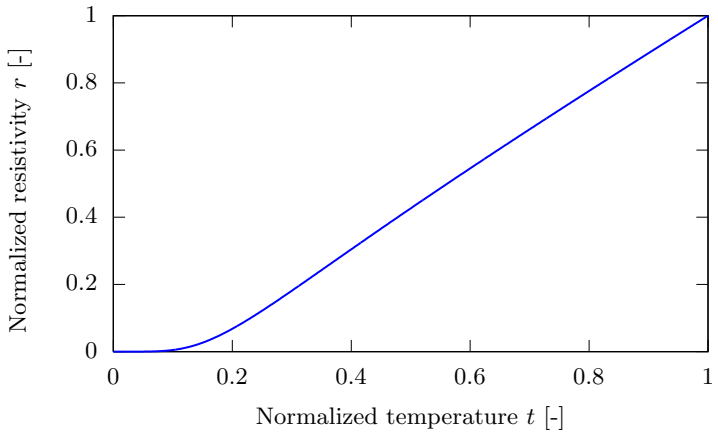

Figure A.6: Grüneisen formula for electrical resistivity.

A.3.1 Magnetoresistivity

In pure metals at low temperatures, the resistance of a specimen increases as the material is exposed to a magnetic field. This phenomenon is called *magnetoresistivity* and it is due to the Lorentz forces acting on electrons. An important experimental result valid for many materials is the *Kohler's rule* [93], which states that the

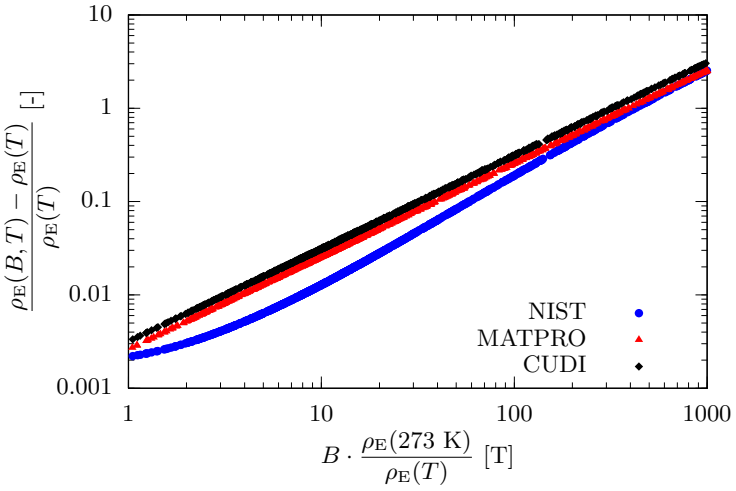

Figure A.7: Kohler's plot for copper as computed by different fit functions.

electrical resistivity difference $\Delta\rho_E$ due to magnetoresistivity can be expressed as:

$$\frac{\Delta\rho_E}{\rho_E} = \phi_K\left(\frac{B}{\rho_E}\right), \tag{A.23}$$

where ϕ_K is a suitable function that depends only on the material and the relative orientation of magnetic induction and electrical current. Following this rule, very often the magnetoresistivity is represented through a *Kohler's plot*, that is a log-log graph of the function ϕ_K, that can be commonly represented as a straight line or a polynomial. An example of Kohler's plot of copper is reported in Figure A.7.

A.3.2 Copper

In the following, three different sources for the copper resistivity will be considered: NIST, MATPRO and CUDI.

NIST

The NIST equation for copper resistivity comes from [59] but it can be found in a lot of sources (among the others [15] [148] [151]). It contains temperature and RRR dependence:

$$\rho_E(T, \mathrm{RRR}) = \rho_0 + \rho_i + \rho_{i0} \tag{A.24}$$

with:

$$\rho_0 = \frac{1.553 \cdot 10^{-8}}{\mathrm{RRR}} \tag{A.25}$$

$$\rho_\mathrm{i} = \frac{P_1 T^{P_2}}{1 + P_1 P_3 T^{P_2 - P_4} \exp\left[-\left(\frac{P_5}{T}\right)^{P_6}\right]} \tag{A.26}$$

$$\rho_\mathrm{i0} = P_7 \frac{\rho_\mathrm{i}\rho_0}{\rho_\mathrm{i} + \rho_0} \tag{A.27}$$

Since copper follows Kohler's rule, a polynomial in the Kohler's plot is used to model magnetoresistivity (see Figure A.7):

$$\rho_\mathrm{E}(T, \mathrm{RRR}, B) = \rho_\mathrm{E}(T, \mathrm{RRR})(1 + 10^{a(x)}) \tag{A.28}$$

with:

$$a(x) = \sum_{n=0}^{4} a_n (\log_{10} x)^n \tag{A.29}$$

$$x = S(T, \mathrm{RRR}) \cdot B = \frac{\rho_\mathrm{E}(T = 273\ \mathrm{K}, \mathrm{RRR})}{\rho_\mathrm{E}(T, \mathrm{RRR})} \cdot B \approxeq \frac{1.553 \cdot 10^{-8}}{\rho_\mathrm{E}(T, \mathrm{RRR})} \cdot B \tag{A.30}$$

In Eqs. (A.28) and (A.30) $\rho_\mathrm{E}(T, \mathrm{RRR})$ refers to Eq. (A.24). All fit constants are reported in Table A.14.

Table A.14: Fit parameters for NIST copper electrical resisitivity.

P_1	P_2	P_3	P_4	P_5	P_6	P_7
$1.171 \cdot 10^{-17}$	4.49	$3.841 \cdot 10^{10}$	1.14	50	6.428	0.4531

a_0	a_1	a_2	a_3	a_4
−2.662	0.3168	0.6229	−0.1839	0.01827

It's important to highlight that the polynomial $a(x)$ exhibits a minimum at $x_\mathrm{min} \approx 0.589$, therefore if $S(T, \mathrm{RRR}) \cdot B$ is lower than x_min the resistivity would increase with decreasing magnetic induction [151]. Thus, there is a minimum magnetic induction $B_\mathrm{min}(T)$ at which Eq. (A.28) fails. B_min at room temperature is in the order of 1 T, and it decreases with lower temperatures depending on RRR.

MATPRO

An analytical formula for electrical resistivity is used in MATPRO, with temperature, RRR and magnetic induction dependence. The original reference is [37]. MATPRO formula leads to inaccurate values (25-30% lower) if the following conditions are present at the same time:

- RRR > 200;
- $B \approxeq 0$ T;
- 20 K $< T <$ 30 K.

Also with very low values of RRR (less than 11) the dataset is reported to be less accurate.

CUDI

Copper resistivity is computed in CUDI with a fit function similar to the one proposed in [119]:

$$\rho_{\mathrm{E}}(T, \mathrm{RRR}) = 10^{-8} \left[\frac{1.7}{\mathrm{RRR}} + \left(\frac{2.32547 \cdot 10^9}{T^5} + \frac{9.57137 \cdot 10^5}{T^3} + \frac{1.62735 \cdot 10^2}{T} \right)^{-1} \right] + \mathrm{MR} \cdot B \tag{A.31}$$

with MR $= 0.5 \cdot 10^{-10}$ Ω·m/T. In the original fit function the coefficient 1.7 was replaced by 1.545 and the magnetoresistivity effect was not included.

A.3.3 Normal-Conducting Nb-Ti and Nb_3Sn

Data on normal-state resistivity of niobium-titanium and niobium-tin can be found both in MATPRO and in EFDA material properties database. The original reference for MATPRO is [33] for both materials, whereas EFDA cites both MATPRO and alternative sources. In the case of Nb-Ti, a linear function of temperature is proposed:

$$\rho_{\mathrm{E}}(T) = 5.58 \cdot 10^{-10}\, T + 5.5668 \cdot 10^{-7}. \tag{A.32}$$

Data are largely scattered (see Figure A.9), but in any case the normal-state resistivity of these materials is much higher than copper. Thus, when modeling copper-stabilized superconducting wires, the contribute of normal-conducting niobium composites to electrical resistivity is generally neglected.

A.3.4 Insulating Materials

The order of magnitude of electrical resistivity in insulating materials like G10 is $10^{13} - 10^{15}$ Ω·m [89], that is more than 20 orders of magnitude higher than room temperature copper, thus it can be considered as infinite in computations.

A.4 Thermal Conductivity

The *thermal conductivity* k is the constitutive property that relates the temperature gradient ∇T to the heat flux $\mathbf{q}$ in the *Fourier's law*:

$$\mathbf{q} = -k \nabla T, \tag{A.33}$$

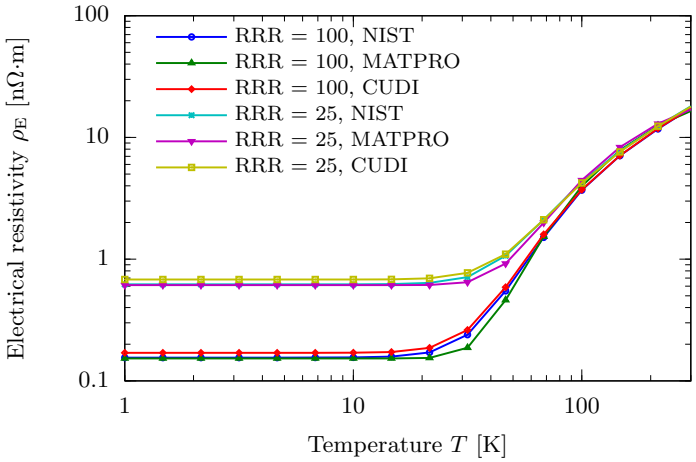

(a) RRR dependence at zero magnetic induction.

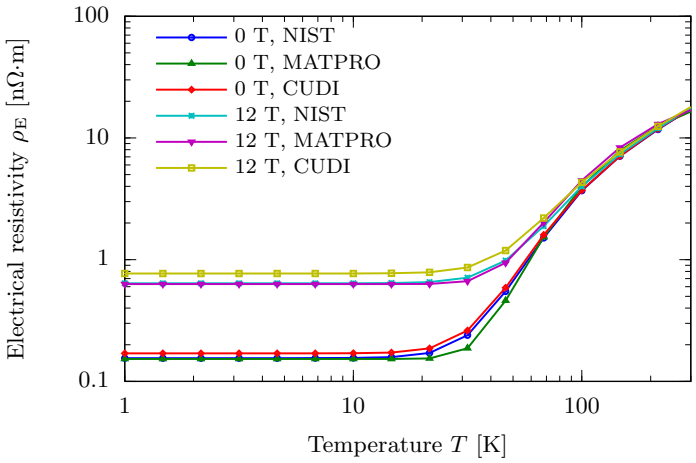

(b) Magnetic induction dependence, RRR = 100.

Figure A.8: Copper electrical resistivity as a function of temperature.

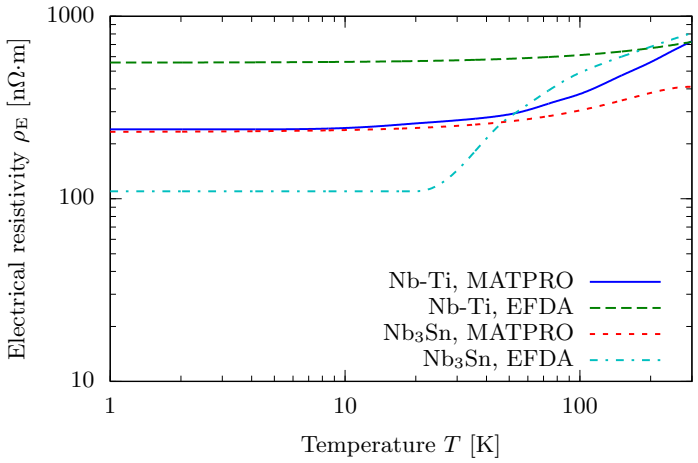

Figure A.9: Normal-conducting Nb-Ti and Nb_3Sn electrical resistivity as a function of temperature.

and its units are W/(K·m). The conduction of heat is due to both electrons and lattice vibrations (phonons). In pure metals, the electron contribute is dominant, whereas in impure materials and alloys the phononic contribute can be as large as the electronic [91]. In insulating materials the conduction is practically due to only to phonons.

In metals, the thermal conductivity is often expressed through the *Wiedemann-Franz* law that correlates it to the electrical resistivity ρ_E:

$$\rho_E k = L_0 T, \tag{A.34}$$

with the so-called *Lorenz number* L_0 that is according to solid state theory [91]:

$$L_0 = \frac{\pi^2}{3}\left(\frac{k_B}{e}\right)^2 \approxeq 2.45 \cdot 10^{-8}\ \mathrm{W \cdot \Omega / K^2}, \tag{A.35}$$

where $k_B = 1.38 \cdot 10^{-23}$ J/K is the Boltzmann constant and $e = 1.6 \cdot 10^{-19}$ C is the elementary charge. In real specimens, Lorenz number depends on the material considered. Some experimental values of Lorenz number at room temperature are reported in Table A.15.

Table A.15: Lorenz number L_0 for some metals at 273 K [91]. Units are 10^{-8} W·Ω/K^2.

Ag	Au	Cd	Cu	Ir	Mo	Pb	Pt	Sn	W	Zn
2.31	2.35	2.42	2.23	2.49	2.61	2.47	2.51	2.52	3.04	2.31

Moreover, the Lorenz number is constant with temperature only if the conduction electrons are scattered elastically, and this condition is quite well verified at high and

very low temperatures. Typically the Debye temperature θ_D is used as reference. At intermediate temperatures the Lorenz number tends to be smaller, so Eq. (A.34) with a constant L_0 leads to higher values for thermal conductivity than the real ones. For example, in [33] a minimum value of $0.7 \cdot 10^{-8}$ W·Ω/K^2 at 25 K is reported for copper. Furthermore, the Lorenz number changes with RRR and is anisotropically dependent on magnetic induction [151].

A.4.1 Copper

Differently from electrical resistivity, where different fit functions lead almost to the same results, for thermal conductivity larger discrepancies can be found, as it can be seen for example from the equivalent Lorenz number for NIST and MATPRO datasets is plotted in Figure A.10 at zero magnetic induction.

(a) NIST fit. (b) MATPRO fit.

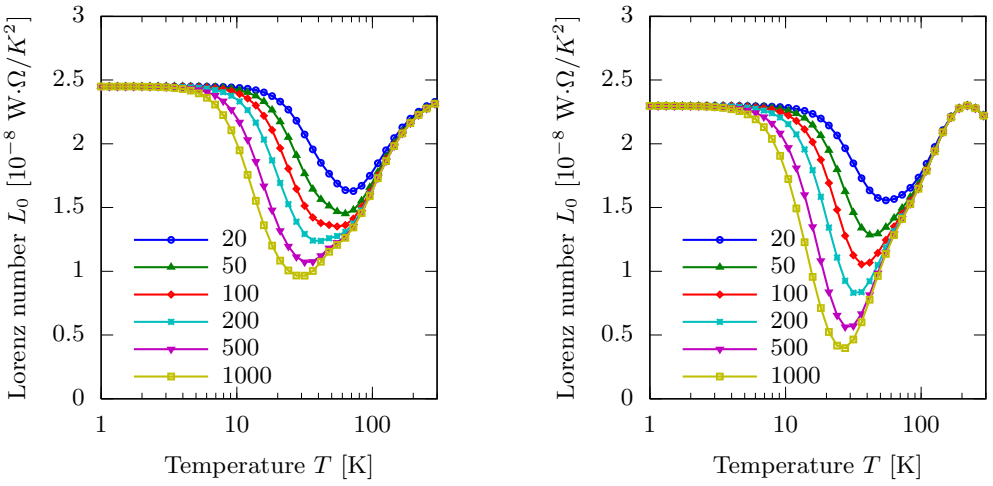

Figure A.10: Copper Lorenz number as a function of temperature and RRR, $B = 0$ T.

NIST

In [59] an analytical equation for k as a function of temperature and RRR is introduced:

$$k(T, \mathrm{RRR}) = \frac{1}{W_0 + W_i + W_{i0}} \tag{A.36}$$

with:

$$W_0 = \frac{\beta}{T} \tag{A.37}$$

$$W_{\mathrm{i}} = \frac{P_1 T^{P_2}}{1 + P_1 P_3 T^{P_2+P_4} \exp\left[-\left(\frac{P_5}{T}\right)^{P_6}\right]} \tag{A.38}$$

$$W_{\mathrm{i0}} = P_7 \frac{W_{\mathrm{i}} W_0}{W_{\mathrm{i}} + W_0} \tag{A.39}$$

The fit constants are reported in Table A.16.

Table A.16: Fit parameters for NIST copper thermal conductivity.

	β	β_{r}				
	$0.634/\,\mathrm{RRR}$	$\beta/0.0003$				
P_1	P_2	P_3	P_4	P_5	P_6	P_7
$1.754 \cdot 10^{-8}$	2.763	1102	-0.165	70	1.756	$0.838/\beta_{\mathrm{r}}^{0.1661}$

From Eqs. (A.28) and (A.36) it's possible to compute the Lorenz number as a function of temperature and RRR in NIST model:

$$L_0(T, \mathrm{RRR}) = \frac{\rho_{\mathrm{E}}(T, \mathrm{RRR}, B = 0\ \mathrm{T}) k(T, \mathrm{RRR})}{T} \tag{A.40}$$

To include also magnetic induction dependence in k, Wiedemann-Franz law can be used together with Eqs. (A.28) and (A.40):

$$k(T, \mathrm{RRR}, B) = \frac{L_0(T, \mathrm{RRR}) T}{\rho_{\mathrm{E}}(T, \mathrm{RRR}, B)} = \frac{\rho_{\mathrm{E}}(T, \mathrm{RRR}, B = 0\ \mathrm{T}) k(T, \mathrm{RRR})}{\rho_{\mathrm{E}}(T, \mathrm{RRR}, B)} \tag{A.41}$$

This approach is used also in CUDI, but in this case the electrical resistivity is modeled with Eq. (A.31) instead than Eq. (A.28).

MATPRO

An analytical equation is provided for k as a function of temperature, RRR and magnetic induction [37]. In [113] this dataset is reported to be less accurate (values 25-30% lower) if the following conditions are present at the same time:

- $\mathrm{RRR} > 200$;
- $B > 10$ T;
- $15\ \mathrm{K} < T < 40\ \mathrm{K}$.

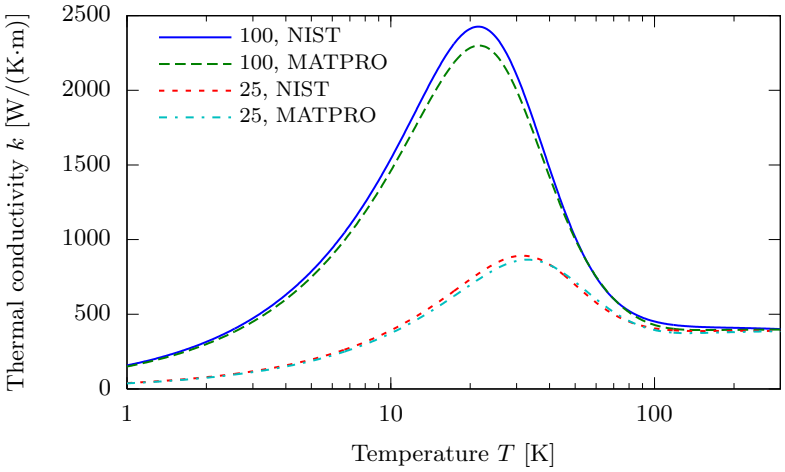

(a) RRR dependence at zero magnetic induction.

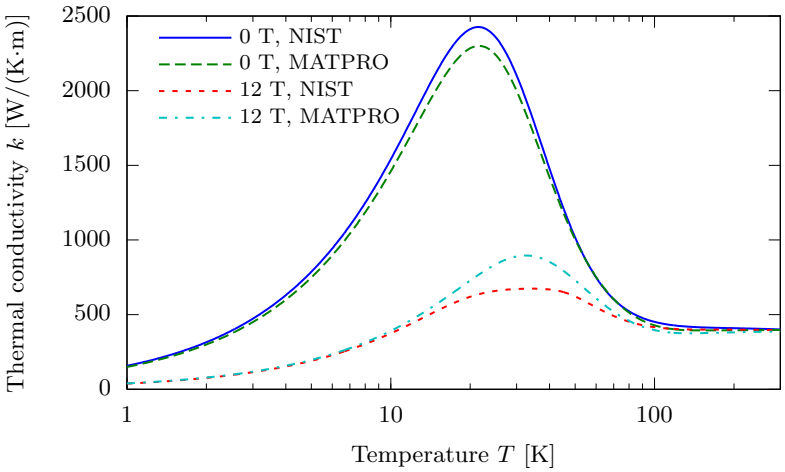

(b) Magnetic induction dependence, RRR = 100.

Figure A.11: Copper thermal conductivity as a function of temperature.

A.4.2 Nb-Ti and Nb_3Sn

As for the electrical resistivity, the thermal conductivity of normal-state Nb-Ti and Nb_3Sn is not well documented. However, also in this case their contribution to the transport properties in a superconducting wire is tiny, since values lower than 10 W/(K·m) are expected along all the temperature range (see Figure A.12), much lower than copper, that is always higher than 100 W/(K·m). Datasets for both Nb-Ti and Nb_3Sn are present in MATPRO from [33], whereas a 6^{th} order polynomial fit is proposed for Nb-Ti by EFDA with the coefficients reported in Table A.17.

Table A.17: Polynomial coefficients $k = \sum_{i=0}^{6} c_i T^i$ for EFDA Nb-Ti thermal conductivity.

c_6	c_5	c_4	c_3	c_2	c_1	c_0
$-5 \cdot 10^{-14}$	$1.5 \cdot 10^{-11}$	$6 \cdot 10^{-9}$	$-3 \cdot 10^{-6}$	0.0003	0.0456	0.066

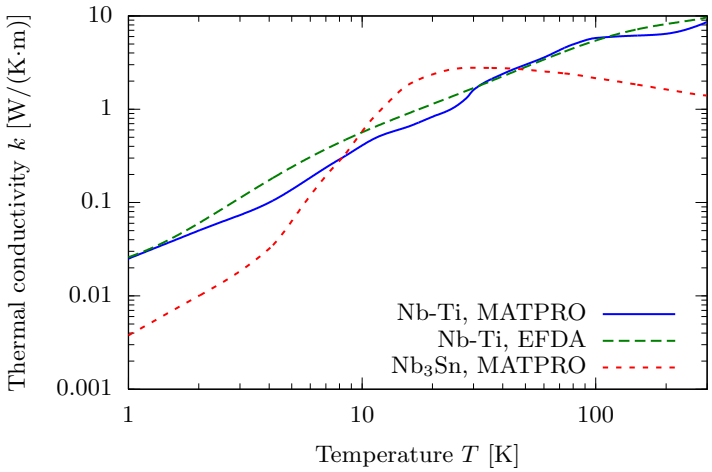

Figure A.12: Nb-Ti and Nb_3Sn thermal conductivity as a function of temperature.

A.4.3 Polyimide

Data of measured thermal conductivity for different samples of polyimide (Kapton) are reported in [147]. The results can be fitted by the polynomial function:

$$k(T) = \sum_{n=1}^{4} a_n [\ln (T+1)]^n \tag{A.42}$$

The fit parameters a_n for the samples of Kapton H and Kapton HN are reported in Table A.18. This fit for Kapton H is employed also in MATPRO.

Table A.18: Fit parameters for polyimide thermal conductivity from [147].

Type	a_1	a_2	a_3	a_4
Kapton H	$15.549\,709 \cdot 10^{-3}$	$-17.417\,525 \cdot 10^{-3}$	$82.690\,158 \cdot 10^{-4}$	$-81.952\,869 \cdot 10^{-5}$
Kapton HN	$30.792\,762 \cdot 10^{-3}$	$-32.061\,706 \cdot 10^{-3}$	$12.444\,129 \cdot 10^{-3}$	$-10.070\,564 \cdot 10^{-4}$

In NIST database, a log-log polynomial interpolation based on Eq. (A.1) is proposed, with a range of validity between 4 and 300 K and a curve fit error to data of 2%. The fit parameters are reported in Table A.19. The results are very similar to the previous data regarding Kapton H.

Table A.19: Fit parameters for NIST polyimide thermal conductivity.

a_0	a_1	a_2	a_3	a_4	a_5	a_6	a_7
5.73101	−39.5199	79.9313	−83.8572	50.9157	−17.9835	3.42413	−0.27133

This NIST fit is divergent under 4 K, therefore in CUDI a linear approximation is suggested under 4.3 K:

$$k(T) = 0.010703 - 0.00161 \cdot (4.3 - T) = 0.00378 + 0.00161 \cdot T \tag{A.43}$$

A.4.4 Glass-Epoxy Resin

G10 is an highly anisotropic material, since the heat conduction in the direction parallel to the glass fibers is much faster than in the normal direction. NIST proposes the polynomial function (Eq. A.1), with the parameters reported in Table A.20. The range of validity is [10; 300] K for normal direction and [12; 300] K for parallel one. In both cases the fit error is reported to be about 5%.

Table A.20: Fit parameters for NIST G10 thermal conductivity.

Direction	a_0	a_1	a_2	a_3	a_4	a_5	a_6	a_7	a_8
Normal	−4.1236	13.788	−26.068	26.272	−14.663	4.4954	−0.6905	0.0397	0
Parallel	−2.648 27	8.802 28	−24.8998	41.1625	−39.8754	23.1778	−7.956 35	1.488 06	−0.117 01

In MATPRO, a dataset from [89] is present and it is quite similar to NIST data. However, large uncertainties are present, since data with differences large as 50% compared to MATPRO are reported in a dataset from Fermilab [115] (see Figure A.13b).

A.4.5 Epoxy Resin

Data for thermal conductivity of epoxy resin can be found in [71]. A NIST log-log polynomial interpolation based on Eq. (A.1) can be obtained, with a range of validity between 2 and 300 K. The fit parameters are reported in Table A.21.

Table A.21: Fit parameters for epoxy thermal conductivity.

a_0	a_1	a_2	a_3	a_4	a_5	a_6	a_7
−2.69593	8.66066	−22.83492	32.28179	−25.96136	11.91945	−2.89189	0.28646

(a) Polyimide and epoxy resin.

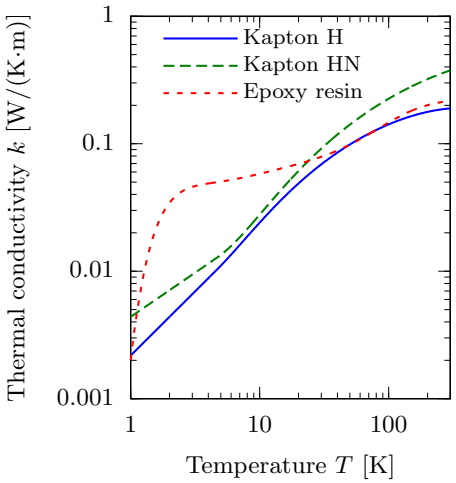

(b) G10, parallel and normal direction.

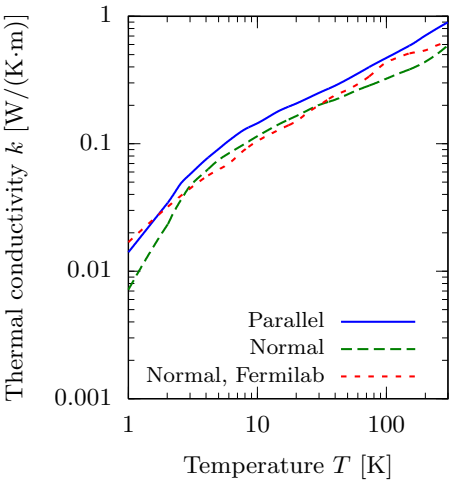

Figure A.13: Thermal conductivity in some insulating materials.

A.5 Helium Properties

Due to its peculiar nature and function in cryogenics, helium properties are presented together. The phase diagram of helium is reported in Figure A.14. Vapor and liquid phases can exist separately only up to the *critical point* (T_c, P_c), that is at (5.1953 K, 0.22746 MPa). Over critical point, helium is referred to as *super-critical*. Differently from common gases, four instead than three phases exist, since liquid phase is characterized by two different states, called He-I and He-II. The latter, also called *super-fluid helium*, is characterized by a null viscosity, due to quantum phenomena correlated to the Bose-Einstein condensate. The temperature at which the transition between He-I and He-II happens is called *lambda point*, and it ranges between 2.172 K at about 5 kPa to 1.835 K at about 3 MPa. The so-called *lambda line* separates He-I from He-II in the phase diagram. No conventional triple point exists in helium, since there is no place in the phase diagram where solid, liquid and vapor phases can coexist.

In Figure A.15, A.16 and A.17 respectively mass density ρ, specific heat at constant pressure c_p and thermal conductivity k are reported as a function of temperature for different values for pressure, with data from [173]. At the lambda point, the helium exhibits a peak in the specific heat that is not represented in Figure A.16 for clarity purposes. This pressure-dependent peak is in the range $100 - 120$ kJ/(K·kg),

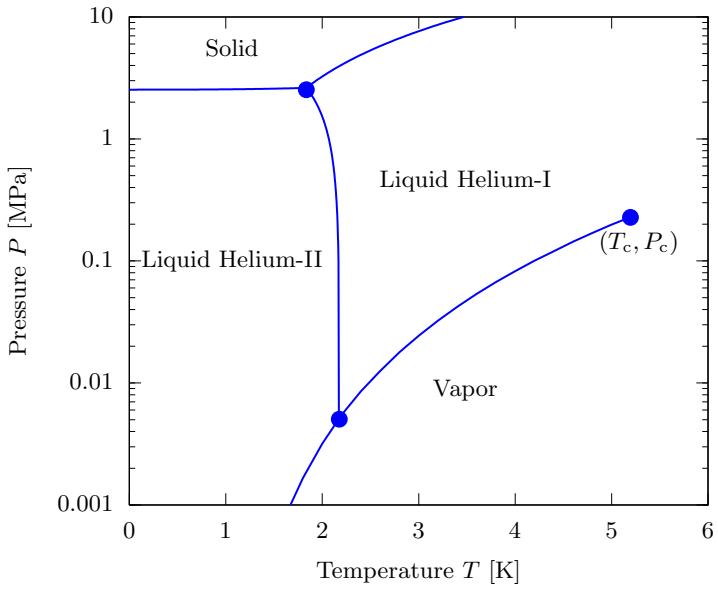

Figure A.14: Helium phase diagram at low temperatures.

i.e. one-two orders of magnitude larger than the specific heat at the neighboring temperatures. In Figure A.17 the thermal conductivity is not reported below the lambda point, since superfluid helium is characterized by an huge increase in k. In [151] a value of 100 kW/(K·m) is reported, orders of magnitude larger than copper. In these conditions, the helium can be considered as a perfect heat conductor. On the other hand, thermal conductivity in He-I is very small and it is generally neglected compared to solids.

Finally, in Figure A.18 the *specific enthalpy* h is plotted. Enthalpy H is a state function defined as:

$$H = U + PV, \tag{A.44}$$

where U is the internal energy, P the pressure and V the volume. Specific enthalpy h is the enthalpy H normalized to the mass.

Forced-flow cooled conductors generally employ super-critical helium as coolant, to avoid phase transitions and to obtain a therefore more regular heat transfer [188]. In the other cases, superfluid helium is generally preferred, because of the lower temperatures and high heat capacities that can be obtained.

A.5.1 Heat Exchange

The *convective heat transfer coefficient* h_c is defined through a relation similar to Fourier's law Eq. (A.33):

$$Q = A_{\text{wet}}\, h_c\, (T_s - T_{fl}), \tag{A.45}$$

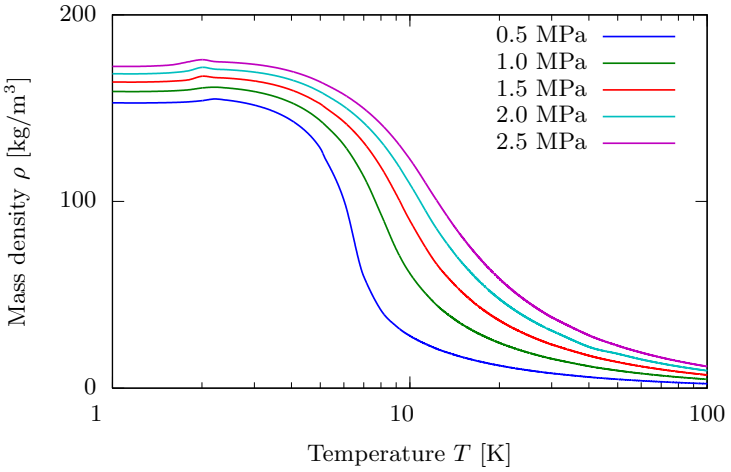

Figure A.15: Helium mass density ρ for different values of pressures.

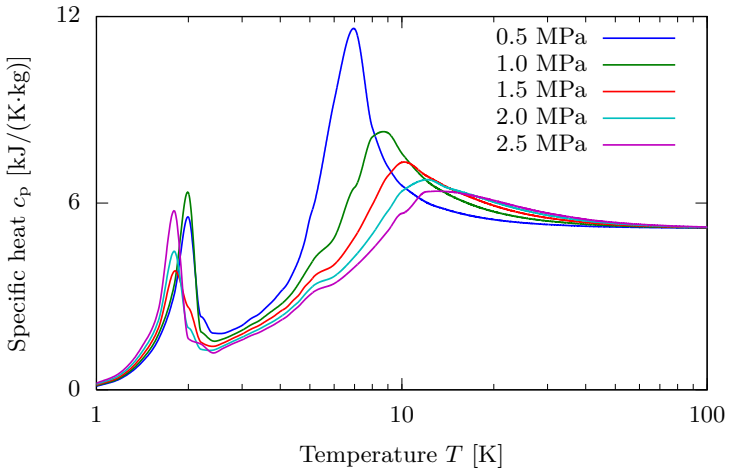

Figure A.16: Helium specific heat at constant pressure c_p for different values of pressures. The peak at the lambda point is not reported for clarity purposes.

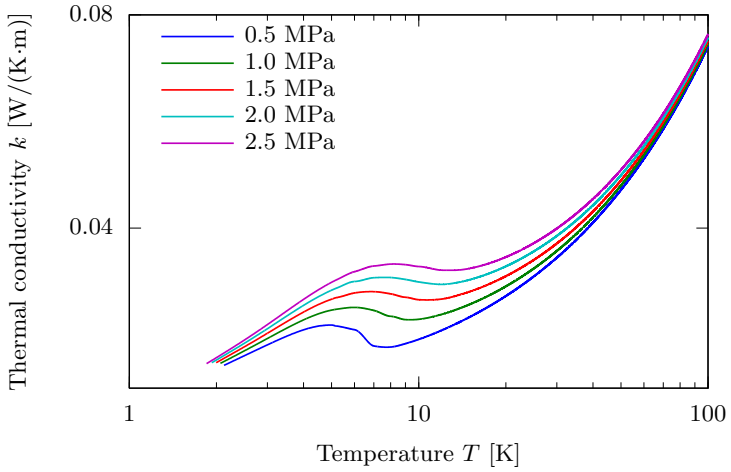

Figure A.17: Helium thermal conductivity k for different values of pressures between 0.25 and 2.5 MPa.

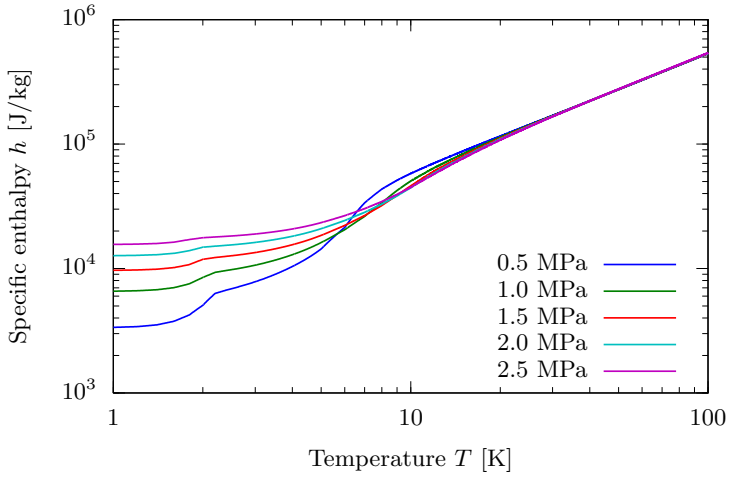

Figure A.18: Helium specific enthalpy h for different values of pressures.

where Q is the power exchanged between the fluid and the solid, A_{wet} is the wetted area, T_{s} is the solid temperature and T_{fl} is the fluid temperature. h_{c} is measured in units of W/(m$^2\cdot$ K). Strong variations in the heat transfer coefficient are present among the different helium phases and even in the same phase. A wide review on helium cooling and its consequences on superconducting cables can be found in [187].

Super-Fluid Helium

The thermal conductance is limited by the acoustic mismatch at the interface between two different materials. This phenomenon, related to the phonon scattering, is called *thermal boundary resistance* or *Kapitza resistance*. In practical applications the exchanged thermal power Q_{Kap} is generally expressed by the relation:

$$Q_{\mathrm{Kap}} = A_{\mathrm{wet}}\,\alpha_{\mathrm{Kap}}\,(T_{\mathrm{s}}^{n_{\mathrm{Kap}}} - T_{\mathrm{fl}}^{n_{\mathrm{Kap}}}). \tag{A.46}$$

The values of α_{Kap} and n_{Kap} are affected by the composition of the solid surface. Typical values are $\alpha_{\mathrm{Kap}} = 200$ W/(m$^2\cdot$ K$^{n_{\mathrm{Kap}}}$) and $n_{\mathrm{Kap}} = 4$ [175].

If the solid surface becomes much hotter than the fluid because of large heat fluxes, a film of vapor gas can be induced near the surface. This thin film can drastically decrease the heat exchange compared to Kapitza regime due to its thermal insulating effect. In this case a *film boiling coefficient* $h_{\mathrm{c,fb}}$ is assumed, with typical values of 250-500 W/(m$^2\cdot$K) [175] [187].

Sub-Critical Liquid Helium

Two main regimes are distinguished in heat transfer to liquid He-I [36]. When the heat flux is low, in the so-called *nucleate boiling* regime, separated vapor bubbles appear on the surface of the solid, and also in this case Kapitza resistance is the limiting mechanism. In [36] values of $\alpha_{\mathrm{Kap}} = 242$ W/(m$^2\cdot$ K$^{n_{\mathrm{Kap}}}$) and $n_{\mathrm{Kap}} = 2.8$ are assumed. When the heat flux becomes huge, also in this case a film boiling regime can arise, with values for the heat exchange coefficient between 250 [36], [175] and 300 W/(m$^2\cdot$K) [187].

Super-Critical Helium and Forced-Flow Cooling

In super-critical helium, two different regimes can be discriminated [152] [187]. In fast transients, experimental results indicate that heat transfer takes place in a thin helium layer in contact with the solid [22], therefore conduction of heat dominates in these conditions. After an initial peak, the heat transfer coefficient is reported to decrease inversely with the square root of time t:

$$h_{\mathrm{c,trans}} = \frac{1}{2}\sqrt{\frac{\pi k \rho c_{\mathrm{p}}}{t}} \tag{A.47}$$

When steady-state conditions are reached, a value of 500 W/(m$^2\cdot$K) is often proposed for natural convection [175]. Conversely, in *forced-flow cooling* the heat transfer coefficient approaches a steady-state value $h_{\mathrm{c,ss}}$ when the thermal boundary is

fully developed, about $10 - 100$ ms after the transient. In this case, correlations similar to the *Dittus-Bölter correlation* for turbulent flow have proven to be quite accurate [152]:

$$\mathrm{Nu} = 0.0259\,\mathrm{Re}^{0.8}\,\mathrm{Pr}^{0.4}, \tag{A.48}$$

where Re, Pr and Nu are respectively the adimensional *Reynolds, Prandtl* and *Nusselt numbers* defined as:

$$\mathrm{Re} = \frac{\rho v D}{\mu}, \tag{A.49}$$

$$\mathrm{Pr} = \frac{c_\mathrm{p}\mu}{k}, \tag{A.50}$$

$$\mathrm{Nu} = \frac{h_\mathrm{c} D}{k}, \tag{A.51}$$

where v is the fluid mean velocity, μ is the *dynamic viscosity*[2] and D is the *equivalent hydraulic diameter*. Eq. (A.47) can be therefore expressed in terms of heat exchange coefficient as:

$$h_\mathrm{c,ss} = 0.0259\frac{(\rho\, v)^{0.8}\, k^{0.6}}{D^{0.2}}\left(\frac{c_\mathrm{p}}{\mu}\right)^{0.4}. \tag{A.52}$$

Sometimes a further multiplicative factor $(T_\mathrm{fl}/T_\mathrm{s})^{0.716}$ is present in Eq. (A.48) to account for large temperature gradients with the wetted surface [188].

[2]Dynamic viscosity is a physical quantity that represents the fluid resistance to shearing flows. It is measured in Pa·s.

Appendix B

Statistical Approach for Voltage-Current Characteristics

In this Appendix, based on [112], the voltage-current characteristic (VAC) of superconducting wires is studied, focusing in particular on the impact of different critical current statistical distributions.

Jones et al. [87] studied the non-linearity in superconductor voltage-current characteristic (VAC), suggesting the existence of a critical current statistical distribution along the wire due to non-uniformities and defects. Starting from the classical flux-flow mechanism:

$$E(J) = \rho_{\mathrm{ff}}(J_{\mathrm{t}} - J_{\mathrm{c}}), \tag{B.1}$$

the non-linear characteristic can be considered as the result of the superposition of several linear effects described by Eq. (B.1):

$$E(I) = r_{\mathrm{ff}} \sum_{I>I_{\mathrm{c},i}}^{n} (I - I_{\mathrm{c},i}), \tag{B.2}$$

where $r_{\mathrm{ff}} = \rho_{\mathrm{ff}}/A$, being A the sample cross-section area. If the characteristic length along which I_{c} varies is much smaller than the sample length, the critical current can be modeled as a random variable described by a continuous statistical distribution $f(i_{\mathrm{c}})$ and the limit of Eq. (B.2) for $n \to \infty$ leads to:

$$E(I) = r_{\mathrm{ff}} \int_0^I f(i_{\mathrm{c}})(I - i_{\mathrm{c}})\, \mathrm{d}i_{\mathrm{c}}. \tag{B.3}$$

Equation (B.3) can be written as the sum of two integrals:

$$E(I) = r_{\parallel} I \underbrace{\int_0^I f(i_{\mathrm{c}})\, \mathrm{d}i_{\mathrm{c}}}_{A_1} - r_{\parallel} \underbrace{\int_0^I i_{\mathrm{c}} f(i_{\mathrm{c}})\, \mathrm{d}i_{\mathrm{c}}}_{A_2}. \tag{B.4}$$

The first is the definition of the cumulative distribution function, whereas the second is the statistical mean value of the critical currents lower than the current I.

A direct consequence of Eq. (B.3) is the so-called formula for deconvolution:

$$\frac{\partial^2 E}{\partial I^2} = r_{\mathrm{ff}} f(i_{\mathrm{c}}). \tag{B.5}$$

The meaning of this equation is that the inhomogeneities in the wire can lead to a macroscopic non-linear behavior even if the basic mechanism of loss is linear. Baixeras and Fournet [9] obtained the same result starting from the pinning forces distribution. It is quite clear from Eq. (B.5) that the experimental estimation of $f(i_{\mathrm{c}})$ is very difficult, since the evaluation of a second derivative is highly sensitive to noise. Furthermore, only the tail of the distribution is experimentally accessible: indeed, at high electric field the wire self-heating prevents an isothermal evaluation of the characteristic. Some theoretical assumptions on the shape of $f(i_{\mathrm{c}})$ must therefore be made.

Defining $\overline{I}_{\mathrm{c}}$ as the statistic mean value of the critical current distribution $f(i_{\mathrm{c}})$, Eq. (B.3) becomes:

$$E(I) \approx \begin{cases} 0, & I \ll \overline{I}_{\mathrm{c}}, \\ r_{\mathrm{ff}}(I - \overline{I}_{\mathrm{c}}), & I \gg \overline{I}_{\mathrm{c}}, \end{cases} \tag{B.6}$$

that is, at very high and very low currents Eq. (B.3) is equivalent to Eq. (B.1), with I_{c} replaced by $\overline{I}_{\mathrm{c}}$. The behavior for $I \sim \overline{I}_{\mathrm{c}}$ depends on $f(i_{\mathrm{c}})$ and in particular on the standard deviation of the distribution $\sigma_{I_{\mathrm{c}}}$. In the following the normalized standard deviation, defined by:

$$\sigma_{\mathrm{n}} = \frac{\sigma_{I_{\mathrm{c}}}}{\overline{I}_{\mathrm{c}}}, \tag{B.7}$$

is used, being very useful to describe the link between the VAC and the statistical dispersion of the critical current.

B.1 Multifilamentary Composites

In later works, more complete models for composite stabilized wires have been presented, to take into account the contribution of the resistive matrix. For example Warnes [183] obtained two models:

- in the monofilamentary case, r_{ff} is replaced by $r_{\parallel}$, that is the parallel connection of r_{ff} and the longitudinal resistive matrix resistance r_{mat};
- in the multifilamentary case, a further contribute is added to Eq. (B.3), to take into account the role of the transverse matrix resistivity r_{trans}. This contribute depends on the critical current distribution of the single filament $g(i_{\mathrm{c}})$, on the wire current I and on the ratio between the longitudinal and transverse current.

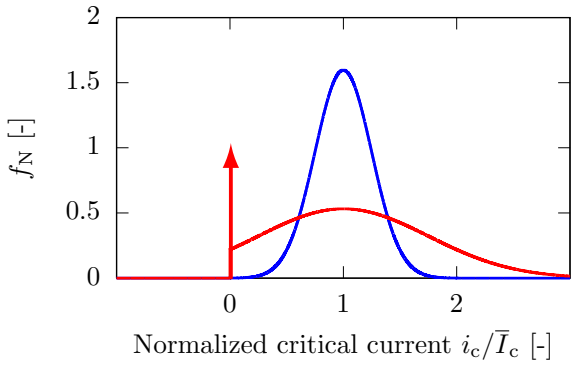

Figure B.1: Schematic sketch of the negative tail drawback for Normal distribution and the solution proposed in [60].

For the sake of simplicity, in the following only the first model will be considered, since the second one is quite complicated and involves a large number of unknown parameters, making it difficult to verify experimentally. This means that the contribution of the transverse current redistribution on the longitudinal electric field will be neglected. This is a reasonable assumption either where no redistribution is possible at all (monofilamentary-like wire) or where r_{trans} is so small that the current can freely redistribute between filaments (ideal multifilamentary wire).

Finally, the order of magnitude of normal-state resistivity of Nb-Ti and Nb_3Sn at cryogenic temperatures is 100 nΩ·m (see Section A.3.3), and this is also the order of magnitude of ρ_{ff}[1]. On the other hand, copper resistivity at room temperature is about 17 nΩ·m, and decreases at cryogenic temperatures according to the residual resistivity ratio, whose typical range is between some tens and some hundreds. Since the copper resistivity is at least two orders of magnitude lower than Nb-Ti and Nb_3Sn normal-state resistivities, for practical wires $r_{\text{ff}} \gg r_{\text{mat}}$, that means $r_{\parallel} \approx r_{\text{mat}}$.

B.2 Normal Distribution

Very often, following the central limit theorem, the Normal (or Gaussian) distribution has been used to model the critical current, for example in [79] [80]. The drawback in this approach is that while I_c is a non-negative random variable, the Normal distribution probability density function $f_N(i_c)$ is defined for $i_c \in \mathbb{R}$: the consequence is that the VAC doesn't tend to zero as the current tends to zero, and this is obviously not physical.

A possible solution was proposed in [60], in which the negative tails are replaced by a δ function centered for $I = 0$ with the same area (see Figure B.1). In this way the VAC correctly tends to zero as the current tends to zero, and it's also possible to compute analytically the equivalent n-index as a function of current (although the

[1] See Eq. (1.20), page 16.

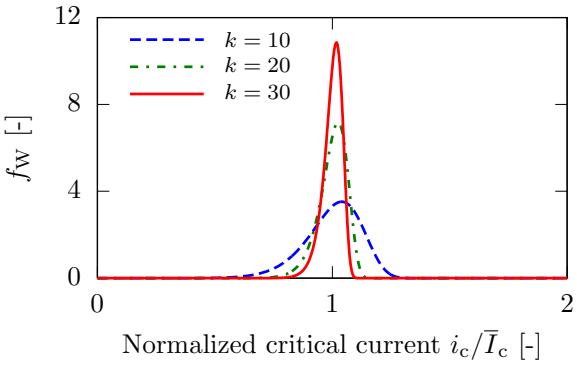

Figure B.2: Weibull probability density function for three different values of k. The corresponding σ_n is about 12%, 6% and 4% respectively.

expression is quite complex). This solution will not be considered in the following, since other statistical distributions are more suitable than the Normal to model the critical current, from both the theoretical and the experimental point of view.

B.3 Weibull Distribution

The Weibull distribution is mainly used in reliability engineering, and it is based on the weakest link model [184]. It is used to model failure times in series systems, in which the breakdown of one component causes the failure of the whole system [192]. Such a model could also be reasonable to describe the critical current in a single superconducting filament or in a monofilamentary-like wire: indeed, the wire will start to develop a loss as soon as the minimum critical current is reached, because no redistribution is possible. A 3-parameter Weibull distribution has been already used in [85] to model the VAC of some superconducting wires. In this work a 2-parameter distribution will be considered, in order to limit the number of unknowns and permit a more simple and straightforward comparison with experimental data.

This 2-parameter Weibull distribution is defined for $i_c \in [0, +\infty)$ with the probability distribution function:

$$f_W(i_c) = \frac{k}{I_0}\left(\frac{i_c}{I_0}\right)^{k-1} \exp\left[-\left(\frac{i_c}{I_0}\right)^k\right], \tag{B.8}$$

with k shape parameter and I_0 scaling parameter. In Figure B.2 $f_W(i_c)$ is plotted for three different values of k. The expected value of the distribution is:

$$\overline{I}_c = I_0\,\Gamma\left(1 + \frac{1}{k}\right), \tag{B.9}$$

where the Gamma function $\Gamma(s)$ is defined as:

$$\Gamma(s) = \int_0^\infty t^{s-1} e^{-t}\,\mathrm{d}t. \tag{B.10}$$

The normalized standard deviation is in this case:

$$\sigma_{\mathrm{n}} = \frac{\sqrt{2k\Gamma(2/k) - [\Gamma(1/k)]^2}}{\Gamma(1/k)}. \tag{B.11}$$

Its value depends only on the shape parameter k, that is therefore a measure of the dispersion of the distribution around its mean value. Equation (B.11) can be practically approximated with the function $1/k$ with an accuracy of 25%, therefore σ_{n} can be considered inversely proportional to the shape parameter.

It is possible to compute analytically Eq. (B.3) in the case of Weibull distribution, considering Eq. (B.4). The cumulative distribution function in the case of Weibull random variable is:

$$A_1 = \int_0^I f_{\mathrm{W}}(i_{\mathrm{c}})\,\mathrm{d}i_{\mathrm{c}} = 1 - \exp\left[-\left(\frac{I}{I_0}\right)^k\right]. \tag{B.12}$$

The second integral A_2, after replacing Eq. (B.8), becomes:

$$A_2 = k\int_0^I \left(\frac{i_{\mathrm{c}}}{I_0}\right)^k \exp\left[-\left(\frac{i_{\mathrm{c}}}{I_0}\right)^k\right]\mathrm{d}i_{\mathrm{c}}. \tag{B.13}$$

With a change of variables $t = (i_{\mathrm{c}}/I_0)^k$ the result is:

$$A_2 = I_0\int_0^{(I/I_0)^k} t^{\frac{1}{k}} \exp(-t)\,\mathrm{d}t, \tag{B.14}$$

that can be solved with integration by parts:

$$A_2 = -I\exp\left[-\left(\frac{I}{I_0}\right)^k\right] + \frac{I_0}{k}\int_0^{(I/I_0)^k} t^{\frac{1}{k}-1}\exp(-t)\,\mathrm{d}t. \tag{B.15}$$

Replacing Eqs. (B.12) and (B.15) in Eq. (B.4) it can obtained:

$$E(I) = r_{\|}\left[I - \frac{I_0}{k}\int_0^{(I/I_0)^k} t^{\frac{1}{k}-1}\exp(-t)\,\mathrm{d}t\right]. \tag{B.16}$$

Employing the formalism of the *normalized lower incomplete Gamma function* [2], defined by:

$$\mathrm{P}(s,x) = \frac{1}{\Gamma(s)}\int_0^x t^{s-1}e^{-t}\,\mathrm{d}t, \tag{B.17}$$

the final result is:

$$E(I) = r_{\|}\left[I - \frac{I_0}{k}\Gamma\left(\frac{1}{k}\right)\mathrm{P}\left(\frac{1}{k},\left(\frac{I}{I_0}\right)^k\right)\right], \tag{B.18}$$

that leads to:

$$E(I) = r_{\|}\left[I - \overline{I}_{\mathrm{c}}\,\mathrm{P}\left(\frac{1}{k},\left(\frac{I}{I_0}\right)^k\right)\right], \tag{B.19}$$

since:

$$\frac{I_0}{k}\Gamma\left(\frac{1}{k}\right) = I_0\Gamma\left(1+\frac{1}{k}\right) = \overline{I}_{\mathrm{c}}, \tag{B.20}$$

because of the well-known property of the Γ function:

$$\Gamma(s+1) = s\Gamma(s). \tag{B.21}$$

An important result can be obtained considering the series development of the function $\mathrm{P}(s,x)$ [2]:

$$\mathrm{P}(s,x) = \frac{x^s}{\Gamma(s)}\sum_{n=0}^{\infty}\frac{(-x)^n}{(s+n)n!}, \tag{B.22}$$

and retaining only the first two terms of the expansion:

$$\mathrm{P}(s,x) = \frac{x^s}{\Gamma(s)}\left(\frac{1}{s} - \frac{x}{s+1} + \mathcal{O}(x^2)\right). \tag{B.23}$$

Replacing it in Eq. (B.19), in the limit $(I/I_0)^{2k} \to 0$:

$$E(I) \approx r_{\parallel}\left[I - I + \left(\frac{I}{I_0}\right)^k \frac{I}{1+k}\right], \tag{B.24}$$

the final result is:

$$E(I) \cong \frac{I_0 r_{\parallel}}{1+k}\left(\frac{I}{I_0}\right)^{k+1}, \tag{B.25}$$

which is the well-known power law[2], considering:

$$n = 1 + k, \tag{B.26}$$

$$I_{\mathrm{c}} = I_0\left(\frac{nE_{\mathrm{c}}}{r_{\parallel}I_0}\right)^{\frac{1}{n}}. \tag{B.27}$$

Since usually $n \gg 1$, from Eq. (B.9) $\overline{I}_{\mathrm{c}} \approx I_0$ and $(I/I_0)^{2k}$ tends to zero quite quickly.

It's possible also to compute analytically the equivalent n-index applying Eq. (1.22) to Eq. (B.19), obtaining:

$$n = \frac{I}{E}\frac{\mathrm{d}E}{\mathrm{d}I} = \frac{1 - \exp\left[-\left(\frac{I}{I_0}\right)^k\right]}{1 - \frac{\overline{I}_{\mathrm{c}}}{I}\ \mathrm{P}\left(\frac{1}{k}, \left(\frac{I}{I_0}\right)^k\right)}. \tag{B.28}$$

This function is reported is Figure B.3 as a function of the normalized current $I_{\mathrm{n}} = I/\overline{I}_{\mathrm{c}}$ for three different values of k. As already demonstrated by Eq. (B.25), at low current there is a "power law regime" in which Eq. (B.19) is equivalent to a power law with $n = k + 1$. For $I > \overline{I}_{\mathrm{c}}$, the n-index decreases down to unity and becomes independent on the value of k, as expected from Eq. (B.6).

The following conclusions can be therefore drawn:

[2] Equation (1.21), page 17.

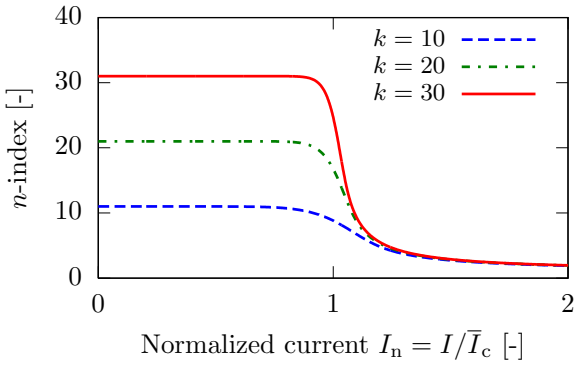

Figure B.3: Equivalent n-index for Weibull critical current distribution as a function of normalized current, for three different values for the shape parameter k.

1. a weak-link statistical description of the superconducting wire is able to explain the power law commonly used to experimentally parametrize the VAC;
2. in the "power law regime" the n-index is directly related to the parameter k of the Weibull distribution, and this creates also a link between this experimental parameter and the critical current statistical dispersion through Eq. (B.11);
3. the power law behavior is not a property of the superconductor itself, but of the whole composite wire. Indeed, considering Eq. (B.26) I_c is dependent also on the parallel resistance $r_{\|}$, that is dominated by the matrix resistance as explained in Section B.1.

Weibull distribution is therefore very important since it can theoretically justify what is commonly observed in practical wires. Nevertheless, deviations from power law, in particular at low fields, have been demonstrated experimentally [60], which suggests that other statistical approaches may be more suitable in these cases. Other distributions should therefore be considered, more appropriate in the case of an ideal multifilamentary wire as shown below.

B.4 Gamma Distribution

The Gamma distribution can be considered the dual distribution as regards the Weibull's one, since it's used to model failure times in systems with redundancy, like the parallel connection of multiple components [192]. Therefore it can be a reasonable description in a wire whose current can freely redistribute between its filaments, and the macroscopic critical current is the sum of the critical currents of the single filaments.

The probability density function of the Gamma distribution is:

$$f_G(i_c) = \frac{i_c^{k-1}}{\Gamma(k) I_0^k} \exp\left(-\frac{i_c}{I_0}\right), \tag{B.29}$$

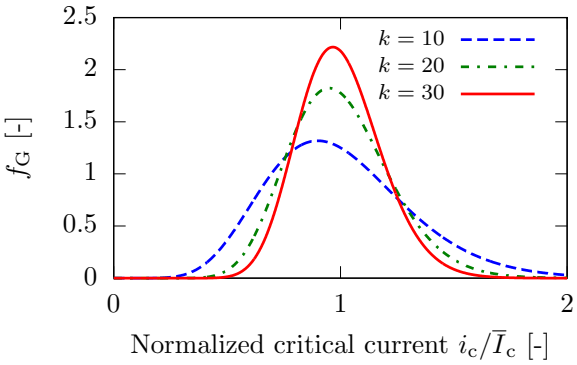

Figure B.4: Gamma probability density function for three different values of k. The corresponding σ_n is about 31%, 22% and 18% respectively.

whose expected value is:

$$\overline{I}_c = kI_0, \tag{B.30}$$

and the normalized standard deviation is:

$$\sigma_n = \frac{1}{\sqrt{k}}. \tag{B.31}$$

Like in Weibull distribution, the parameter k is a direct measure of the spread of the distribution, but the relation between σ_n and k is quite different. Indeed, comparing Figure B.2 and Figure B.4 we see that $f_G(i_c)$ is much wider than $f_W(i_c)$ for the same values for k.

Starting from Eq. (B.4), from the Gamma cumulative distribution function the result for A_1 is:

$$A_1 = \int_0^I f_G(i_c)\,\mathrm{d}i_c = \mathrm{P}\left(k, \frac{I}{I_0}\right), \tag{B.32}$$

while for A_2:

$$A_2 = \frac{1}{\Gamma(k)} \int_0^I \left(\frac{i_c}{I_0}\right)^k \exp\left(-\frac{i_c}{I_0}\right) \mathrm{d}i_c. \tag{B.33}$$

With the change of variables $t = i_c/I_0$:

$$A_2 = \frac{I_0}{\Gamma(k)} \int_0^{I/I_0} t^k \exp(-t)\,\mathrm{d}t. \tag{B.34}$$

Considering Eqs. (B.21) and (B.17):

$$A_2 = I_0 k\,\mathrm{P}\left(k+1, \frac{I}{I_0}\right) = \overline{I}_c\,\mathrm{P}\left(k+1, \frac{I}{I_0}\right), \tag{B.35}$$

because of the definition of $\overline{I}_c$ (see Eq. B.30). Putting A_1 and A_2 together the result is:

$$E(I) = r_{\|}\left[I\ \mathrm{P}\left(k, \frac{I}{I_0}\right) - \overline{I}_c\ \mathrm{P}\left(k+1, \frac{I}{I_0}\right)\right], \tag{B.36}$$

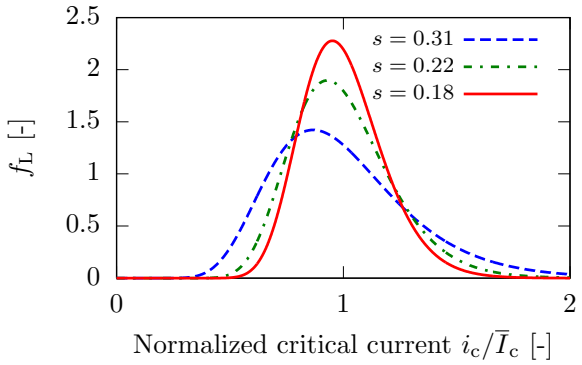

Figure B.5: Log-normal probability density function for three different values of s. The corresponding σ_n is about 31%, 22% and 18% respectively.

and the equivalent n-index is:

$$n = \left[1 - \frac{\overline{I}_c}{I} \frac{\mathrm{P}\left(k+1, I/I_0\right)}{\mathrm{P}\left(k, I/I_0\right)}\right]^{-1}. \tag{B.37}$$

A picture of n as a function of $I/\overline{I}_c$ will be given below, in Figure B.6. Replacing the series development Eq. (B.22) in Eq. (B.37) and retaining only the first term of the expansion:

$$n \to \left[1 - \frac{\overline{I}_c}{I} \frac{\Gamma(k)}{\Gamma(k+1)} \left(\frac{I}{I_0}\right)^{k+1} \left(\frac{I_0}{I}\right)^{k} \frac{k}{k+1}\right]^{-1}, \qquad \frac{I}{I_0} \to 0, \tag{B.38}$$

therefore for $I \to 0$:

$$n \to k+1, \tag{B.39}$$

like in Weibull case. However, Eq. (B.36) cannot be approximated with a power law with a constant n-index, since Eq. (B.39) is valid only asymptotically for $I \to 0$, while the n-index in Weibull case is almost constant up to larger current values.

B.5 Log-normal Distribution

An alternative way to solve the problem of the negative tail of the Normal distribution mentioned in Section B.2 is to consider a Log-normal distribution. A random variable is Log-normal if its logarithm is a Normal random variable [192]. This distribution is characterized by the parameters μ and s:

$$f_L(i_c) = \frac{1}{s\sqrt{2\pi} i_c} \exp\left[-\left(\frac{\ln(i_c) - \mu}{\sqrt{2}s}\right)^2\right]. \tag{B.40}$$

The expected value is:

$$\overline{I}_{\mathrm{c}} = \exp\left(\mu + \frac{s^2}{2}\right), \tag{B.41}$$

and the normalized standard deviation:

$$\sigma_{\mathrm{n}} = \sqrt{\exp\left(s^2\right) - 1}. \tag{B.42}$$

The parameter s, being a function only of σ_{n}, is therefore a direct measure of the spread of the distribution (like the parameter k for the Weibull and Gamma distributions). In particular, if $s \ll 1$, $\sigma_{\mathrm{n}} \approx s$. In Figure B.5 $f_{\mathrm{L}}(i_{\mathrm{c}})$ is plotted for three different values of s, chosen on purpose to obtain the same σ_{n} of Figure B.4. The Gamma and Log-Normal distributions can be quite similar if the parameters are chosen properly.

A_1 comes from the Log-normal cumulative distribution function:

$$A_1 = \int_0^I f_{\mathrm{L}}(i_{\mathrm{c}})\,\mathrm{d}i_{\mathrm{c}} = \frac{1}{2}\,\mathrm{erfc}\left(-\frac{\ln\left(I\right) - \mu}{s\sqrt{2}}\right), \tag{B.43}$$

where $\mathrm{erfc}(x)$ is the complementary error function, defined by:

$$\mathrm{erfc}\left(x\right) = \frac{2}{\sqrt{\pi}} \int_x^\infty e^{-t^2}\mathrm{d}t. \tag{B.44}$$

Considering from Eq. (B.41):

$$\mu = \ln(\overline{I}_{\mathrm{c}}) - \frac{s^2}{2}, \tag{B.45}$$

and replacing it into Eq. (B.43):

$$A_1 = \frac{1}{2}\,\mathrm{erfc}\left(\frac{1}{s\sqrt{2}} \ln\left(\frac{\overline{I}_{\mathrm{c}}}{I}\right) - \frac{s}{2\sqrt{2}}\right) = \frac{1}{2}\,\mathrm{erfc}\left(\alpha - \beta\right), \tag{B.46}$$

where α and β are defined as:

$$\alpha = \frac{1}{s\sqrt{2}} \ln\left(\frac{\overline{I}_{\mathrm{c}}}{I}\right), \tag{B.47}$$

$$\beta = \frac{s}{2\sqrt{2}}. \tag{B.48}$$

On the other hand A_2 is:

$$A_2 = \frac{1}{s\sqrt{2\pi}} \int_0^I \exp\left[-\left(\frac{\ln\left(i_{\mathrm{c}}\right) - \mu}{\sqrt{2}s}\right)^2\right] \mathrm{d}i_{\mathrm{c}}. \tag{B.49}$$

The change of variables $x = \left(\ln\left(i_{\mathrm{c}}\right) - \mu\right)/(\sqrt{2}s)$ should now be considered. In particular, the initial boundary of integration tends to $-\infty$, the upper:

$$\frac{\ln\left(I\right) - \mu}{\sqrt{2}s} = -\alpha + \beta. \tag{B.50}$$

The result is:

$$A_2 = \frac{\exp(\mu)}{\sqrt{\pi}} \int_{-\infty}^{-\alpha+\beta} \exp\left(-x^2 + \sqrt{2}sx\right) \mathrm{d}x, \tag{B.51}$$

summing and subtracting the constant $s^2/2$ in the argument of the exponential:

$$A_2 = \frac{\exp(\mu + s^2/2)}{\sqrt{\pi}} \int_{-\infty}^{-\alpha+\beta} \exp\left(-x^2 + \sqrt{2}sx - \frac{s^2}{2}\right) \mathrm{d}x. \tag{B.52}$$

Making a second change of variables $t = s/\sqrt{2} - x = 2\beta - x$:

$$A_2 = \frac{\overline{I}_\mathrm{c}}{\sqrt{\pi}} \int_{\alpha+\beta}^{\infty} \exp\left(-t^2\right) \mathrm{d}t, \tag{B.53}$$

in which $\overline{I}_\mathrm{c}$ has been replaced according to Eq. (B.41). Following Eq. (B.44) the final result is:

$$A_2 = \frac{\overline{I}_\mathrm{c}}{2} \operatorname{erfc}(\alpha + \beta), \tag{B.54}$$

and the resulting VAC is:

$$E(I) = \frac{r_\parallel}{2} \left[I \operatorname{erfc}(\alpha - \beta) - \overline{I}_\mathrm{c} \operatorname{erfc}(\alpha + \beta) \right]. \tag{B.55}$$

The equivalent n-index can be calculated as:

$$n = \left[1 - \frac{\overline{I}_\mathrm{c}}{I} \frac{\operatorname{erfc}(\alpha + \beta)}{\operatorname{erfc}(\alpha - \beta)} \right]^{-1}. \tag{B.56}$$

B.6 Comparison Between Equivalent n-indexes

In Figure B.6 the Eqs. (B.28), (B.37) and (B.56) are compared at the same levels of σ_n, respectively 10% and 20%. As expected, all three distributions behave in the same way for $I \gg \overline{I}_\mathrm{c}$. Differently, the behavior at low current is quite different:

- Weibull distribution n-index tends to $k + 1$, as already explained in Section B.3;
- Gamma distribution n-index tends to $k + 1$ like Weibull, but a "power law regime", like in Weibull case, cannot be considered;
- Log-normal distribution n-index diverges as the current goes to zero.

This means that, in the case of an ideal multifilamentary wire, the slope of the VAC is much steeper, since the redistribution between filaments can hamper the resistive voltage development up to higher value of transport current.

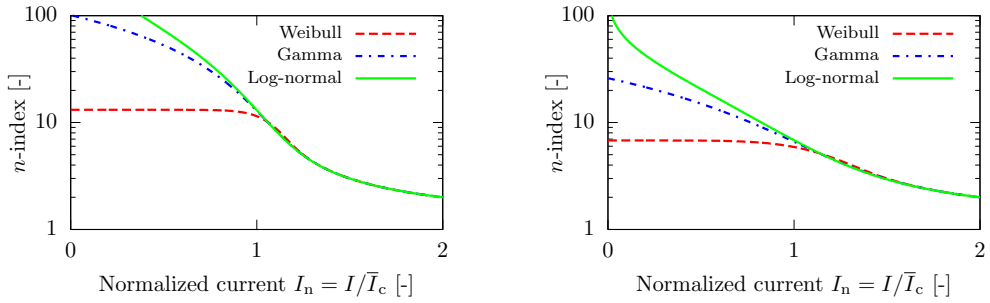

Figure B.6: Equivalent n-index comparison at the same value of σ_n, 10% (left) and 20% (right).

B.7 Comparison with Experimental Data

The theoretical models presented above have been applied on high accuracy measurements of VAC on a NIST Nb-Ti wire [4]. The sample of Nb-Ti was measured at different levels of magnetic induction, in the range 4-10 T, in a liquid helium bath at 4.2 K with voltage taps at a distance of 44 cm. The wire, containing 180 superconducting filaments, was characterized by a diameter of 0.5 mm and a Cu/non-Cu ratio of 1.46.

The experimental datasets have been fitted with a non-linear least-square regression with the proposed theoretical models Eqs. (B.19), (B.36) and (B.55). Three free parameters are present in each of the theoretical VACs: the shunt resistance per unit length $r_{\parallel}$, a scaling parameter (I_0 for Weibull and Gamma, μ for Log-normal) and a shape parameter (k for Weibull and Gamma, s for Log-normal). $r_{\parallel}$ has been either considered a free parameter or a fixed one, computed from the cross-section area of the wire and the copper resistivity as a function of residual resistivity ratio, magnetic field and temperature (see Section A.3.2). No significant differences in terms of goodness of fit have been found between these two cases.

In Figure B.7 examples of comparison between experimental data and fit functions are plotted for three different levels of magnetic induction. The range of the analysis in terms of electric field is more than two decades. The lower limit at 0.2 μV/m (1 μV/m for measurements at 9, 9.5 and 10 T) has been chosen to avoid points affected by the experimental noise. Over 30 μV/m the self-heating sets a upper bound to the analysis: for example in Figure B.7 a steep increase in the estimated n-index is easily noticeable. Data over that threshold have been therefore discarded during the fitting procedure.

To summarize the results in terms of goodness of fit, for each dataset the reduced chi-squared χ^2_{red} has been computed:

$$\chi^2_{\mathrm{red}} = \frac{1}{\nu} \sum_i \frac{[E_{\mathrm{meas}}(I_i) - E_{\mathrm{fit}}(I_i)]^2}{\sigma^2_{\mathrm{meas},i}}, \tag{B.57}$$

where $E_{\mathrm{meas}}(I_i)$ is measured value of the electric field at the current I_i, $E_{\mathrm{fit}}(I_i)$ is

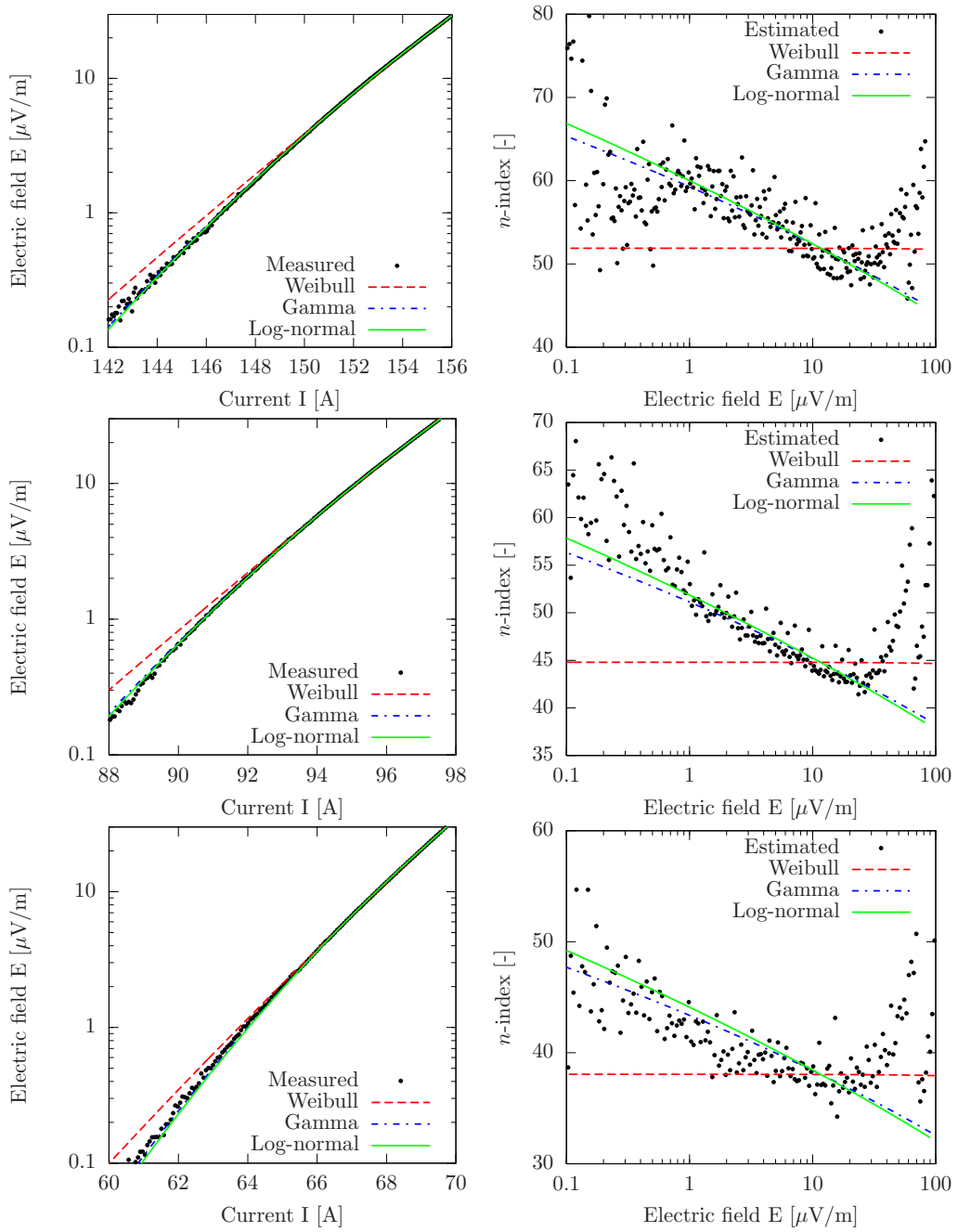

Figure B.7: On the left, comparison between experimental data and fitted functions, for 5 T (upper), 7 T (middle) and 8 T (lower) datasets. On the right, n-index as a function of the electric field, for the same datasets. The experimental n-index has been estimated with a numerical differentiation of the VAC filtered with a moving average to mitigate the experimental noise. The theoretical curves have been computed using the best fit parameters obtained with the non-linear regression.

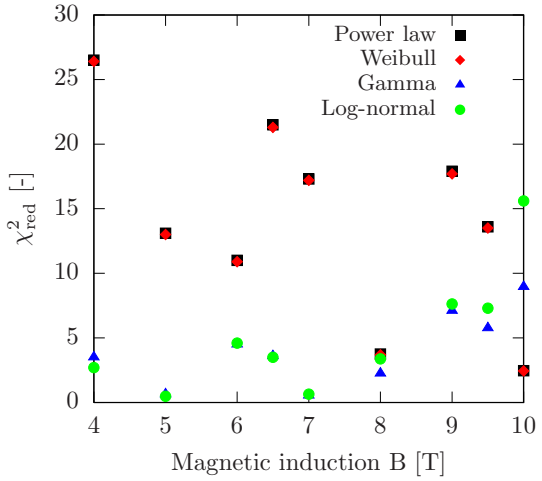

Figure B.8: Reduced chi-squared χ^2_{red} for the different fit functions at different magnetic induction.

the result of the fitting procedure at the same current, $\sigma_{meas,i}$ is the statistical error on the measure and ν is the number of degrees of freedom. Typically, $\nu = N - n - 1$, where N is the number of observations and n is the number of fitting parameters. The goodness of fit is plotted in Figure B.8 for the three VACs as a function of the magnetic induction, along with the goodness of fit of the common power law as a reference. The purpose of this analysis is to have a relative, rather than absolute, measure of the goodness of fit between the different models. Indeed, the absolute value of χ^2_{red} is in any case quite high, a sign that the fitting error cannot be explained only in terms of the statistical error.

The conclusion is that Weibull distribution, as expected, is performing in the same way as a power law with a constant n. It was also expected that Gamma and Log-normal distributions lead to comparable results, since the two distributions can be quite similar with an adequate set of parameters (see Section B.5). On the other hand, for this sample Gamma and Log-normal distributions show better agreement to experimental data than Weibull and power law in almost all the cases, due to the relevant variation of the n-index with the electric field, clearly visible in Figure B.7.

B.8 Conclusions

The non-linearity of the VAC can be justified by the presence of a statistical distribution of the critical current along the sample. Weibull distribution, based on a series/weak-link statistical description of the sample, can be reasonable in the case of a single superconducting filament or in a composite wire where the current redistribution is difficult. It is possible to demonstrate that Weibull distribution is able to theoretically justify the commonly used power law with a n-index constant with electric field, and it implies a direct relationship between the n-index and the stan-

dard deviation of the statistical distribution. On the other hand other distributions, like Gamma and Log-normal, can effectively reproduce data in which the n-index is not constant with the electric field. From a theoretical point of view, these two distributions are more reasonable than the Normal distribution that is often used in these analyses. Unlike Weibull case, they are not based on a weak-link model, and therefore they can be suitable in the case of a wire with current redistribution among the filaments.

Appendix C

Proof of the Rutherford Cable Geometry Equations

In this short Appendix the proof of the equations describing the circle arcs employed in the smoothed Rutherford geometry is reported[1]. The general parametric equation for a tri-dimensional circle is:

$$x_i(\theta) = c_i + r(a_i \cos\theta + b_i \sin\theta), \qquad i = 1, 2, 3 \tag{C.1}$$

where a_i, b_i and c_i are constants to be determined and r is the circle radius. The following conditions should be applied, as shown in Figure C.1:

$$\mathbf{x}(0) = \mathbf{x}^{\text{ini}}, \tag{C.2}$$

$$\mathbf{u}_{\text{t}}(0) = \mathbf{u}_{\text{t}}^{\text{ini}}, \tag{C.3}$$

$$\mathbf{u}_{\text{t}}(\Theta) = \mathbf{u}_{\text{t}}^{\text{fin}}. \tag{C.4}$$

Since the circle radius r is a parameter difficult to handle in the case of the Rutherford cable, a further condition is added to replace r with a parameter related to the cable axis curvilinear coordinate:

$$x_3(\Theta) = x_3(0) + s_{\text{sm}}. \tag{C.5}$$

The unit vector $\mathbf{u}_{\text{t}}$ tangent to the circle arc can be obtained by deriving Eq. (C.1) along the curvilinear coordinate $s = r\theta$:

$$u_{\text{t,i}}(\theta) = \frac{\mathrm{d}x_i}{\mathrm{d}s} = -a_i \sin\theta + b_i \cos\theta, \qquad i = 1, 2, 3. \tag{C.6}$$

Equation (C.3) leads to a condition for b_i:

$$b_i = u_{\text{t,i}}^{\text{ini}}, \qquad i = 1, 2, 3, \tag{C.7}$$

[1] See Section 3.2.1, page 58.

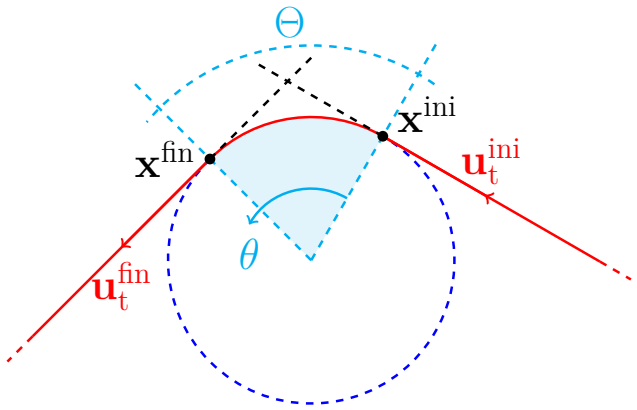

Figure C.1: 2D view of the circle arc employed in the Rutherford cable model.

Eq. (C.4) to a condition for a_i:

$$a_i = \frac{b_i \cos\Theta - u_{\mathrm{t,i}}^{\mathrm{fin}}}{\sin\Theta} = \frac{u_{\mathrm{t,i}}^{\mathrm{ini}} \cos\Theta - u_{\mathrm{t,i}}^{\mathrm{fin}}}{\sin\Theta}, \qquad i = 1, 2, 3, \tag{C.8}$$

Eq. (C.5) to a condition for the radius:

$$r = \frac{s_{\mathrm{sm}}}{a_3(\cos\Theta - 1) + b_3 \sin\Theta} = \frac{s_{\mathrm{sm}}}{(u_{\mathrm{t,3}}^{\mathrm{ini}} + u_{\mathrm{t,3}}^{\mathrm{fin}})} \frac{\sin\Theta}{(1 - \cos\Theta)}, \tag{C.9}$$

and finally Eq. (C.2) to a condition for c_i:

$$c_i = x_i^{\mathrm{ini}} - r a_i = x_i^{\mathrm{ini}} - \frac{s_{\mathrm{sm}}}{(u_{\mathrm{t,3}}^{\mathrm{ini}} + u_{\mathrm{t,3}}^{\mathrm{fin}})} \frac{u_{\mathrm{t,i}}^{\mathrm{ini}} \cos\Theta - u_{\mathrm{t,i}}^{\mathrm{fin}}}{(1 - \cos\Theta)}, \qquad i = 1, 2, 3. \tag{C.10}$$

Replacing these conditions in Eqs. (C.1) and (C.6) the result is:

$$x_i(\theta) = x_i^{\mathrm{ini}} + s_{\mathrm{sm}} \frac{u_{\mathrm{t,i}}^{\mathrm{ini}}[\cos(\Theta - \theta) - \cos\Theta] + u_{\mathrm{t,i}}^{\mathrm{fin}}(1 - \cos\theta)}{(u_{\mathrm{t,3}}^{\mathrm{ini}} + u_{\mathrm{t,3}}^{\mathrm{fin}})(1 - \cos\Theta)}, \tag{C.11}$$

$$u_{\mathrm{t,i}}(\theta) = \frac{u_{\mathrm{t,i}}^{\mathrm{ini}} \sin(\Theta - \theta) + u_{\mathrm{t,i}}^{\mathrm{fin}} \sin\theta}{\sin\Theta}, \tag{C.12}$$

that leads to Eqs. (3.36)-(3.45) considering the suitable values for $x_{\mathrm{i}}^{\mathrm{ini}}$, $x_{\mathrm{i}}^{\mathrm{fin}}$, $u_{\mathrm{t,i}}^{\mathrm{ini}}$ and $u_{\mathrm{t,i}}^{\mathrm{fin}}$. In particular, for $x_3 = s_{\mathrm{ax}}$ in the region $s_{\mathrm{ax}} \in [s_{\mathrm{ax}}^a - s_{\mathrm{sm}}/2, s_{\mathrm{ax}}^a + s_{\mathrm{sm}}/2]$ the result is:

$$s_{\mathrm{ax}}(\theta) = s_{\mathrm{ax}}^a + \frac{s_{\mathrm{sm}}}{2} \frac{\cos(\Theta - \theta) - \cos\theta}{(1 - \cos\Theta)}, \tag{C.13}$$

that can be rewritten as:

$$\frac{s_{\mathrm{ax}}(\theta) - s_{\mathrm{ax}}^a}{s_{\mathrm{sm}}} = \frac{\cos(\Theta^a - \theta^a) - \cos\theta^a}{2(1 - \cos\Theta^a)} = \frac{(\cos\Theta^a - 1)\cos\theta^a + \sin\Theta^a \sin\theta^a}{2(1 - \cos\Theta^a)}, \tag{C.14}$$

where the first member is exactly the definition of t^a in Eq. (3.35). With the change of variables $p = \cos\theta^a \Longrightarrow \sin\theta^a = \sqrt{1-p^2}$ the following equation can be obtained:

$$(1-\cos\Theta^a)(p+2t^a) = \sin\Theta^a\sqrt{1-p^2}, \tag{C.15}$$

that leads to a second order equation:

$$(1-\cos\Theta^a)^2(p+2t^a)^2 = \sin^2\Theta^a(1-p^2) \quad \Longrightarrow \quad (1+\alpha)p^2 + 4t^a p + 4(t^a)^2 - \alpha = 0, \tag{C.16}$$

where:

$$\alpha = \frac{\sin^2\Theta^a}{(1-\cos\Theta^a)^2} = \cot^2\left(\frac{\Theta^a}{2}\right). \tag{C.17}$$

The solution of Eq. (C.16) permits to express θ^a as a function of s_{ax}:

$$p = \cos\theta^a = \sin\Theta^a\sqrt{\frac{1}{2(1-\cos\Theta^a)} - (t^a)^2} + (\cos\Theta^a - 1)t^a, \tag{C.18}$$

leading to Eq. (3.34).

Appendix D

Runge-Kutta Methods

The aim of this Appendix is to describe of the most important aspects regarding the numerical integration of systems of differential equations with Runge-Kutta methods. This class of numerical solvers is very wide, and there is not a general-purpose method suitable for all the cases. Thus, it is a good practice to consider different solution methods, in order to find the most efficient choice in terms of computational effort and results accuracy.

A generic Runge-Kutta method with step-size h applied to the problem:

$$\frac{\mathrm{d}y}{\mathrm{d}t} = f(t, y), \tag{D.1}$$

can be defined by the algebraic equation:

$$y_{n+1} = y_n + \sum_{i=1}^{s} b_i k_i, \tag{D.2}$$

where:

$$k_i = hf\left(t_n + c_i h, y_n + \sum_{j=1}^{s} a_{ij} k_j\right). \tag{D.3}$$

The coefficients a_{ij}, b_i and c_i are generally arranged in the so-called *Butcher tableau*, as shown in Table D.1.

Table D.1: Generic Butcher tableau.

0	a_{11}	a_{12}	$\dots$	a_{1s}
c_2	a_{21}	a_{22}	$\dots$	a_{2s}
$\vdots$	$\vdots$	$\vdots$	$\ddots$	$\vdots$
c_s	a_{s1}	a_{s2}	$\dots$	a_{ss}
	b_1	b_2	$\dots$	b_s
	b_1^*	b_2^*	$\dots$	b_s^*

c	$\mathbf{A}$
	b^T
	$b^{*\mathsf{T}}$

A is the *Runge-Kutta matrix*, the coefficients b_i are the *weights*, c_i are the *nodes* and s is the number of *stages*. The method has an *order* p if the error, defined as the difference between the exact solution of Eq. (D.1) and the computed value of Eq. (D.2) is $\mathcal{O}(h^{p+1})$. The coefficients b_i^* are generally used for adaptive step-size control. Indeed, b_i^* are the weights of a Runge-Kutta method with the same Runge-Kutta matrix and the same nodes, but with a different order. Therefore, the error can be estimated with:

$$e_{n+1} = y_{n+1} - y_{n+1}^* = h \sum_{i=1}^{s} (b_i - b_i^*) k_i, \tag{D.4}$$

and then employed to decide the next step-size.

Depending on the shape of the Runge-Kutta matrix, the methods can be classified as:

- *explicit*, if **A** is lower triangular and every element of the main diagonal is zero. Indeed, in this case Eqs. (D.3) are decoupled and can be directly solved computing the function f;
- *implicit*, in all the other cases, and Eqs. (D.3) must be solved with an iterative approach.

Generally, the computational effort required by implicit methods is much larger than explicit methods of the same order, because of the iterative solution required. However, there is a class of problems, called *stiff equations*, for which the application of certain numerical methods leads to unstable results unless a very short step-size is adopted. This is generally due to some terms of the solution that are characterized by much smaller time constants than the others.

To analyze this problem, the notion of *A-stability* and *L-stability* is introduced [78], considering the *test equation*:

$$\frac{\mathrm{d}y}{\mathrm{d}t} = \lambda y, \qquad \lambda \in \mathbb{C}, \tag{D.5}$$

whose numerical solution with a generic Runge-Kutta method can be expressed as:

$$y_{n+1} = R(h\lambda) y_n = R(z) y_n, \tag{D.6}$$

where $R(z)$ is the method *stability function*. The method is called *A-stable* if:

$$|R(z)| < 1, \qquad \forall z : \Re\{z\} < 0. \tag{D.7}$$

This property ensures that the solution remains finite for every time step. The *L-stability* is instead verified if the method is A-stable and:

$$\lim_{z \to -\infty} R(z) = 0. \tag{D.8}$$

L-stability assures that all oscillations are damped, and this is a fundamental property if the stiffness is severe. It can be demonstrated that:

- no explicit method is A-stable;
- no explicit method can be considered more stable than another in the sense of A-stability.

Thus, in the case of stiff problems implicit methods can be more attractive than explicit ones, despite of their increased complexity.

A brief description of the some common explicit and implicit Runge-Kutta methods is reported in the following sections.

D.1 Explicit Methods

D.1.1 Bogacki-Shampine

The Bogacki-Shampine method [23] is a four stages, third order method, proposed in 1989. It is a *First Same As Last* (FSAL) method: it means that the last stage is evaluated at the same node than the first stage of the following step, so the number of $f(t, y)$ evaluations per step is $s - 1$ instead than s. The coefficients b_i^* describe an embedded second order method for step-size control.

Table D.2: Butcher tableau for Bogacki-Shampine method.

0				
1/2	1/2			
3/4	0	3/4		
1	2/9	1/3	4/9	
	2/9	1/3	4/9	0
	7/24	1/4	1/3	1/8

D.1.2 Runge-Kutta-Fehlberg

The Runge-Kutta-Fehlberg method [66] is a six stages, fourth order method, proposed in 1969. It features an embedded fifth order method for step-size control.

Table D.3: Butcher tableau for Runge-Kutta-Fehlberg method.

0						
1/4	1/4					
3/8	3/32	9/32				
12/13	1932/2197	-7200/2197	7296/2197			
1	439/216	-8	3680/513	-845/4104		
1/2	-8/27	2	-3544/2565	1859/4104	-11/40	
	25/216	0	1408/2565	2197/4104	-1/5	0
	16/135	0	6656/12825	28561/56430	-9/50	2/55

D.1.3 Dormand-Prince

The Dormand-Prince method [56] is a seven stages, fifth order method, proposed in 1980. Like the Bogacki-Shampine method it is FSAL, therefore it needs six, not seven function evaluations. It contains an embedded fourth order method for step-size control.

Table D.4: Butcher tableau for Dormand-Prince method.

0							
1/5	1/5						
3/10	3/40	9/40					
4/5	44/45	-56/15	32/9				
8/9	19372/6561	-25360/2187	64448/6561	-212/729			
1	9017/3168	-355/33	46732/5247	49/176	-5103/18656		
1	35/384	0	500/1113	125/192	-2187/6784	11/84	
	35/384	0	500/1113	125/192	-2187/6784	11/84	0
	5179/57600	0	7571/16695	393/640	-92097/339200	187/2100	1/40

D.1.4 Cash-Karp

The Cash-Karp method [44] is a six stages, fifth order method, proposed in 1990. Like the Dormand-Prince method, it contains an embedded fourth order method for step-size control.

Table D.5: Butcher tableau for Cash-Karp method.

0						
1/5	1/5					
3/10	3/40	9/40				
3/5	3/10	-9/10	6/5			
1	-11/54	5/2	-70/27	35/27		
7/8	1631/55296	175/512	575/13824	44275/110592	253/4096	
	37/378	0	250/621	125/594	0	512/1771
	2825/27648	0	18575/48384	13525/55296	277/14336	1/4

D.2 Implicit Methods

The solution of a generic implicit method could be quite complex, because the system of Eq. (D.3) cannot be decoupled in independent stages. Because of that, the class of *Diagonal Implicit Runge-Kutta* (DIRK) methods is more attractive for implementation, since for these methods the Runge-Kutta matrix $\mathbf{A}$ is lower triangular, therefore the system of equations (D.3) can be solved as s independent implicit systems. If the iterative method employed is Newton-Raphson, the iteration matrix

$\mathbf{A}_{\mathrm{NR}}$ at the i^{th} stage has the form:

$$\mathbf{A}_{\mathrm{NR}} = \mathbf{I} - ha_{ii}\mathbf{J} \tag{D.9}$$

where $\mathbf{I}$ is the identity matrix and $\mathbf{J}$ is the jacobian of the vector of functions $f(t, y)$.

An important subclass of DIRK methods are the *Singly Diagonal Implicit Runge-Kutta* (SDIRK) methods, that means that all the elements on the main diagonal of the matrix $\mathbf{A}$ are equal. In this case, the iteration matrix of Eq. (D.9) remains the same through all the stages in one step, reducing the computational cost.

D.2.1 TR-BDF2

The TR-BDF2 method was proposed for the first time in 1985 in the context of electronical devices simulation [12], but it has been later on intensively studied because of its good properties [81]. It is composed by two stages. The first stage is based on the *trapezoidal rule*, whereas the second is *backwards-differentiation formula* of order 2. The method is a member of the class of the order 2 DIRK methods (DIRK2). Indeed, the Butcher tableau is:

Table D.6: Butcher tableau for TR-BDF2 method. $\gamma = 2-\sqrt{2}$, $d = \gamma/2$, $w = \sqrt{2}/4$.

0			
γ	d	d	
1	w	w	d
	w	w	d
	$(1-w)/3$	$(3w+1)/3$	$d/3$

From the point of view of standard Runge-Kutta methods, the method has three stages, but it is FSAL, therefore only the second and the third implicit stages must be calculated. Furthermore, TR-BDF2 is "almost" a SDIRK method, because only a_{11} is not equal to d. However, since the first stage is not computed, the Newton-Raphson matrix $\mathbf{A}_{\mathrm{NR}}$ can be maintained through all the stages. The method provides a third order embedded companion for adaptive step-size computation. It can be demonstrated that the TR-BDF2 method is L-stable, thus it is very appropriate for stiff problems.

D.2.2 TRX2

The TRX2 method [81] is based on the application of two subsequent trapezoidal rules in the intervals $[t_n, t_n + h/2]$ and $[t_n + h/2, t_n + h]$, and it features an embedded method for step-size control based on the Simpson's rule. The Butcher tableau is reported in Table D.7.

The method shares a lot of properties with TR-BDF2, since it is FSAL and "almost" SDIRK. It is generally more efficient than TR-BDF2 [81] but it is not L-stable.

Table D.7: Butcher tableau for TRX2 method.

0			
1/2	1/4	1/4	
1	1/4	1/2	1/4
	1/4	1/2	1/4
	1/6	2/3	1/6

D.2.3 L-Stable SDIRK4

A L-stable SDIRK, order 4 is reported in [78]. This method is generally less efficient than the order two methods previously reported for the large effort needed in several iterative steps.

Table D.8: Butcher tableau for L-stable SDIRK4.

0					
1/4	1/4				
3/4	1/2	1/4			
11/20	17/50	-1/25	1/4		
1/2	371/1360	-137/2720	15/544	1/4	
1	25/24	-49/48	125/16	-85/12	1/4
	25/24	-49/48	125/16	-85/12	1/4
	59/48	-17/96	225/32	-85/12	0

Appendix E

Steady-State Current Diffusion in a CICC Triplet

In this Appendix the current diffusion during an inter-strand resistance measurement in a CICC triplet is analyzed[1]. The following assumptions are considered:

- the effect of adjacent neighboring triplets is neglected;
- the triplet is constituted by two superconducting (SC) strands and one normal-conducting (NC) strand, since it is the most common composition. The analysis can be easily generalized to the case of a triplet composed by two NC strands and one SC strand;
- the contact resistance per unit length r_c [Ω·m] is the same for the NC and the SC strands;
- the SC strands working condition is far from the critical surface, i.e. the longitudinal resistance of the SC strand can be modeled as a short-circuit.

The triplet is preliminary discretized into a set of longitudinal segments, each with a length Δz. The equivalent circuit of the sample is represented in Figure E.1. The following parameters will be considered:

$$R_l = \frac{\rho_E}{A_{str}}\Delta z = r_l \Delta z, \tag{E.1}$$

$$R_c = \frac{r_c}{\Delta z}, \tag{E.2}$$

where Δz is the segment length and A_{str} is the NC strand cross-section area. The resistances R_c between the two SC strands are in parallel and therefore they can be merged into a single resistance:

$$R_{c,L} = \frac{r_c}{L}, \tag{E.3}$$

where L is the sample length.

[1] A similar model for the current redistribution between a normal-conducting and superconducting specimens can be found in [188], chapter 10 page 234.

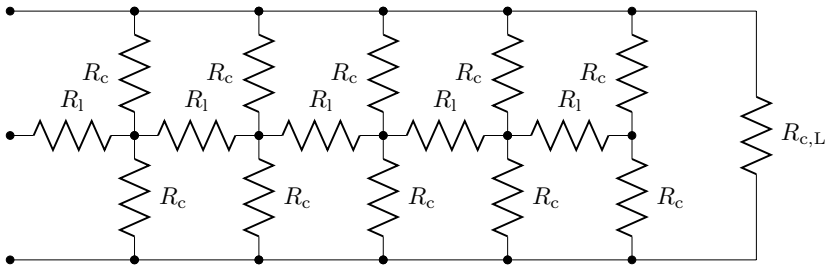

Figure E.1: Triplet equivalent circuit.

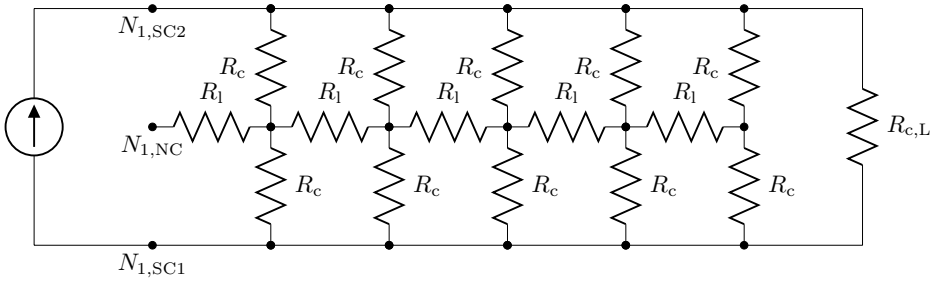

Figure E.2: Model of the inter-strand resistance measurement between two superconducting strands.

E.1 Superconductor/Superconductor

In the case of SC-SC inter-strand resistance measure, the current generator is inserted between nodes $N_{1,\mathrm{SC1}}$ and $N_{1,\mathrm{SC2}}$, as shown in Figure E.2. The voltage is defined at coordinates $z_k = k\Delta z$ and the currents at coordinates $z_k^{'} = (k + 1/2)\Delta z$. For the NC nodes the following equations can be written:

$$\begin{cases} V(z+\Delta z) - V(z) = -R_{\mathrm{l}} I\left(z + \dfrac{\Delta z}{2}\right), \\ I\left(z + \dfrac{\Delta z}{2}\right) - I\left(z - \dfrac{\Delta z}{2}\right) = \dfrac{-2V(z) + V_{1,\mathrm{SC}} + V_{2,\mathrm{SC}}}{R_{\mathrm{c}}}, \end{cases} \tag{E.4}$$

where $V_{1,\mathrm{SC}}$ and $V_{2,\mathrm{SC}}$ are respectively the voltage of the first and the second SC strand. Taking $N_{1,\mathrm{SC1}}$ as mass node, dividing both sides by Δz and considering the limit for $\Delta z \to 0$:

$$\begin{cases} \dfrac{\partial V}{\partial z} = -r_{\mathrm{l}} I(z), \\ \dfrac{\partial I}{\partial z} = -\dfrac{2V(z) - V_{2,\mathrm{SC}}}{r_{\mathrm{c}}}, \end{cases} \tag{E.5}$$

Replacing the second equation in the first:

$$\frac{\partial^2 I}{\partial z^2} = 2\frac{r_{\mathrm{l}}}{r_{\mathrm{c}}} I(z) = \frac{I(z)}{l_{\mathrm{diff}}^2}, \tag{E.6}$$

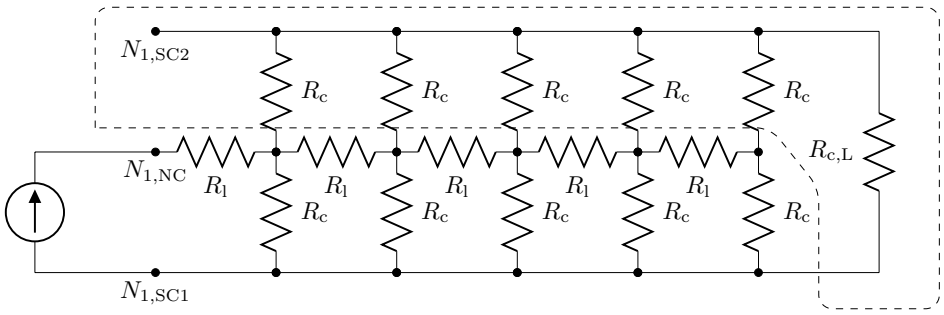

Figure E.3: Model of the inter-strand resistance measurement between one superconducting and one normal-conducting strand. The network enclosed in the dashed line is simplified with the star-mesh transformation.

being $\partial V_{2,\mathrm{SC}}/\partial z = 0$ and l_diff an equivalent *diffusion length*. The general solution for a domain $z \in [0; L]$ is:

$$I(z) = C_1 \exp\left(\frac{L-z}{l_\mathrm{diff}}\right) + C_2 \exp\left(\frac{z-L}{l_\mathrm{diff}}\right). \tag{E.7}$$

Applying the boundary condition $I(0) = I(L) = 0$, the solution is $I(z) = 0$, therefore no longitudinal current is present on the NC strand and the measured inter-strand resistance is, as expected:

$$R_{\mathrm{SC-SC}} = R_{\mathrm{c,L}}. \tag{E.8}$$

E.2 Resistive/Superconductor

To measure the NC-SC inter-strand resistance, the current generator should be inserted between nodes $N_{1,\mathrm{NC}}$ and $N_{1,\mathrm{SC1}}$, like in Figure E.3. The *star-mesh resistance transformation* can be employed to simplify the network:

$$R^{\boxtimes}_{i,j} = R^{\star}_i R^{\star}_j \sum_k \left(\frac{1}{R^{\star}_k}\right), \tag{E.9}$$

where $R^{\boxtimes}_{i,j}$ is the mesh resistance between nodes i and j, and $R^{\star}_i$ is the star resistance between the node i and the star center. Node $N_{1,\mathrm{SC2}}$ can be considered as star center, eliminating the SC strand not measured. Two further types of resistance are present in the resulting network:

- $R^{\boxtimes}_\mathrm{A}$, that are connected in parallel to the already existing inter-strand resistances between SC1 and NC. Their value can be computed with the sum of the inverse of the star resistances:

$$\sum_k \left(\frac{1}{R^{\star}_k}\right) = \frac{2L}{r_\mathrm{c}}. \tag{E.10}$$

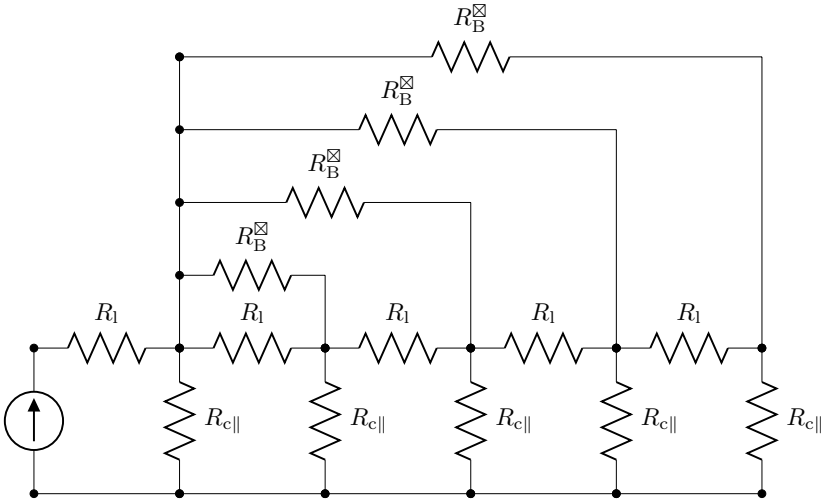

Figure E.4: Equivalent lumped network after star-mesh transformation. For clarity purposes, $R_{\mathrm{B}}^{\boxtimes}$ are represented only for the first NC node.

Therefore:

$$R_{\mathrm{A}}^{\boxtimes} = R_{\mathrm{c}} R_{\mathrm{c,L}} \frac{2L}{r_{\mathrm{c}}} = \frac{2r_{\mathrm{c}}}{\Delta z} = 2R_{\mathrm{c}}. \tag{E.11}$$

The resulting parallel resistance is:

$$R_{\mathrm{c}\parallel} = R_{\mathrm{A}}^{\boxtimes} \parallel R_{\mathrm{c}} = \frac{2}{3} R_{\mathrm{c}}. \tag{E.12}$$

- $R_{\mathrm{B}}^{\boxtimes}$, that are connected between one node of the NC strand and all the others. Their value is:

$$R_{\mathrm{B}}^{\boxtimes} = R_{\mathrm{c}} R_{\mathrm{c}} \frac{2L}{r_{\mathrm{c}}} = 2R_{\mathrm{c}} \frac{L}{\Delta z}. \tag{E.13}$$

The simplified circuit is represented in Figure E.4.

The following system of equations, similar to Eqs. (E.4), can be written at each NC network node:

$$\begin{cases} V(z+\Delta z) - V(z) = -R_{\mathrm{l}} I\left(z + \dfrac{\Delta z}{2}\right), \\ I\left(z + \dfrac{\Delta z}{2}\right) - I\left(z - \dfrac{\Delta z}{2}\right) = -\dfrac{V(z)}{R_{\mathrm{c}\parallel}} + \dfrac{\Delta z}{2R_{\mathrm{c}} L} \displaystyle\sum_{z'=0}^{L} [V(z') - V(z)]. \end{cases} \tag{E.14}$$

The sum can be rewritten as:

$$\frac{\Delta z}{2R_{\mathrm{c}} L} \sum_{z'=0}^{L} [V(z') - V(z)] = -\frac{V(z)}{2R_{\mathrm{c}}} + \frac{\Delta z}{2R_{\mathrm{c}} L} \sum_{z'=0}^{L} V(z'), \tag{E.15}$$

and Eqs. (E.14) become, replacing Eq. (E.12):

$$\begin{cases} V(z+\Delta z) - V(z) = -R_{\mathrm{l}} I\left(z + \dfrac{\Delta z}{2}\right), \\ I\left(z + \dfrac{\Delta z}{2}\right) - I\left(z - \dfrac{\Delta z}{2}\right) = -2\dfrac{V(z)}{R_{\mathrm{c}}} + \dfrac{\Delta z}{2R_{\mathrm{c}}L}\displaystyle\sum_{z'=0}^{L} V(z'). \end{cases} \tag{E.16}$$

Dividing each side by Δz and taking the limit for $\Delta z \to 0$:

$$\begin{cases} \dfrac{\partial V}{\partial z} = -r_{\mathrm{l}} I(z), \\ \dfrac{\partial I}{\partial z} = -2\dfrac{V(z)}{r_{\mathrm{c}}} + \dfrac{1}{2r_{\mathrm{c}}L}\displaystyle\int_0^L V(z')dz', \end{cases} \tag{E.17}$$

since the difference quotients tend to the space derivative and the sum tends to an integral. Deriving the second equation with z:

$$\frac{\partial^2 I}{\partial z^2} = -\frac{2}{r_{\mathrm{c}}}\frac{\partial V}{\partial z}, \tag{E.18}$$

since the last integral term is constant with space. Replacing the first equation in the second:

$$\frac{\partial^2 I}{\partial z^2} = 2\frac{r_{\mathrm{l}}}{r_{\mathrm{c}}} I(z) = \frac{I(z)}{l_{\mathrm{diff}}^2}, \tag{E.19}$$

where l_{diff} is the *diffusion length*:

$$l_{\mathrm{diff}} = \sqrt{\frac{1}{2}\frac{r_{\mathrm{c}}}{r_{\mathrm{l}}}} = \sqrt{\frac{1}{2}\frac{A_{\mathrm{str}} r_{\mathrm{c}}}{\rho_{\mathrm{E}}}} = d_{\mathrm{str}}\sqrt{\frac{\pi}{8}\frac{r_{\mathrm{c}}}{\rho_{\mathrm{E}}}}, \tag{E.20}$$

where d_{str} is the strand diameter.

The general solution is again Eq. (E.7), but the following boundary condition should be applied:

$$\begin{cases} I(0) = I_0, \\ I(L) = 0, \end{cases} \tag{E.21}$$

and the final solution is:

$$I(z) = I_0 \frac{\sinh\left(\dfrac{L-z}{l_{\mathrm{diff}}}\right)}{\sinh\left(\dfrac{L}{l_{\mathrm{diff}}}\right)}, \tag{E.22}$$

whereas for the voltage:

$$V(z) = \frac{r_{\mathrm{c}} I_0}{2\, l_{\mathrm{diff}}} \frac{\cosh\left(\dfrac{L-z}{l_{\mathrm{diff}}}\right)}{\sinh\left(\dfrac{L}{l_{\mathrm{diff}}}\right)} + \frac{1}{4\,L}\int_0^L V(z')dz'. \tag{E.23}$$

Integrating both sides between 0 and L:

$$Q = \int_0^L V(z')dz' = \frac{r_c I_0}{2} + \frac{Q}{4} \quad \Longrightarrow \quad Q = \frac{2}{3} r_c I_0, \tag{E.24}$$

therefore:

$$V(z) = I_0 R_0 \left(\frac{\cosh\left(\frac{L-z}{l_{diff}}\right)}{\sinh\left(\frac{L}{l_{diff}}\right)} + \frac{l_{diff}}{3L} \right), \tag{E.25}$$

where R_0 is:

$$R_0 = \frac{1}{2}\frac{r_c}{l_{diff}} = \frac{1}{d_{str}}\sqrt{\frac{2}{\pi}\rho_E r_c}. \tag{E.26}$$

The current and the voltage along the z coordinate are reported in Figure E.5a in terms of normalized quantities for $L = 10\, l_{diff}$.

The measured inlet resistance between NC and SC strand is therefore:

$$R_{NC-SC} = \frac{V(0)}{I(0)} = R_0 \left[\coth\left(\frac{L}{l_{diff}}\right) + \frac{l_{diff}}{3L} \right] \approx R_0, \tag{E.27}$$

where the approximation is valid if $L \gg l_{diff}$. For example, as shown in Figure E.5b, for $L = 10\, l_{diff}$ the term in parenthesis is 3% larger than unity.

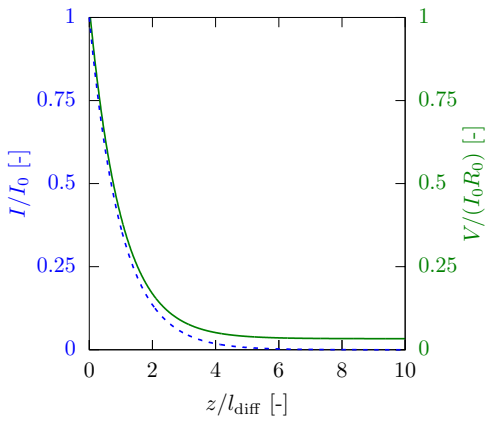

(a) Voltage (solid) and current (dashed) as a function of z/l_{diff} for $L = 10\, l_{diff}$.

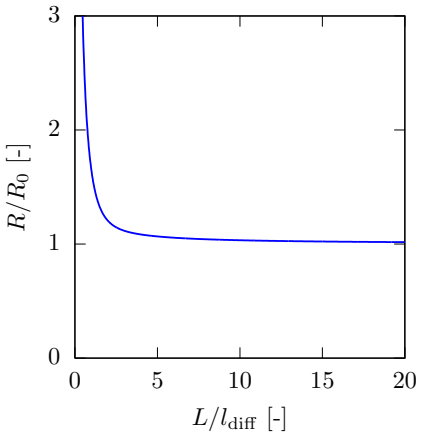

(b) Normalized resistance as a function of L/l_{diff}.

Figure E.5: Normalized voltage, current and resistance in the diffusion between a normal-conducting and a superconducting strand.

Acknowledgments

It is very difficult to describe the last three years, since they have been a strange mixture of conflicting experiences. During the PhD activities, I have been involved in challenging collaborations with some important scientific institutions, that have allowed me to meet and discuss with nice people and to learn from very talented scientists from all over the world. I will always be proud and grateful for the pleasant time and for the open-mindedness and that these experiences have given me. Nevertheless, during the PhD I have learned the difficulty in the pursuit of an objective: hard work is fundamental, but it is hardly sufficient in most cases. This aspect has been very frustrating for me, but it has been an absolutely necessary step for my personal maturation. These years have indeed taught me respect, humility, patience, sense of duty, that are more important than the complete understanding of a set of experimental data or the submission a scientific paper. This is the most important baggage that I will always carry with me.

Nothing of what I have done would have been possible without the collaboration of several people. First of all, I must thank enormously my supervisor Prof. Fabrizio Bellina, for its continuous support and its suggestions, in particular when my impatience and my lack of confidence were really above the alert level. I am very grateful to have worked with him, since I have learned a lot, from both a scientific and a human point of view.

Special thanks must be given to Prof. Pierluigi Ribani from University of Bologna, for our fruitful collaboration in the development of the THELMA code. I have really appreciated his availability in answering to each of my requests and questions, even when they were quite demanding and time-consuming.

I would like to thank the Centro Ricerche Frascati - ENEA in the persons of Dr. Antonio della Corte and Dr. Valentina Corato, that have involved us in the NAFASSY project, that has been something like the "fuse" that started my PhD activity. This thesis would have been poorer without their support.

I am very thankful to all the people at the laboratory SM18 - CERN (Geneva), in particular Dr. Marta Bajko and Dr. Hugo Bajas. I will never forget their kindness during my permanence at CERN. It has been a valuable experience for me and very profitable for the PhD activity, since it has enabled all the studies and analyses regarding Rutherford cables.

I want to thank people at Laboratorio LASA - INFN Milano for their nice collab-

oration, in particular Dr. Giovanni Volpini, for the support and advice he gave me since my degree dissertation, and for its contributions to the present work. I am also very thankful to Prof. Massimo Sorbi and to my colleague Vittorio Marinozzi, that have involved me in a collaboration regarding the quench protection of accelerator magnets [110], whose results are not reported here being a bit collateral to the main topic of this work.

Finally, I want to thank Prof. Carlo Nonino (University of Udine) for helpful discussions on numerical heat transfer, Prof. René Flükiger (University of Geneva) for remarks regarding the studies on voltage-current characteristics in superconducting wires, Dr. Peter J. Lee (NHMFL-FSU), Prof. Damian Hampshire (Durham University) and Dr. Denis Bessette (ITER/IO) for their consent to the reproduction of some images and data present in this work.

Ultimi, ma non per importanza, i ringraziamenti a chi mi è stato vicino e mi ha pazientemente supportato e sopportato in questi anni. Non posso che cominciare da mia moglie Michela, che è stata, è e sarà la persona più importante e speciale della mia vita. Un grazie immenso a mia madre, mio padre e mio fratello, che non mi hanno mai fatto mancare affetto e consigli, e alla famiglia di mia moglie, che mi ha accolto come un figlio. Come dimenticare poi i Tahita, Nicola, Simone, Tommaso e tutti i miei amici, con i quali ho condiviso tanti bei momenti di divertimento. Infine, un grazie sentito anche a tutti i compagni di ufficio che hanno reso un po' meno seriosi questi anni di lavoro, in particolare Davide a Ginevra, Michele e Piera a Udine.

Bibliography

A

[1] W. Abbas, A. Nijhuis, Y. Ilyin, B. ten Haken, and H. H. J. ten Kate. A fully automatic press for mechanical and electrical testing of full-size ITER conductors under transverse cyclic load. *AIP Conf. Proc.*, 711(1):51–58, 2004.

[2] M. Abramowitz and I. Stegun. *Handbook of Mathematical Functions with Formulas, Graphs, and Mathematical Tables*. Selected Government Publications. Wiley, 1972.

[3] A. A. Abrikosov. Magnetic properties of superconductors of the second group. *Sov. Phys. JETP*, 5(6), 1957.

[4] E. Acerbi, G. Ambrosio, L. Rossi, and G. Volpini. A detailed experimental investigation on the E-J characteristics of NbTi filaments and comparison with theoretical models. *IEEE T. Magn.*, 30(4):2296 – 2299, July 1994.

[5] A. Akhmetov, L. Bottura, M. Breschi, and P. Ribani. A theoretical investigation on current imbalance in flat two-layer superconducting cables. *Cryogenics*, 40(8–10):627–635, 2000.

[6] A. Akhmetov, A. Devred, and T. Ogitsu. Periodicity of crossover currents in a Rutherford-type cable subjected to a time-dependent magnetic field. *J. Appl. Phys.*, 75(6):3176–3183, 1994.

[7] A. Anghel and P. Bruzzone. JORDI, a test facility for measurement of contact resistance distribution in full-size conductor terminations. *IEEE T. Appl. Supercond.*, 14(2):1460–1463, June 2004.

[8] D. Arbelaez, A. Godeke, and S. O. Prestemon. An improved model for the strain dependence of the superconducting properties of Nb_3Sn. *Supercond. Sci. Technol.*, 22(2):025005, December 2009.

B

[9] J. Baixeras and G. Fournet. Pertes par deplacement de vortex dans un supraconducteur de type II non ideal. *J. Phys. Chem. Solids*, 28(8):1541–1547, 1967.

[10] M. Bajko, B. Bordini, S. Canfer, G. Ellwood, J. Feuvrier, M. Guinchard, M. Karppinen, C. Kokkinos, P. Manil, A. Milanese, L. Oberli, J. Perez, F. Regis, and G. de Rijk. The Short Model Coil (SMC) dipole: An R&D program towards Nb_3Sn accelerator magnets. *IEEE T. Appl. Supercond.*, 22(3):4002704, June 2012.

[11] A. Ballarino. Development of superconducting links for the Large Hadron Collider machine. *Supercond. Sci. Technol.*, 27(4):044024, 2014.

[12] R. E. Bank, W. M. Coughran, Jr., W. Fichtner, E. H. Grosse, and D. J. Rose. Transient simulation of silicon devices and circuits. *IEEE T. Electron Dev.*, 32(4):1992–2007, October 1985.

[13] J. Bardeen, L. N. Cooper, and J. R. Schrieffer. Theory of superconductivity. *Phys. Rev.*, 108:1175–1204, December 1957.

[14] E. Barzi, N. Andreev, M. Karppinen, V. Lombardo, F. Nobrega, D. Turrioni, R. Yamada, and A. Zlobin. Development and fabrication of Nb_3Sn Rutherford cable for the 11 T DS dipole demonstrator model. *IEEE T. Appl. Supercond.*, 22(3):6000805, June 2012.

[15] P. Bauer, H. Rajainmaki, and E. Salpietro. EFDA material data compilation for superconductor simulation. Technical report, EFDA, April 2007.

[16] J. Bednorz and K. Müller. Possible high t_c superconductivity in the Ba-La-Cu-O system. *Z. Phys. B Con. Mat.*, 64(2):189–193, 1986.

[17] F. Bellina. Defect detection in superconducting CICC joints by means of magnetic field measurements. *IEEE T. Appl. Supercond.*, 22(3):4804704, June 2012.

[18] F. Bellina, P. Bettini, and F. Trevisan. Electromagnetic analysis of superconducting cables and joints in transient regime. *IEEE T. Appl. Supercond.*, 14(2):1356–1359, June 2004.

[19] F. Bellina, D. Boso, B. Schrefler, and G. Zavarise. Modeling a multistrand SC cable with an electrical DC lumped network. *IEEE T. Appl. Supercond.*, 12(1):1408–1412, March 2002.

[20] F. Bellina and G. Manfreda. Electromagnetic and thermal analysis of the Enfasi magnet. Technical report, University of Udine, 2014.

[21] F. Bellina and G. Manfreda. Models of the resistive contact distribution in superconducting ITER CICC full size joints and terminations. *IEEE T. Appl. Supercond.*, 25(3):1–6, 2014.

[22] W. Bloem. Transient heat transfer to a forced flow of supercritical helium at 4.2 K. *Cryogenics*, 26(5):300 – 308, 1986.

[23] P. Bogacki and L. Shampine. A 3(2) pair of Runge - Kutta formulas. *Applied Mathematics Letters*, 2(4):321–325, 1989.

[24] B. Bordini, L. Bottura, G. Mondonico, L. Oberli, D. Richter, B. Seeber, C. Senatore, E. Takala, and D. Valentinis. Extensive characterization of the 1 mm PIT Nb_3Sn strand for the 13 T FRESCA2 magnet. *IEEE T. Appl. Supercond.*, 22(3):6000304, June 2012.

[25] L. Bottura. Modelling stability in superconducting cables. *Phys. C*, 310(1-4):316 –326, 1998.

[26] L. Bottura. A practical fit for the critical surface of Nb-Ti. *IEEE T. Appl. Supercond.*, 10(1):1054–1057, March 2000.

[27] L. Bottura and B. Bordini. $J_c(B, T, \varepsilon)$ parameterization for the ITER Nb_3Sn production. *IEEE T. Appl. Supercond.*, 19(3):1521–1524, June 2009.

[28] L. Bottura, M. Breschi, and M. Fabbri. Analytical solution for the current distribution in multistrand superconducting cables. *J. Appl. Phys.*, 92(12):7571–7580, 2002.

[29] L. Bottura, M. Breschi, and C. Rosso. Analysis of electrical coupling parameters in superconducting cables. *Cryogenics*, 43(3-5):233–239, 2003.

[30] L. Bottura, C. Rosso, and M. Breschi. A general model for thermal, hydraulic and electric analysis of superconducting cables. *Cryogenics*, 40(8-10):617–626, 2000.

[31] L. Bottura and O. Zienkiewicz. Quench analysis of large superconducting magnets. Part I: model description. *Cryogenics*, 32(7):659 – 667, 1992.

[32] T. Boutboul, L. Oberli, A. den Ouden, D. Pedrini, B. Seeber, and G. Volpini. Heat treatment optimization studies on PIT Nb_3Sn strand for the NED project. *IEEE T. Appl. Supercond.*, 19(3):2564–2567, June 2009.

[33] H. Brechna. *Superconducting Magnet Systems.* Technische Physik Einzeldarstellungen. Springer, Berlin, 1973.

[34] M. Breschi and P. Ribani. Electromagnetic modeling of the jacket in cable-in-conduit conductors. *IEEE T. Appl. Supercond.*, 18(1):18–28, March 2008.

[35] M. Breschi, P. Ribani, and F. Bellina. Electromagnetic analysis of the voltage-temperature characteristics of the iter tf conductor samples. *IEEE T. Appl. Supercond.*, 19(3):1512–1515, June 2009.

[36] M. Breschi, L. Trevisani, M. Boselli, L. Bottura, A. Devred, P. Ribani, and F. Trillaud. Minimum quench energy and early quench development in NbTi superconducting strands. *IEEE T. Appl. Supercond.*, 17(2):2702–2705, June 2007.

[37] F. Broggi. Progetto dei passanti di corrente per il ciclotrone superconduttore dell'Università di Milano. Master's thesis, Physics Department of Milan University, 1983.

[38] P. Bruzzone. The index n of the voltage-current curve, in the characterization and specification of technical superconductors. *Phys. C*, 401(1-4):7–14, 2004.

[39] P. Bruzzone, A. Anghel, A. Fuchs, G. Pasztor, B. Stepanov, M. Vogel, and G. Vecsey. Upgrade of operating range for SULTAN test facility. *IEEE T. Appl. Supercond.*, 12(1):520–523, March 2002.

[40] P. Bruzzone, M. Bagnasco, M. Calvi, F. Cau, D. Ciazynski, A. della Corte, A. Di Zenobio, L. Muzzi, A. Nijhuis, E. Salpietro, L. Richard, S. Turtu, A. Vostner, R. Wesche, and R. Zanino. Test results of two european ITER TF conductor samples in SULTAN. *IEEE T. Appl. Supercond.*, 18(2):1088–1091, June 2008.

[41] P. Bruzzone, B. Stepanov, R. Dettwiler, and F. Staehli. Results of contact resistance distribution in NbTi and Nb_3Sn ITER conductor termination. *IEEE T. Appl. Supercond.*, 17(2):1378–1381, June 2007.

[42] P. Bruzzone, B. Stepanov, and Y. Ilyin. Instrumentation of TFPRO2. Technical report, CRPP, October 2007.

[43] P. Bruzzone, B. Stepanov, R. Wesche, E. Salpietro, A. Vostner, K. Okuno, T. Isono, Y. Takahashi, H. C. Kim, K. Kim, A. Shikov, and V. Sytnikov. Results of a new generation of ITER TF conductor samples in SULTAN. *IEEE T. Appl. Supercond.*, 18(2):459–462, June 2008.

C

[44] J. R. Cash and A. H. Karp. A variable order Runge-Kutta method for initial value problems with rapidly varying right-hand sides. *ACM Trans. Math. Softw.*, 16(3):201–222, September 1990.

[45] F. Cau, P. Bruzzone, and M. Calvi. Interstrand resistance and contact resistance distribution on terminations of ITER short samples. *IEEE T. Appl. Supercond.*, 20(3):478–481, June 2010.

[46] L. Chua, C. Desoer, and E. Kuh. *Linear and Nonlinear Circuits*. McGraw-Hill series in electrical and computer engineering. McGraw-Hill, 1987.

[47] M. Ciotti, A. Nijhuis, P. L. Ribani, L. S. Richard, and R. Zanino. THELMA code electromagnetic model of ITER superconducting cables and application to the ENEA stability experiment. *Supercond. Sci. Technol.*, 19(10):987, 2006.

[48] A. Clark and J. Ekin. Defining critical current. *IEEE T. Magn.*, 13(1):38 – 40, January 1977.

[49] E. Collings, M. Sumption, E. Barzi, D. Turrioni, R. Yamada, A. Zlobin, Y. Ilyin, and A. Nijhuis. Effect of core width, placement, and condition on calorimetrically measured AC loss and interstrand contact resistance of stainless-steel-cored Nb_3Sn Rutherford cables. *IEEE T. Appl. Supercond.*, 18(2):1370–1373, June 2008.

[50] L. Cooley, P. Lee, and L. David. Conductor processing of low T_c materials: the alloy Nb–Ti. In *Handbook of superconducting materials*. CRC, 2003.

[51] M. Cooper, B. Mikic, and M. Yovanovich. Thermal contact conductance. *Int. J. Heat Mass Transfer*, 12(3):279–300, 1969.

[52] V. Corato, L. Affinito, A. Anemona, U. B. Vetrella, A. D. Zenobio, C. F. Zignani, R. Freda, G. Messina, L. Muzzi, M. Perrella, L. Reccia, G. Tomassetti, S. Turtù, and A. della Corte. Detailed design of the large-bore 8 T superconducting magnet for the NAFASSY test facility. *Supercond. Sci. Technol.*, 28(3):034005, 2015.

D

[53] W. M. de Rapper. *Thermal Stability of Nb_3Sn Rutherford Cables for Accelerator Magnets*. PhD thesis, University of Twente, 2014.

[54] A. Devred, I. Backbier, D. Bessette, G. Bevillard, M. Gardner, M. Jewell, N. Mitchell, I. Pong, and A. Vostner. Status of ITER conductor development and production. *IEEE T. Appl. Supercond.*, 22(3):4804909, June 2012.

[55] A. Devred, I. Backbier, D. Bessette, G. Bevillard, M. Gardner, C. Jong, F. Lillaz, N. Mitchell, G. Romano, and A. Vostner. Challenges and status of ITER conductor production. *Supercond. Sci. Technol.*, 27(4):044001, 2014.

[56] J. Dormand and P. Prince. A family of embedded Runge-Kutta formulae. *J. Comput. Appl. Math.*, 6(1):19–26, March 1980.

[57] G. Dorofejev, A. Imenitov, and E. Klimenko. Voltage current characteristics of type III superconductors. *Cryogenics*, 20(6):307–312, 1980.

[58] L. Dresner. *Stability of superconductors*. Selected topics in superconductivity. Plenum, New York, NY, 1995.

[59] E. S. Drexler, R. P. Reed, and N. J. Simon. *Properties of Copper and Copper Alloys at Cryogenic Temperatures*. NIST Mono. National Institute of Standards and Technology, Gaithersburg, MD, 1992.

E

[60] H. S. Edelman and D. C. Larbalestier. Resistive transitions and the origin of the n value in superconductors with a gaussian critical-current distribution. *J. Appl. Phys.*, 74(5):3312–3315, 1993.

[61] S. Egorov, I. Rodin, M. Astrov, and S. Fedotova. Periodicity of contacts between subcables in the multistage cable-in-conduit conductors and its effect on computation of AC losses and supercoupling currents. *IEEE T. Appl. Supercond.*, 19(3):2379–2382, June 2009.

[62] J. Ekin. Strain scaling law for flux pinning in practical superconductors. Part 1: Basic relationship and application to Nb_3Sn conductors. *Cryogenics*, 20(11):611–624, 1980.

[63] J. Ekin. Irregularity in NbTi filament area and electric field versus current characteristics. *Cryogenics*, 27(11):603–607, 1987.

[64] G. Eliashberg. Interactions between electrons and lattice vibrations in a superconductor. *Sov. Phys. JETP*, 11(3), 1960.

[65] L. Evseeva and S. Tanaeva. Thermophysical properties of epoxy composite materials at low temperatures. *Cryogenics*, 35(4):277–279, 1995.

F

[66] E. Fehlberg. Low order classical Runge-Kutta formulas with step-size control and their application to some heat transfer problems. Technical Report R-315, NASA, July 1969.

[67] P. Ferracin, G. Ambrosio, M. Anerella, F. Borgnolutti, R. Bossert, D. Cheng, D. Dietderich, H. Felice, A. Ghosh, A. Godeke, S. Bermudez, P. Fessia, S. Krave, M. Juchno, J. Perez, L. Oberli, G. Sabbi, E. Todesco, and M. Yu. Magnet design of the 150 mm aperture low-β quadrupoles for the high luminosity LHC. *IEEE T. Appl. Supercond.*, 24(3):1–6, June 2014.

[68] W. A. Fietz and W. W. Webb. Hysteresis in superconducting alloys - Temperature and field dependence of dislocation pinning in niobium alloys. *Phys. Rev.*, 178:657–667, February 1969.

[69] R. Flükiger, W. Goldacker, and R. Isernhagen. Characterization of bulk and multifilamentary Nb_3Sn and Nb_3Al by diffractometric and resistive measurements. In R. Reed and A. Clark, editors, *Advances in Cryogenic Engineering Materials*, volume 32 of *Advances in Cryogenic Engineering Materials*, pages 925–936. Springer US, 1986.

[70] N. Fogel and A. Sidorenko. Scaling behavior of resistive transitions in thin superconducting films. *Phys. Lett. A*, 68(5–6):456–458, 1978.

G

[71] K. W. Garrett and H. M. Rosenberg. The thermal conductivity of epoxy-resin / powder composite materials. *J. Phys. D: Appl. Phys.*, 7(9):1247, 1974.

[72] A. Godeke. *Performance Boundaries in Nb_3Sn Superconductors*. PhD thesis, University of Twente, June 2005.

[73] A. Godeke, A. den Ouden, A. Nijhuis, and H. ten Kate. State of the art powder-in-tube niobium–tin superconductors. *Cryogenics*, 48(7–8):308–316, 2008.

[74] A. Godeke, B. Haken, H. H. J. ten Kate, and D. C. Larbalestier. A general scaling relation for the critical current density in Nb_3Sn. *Supercond. Sci. Technol.*, 19(10):100, October 2006.

[75] L. P. Gorkov. Microscopic derivation of the Ginzburg-Landau equations in the theory of superconductivity. *Sov. Phys. JETP*, 9(6):1364–1367, 1959.

[76] C. Gorter and H. Casimir. On supraconductivity I. *Physica*, 1:306–320, 1934.

[77] V. Guritanu, W. Goldacker, F. Bouquet, Y. Wang, R. Lortz, G. Goll, and A. Junod. Specific heat of Nb_3Sn: the case for a second energy gap. *Phys. Rev. B*, 70:184526, November 2004.

H

[78] E. Hairer and G. Wanner. *Solving Ordinary Differential Equations II. Stiff and Differential-Algebraic Problems*. Springer, Berlin, 1996.

[79] D. Hampshire and H. Jones. Analysis of the general structure of the EI characteristic of high current superconductors with particular reference to a NbTi SRM wire. *Cryogenics*, 27(11):608–616, 1987.

[80] D. P. Hampshire and H. Jones. A detailed investigation of the E-J characteristic and the role of defect motion within the flux-line lattice for high-current-density, high-field superconducting compounds with particular reference to data on NbSn throughout its entire field-temperature phase space. *J. Phys. C Solid State*, 20(23):3533, 1987.

[81] M. Hosea and L. Shampine. Analysis and implementation of TR-BDF2. *Appl. Numer. Math.*, 20(1-2):21–37, February 1996.

I

[82] Y. Ilyin, A. Nijhuis, W. Abbas, P. Bruzzone, B. Stepanov, L. Muzzi, P. Gislon, and L. Zani. Effect of cyclic loading and conductor layout on contact resistance of full-size ITER PFCI conductors. *IEEE T. Appl. Supercond.*, 15(2):1359–1362, June 2005.

[83] Y. Ilyin, A. Nijhuis, and E. Krooshoop. Scaling law for the strain dependence of the critical current in an advanced ITER Nb_3Sn strand. *Supercond. Sci. Technol.*, 20(3):186, 2007.

[84] L. Imbasciati, G. Ambrosio, P. Bauer, D. Pedrini, V. Previtali, L. Rossi, and G. Volpini. Measurements and modeling of thermal conductivity of impregnated Nb_3Sn cable stacks. Technical Report TD-03-019, Fermilab, May 2003.

[85] F. Irie, Y. Tsujioka, and T. Chiba. Characteristics of critical current distributions for oxide superconductors estimated from V-I characteristics using Weibull function. *Supercond. Sci. Technol.*, 5(1S):S379, 1992.

J

[86] J. E. Jensen, R. B. Stewart, W. A. Tuttle, H. Brechna, and A. Prodell. *Selected Cryogenic Data Notebook*. Brookhaven National Laboratory, Upton, N.Y., 1980. Available at `http://www.bnl.gov/magnets/Staff/Gupta/cryogenic-data-handbook/index.htm`.

[87] R. Jones, E. Rhoderick, and A. Rose-Innes. Non-linearity in the voltage-current characteristic of a type-2 superconductor. *Phys. Lett. A*, 24(6):318–319, 1967.

[88] C. H. Joshi. *Thermal and Electrical Characteristics of Adiabatic Superconducting Solenoids during a Spontaneous Transition to the Resistive State*. PhD thesis, MIT, Boston, 1987.

K

[89] M. Kasen, G. R. MacDonald, J. D. H. Beekman, and R. E. Schramm. Mechanical, electrical and thermal characterization of G-10CR and G-11CR glass-cloth/epoxy laminates between room temperature and 4 K. In *Advances in Cryogenic Engineering*, volume 26, pages 235–244, New York, NY, 1980. Plenum.

[90] A. Kaufman and J. Pickett. Multifilament Nb_3Sn superconductor wire. *Bull. Am Phys*, 1970.

[91] C. Kittel and P. McEuen. *Introduction to solid state physics*. Wiley New York, 1976.

[92] G. S. Knapp, S. D. Bader, and Z. Fisk. Phonon properties of A15 superconductors obtained from heat-capacity measurements. *Phys. Rev. B*, 13(9):3783–3789, May 1976.

[93] M. Kohler. Zur magnetischen widerstandsänderung reiner metalle. *Ann. Phys.*, 424(1-2):211–218, 1938.

[94] N. Kozlenkova, V. Pantsyrnyi, A. Shikov, A. Vorobieva, and A. Mitin. Scaling of the V-I characteristics in the ITER type Nb_3Sn strands in relation to the applied field and temperature. *IEEE T. Appl. Supercond.*, 15(2):3450–3453, June 2005.

[95] N. Kozlenkova, G. Vedernikov, A. Shikov, L. Potanina, A. V. Filatov, A. Vorobieva, V. Pantsyrnyi, and I. Gubkin. Study on I_c(T, B) for the NbTi strand intended for ITER PF insert coil. *IEEE T. Appl. Supercond.*, 14(2):1028–1030, June 2004.

[96] E. J. Kramer. Scaling laws for flux pinning in hard superconductors. *J. Appl. Phys.*, 44(3):1360–1370, 1973.

[97] V. Z. Kresin. On the critical temperature for any strength of the electron-phonon coupling. *Phys. Lett. A*, 122(8):434–438, 1987.

L

[98] L. D. Landau and V. L. Ginzburg. On the theory of superconductivity. *Zh. Eksp. Teor. Fiz.*, 20:1064, 1950.

[99] H.-W. Lee, K.-C. Kim, and J. Lee. Review of maglev train technologies. *IEEE T. Magn.*, 42(7):1917–1925, July 2006.

[100] P. J. Lee. A comparison of superconductor critical currents. Available at `http://www.magnet.fsu.edu/magnettechnology/research/asc/plots.html`, September 2014.

[101] Y. Lei, Y. Yu, Y. Dai, and H. Nan. Measurements of interstrand thermal and electrical conductance in multistrand superconducting cables. *IEEE T. Appl. Supercond.*, 12(1):1052–1055, 2002.

[102] F. London and H. London. The Electromagnetic Equations of the Supraconductor. *Royal Society of London Proceedings Series A*, 149:71–88, March 1935.

[103] B. Lu and C. A. Luongo. Parametric estimation study of interstrand conductance in multi-strand superconducting cables. *Cryogenics*, 47(11-12):546–552, 2007.

[104] X. F. Lu and D. P. Hampshire. The field, temperature and strain dependence of the critical current density of a powder-in-tube Nb_3Sn superconducting strand. *Supercond. Sci. Technol.*, 23(2):025002, 2010.

[105] Y. Lvovsky, E. W. Stautner, and T. Zhang. Novel technologies and configurations of superconducting magnets for MRI. *Supercond. Sci. Technol.*, 26(9):093001, 2013.

M

[106] H. Maeda, Y. Tanaka, M. Fukutomi, and T. Asano. A new high-T_c oxide superconductor without a rare earth element. *JPN J. Appl. Phys.*, 27(2A):L209, 1988.

[107] G. Manfreda. Analysis of the quench propagation in Short Model Coil 3. TE-MSC internal note 23, CERN, December 2011.

[108] G. Manfreda. Nb_3Sn specific heat fit function for quench simulation. TE-MSC internal note 22, CERN, December 2011.

[109] G. Manfreda. Review of ROXIE's material properties database for quench simulation. TE-MSC internal note 24, CERN, December 2011.

[110] G. Manfreda, G. Ambrosio, V. Marinozzi, T. Salmi, M. Sorbi, and G. Volpini. Quench protection study of the Nb_3 Sn low-β quadrupole for the LHC luminosity upgrade. *IEEE T. Appl. Supercond.*, 24(3):1–5, June 2014.

[111] G. Manfreda, F. Bellina, V. Corato, A. della Corte, and P. L. Ribani. Coupled thermal and electromagnetic analysis of the NAFASSY magnet. *IEEE T. Appl. Supercond.*, 25(3):1–6, 2014.

[112] G. Manfreda, F. Bellina, and G. Volpini. Critical current statistical distribution and voltage–current characteristics in superconducting wires. *Supercond. Sci. Technol.*, 27(12):125005, 2014.

[113] G. Manfreda, L. Rossi, and M. Sorbi. MATPRO upgraded version 2012: a computer library of material property at cryogenic temperature. Technical Report INFN-12-04/MI, INFN, April 2012.

[114] P. Manil, F. Regis, J. Rochford, P. Fessia, S. Canfer, E. Baynham, F. Nunio, G. de Rijk, and P. Védrine. Magnetic design and code benchmarking of the SMC (Short Model Coil) dipole magnet. *IEEE T. Appl. Supercond.*, 20(3):184, June 2010.

[115] E. Marscin, R. Yamada, and A. Lee. 2D/3D ANSYS quench simulation manual. Technical Report TD-02-031, Fermilab, Batavia, Illinois, July 2002.

[116] T. Masuda, H. Yumura, M. Watanabe, H. Takigawa, Y. Ashibe, C. Suzawa, H. Ito, M. Hirose, K. Sato, S. Isojima, C. Weber, R. Lee, and J. Moscovic. Fabrication and installation results for Albany HTS cable. *IEEE T. Appl. Supercond.*, 17(2):1648–1651, June 2007.

[117] B. T. Matthias, T. H. Geballe, and V. B. Compton. Superconductivity. *Rev. Mod. Phys.*, 35:1–22, January 1963.

[118] B. T. Matthias, T. H. Geballe, S. Geller, and E. Corenzwit. Superconductivity of Nb_3Sn. *Phys. Rev.*, 95:1435, September 1954.

[119] M. S. McAshan. MIITs integrals for copper and for Nb-46.5wt% Ti. Technical Report SSC-N-468, SSC Laboratory, February 1988.

[120] W. L. McMillan. Transition temperature of strong-coupled superconductors. *Phys. Rev.*, 167:331–344, March 1968.

[121] W. Meissner and R. Ochsenfeld. Ein neuer Effekt bei Eintritt der Supraleitfähigkeit. *Naturwissenschaften*, 21:787–788, November 1933.

[122] N. Mitchell, A. Devred, P. Libeyre, B. Lim, and F. Savary. The ITER magnets: Design and construction status. *IEEE T. Appl. Supercond.*, 22(3):4200809, June 2012.

[123] Y. Miyoshi, Y. Ilyin, W. Abbas, and A. Nijhuis. AC loss, inter-strand resistance, and mechanical properties of an option-II ITER CICC up to 30,000 cycles in the press. *IEEE T. Appl. Supercond.*, 21(3):1944–1947, 2011.

[124] D. Montgomery and H. Wizgall. Measurement of the upper critical field vanadium - gallium alloys. *Physics Letters*, 22(1):48 – 50, 1966.

[125] G. H. Morgan. Eddy currents in flat metal-filled superconducting braids. *J. Appl. Phys.*, 44(7):3319–3322, 1973.

[126] G. Moritz. Rapidly-cycling superconducting accelerator magnets for FAIR at GSI. In *Particle Accelerator Conference, 2007. PAC. IEEE*, pages 3745–3749, June 2007.

N

[127] J. Nagamatsu, N. Nakagawa, T. Muranaka, Y. Zenitani, and J. Akimitsu. Superconductivity at 39 K in magnesium diboride. *Nature*, 410(6824):63–64, March 2001.

[128] C. Nichols and D. Clarke. Critical currents in inhomogeneous triangular Josephson arrays: a model for polycrystalline superconductors. *Acta Metall. Mater.*, 39(5):995–1002, 1991.

[129] A. Nijhuis, Y. Ilyin, W. Abbas, B. ten Haken, and H. ten Kate. Change of interstrand contact resistance and coupling loss in various prototype ITER NbTi conductors with transverse loading in the Twente cryogenic cable press up to 40,000 cycles. *Cryogenics*, 44(5):319–339, 2004.

[130] A. Nijhuis, H. Knoopers, Y. Ilyin, A. Godeke, B. ten Haken, and H. ten Kate. Effect of self-field and current non-uniformity on the voltage–temperature characteristic of the ITER central solenoid insert coil by numerical calculations. *Cryogenics*, 42(8):469–483, 2002.

[131] A. Nijhuis, N. Noordman, H. ten Kate, N. Mitchell, and P. Bruzzone. Electromagnetic and mechanical characterisation of ITER CS-MC conductors affected by transverse cyclic loading. II. Interstrand contact resistances. *IEEE T. Appl. Supercond.*, 9(2):754–757, 1999.

[132] S. Nishijima, S. Eckroad, A. Marian, K. Choi, W. S. Kim, M. Terai, Z. Deng, J. Zheng, J. Wang, K. Umemoto, J. Du, P. Febvre, S. Keenan, O. Mukhanov, L. D. Cooley, C. P. Foley, W. V. Hassenzahl, and M. Izumi. Superconductivity and the environment: a roadmap. *Supercond. Sci. Technol.*, 26(11):113001, 2013.

[133] NIST. Material properties database. Available at `http://cryogenics.nist.gov/MPropsMAY/materialproperties.htm`, September 2014.

O

[134] D. K. Oh, S. Oh, H. C. Kim, H. Choi, C. Lee, W. Park, and K. Kim. Transverse load versus mechanical characteristics and inter-strand resistances in the cable of the Option 2 specification for ITER TF conductor. *IEEE T. Appl. Supercond.*, 20(3):495–498, 2010.

[135] H. K. Onnes. The liquefaction of helium. *Leiden Commun.*, 108, July 1908.

[136] H. K. Onnes. Further experiments with liquid helium. G: On the electrical resistance of pure metals, etc. VI. On the sudden change in the rate at which the resistance of mercury disappears. *Leiden Commun.*, 124C, 1911.

P

[137] S. Patankar. *Numerical Heat Transfer and Fluid Flow.* Series in computational methods in mechanics and thermal sciences. Taylor & Francis, 1980.

R

[138] F. Regis, P. Manil, P. Fessia, M. Bajko, and G. de Rijk. Mechanical design of the SMC (Short Model Coil) dipole magnet. *IEEE T. Appl. Supercond.*, 20(3):204–207, June 2010.

[139] P. L. Ribani. Influence of wiring in the signal from two voltage taps during current ramp. Technical report, University of Bologna, December 2007.

[140] L. S. Richard, M. Bagnasco, and R. Zanino. Multi-solid multi-channel Mithrandir (M^3) code for thermal–hydraulic modelling of ITER cable-in-conduit superconductors. *Fusion Eng. Des.*, 82(5-14):1607–1613, 2007.

[141] D. Richter, J. D. Adam, J.-M. Depond, D. Leroy, and L.-R. Oberli. DC measurement of electrical contacts between strands in superconducting cables for the LHC main magnets. *IEEE T. Appl. Supercond.*, 7(2):786–792, June 1997.

[142] B. W. Roberts. Survey of superconductive materials and critical evaluation of selected properties. *J. Phys. Chem. Ref. Data*, 5(3):581–822, 1976.

[143] G. Rolando. *Cable-In-Conduit-Conductors for Fusion Magnets.* PhD thesis, University of Twente, 2013.

[144] G. Rolando, E. van Lanen, J. van Nugteren, W. Offringa, H. ten Kate, Y. Ilin, B. Lim, F. Simon, and A. Nijhuis. Analysis of heat load, current margin and current nonuniformity in ITER PF coil joints. *IEEE T. Appl. Supercond.*, 23(3):4201405, June 2013.

[145] L. Rossi. Superconductivity: its role, its success and its setbacks in the Large Hadron Collider of CERN. *Supercond. Sci. Technol.*, 23(3):034001, 2010.

[146] L. Rossi and M. Sorbi. QLASA: a computer code for quench simulation in adiabatic multicoil superconducting windings. Technical Report TC-04-13, INFN, 2004.

[147] D. L. Rule, D. R. Smith, and L. L. Sparks. Thermal conductivity of polypyromellitimide film with alumina filler particles from 4.2 to 300 K. *Cryogenics*, 36(4):283–290, August 1990.

[148] S. Russenschuck. *Field computation for accelerator magnets: analytical and numerical methods for electromagnetic design and optimization*. Wiley, Weinheim, 2010.

S

[149] L. Salerno and P. Kittel. Thermal contact conductance. Technical Report 110429, NASA, February 1997.

[150] C. Scheuerlein, G. Willering, A. Verweij, A. Bonasia, L. Oberli, M. Taborelli, and R. Richter. Aluminum strand coating for increasing the interstrand contact resistance in Rutherford type superconducting cables. *IEEE T. Appl. Supercond.*, 19(3):2463–2465, June 2009.

[151] N. Schwerg, H. Henke, and S. Russenschuck. *Numerical calculation of transient field effects in quenching superconducting magnets*. PhD thesis, Berlin, Berlin, Tech. U., Berlin, November 2009.

[152] B. Seeber. *Handbook of applied superconductivity*, volume 2. CRC press, 1998.

[153] K. Seo, K. Fukuhara, and M. Hasegawa. Analyses for inter-strand coupling loss in multi-strand superconducting cable with distributed contact resistance between strands. *Cryogenics*, 41(2):131 – 137, 2001.

[154] A. Shikov, V. Pantsyrny, A. Vorobieva, S. Sudyev, S. Sergeev, N. Beliakov, N. Kozlenkova, V. Sytnikov, A. Taran, A. Rychagov, and P. Bruzzone. Development of a new RF produced internal tin ITER TF conductor sample for testing in SULTAN facility. *IEEE T. Appl. Supercond.*, 18(2):1076–1079, June 2008.

[155] L. Shubnikov, V. Khotkewitsch, Y. D. Schepelev, and Y. N. Rjabinin. Magnetic properties of superconducting metals and alloys. *Zh. Eksp. Teor. Fiz*, 7:221–237, 1937.

[156] R. J. Soulen. Possible explanation for the shape of I-V curves of superconductors and a more meaningful definition of I_c. *IEEE T. Appl. Supercond.*, 3(1):1261–1264, March 1993.

[157] Z. Stekly and J. Zar. Stable superconducting coils. *IEEE T. Nucl. Sci.*, 12:367, June 1965.

[158] M. Stemmle, F. Merschel, M. Noe, and A. Hobl. AmpaCity - installation of advanced superconducting 10 kV system in city center replaces conventional 110 kV cables. In *2013 IEEE International Conference on Applied Superconductivity and Electromagnetic Devices (ASEMD)*, pages 323–326, October 2013.

[159] N. Steve, M. Nassi, M. Bechis, P. Ladiè, N. Kelley, and C. Wakefield. High temperature superconducting cable field demonstration at Detroit Edison. *Phys. C*, 354(1–4):49 –54, 2001.

[160] L. Summers, M. Guinan, J. Miller, and P. Hahn. A model for the prediction of Nb_3Sn critical current as a function of field, temperature, strain, and radiation damage. *IEEE T. Magn.*, 27(2):2041–2044, March 1991.

T

[161] D. M. J. Taylor and D. P. Hampshire. Relationship between the n-value and critical current in Nb_3Sn superconducting wires exhibiting intrinsic and extrinsic behaviour. *Supercond. Sci. Technol.*, 18(12):S297, 2005.

[162] D. M. J. Taylor and D. P. Hampshire. The scaling law for the strain dependence of the critical current density in Nb_3Sn superconducting wires. *Supercond. Sci. Technol.*, 18(12):S241, 2005.

[163] D. M. J. Taylor, S. Keys, and D. P. Hampshire. E–J characteristics and n-values of a niobium-tin superconducting wire as a function of magnetic field, temperature and strain. *Phys. C*, 372–376(3):1291–1294, 2002.

[164] M. Tinkham. Resistive transition of high-temperature superconductors. *Phys. Rev. Lett.*, 61:1658–1661, October 1988.

[165] M. Tinkham. *Introduction to superconductivity.* McGraw Hill, 1996.

[166] E. Todesco, H. Allain, G. Ambrosio, G. Arduini, F. Cerutti, R. De Maria, L. Esposito, S. Fartoukh, P. Ferracin, H. Felice, R. Gupta, R. Kersevan, N. Mokhov, T. Nakamoto, I. Rakno, J. Rifflet, L. Rossi, G. Sabbi, M. Segreti, F. Toral, Q. Xu, P. Wanderer, and R. van Weelderen. A first baseline for the magnets in the high luminosity LHC insertion regions. *IEEE T. Appl. Supercond.*, 24(3):1–5, June 2014.

[167] E. Tonti. A direct discrete formulation of field laws: The cell method. *Comput. Model. Eng. Sci.*, 2(2):237–258, 2001.

[168] Y. Tsui and D. P. Hampshire. Critical current scaling and the pivot-point in Nb_3Sn strands. *Supercond. Sci. Technol.*, 25(5):054008, 2012.

V

[169] D. F. Valentinis, C. Berthod, B. Bordini, and L. Rossi. A theory of the strain-dependent critical field in Nb_3Sn based on anharmonic phonon generation. *Supercond. Sci. Technol.*, 27(2):025008, 2014.

[170] D. Van Delft and P. Kes. The discovery of superconductivity. *Phys. Today*, 63(9):38–43, 2010.

[171] H. van der Vorst. Bi-CGSTAB: A fast and smoothly converging variant of Bi-CG for the solution of nonsymmetric linear systems. *SIAM J. Sci. Stat. Comp.*, 13(2):631–644, 1992.

[172] E. van Lanen and A. Nijhuis. JackPot: A novel model to study the influence of current non-uniformity and cabling patterns in cable-in-conduit conductors. *Cryogenics*, 50(3):139–148, 2010.

[173] S. W. Van Sciver. *Helium Cryogenics*. International cryogenics monograph series. Plenum, New York, NY, 1986.

[174] A. P. Verweij. *Electrodynamics of superconducting cables in accelerator magnets*. PhD thesis, Twente University, September 1995.

[175] A. P. Verweij. CUDI: A model for calculation of electrodynamic and thermal behaviour of superconducting Rutherford cables. Technical Report CERN-AT-2006-005, CERN, Geneva, August 2006.

[176] F. Voelker. Resistance in small, twisted, multicore superconducting wires. *Part. Accel.*, 1:205–207, 1970.

[177] G. Volpini, F. Alessandria, G. Bellomo, P. Fabbricatore, S. Farinon, U. Gambardella, G. Manfreda, R. Musenich, M. Quadrio, and M. Sorbi. AC losses measurement of the DISCORAP model dipole magnet for the SIS300 synchrotron at FAIR. *IEEE T. Appl. Supercond.*, 24(3):4000205, 2014.

[178] G. Volpini, F. Alessandria, G. Bellomo, P. Fabbricatore, S. Farinon, U. Gambardella, R. Musenich, M. Sorbi, B. Karlemo, and M. Holm. Low loss Nb-Ti superconducting Rutherford cable manufacture for the SIS300 INFN model dipole. *IEEE T. Appl. Supercond.*, 21(3):3334–3337, June 2011.

[179] A. Vostner, P. Bauer, R. Wesche, U. Besi Vetrella, B. Stepanov, A. della Corte, A. Portone, E. Salpietro, and P. Bruzzone. Development of the EFDA dipole high field conductor. *IEEE T. Appl. Supercond.*, 18(2):544–547, June 2008.

W

[180] F. J. Walker and A. C. Anderson. Thermal conductivity and specific heat of a glass-epoxy composite at temperatures below 4 K. *Rev. Sci. Instrum.*, 52(3):471–472, 1981.

[181] C. R. Walters. Design of multistrand conductors for superconducting magnet windings. Technical Report BNL-18928. AADD-74-2, Brookhaven National Laboratory, Upton, NY, January 1974.

[182] X. Wang, G. Ambrosio, F. Borgnolutti, M. Buehler, G. Chlachidze, D. Dietderich, J. DiMarco, H. Felice, P. Ferracin, A. Ghosh, A. Godeke, M. Marchevsky, D. Orris, S. Prestemon, G. Sabbi, C. Sylvester, M. Tartaglia, E. Todesco, G. Velev, and P. Wanderer. Multipoles induced by inter-strand coupling currents in LARP Nb_3Sn quadrupoles. *IEEE T. Appl. Supercond.*, 24(3):4002607, June 2014.

[183] W. H. Warnes. A model for the resistive critical current transition in composite superconductors. *J. Appl. Phys.*, 63(5):1651–1662, 1988.

[184] W. Weibull. A statistical distribution function of wide applicability. *J. Appl. Mech.*, 18:293–297, 1951.

[185] C. N. Whetstone and C. E. Roos. Thermal phase transitions in superconducting Nb-Zr alloys. *J. Appl. Phys.*, 36(3):783–791, 1965.

[186] G. K. White and S. J. Collocott. Heat capacity of reference materials: Cu and W. *J. Phys. Chem. Ref. Data*, 13(4):1251–1257, 1984.

[187] G. Willering. *Stability of Superconducting Rutherford Cables for Accelerator Magnets*. PhD thesis, University of Twente, 2009.

[188] M. N. Wilson. *Superconducting magnets*. Mono. Cryog. Clarendon Press, Oxford, 1983.

[189] M. N. Wilson. NbTi superconductors with low AC loss: A review. *Cryogenics*, 48(7–8):381 – 395, 2008.

[190] M. K. Wu, J. R. Ashburn, C. J. Torng, P. H. Hor, R. L. Meng, L. Gao, Z. J. Huang, Y. Q. Wang, and C. W. Chu. Superconductivity at 93 K in a new mixed-phase Y-Ba-Cu-O compound system at ambient pressure. *Phys. Rev. Lett.*, 58:908–910, March 1987.

Y

[191] H. Yumura, Y. Ashibe, H. Itoh, M. Ohya, M. Watanabe, T. Masuda, and C. Weber. Phase II of the Albany HTS Cable Project. *IEEE T. Appl. Supercond.*, 19(3):1698–1701, June 2009.

Z

[192] S. Zacks. *Introduction to reliability analysis*. Springer, 1992.

[193] T. Zickler. Basic design and engineering of normal-conducting, iron-dominated electromagnets. *ArXiv e-prints*, March 2011.

List of Figures

List of Tables

List of Symbols

$\mathbf{A}$	Magnetic vector potential	(V·s)/m
A_{st}	Strand cross-section area	m^2
$\mathbf{B}$	Magnetic induction	T
B_{c}	Critical induction	T
B_{c2}	Upper critical induction	T
$B_{\mathrm{c2,0}}$	Upper critical induction at zero kelvin	T
c_{p}	Specific heat capacity at constant pressure	J/(K· kg)
d_{st}	Strand diameter	m
$\mathbf{E}$	Electric field	V/m
E_{c}	Critical electric field	V/m
ε	Strain	%
ε_{A}	Applied strain	%
ε_{m}	Intrinsic strain	%
f_{void}	Void fraction	%
G	Generation function	$\mathrm{W/m}^3$
$\mathbf{H}$	Magnetic field	A/m
h	Specific entalphy	J/K
h_{c}	Convective heat transfer coefficient	$\mathrm{W/(m}^2\mathrm{\cdot K)}$
I	Current	A
I_{c}	Critical current	A
$\mathbf{J}_{\mathrm{c}}$	Critical current density	$\mathrm{A/m}^2$
$\mathbf{J}_{\mathrm{e}}$	Engineering critical current density	$\mathrm{A/m}^2$
$\mathbf{J}_{\mathrm{t}}$	Transport current density	$\mathrm{A/m}^2$

k	Thermal conductivity	W/(K· m)
l_{diff}	Diffusion length	m
l_{tr}	Transposition pitch	m
$\dot{m}$	Mass flow rate	kg/s
n	n-index or n-value	-
N_{ce}	Number of cable elements	-
N_{em}	Number of longitudinal electromagnetic elements	-
N_{je}	Number of jacket elements	-
N_{st}	Number of cable strands	-
N_{th}	Number of longitudinal thermal elements	-
R_{a}	Adjacent inter-strand resistance in Rutherford cables	Ω
R_{c}	Cross-over inter-strand resistance in Rutherford cables	Ω
r_{c}	Equivalent inter-strand resistance per unit length in CICCs	Ω·m
$r_{\mathrm{c}}^{\mathrm{jck-pet}}$	Equivalent jacket-petal resistance per unit length in CICCs	Ω·m
$r_{\mathrm{c}}^{\mathrm{pet}}$	Equivalent inter-petal resistance per unit length in CICCs	Ω·m
ρ	Mass density	kg/m^3
ρ_{E}	Electrical resistivity	Ω· m
ρ_{ff}	Flux-flow resistivity	Ω· m
RRR	Residual resistivity ratio	-
t	Time	s
T	Temperature	K
T_0	Coolant temperature	K
T_{c}	Critical temperature	K
$T_{\mathrm{c},0}$	Critical temperature at zero field	K
T_{cs}	Current-sharing temperature	K
T_{g}	Generation temperature	K
$\boldsymbol{\Theta}$	Phase set	rad
t_i	Twist pitch of the i^{th} stage	m
v	Electric voltage	V
v_{lq}	Longitudinal quench propagation velocity	m/s

Index